A COMBINATORIAL APPROACH FOR EXPLORING FUEL CELL ELECTROCATALYSTS

A Dissertation

Presented to the Faculty of the Graduate School

of Cornell University

In Partial Fulfillment of the Requirements for the Degree of

Doctor of Philosophy

by

Michele Evelyn Tague

August 2011

A COMBINATORIAL APPROACH FOR EXPLORING FUEL CELL ELECTROCATALYSTS

Michele Evelyn Tague, Ph. D.

Cornell University 2011

Fuel cells represent an alternative energy technology with the potential for providing more efficient means for energy conversion. However, their widespread deployment has been hampered by materials limitations, especially for the catalysts as they can be expensive, easily poisoned, and/or unstable over time. In order to accelerate the discovery and development of electrocatalysts that enhance fuel cell performance, a high throughput method is employed to screen many compositions and phases simultaneously. Preparation of the composition-spread libraries is achieved via cosputtering of multiple elements onto a Ta- or Ti-coated 3-inch Si wafer. These samples are screened as anode electrocatalysts using a fluorescence assay with quinine as the fluorescent probe. A key development is the characterization of these thin films via X-ray diffraction at Cornell's High Energy Synchrotron Source (CHESS). Systems of interest are discussed, including Pt-Zn, Pt-Ta, Pt-M alloys (M= transition metal at concentrations below 40%). Compositions exhibiting promising activity for specific fuels in the fluorescence tests are further characterized using a scanning electrochemical minicell. Alternative materials are introduced, i.e. nitrides and carbides, as well as non-Pt containing metal compositions. Fundamental studies on understanding fuel oxidation in neutral pH are described and further development of the fluorescence screening methodology for the cathode is presented.

BIOGRAPHICAL SKETCH

Michele Evelyn Tague was born in San Angelo, Texas on October 11, 1985 to Thomas Joseph Tague, Jr., and Judith Tague. Her parents did not know it at the time but she would be the oldest of six children and as a result she had many opportunities to care for and teach her younger siblings. She willingly accepted responsibilities and her parents even commented how she was "born older."

Her love for science began in grade school and blossomed from her love of mathematics. She fondly recalls a time when her father was a post-doctoral researcher at the University of Virginia, Charlottesville, VA, and as she waited for him, he would assign her algebra problems to work out. She loved solving these problems; they made sense to her and came easily. In later years, her father would often come to her classroom for science demonstrations especially related to his career. "Mol-a-q-lar spec-tra-sco-py" (molecular spectroscopy) would be what he recited to the children and with much difficulty the children would repeat it back to him with some practice. The 4th grade students could not completely grasp the idea of molecular spectroscopy but the model kits and demonstrations were exciting and were what began this young girl's curiosity in science.

Throughout the years Michele took every opportunity she could to learn and excel in mathematics. For instance in 5th grade, her teacher, Mr. Barnacoat, contrived a model for students to understand the relationship between large numbers (i.e. 1 million) and the volume the amount would consume. To visualize a million of something, the students had the menial task of collecting Snap-caps (milk-jug caps) on a weekly basis from all the classes in the school and perform statistical calculations to monitor the growth of the bottle caps over time. The ultimate goal was 1 million snap-caps and then to exhibit the amount to the entire school. As added incentive, the students gained snap-cap money which could be spent on different items at the end

of the year. Michele greatly enjoyed this process and excitedly volunteered to be treasurer for this project.

The manipulation of numbers continued to fascinate her throughout middle school and high school both in her classes and various clubs, i.e. math club and treasurer for many other clubs. Because of this motivation, she was always the youngest in her math classes, taking algebra 1 in middle school continuing on to finish calculus in her junior year in high school. Her family moved to Richmond, NH, during her junior year and because there were no upper level math courses offered in her high school, she opted to take college level classes during her senior year. At Franklin Pierce College, she took Chemistry I, Calculus III, and Physics. During the second half of her senior year, she transferred some of her classes to Keene State College, continuing with Chemistry II and Differential Equations.

She decided to continue her undergraduate education at Keene State College, where she eventually settled on a chemistry degree with a mathematics minor after contemplating pursuing a dual PhD/MD program then a mathematics major and finally chemistry. She not only found that chemistry was a good way to implement what she learned in math but also that chemistry applied to EVERYTHING! The possibilities were endless! She also found great joy in sharing her excitement through tutoring and as a teaching assistant.

The logical next step was to continue on to graduate school, and with encouragement from her professors, parents, and mentors at Markem, she applied and was accepted to a graduate program in chemistry at Cornell University beginning Fall 2006. During her first year of rigorous physical chemistry classes, she joined Professor Héctor D. Abruña's research lab, where the application of energy research excited her. Her main research projects were high throughput combinatorial screening for fuel cell anode electrocatalysts and developing a general platform for antibody detection using the Antibody Catalyzed Water Oxidation Pathway

(ACWOP). The experiences she had while at Cornell are invaluable to her, where she participated in many conferences, collaborated with many diverse groups on campus, some of which include: materials science, immunology, biology, and veterinary medicine, and had many opportunities to learn and work with a wide range of instrumentation such as SECM, CHESS, STM, AFM, etc. Her time at Cornell also helped her grow as an individual, gaining confidence and leadership qualities as she organized and directed projects. Outside the lab, she enjoyed time with friends, especially Emily Hallstrom, Ashley Egan, and Mindi Martin, participated in intramural sports (basketball, flag football and softball), and many church activities. After graduation, she has plans to pursue a post-doc position at Northeastern University, Boston, MA, with Prof. Eugene Smotkin.

To my family and friends.

ACKNOWLEDGMENTS

First of all, I would like to express my appreciation to my advisor, Prof. Héctor Abruña, for his guidance, encouragement and willingness to involve me in many projects over my graduate career. He has been seminal to my growth in confidence in the lab as well as at conferences and as an individual. I always appreciated his confidence in his students and postdocs, always saying they were the experts in the area or in a technique. He has made the working environment one for instigating complex ideas and problems and asking tough questions.

Professors Frank DiSalvo and Bruce van Dover not only served on my committee but also greatly aided in my research with discussions in our combi meetings and in my academic endeavors. Their guidance has been crucial to our progress in the combi efforts and brought to the table their much needed expertise. Additionally, I would like to thank Professor Abraham Stroock for serving as proxy for my A-exam at such short notice.

I would especially like to thank John Gregoire for the instrumental setup, computer programming, thin film synthesis and assistance with physical characterization (XRD, SEM, AFM). My work would not be possible without his help. Maxim Kostylev played an important role in sputtering thin films for the Pt-Zn and Pt-Sn-X series as well as XRD and SEM on these samples. Anna Legard provided insight on the data organization, the generation of Pd-Rh-Ta samples, and help with reviewing my electrochemistry on a regular basis. Eva Smith assisted with DFT calculations especially for the Pt-M alloys and the carbides. In the Pt-Mo-N system, after John Gregoire sputtered the Pt-Mo film, Akira Miura provided the nitride synthesis and physical characterization including XRD, SEM, and XPS. Jon Petrie implemented the candidate fluorescent indicator, umbelliferone, for oxygen reduction and developed a research project screening for oxygen reduction catalysts.

These combi efforts would not exist without the creation of the combi thrust by Jing Jin and Mark Prochaska. I could not forget the other people who collaborated on the combi project including: Prof. Richard Hennig, Paul Mutolo, Raymond Burns, Chinmayee Subban, Brian Leonard, Deli Wang, and CHESS staff – Darren Dale and Alex Kazimirov. The undergraduates that assisted on the series of projects were: Sophie Cohen, Yu Kambe, Garret Moniz, Sahr Kahn (summer student), Miguel Caban (REU student), and Sumana Raj (in Poul Peterson's group).

I would like to thank all the collaborators for the biosensor project. I started out working with Suddho Nad and Nicolas da Mota and was fortunate to work with such an energizing group that also included: Liz Welch, Norah Smith, and Abhinav Rastogi, Youyoung Xu, and later Hongjun Chen. Helpful discussions were had during our biosensor meetings with Professors Barbara Baird and Christopher Ober. I also appreciated SECM training by Maurizio Carano, a visiting scientist from Italy.

Lastly, my experience at Cornell would not be complete with all the people I have met and gotten to know over the years in Professor Abruña's group. I want to give a special thanks to David Finkelstein and Eric Rus for their friendship and help in understanding all things electrochemistry and more! The other group members I have had the privilege to know are: Mitk'El Santiago, Michael Lowe, Stephen Burkhardt, Sean Conte, Joanna (Cen) Tan, Jimmy John, Nicole Ritzert, Gabriel Rodriguez-Calero, Alex (Yingchao) Yu, Tam Troung, Katie Silberstein, Kenneth Hernandez-Burgos, Dr. Yi Liu, Dr. Hongsen Wang, Dr. Yu-Wu Zhong, Dr. Jean Sanabria, Dr. Neus Cusco, Dr. Nicolas Mota, Dr. Jie Gao, Dr. Hualei Qian, Dr. Josh Parks, Dr. Matt Rigsby, Dr. Joaquin Rodriguez-Lopez, Dr. Weidong Zhou, Dr. Geoffrey Hutchison, Dr. Burak Ulgut, Dr. Jamie Cohen, Dr. Jay Henderson, Dr. Suddhasattwa Nad, Dr. Yasuyuki Kiya, Dr. Futoshi Matsumoto, Tercio Paulo, and Izaura Diogenes (Brazil).

TABLE OF CONTENTS

CHAPTER 1

Introduction to Fuel Cells and Anode Electrocatalysts

1.1 Motivation

As one of the greatest global issues, energy production and storage are imperative research directions with the growing demand for energy in not only the developed countries (United States, Europe, etc.), but also the developing countries (Africa, India, etc.). When considering energy production at the present time, the energy is mainly generated from a form of fossil fuel, some examples being coal, oil, and gases. The global effect of these fuels are detrimental to the Earth and present the challenge of providing energy that is cleaner, more efficient, and ideally also less expensive. Some of the implemented and proposed solutions to converting the energy from clean sources are through solar cells, wind power, hydraulic power, nuclear power, and fuel cells.[1] The basic premise of a fuel cell is converting chemical energy directly to electrical energy. There are a number of different types of fuel cells and these will be mentioned in the following subsection. Thus, we are pursuing fuel cell technologies as an attractive alternative energy conversion device for meeting future energy needs.

1.2 Past Work

The concept of fuel cells began with Sir William Grove in 1839.[2] He used Pt electrodes with hydrogen and oxygen to produce an electrical current and water. Hydrogen is oxidized into electrons and protons at the anode. The electrons pass through an external circuit, generating an electric current, and the protons transport through a membrane to the cathode, where oxygen is reduced and combines with the protons and electrons, forming a clean product (water). Not only

does the fuel cell generate clean products, it also is not limited by the Carnot cycle, which thermodynamically limits the efficiency of a "heat" engine depending on the temperature of the hot and cold reservoirs (T_H and T_C) and the difference in the system. According to this analysis, the maximum efficiency (η) is 1- T_C/T_H. In this case the maximum efficiency is about 20-30%.[3] Fuel cells can obtain an efficiency of 80-90%.

Today, hydrogen-oxygen fuel cells are still researched and not much has changed as far as Pt still being one of the better catalysts for hydrogen oxidation and oxygen reduction. Additionally, hydrogen fuel cells are limited by transport, storage, and widespread availability of hydrogen. When compared to other fuels, the high pressure required for storage and low volumetric density of using a gas is somewhat restricting. Hence, liquid fuels present a promising immediate solution for fuel cell development. In our case, we chose to focus on methanol and ethanol with some experimental work on formic acid. Some of the advantages of using these fuels are their energy densities, easier transportation, and diversity of availability from biosources.[3] Other types of fuel cells have been developed and studied over the years, some of which include Polymer Electrolyte Membrane fuel cells (PEMFCs); solid oxide fuel cells (SOFCs), which are run at temperatures exceeding 600 ^{o}C; alkaline membrane fuel cells (AMFCs), where the ion transported through the membrane is a hydroxide ion and others.[2]

Fuel cells, in general, are not wide-spread mainly due to materials limitations, especially for the catalysts as they can be expensive, and prone to poisoning and degradation over time. Platinum containing materials are used for both the anode and cathode for the low temperature (40-60 ^{o}C) PEMFCs. A wide range of catalyst materials have been studied including: alloys[4, 5], intermetallics[6, 7], core-shell materials[8, 9], surface-modified Pt[10], and non-Pt containing materials (carbides, nitrides, oxides)[11]. When comparing these catalysts, the activity of the catalysts is

characterized by the overpotential (η) for the oxidation reaction or, conversely, the reduction reaction. Thermodynamics dictates the potential at which a reaction should occur and, depending on the kinetics of the reaction, whether slow or fast, or surface inhibition, the potential at which the reaction occurs may be at different potentials than expected. For instance, methanol oxidation should occur at about 0 V vs. NHE and the kinetics of the process on the catalyst are slow so that the measured onset of the oxidation current is 300 mV (or higher) more positive. This difference is defined as the overpotential (η). Similarly, for the oxygen reduction reaction, the potential should be +1.2 V, but because of the very slow kinetics of this reaction, even on Pt, the onset is actually less than 0.9 V. The voltage difference between the methanol oxidation and oxygen reduction gives the output of the fuel cell, but ohmic losses must also be taken into account and these, in turn, decrease the output further. The power of a fuel cell is given by P = IV and therefore, our goal is to expand the voltage range by decreasing the fuel oxidation onset potential and increasing the oxygen reduction onset potential as well as increasing the rates of the reactions.

A contributing factor to improving the catalytic activity is the inhibition of poisoning species on the electrode surface, such as sulfur and CO. Introducing a second element to the Pt lattice can diminish the CO poisoning by inhibiting bonding to the surface, such as in a bridging site. An example of this is PtBi for formic acid oxidation, where the Pt-Pt distance (originally 2.77 Å) increases to 4.32 Å and blocks CO from forming strong bonds on the surface.[7] Another factor that can help with activity is the contribution of an oxygen source for the oxidation process, such as PtRu for methanol oxidation. The proposed mechanism is a bifunctional mechanism, where carbon binds on the Pt and oxygen binds to the Ru in close proximity to the carbon source, to promote the complete oxidation of methanol to CO_2.[12, 13] In the case of ethanol, PtSn is

among the best catalysts. PtSn is a good CO oxidation catalyst and since it is proposed that CO is an intermediate in ethanol oxidation, this provides the increased activity.[14-18]

Now, we do not want to limit our search only to the catalysts that are known but also aim to explore compositions and phases that have not been studied yet, and determine their electrochemical activity towards methanol and ethanol oxidation. Thus, we developed a high throughput screening process, which will be described in more detail in the next section.

1.3 Combinatorial Processes and Advantages

We would like to explore a wide range of materials for optimizing catalytic activity in fuel cells. If we look at the different possible combination of elements, the Pt-based binary systems have 30 combinations and if we add a third element that would result in 30*29 = 870 possibilities. Moreover, with a 5 at% discretization, 30*18 + (30*18)*(29*18) = 282,420 samples can be made and there are millions of Pt-free compositions that can be evaluated.[19] Now, this approximate calculation only includes systems that can be evaluated, and does not take into account the range of phases, surface states or fiber texturing for each system. In order to accelerate the discovery and development of electrocatalysts that enhance fuel cell performance, we employ a high throughput combinatorial method based on sputtering of compositionally graded thin films which are subsequently screened for activity via a fluorescence method. Other groups have developed combinatorial methods by making electrode arrays with composition variations across the matrix as applied to screening for oxygen reduction,[20] oxygen evolution,[21] H_2 oxidation,[22, 23] CO oxidation,[22] and methanol oxidation.[23-25]

The composition spreads (also known as combinatorial libraries) are co-sputtered to allow for intimate mixing of the elements onto a 3-inch Si wafer and enable a large range of the

composition space (from the phase diagram) to be studied simultaneously for catalytic activity. The screening process is based on a method developed by Reddington, et al.[26] and reapplied by Prochaska, et al.,[27] where the proton generation from the fuel oxidation reaction is monitored through fluorescence. Below is an example case of methanol oxidation:

$CH_3OH + H_2O \rightarrow CO_2 + 6H^+ + 6e^-$ $E_0 = 0.02$ V vs. NHE.

As the reaction progresses, the regions (compositions) that exhibit high electrocatalytic activity will have a locally lower pH. The indicator, in this case quinine, has a pH dependent fluorescence, such that the active region will fluoresce first as the potential is swept in the positive direction. Digital images are captured as the potential is swept positive and characteristic potentials can be determined by the onset of the fluorescence for a specific region on the substrate. Following the fluorescence screening, the components of the active spots can be identified, made in bulk, and studied in detail. A couple other groups have implemented the quinine indicator as the fluorescent probe[28, 29] and Gruber, et al. used quinine sulfate as their indicator.[30] Smotkin, et al.[26] also implemented a low pH indicator, 3-pyridin-2-yl-(4,5,6)triazolo[1,5-a]pyridine (also known as PTP, Ni^{2+} complex, pK_a =1.5), where the solution is brought to pH 3.5 before tested for fluorescence.

Recent studies have been performed using a similar fluorescence approach to screen catalysts for oxygen reduction at the cathode of a fuel cell.[31, 32] Instead of the pH decreasing as the reaction progresses, as in the anode case, the pH increases as the reaction occurs at the cathode. Thus, fluorescent pH indicators must be chosen according to their characteristic properties for the pH range of interest. A fluorescent indicator database is compiled and the best performing fluorescent indicators are selected for use as oxygen reduction activity indicators (Chapter 7).

The development of the fluorescence screening method has enabled a wide range of compositions to be tested in parallel and thus in a rapid manner. Throughout this process, however, we must consider the possibility of false positives and false negative as we compare the samples to each other. Chan, et al.[33] recognized the challenges associated with the fluorescence screening making it difficult to correlate to actual fuel cell conditions. For example the screening is performed in a liquid at ambient temperature when the fuel cell is run at higher temperatures with a polymer electrolyte membrane, no conditioning is performed on the electrode which is common in a fuel cell, and the output is in the form of a fluorescence onset potential when a more useful comparison is the current vs. voltage curve.[33] To mitigate these issues, we have constructed and implemented a scanning minicell to obtain cyclic voltammograms in acid pH to better compare to the fuel cell conditions. Also, we have instituted a pretreatment protocol of the sample by scanning to reducing potentials to clean the surface and somewhat replicate the fuel cell conditioning treatment.

1.4 Summary of Chapter Contents

The work presented depicts many of the systems that have been studied over my time at Cornell. To start out, experimental methods will be discussed with detailed descriptions of the setup and improvements that have been made on our screening process as well as the x-ray characterization of our samples at Cornell's High Energy Synchrotron Source (CHESS). Chapters 3, 4, and 5 present specific examples of systems that are studied with our combinatorial method. Chapter 3 covers compositional libraries of Pt-Zn and Pt-Ta as well as two series Pt-Sn-X and Pt-Ni-X (X= transition metal). Along the same lines, Pt-M alloys with low concentrations of a second element, M, (M = Sn, Ta, W, Mo, Ru, Fe, In, Pd, Hf, Zn, Zr, Nb, Sc, Ni, Ti, V, Cr, Rh)

encompass the focus of Chapter 4. Prospective catalysts that contain non-metals, such as carbides, nitrides, and oxides, are included in Chapter 5. For instance, a study is done on Pt-Mo-N to first synthesize the material then characterize it for electrochemical activity towards formic acid and methanol oxidation as well as oxygen reduction. Furthermore, a series of carbides are explored to determine the effect of adding carbon to a binary system (P-M, P= Pt, Pd, Ru and M= W, Ta) and it is found to that they diminished electrochemical activity but they enhanced stability. An interesting find not related to the catalytic properties of the materials is the effect that for carbon intercalation into the lattice structure, at least 4 neighbor interactions with W or Ta must be obtained in order for these phases to form.

Work is done to explore the fundamental effect of quinine, our fluorescent indicator, on the methanol oxidation, and during this study a reversible redox process upon oxidation is observed. The reversible process is attributed to the protons generated by the methanol oxidation that are diffusion limited at the surface. To further understand the mechanisms and intermediates for fuel oxidation, alternate fuels are investigated, for example dimethoxymethane because no C-C bonds must be broken for oxidation, acetic acid because it is in a higher oxidation state than ethanol, and formic acid because it is in a higher oxidization state than methanol. These systems are discussed in detail in Chapter 6.

In an effort to expand our current screening process, Chapter 7 covers the initial indicator search as well as promising candidates for oxygen reduction catalyst screening. Over 87 fluorescent indicators are classified and characterized according to color change, pH change, and what reaction process it is be best suited for, ie. oxidation or reduction. Alternate oxidation indicators, other than quinine, are also briefly discussed.

1.5 References

1. *Annual Energy Outlook 2011*; U.S. Energy Information Administration: 2011.

2. Srinivasan, S., *Fuel Cells: From Fundamentals to Applications*. Springer: New York, NY, 2006.

3. Larminie, J.; Dicks, A., *Fuel cell systems explained*. First ed.; John Wiley & Sons: West Sussex, England, 2000; p 26.

4. Antolini, E.; Salgado, J. R. C.; Gonzalez, E. R., The methanol oxidation reaction on platinum alloys with the first row transition metals - The case of Pt-Co and -Ni alloy electrocatalysts for DMFCs: A short review. *Applied Catalysis B-Environmental* **2006,** 63, (1-2), 137-149.

5. Janssen, M. M. P.; Moolhuysen, J., Binary-Systems of Platinum and a 2nd Metal as Oxidation Catalysts for Methanol Fuel-Cells. *Electrochimica Acta* **1976,** 21, (11), 869-878.

6. Casado-Rivera, E.; Volpe, D. J.; Alden, L.; Lind, C.; Downie, C.; Vazquez-Alvarez, T.; Angelo, A. C. D.; DiSalvo, F. J.; Abruña, H. D., Electrocatalytic activity of ordered intermetallic phases for fuel cell applications. *Journal of the American Chemical Society* **2004,** 126, (12), 4043-4049.

7. Casado-Rivera, E.; Gal, Z.; Angelo, A. C. D.; Lind, C.; DiSalvo, F. J.; Abruña, H. D., Electrocatalytic oxidation of formic acid at an ordered intermetallic PtBi surface. *ChemPhysChem* **2003,** 4, (2), 193-199.

8. Strasser, P.; Koh, S.; Anniyev, T.; Greeley, J.; More, K.; Yu, C.; Liu, Z.; Kaya, S.; Nordlund, D.; Ogasawara, H.; Toney, M. F.; Nilsson, A., Lattice-strain control of the activity in dealloyed core-shell fuel cell catalysts. *Nature (London, United Kingdom)* **2010**.

9. Adzic, R. R.; Zhang, J.; Sasaki, K.; Vukmirovic, M. B.; Shao, M.; Wang, J. X.; Nilekar, A. U.; Mavrikakis, M.; Valerio, J. A.; Uribe, F., Platinum monolayer fuel cell electrocatalysts. *Topics in Catalysis* **2007,** 46, (3-4), 249-262.

10. Clavilier, J.; Fernandezvega, A.; Feliu, J. M.; Aldaz, A., Heterogeneous Electrocatalysis on Well Defined Platinum Surfaces Modified by Controlled Amounts of Irreversibly Adsorbed Adatoms. 1. Formic-Acid Oxidation on the Pt(111) - Bi System. *Journal of Electroanalytical Chemistry* **1989,** 258, (1), 89-100.

11. Ishihara, A.; Doi, S.; Mitsushima, S.; Ota, K., Tantalum (oxy)nitrides prepared using reactive sputtering for new nonplatinum cathodes of polymer electrolyte fuel cell. *Electrochimica Acta* **2008,** 53, (16), 5442-5450.

12. Watanabe, M.; Motoo, S., Electrocatalysis by Ad-atoms. 2. Enhancement of Oxidation of Methanol on Platinum by Ruthenium Ad-atoms. *Journal of Electroanalytical Chemistry* **1975,** 60, (3), 267-273.

13. Watanabe, M.; Motoo, S., Electrocatalysis by Ad-atoms. 3. Enhancement of Oxidation of Carbon-Monoxide on Platinum by Ruthenium Ad-atoms. *Journal of Electroanalytical Chemistry* **1975,** 60, (3), 275-283.

14. Antolini, E.; Gonzalez, E. R., Effect of synthesis method and structural characteristics of Pt-Sn fuel cell catalysts on the electro-oxidation of CH_3OH and CH_3CH_2OH in acid medium. *Catalysis Today* **2011,** 160, (1), 28-38.

15. Antolini, E.; Gonzalez, E. R., A simple model to assess the contribution of alloyed and non-alloyed platinum and tin to the ethanol oxidation reaction on Pt-Sn/C catalysts: Application to direct ethanol fuel cell performance. *Electrochimica Acta* **2010,** 55, (22), 6485-6490.

16. Colmati, F.; Antolini, E.; Gonzalez, E. R., Effect of thermal treatment on phase composition and ethanol oxidation activity of a carbon supported $Pt_{50}Sn_{50}$ alloy catalyst. *Journal of Solid State Electrochemistry* **2008,** 12, (5), 591-599.

17. Jiang, L. H.; Sun, G. Q.; Sun, S. G.; Liu, J. G.; Tang, S. H.; Li, H. Q.; Zhou, B.; Xin, Q., Structure and chemical composition of supported Pt-Sn electrocatalysts for ethanol oxidation. *Electrochimica Acta* **2005,** 50, (27), 5384-5389.

18. Delime, F.; Leger, J. M.; Lamy, C., Enhancement of the electrooxidation of ethanol on a Pt-PEM electrode modified by tin. Part I: Half cell study. *Journal of Applied Electrochemistry* **1999,** 29, (11), 1249-1254.

19. Disalvo, F. J., Solid State Chemistry Lecture Series. In Ithaca, NY, 2008.

20. He, T.; Kreidler, E.; Xiong, L.; Ding, E., Combinatorial screening and nano-synthesis of platinum binary alloys for oxygen electroreduction. *Journal of Power Sources* **2007,** 165, 87-91.

21. Neyerlin, K. C.; Bugosh, G.; Forgie, R.; Liu, Z.; Strasser, P., Combinatorial study of high-surface-area binary and ternary electrocatalysts for the oxygen evolution reaction. *Journal of Electrochemical Society* **2009,** 156, (3), B363-B369.

22. Stevens, D. A.; Rouleau, J. M.; Mar, R. E.; Bonakdarpour, A.; Atanasoski, R. T.; Schmoeckel, A. K.; Debe, M. K.; Dahn, J. R., Characterization and PEMFC Testing of $Pt_{1-x}M_x$ (M= Ru, Mo, Co, Ta, Au, Sn) Anode Electrocatalyst Composition Spreads. *Journal of the Electrochemical Society* **2007,** 154, (6), B566-B576.

23. Smotkin, E. S.; Jiang, J.; Nayar, A.; Liu, R., High-throughput screening of fuel cell electrocatalysts. *Applied Surface Science* **2006,** 252, 2573-2579.

24. Cooper, J. S.; McGinn, P. J., Combinatorial screening of thin film electrocatalysts for a direct methanol fuel cell anode. *Journal of Power Sources* **2006,** 163, (1), 330-338.

25. Strasser, P.; Fan, Q.; Devenney, M.; Weinberg, W. H.; Liu, P.; Norskov, J. K., High throughput experimental and theoretical predictive screening of materials - A comparative study

of search strategies for new fuel cell anode catalysts. *Journal of Physical Chemistry B* **2003,** 107, (40), 11013-11021.

26. Reddington, E.; Sapienza, A.; Gurau, B.; Viswanathan, R.; Sarangapani, S.; Smotkin, E. S.; Mallouk, T. E., Combinatorial electrochemistry: A highly parallel, optical screening method for discovery of better electrocatalysts. *Science* **1998,** 280, (5370), 1735-1737.

27. Prochaska, M.; Jin, J.; Rochefort, D.; Zhuang, L.; DiSalvo, F. J.; Abruña, H. D.; van Dover, R. B., High throughput screening of electrocatalysts for fuel cell applications. *Review of Scientific Instruments* **2006,** 77, (5).

28. Jayaraman, S.; Hillier, A. C., Electrochemical synthesis and reactivity screening of a ternary composition gradient for combinatorial discovery of fuel cell catalysts. *Measurement Science & Technology* **2005,** 16, (1), 5-13.

29. Gurau, B.; Viswanathan, R.; Liu, R.; Lafrenz, T. J.; Ley, K. L.; Smotkin, E. S.; Reddington, E.; Sapienza, A.; Chan, B. C.; Mallouk, T. E.; Sarangapani, S., Structural and Electrochemical Characterization of Binary, Ternary and Quaternary Platinum Alloy Catalysts for Methanol Electro-oxidation. *Journal of Physical Chemistry B* **1998,** 102, (49), 9997-10003.

30. Gruber, K.; Krongberger, H.; Fafilek, G.; Nauer, G.; Besenhard, J.-O., Optical Measurements of Platinum Based Electrocatalysts for the Electrooxidation of Methanol. *Fuel Cells* **2003,** 3, (1-2), 3-7.

31. Liu, J. H.; Jeon, M. K.; Woo, S. I., High-throughput screening of binary catalysts for oxygen electroreduction. *Applied Surface Science* **2006,** 252, 2580-2587.

32. Chen, G. Y.; Delafuente, D. A.; Sarangapani, S.; Mallouk, T. E., Combinatorial discovery of bifunctional oxygen reduction - water oxidation electrocatalysts for regenerative fuel cells. *Catalysis Today* **2001,** 67, (4), 341-355.

33. Chan, B. C.; Liu, R. X.; Jambunathan, K.; Zhang, H.; Chen, G. Y.; Mallouk, T. E.; Smotkin, E. S., Comparison of high-throughput electrochemical methods for testing direct methanol fuel cell anode electrocatalysts. *Journal of the Electrochemical Society* **2005,** 152, (3), A594-A600.

CHAPTER 2

Experimental Methodology

2.1 Electrochemical Setup

A standard testing procedure for cleaning Pt in the fundamental studies of fuel oxidation and fluorescent indicator screening required the use of cyclic voltammetry. Cyclic voltammograms were collected using a three compartment electrochemical cell (figure 2.1.1) with medium porosity glass frits to separate the counter, working and reference electrodes. The working electrode was held in the center compartment and the electrode construction consisted of a Pt bead encased by glass to expose a given Pt surface (approximately 3 mm diameter). A small bead of Buehler diamond paste with 3-4 drops of Buehler extruder was applied to a Buehler polishing cloth with subsequent polishing of the Pt electrode in figure '8's for 10-15 minutes. The counter electrode was a Pt coiled wire and the reference electrode was a Ag/AgCl electrode or, in some cases, a reversible hydrogen electrode (RHE). First, the working electrode, Pt, was mechanically cleaned with diamond paste (1 micron) as described above and electrochemically cleaned by voltage cycling (between 0 and 1.5 V vs RHE) in 0.1 M sulfuric acid until the characteristic Pt cyclic voltammogram was obtained (figure 2.1.2). The solutions were bubbled with N_2 gas for 10-15 minutes before cycling and the atmosphere was deaerated with N_2 gas while testing. When oxygen reduction was performed, the solution was aerated with pure O_2 for 10-15 minutes before cycling.

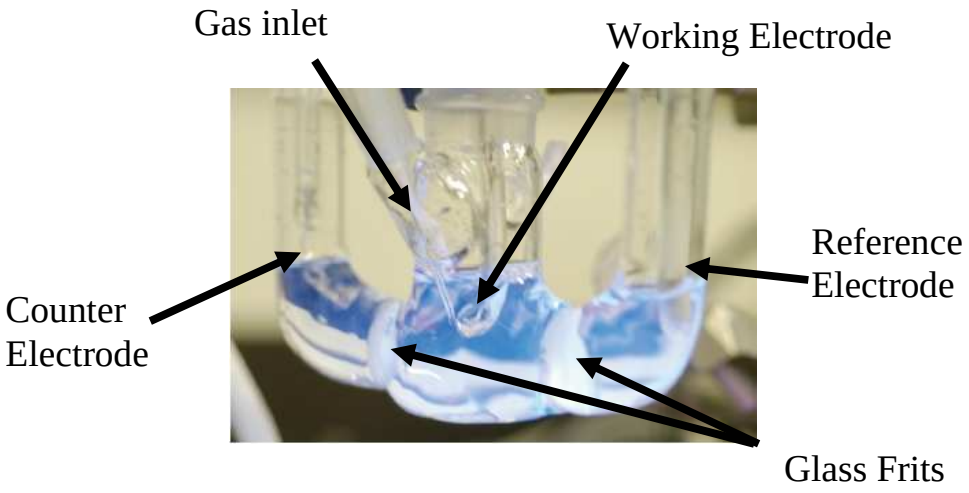

Figure 2.1.1: Three compartment electrochemical cell.

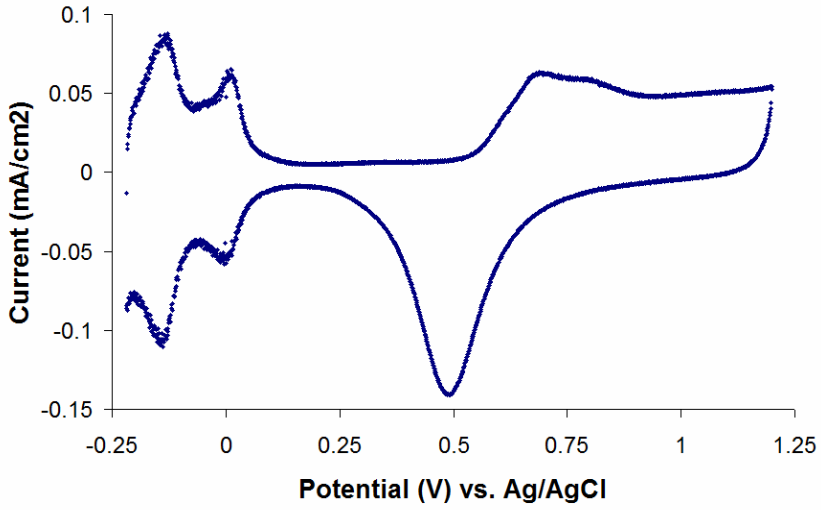

Figure 2.1.2: Characteristic clean Pt cyclic voltammogram in 0.1 M sulfuric acid, Pt counter electrode, scan rate = 100 mV/s.

2.2 Sputtering

Our high throughput search began with the synthesis of thin films through a co-deposition process that enabled intimate mixing of the materials investigated.[1] The deposition occured in a chamber (residual pressure = 10^{-5} Pa), where an ensemble of 4, 2-inch dc-magnetron sputter sources (Angstrom Sciences) was contained (figure 2.2.1). A 4-inch gun (purple gun in the

schematic) was used to create a uniform film (usually a Ta or Ti underlayer). Previous to that, an ion gun was used to remove the insulating SiO_2 layer from the silicon wafers as a cleaning step. Three substrate holders and heaters were within the chamber to enable three samples to be made with a single pump down of the chamber. Four different targets could be mounted and co-sputtered at a time with the orientation of one being on-axis while the three others were centered around the on-axis gun in a 15^o tilt. The tilt enabled the gradient of the metals across the surface of the silicon wafer. An Inficon crystal deposition monitor was mounted on one of the substrate heaters and measured the mass accumulation rate with better than 10 ng/cm^2 resolution. Deposition profiles, according to the position of the quartz crystal monitor in relation to the gun, were constructed. The cryoshroud encased the four deposition guns and liquid nitrogen cooled the guns as it was pumped through the cryoshroud.[1]

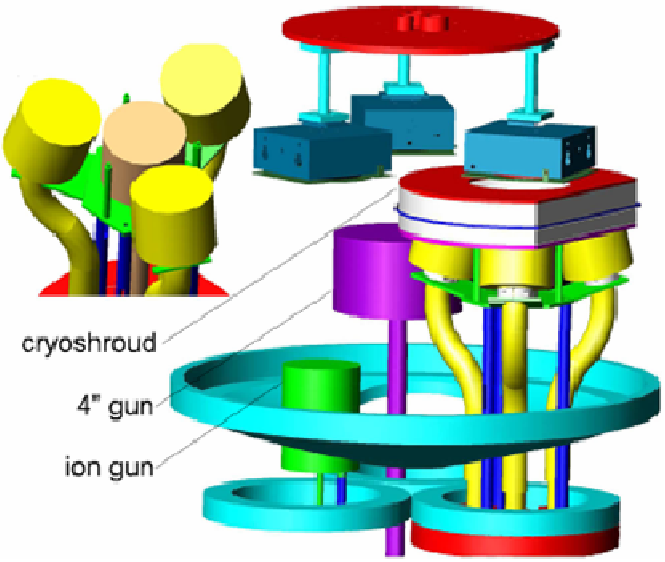

Figure 2.2.1: Sputtering chamber schematic for a chamber called "Tubby." Three samples could be sputtered in one pump down and 4 targets could be loaded with a possibility of gaseous species introduced into the chamber resulting in quaternary and quinary composition spreads.[1]

Combinatorial libraries were generated, first by deposition of an adhesion layer (100 nm Ta or Ti) on a 76.2 mm (3-inch) diameter Si substrate, and then elements (> 99.9% purity) were

codeposited from the separate magnetron sputtering sources in an atmosphere of 0.66 Pa Ar. The background pressure during deposition remained in the 10^{-5} Pa range with the help of a cryoshroud.[1] During and after deposition, the substrate temperature could be controlled from 50 to 600 ^{o}C with radiative heating and could be sustained throughout the process. The substrate could also be heated post-sputtering to anneal compositions on the films, which could result in the formation of different phases.

2.3 Fluorescence Screening for Electrochemical Activity

Over the past decade, a number of publications had presented combinatorial high-throughput methods for efficient exploration of the wide range of possible anode catalysts for direct methanol fuel cells (DMFCs). A fluorescence assay, used to screen catalysts, was first employed by Reddington[2] and further adapted for thin films by Prochaska,et al.[3] The entire film was used as the working electrode in a specially designed electrochemical cell.[4] The electrochemical cell was made of Teflon with an approx. 7 cm inner diameter, slightly smaller than the diameter of the 3 inch Si wafer. Three electrical contacts were made on the film surface at the perimeter of the substrate (not in contact with the solution). To ensure sufficiently conducting film contact, two-point electrical measurements (typically less than 10 Ω) were collected. Raised about 1 cm in the inner perimeter of the cell was a large area Au coil that served as the counter electrode. The cell was covered with a quartz lid to prevent air exposure and allowed for atmospheric control during the experiments. Our apparatus also included 2-L glass storage bottles for the testing solutions, which were bubbled with nitrogen and kept under nitrogen atmosphere to minimize the presence of oxygen. Peristaltic pumps were used for automated filling, draining,

and rinsing of the cell without removal of the lid such that the testing atmosphere was constantly controlled, most commonly with nitrogen. A picture of the setup is shown in figure 2.3.1.

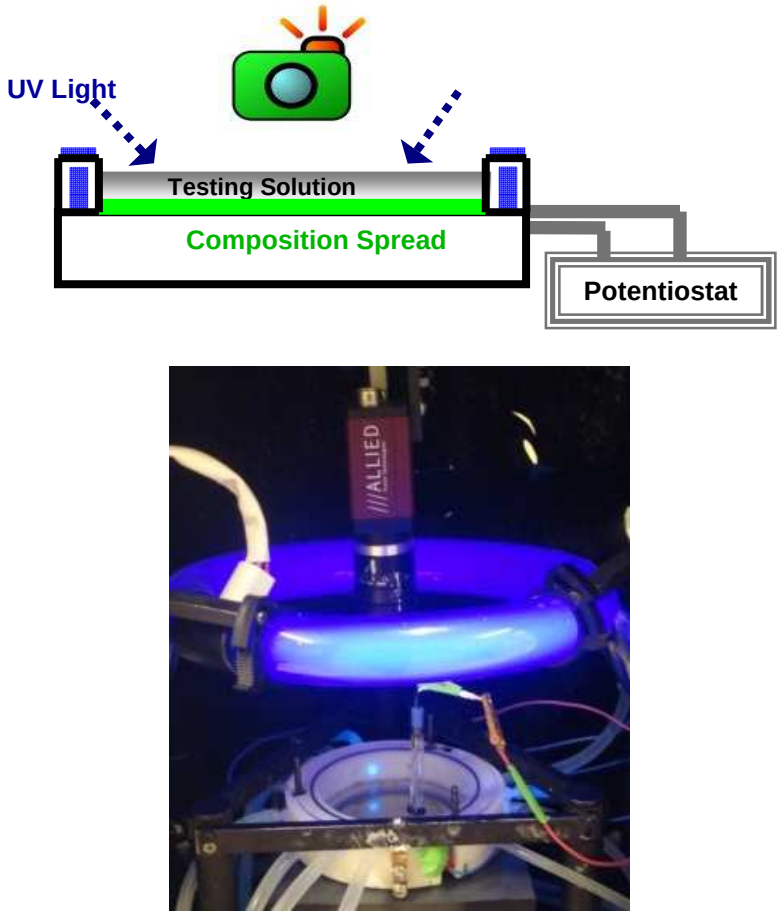

Figure 2.3.1: Top: Depiction of the fluorescence screening arrangement. Pictures were taken at 20 mV intervals as the potential was scanned positively at 5 mV/s. The entire working electrode and testing solution (containing quinine) were exposed to UV light. Bottom: Picture of actual setup.

A reference is made in section 3.1 for an "old fluorescence setup," and the differences between the old setup and new one are listed below:

- Absence of a quartz cover to isolate from air and similarly no atmospheric control over the solutions.
- Manual fill of solutions into the electrochemical cell.

- Absence of computer program for automating scans, solution filling/draining, and fluorescence analysis. The computer program for the fluorescence analysis greatly lessened the amount of time required for sample testing.
- UV exposure with a hand-held UV lamp that was elevated on the side of the electrochemical cell. This UV light could be moved at will and could vary in location between samples.
- Pictures collected on a Nikon camera with a timer that the user synchronized manually with the potentiostat.

Thus, all of these factors must be considered when comparing the new and old setup fluorescence data.

In the screening process, a pH-sensitive fluorescent indicator was used to identify catalytically active regions in a combinatorial library.[3] The potential applied to the film was swept from -100 to 500 mV vs. Ag/AgCl at a scan rate of 5 mV/s. The testing solution consisted of 5 M methanol, ethanol, or ethylene glycol, 3 mM quinine, and 0.1 M potassium triflate (supporting electrolyte). The solution began at neutral pH and as the potential was applied in the positive direction, methanol was oxidized with the released protons causing a decrease in pH below 5. Protonation of the quinine ensued and in this condition the quinine was fluorescent under UV illumination. Although the entire library was a common working electrode, the local generation of protons allowed measurement of catalytic activity with approx. 1 mm resolution via optical detection of fluorescence. Images were taken at 20 mV intervals with a charge-coupled device (CCD) camera, and at a given region of the library, image processing provided a fluorescence intensity vs. applied potential curve. To identify false-positive fluorescence results,

a scan was performed with the same scan parameters without fuel (methanol/ethanol/ethylene glycol).

A model for the fluorescence intensity profile of the oxidation process is shown below:[4]

$$F = An\ln(1+ \mathrm{Exp}((E - E_{1/2})n/f))$$

where F is the fluorescence intensity, E is the applied potential, and f=59.1 mV at ambient temperature. The prefactor A, halfwave potential $E_{1/2}$, and number of electrons n in the rate-limiting reaction were model parameters. In the work presented here, we fixed n = 2 and extracted the figure of merit $E_{1/2}$ through least-squares fitting of the measured profiles.[5]

In addition to the routine fluorescence tests, a pretreatment of the film was performed to ostensibly reduce surface oxides that were formed upon air exposure and to remove other surface contaminants. This pretreatment entailed a linear voltage sweep from 0 to -800 mV vs. Ag/AgCl in an aqueous solution of 0.01 M H_2SO_4 with 1 M Na_2SO_4 as supporting electrolyte.[4] In the case of Pt-Zn (Section 3.2), pretreatment also consisted of holding the potential at 0.6 V vs Ag/AgCl in a pH 2 aqueous H_2SO_4 solution for 10 minutes.

2.4 Electrochemical Minicell

While the fluorescence screening enabled the quick determination of promising catalysts for methanol, ethanol, and ethylene glycol oxidation, localized testing was important for electrochemical characterization under different conditions, such as in acidic media. The localized testing was achieved with a 1-cm inner diameter Teflon cylindrical cell (figure 2.4.1) and, in order position the cell on the wafer, the quartz lid is removed, resulting in air exposure of the film. A Ag/AgCl reference electrode was used for some of the tests but the proximity to the surface introduced Cl^- poisoning. Thus, a reversible hydrogen electrode (RHE) was used.

This minicell was used to collect cyclic voltammograms in aqueous solutions of 5 M methanol and 0.1 M H_2SO_4, mainly in the Pt-Zn study. These tests provided verification that catalysts active near neutral pH in the fluorescence test were also active in pH 1 solutions, the approximate pH encountered in operating fuel cells. Additionally, the minicell was used to determine surface area of the localized positions on the composition spread and is discussed more in detail in *Section 2.6 Surface Area Determination.*

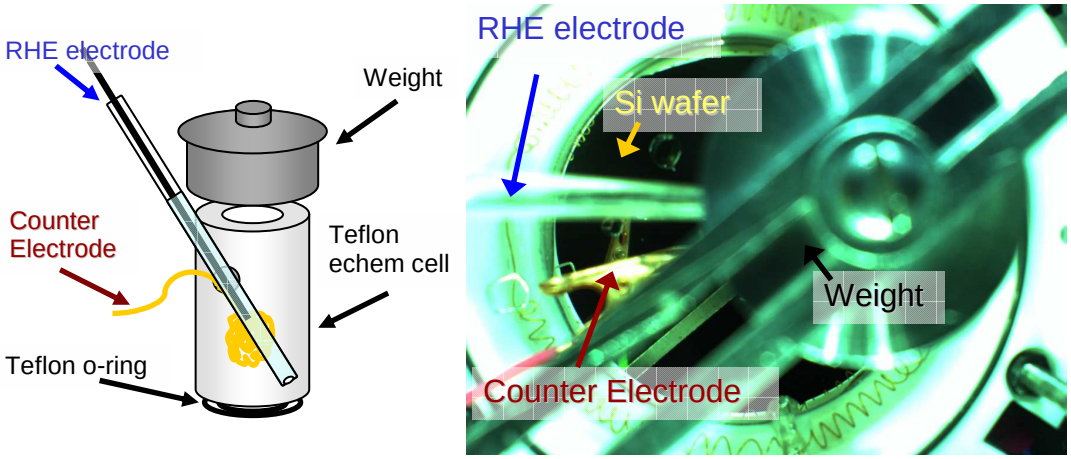

Figure 2.4.1: 1-cm diameter electrochemical minicell that was placed on top of the larger 3-inch wafer to perform specific electrochemical tests, such as in acidic media. A Teflon ring seals the cell as the weight was applied on the top. An RHE was used as the reference and a Au coil served as the counter electrode. Left: schematic of minicell; right: top view of minicell placed on the composition spread.

2.5 Scanning Electrochemical Minicell

While the fluorescence assay allowed us to efficiently identify nominal compositions of promising methanol catalysts, additional testing was required to determine the catalytic properties under realistic fuel cell (low pH) conditions. Localized electrochemical testing was enabled by using a moveable minicell (Fig. 2.5.1) that included a 6 mm inner diameter Teflon cell that isolated a 0.32 cm^2 film region. The combinatorial libraries were sealed in an outer cell with 7 cm inner diameter (the fluorescence cell) and exposed to testing solution under controlled

atmosphere. The 6 mm cell contained counter and reference electrodes. Positioning of the cell at a chosen spots on the substrate allowed for testing of specific regions on the substrate, i.e. typically a 5 at % composition range. Furthermore, a Labview program automated the motor control for cell positioning anywhere over the 3-inch substrate. A pneumatic switch lowered and sealed the minicell with an o-ring such that the area was isolated from the rest of the wafer. Pneumatic activation was used to achieve rapid and gentle vertical motion to avoid scratching or cracking the substrate. To ensure that the solution in the minicell was purged and to refill the minicell, a high pressure bubbling switch was installed inside the minicell to rinse out old solution and release any bubbles trapped in the minicell. The method for purging the minicell was: (1) raised minicell, (2) switched bubbling on/off 2-3x, (3) lowered minicell, (4) repeated steps (1) and (2) 3 times and proceeded with the electrochemical testing. A further improvement could be to scan the position in the x and y by ~2-3 cm with the minicell raised, in order to further mix and refresh the fuel solution.

So far, this technique had been used to acquire cyclic voltammograms (CVs) of select catalyst regions in solutions at a pH of 1. CVs acquired in the absence of fuel provided further characterization of the catalyst, and CVs acquired in the presence of fuel verified the activity of the catalysts in an environment that approaches fuel cell conditions. We planned to use this technique for testing fuel oxidation in alkaline media as well.

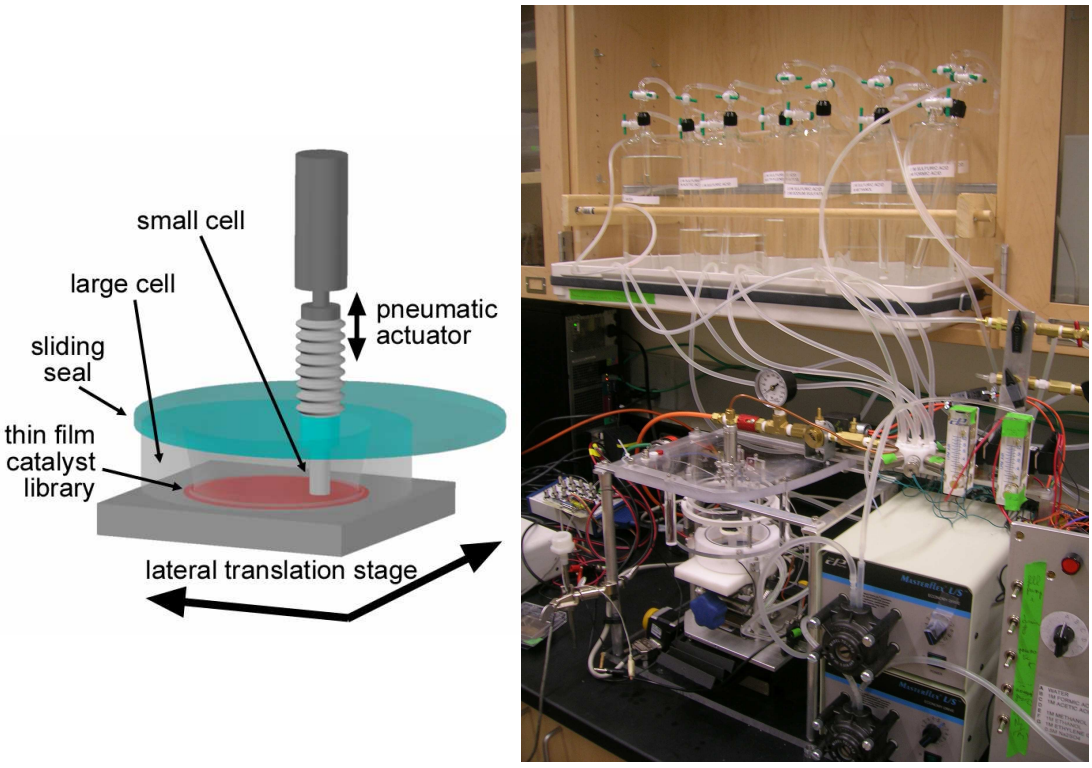

Figure 2.5.1: Schematic (left) and photograph (right) of the scanning electrochemical minicell setup.

2.6 Surface Area Determination

To facilitate comparison of oxidation current densities, specific surface area measurements were performed on select catalysts. Because of surface roughness, the active surface area could be much larger than the projected (plain view) geometric area. A cyclic voltammogram using 1 mM hydroxymethylferrocene in an aqueous solution of 0.1 M potassium triflate (supporting electrolyte) was used to determine the projected specific surface area of films (figure 2.6.1). The ferrocene redox couple was selected due to its low electrode adsorption, easily accessible redox potential in the range of interest for catalysis, fast kinetics which result in readily measured currents, and general insensitivity of the kinetics toward electrode composition. The surface area (A) was determined using the Randles-Sevcik equation:[6]

$$A = 3.72 \times 10^{-6}\, i_p\, \upsilon^{-1/2}\, D^{-1/2}\, C^{-1},$$

where C is the ferrocene concentration, υ is the sweep rate, D is the diffusion coefficient of hydroxymethylferrocene, and i_p is the peak current.

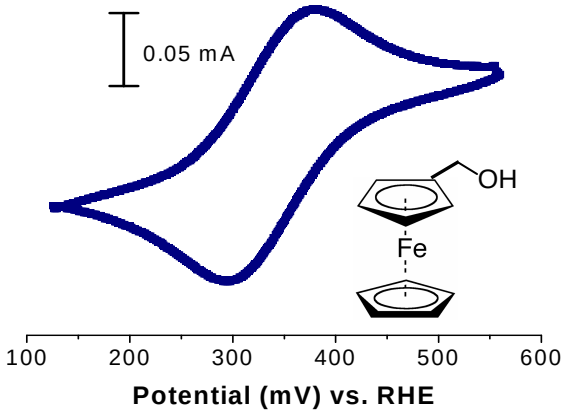

Figure 2.6.1: Cyclic voltammogram on Pt of 1 mM Hydroxymethylferrocene, 0.1 M potassium triflate, 20 mV/s.

For the Pt-Zn study, a different functionalized ferrocene complex, ferrocene monocarboxylic acid (0.2 mM), was chosen and also demonstrated a reversible redox response.[4] The issue with using this compound was that it had lower solubility than the hydoxymethylferrocene, hence the decision to change the redox mediator in later experiments.

Other common methods for surface area determination were H_2 and CO adsorption. While these methods worked well for Pt surfaces, these methods were ill-suited for analysis of heterogeneous catalysts, as the gas adsorption varies with electrode surface composition. Hydrogen adsorption for electrochemically dealloyed Pt-containing films could yield a specific surface area that significantly differs from the methanol-oxidation surface area. However, it could be useful to monitor the change in surface composition of Pt by observing the time-dependent growth of the H_2 adsorption peaks. Hydrogen adsorption would not give a representative electrode surface area because surface atoms in sub-nm pores did not fully

participate in methanol oxidation due to size exclusion of the methanol molecule, while these atoms may adsorb H_2. The ferrocene molecule was somewhat larger than the methanol molecule and had different diffusion dynamics into the small pores of an electrochemically dealloyed film, but gives a semi-quantitative measure of the effective surface area increase due to dealloying.

2.7 Characterization

As a complement to the screening process, it was imperative to have the ability to identify the composition, phase and ideally surface structure of the electrochemically active material. We implemented a number of techniques for studying the properties of the films that were made, including: X-ray based analysis (XRD and GADDS), scanning electron microscopy (SEM), and X-ray photoelectron spectroscopy (XPS).

2.7.1 X-Ray Analysis (XRD and GADDS)

X-ray diffractograms were collected on Cornell's Bruker AXS General Area Diffraction Detector System (GADDS). Many of the samples were also characterized at the Cornell High Energy Synchrotron Source (CHESS) on the A2 beam line. The experimental layout and pictures of the latter setup are shown in figure 2.7.1.1. Monochromatic 60 keV X-rays impinge the thin film and the diffraction image was acquired in transmission geometry using a 345 mm diameter image plate (Mar Research). An X-Flash detector was displaced 90^o from the incident beam and the substrate was oriented with the thin film side facing the Mar345 and X-flash detectors.[7] The sample to Mar345 distance was 0.55 m and calibrated using a Si powder mounted at the sample position. The x-ray energy (60 keV) enabled the detection of Bragg reflections with *d* spacings ranging from 0.05 to 0.5 nm. The collimated incident beam had a 1.2

mm square footprint on the tilted substrate, resulting in each measurement averaging over a ~1 at. % composition range. Data were acquired by defining a rectangular grid of substrate positions and employing an automated system, where diffraction images and fluorescence spectra were acquired. A 1.4 mm thick Al plate was mounted in front of the Mar345 detector as a passive high-pass x-ray energy filter that attenuated XRF that was emitted isotropically by the sample[7] and therefore reduced noise in the diffraction image. Si diffuse scattering from the substrate was present in the diffraction images and in specific detector regions generated scattering orders of magnitude more intense than the thin film. Therefore, Pb pieces were secured with polyimide tape on the Al plate to avoid detector saturation from the Si scattering.

Integration of the images provided diffraction patterns that were compared to patterns of known phases in the Powder Diffraction File (PDF)[8] to construct a phase map of the library. We also noted that sputter deposition commonly yields fiber textured thin films in which the constituent crystallites were randomly oriented with respect to substrate azimuth but aligned with respect to substrate normal.[9] The average crystallite orientation in the film could be determined by analyzing the 2-dimensional diffraction images. This orientation was important, as it dictated the crystal facet presented at the film surface, which may ultimately determine surface chemistry and reactivity.

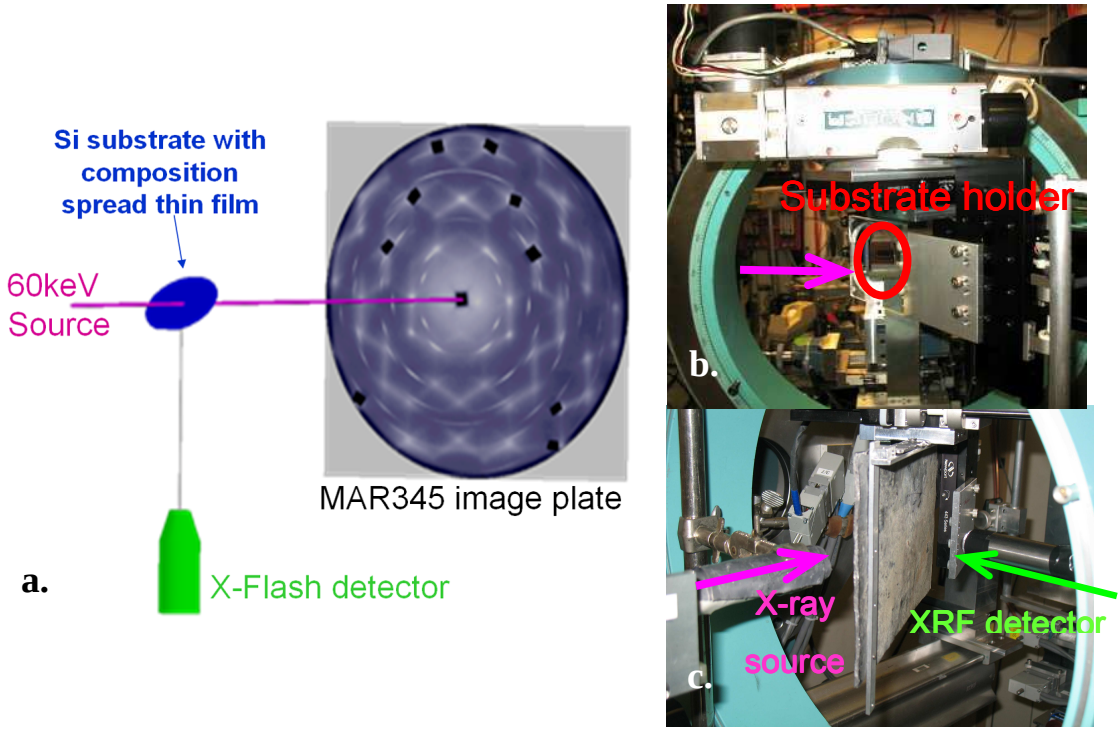

Figure 2.7.1.1: (a) Schematic of the X-ray source and path at CHESS. (b) Photograph of the substrate holder and the arrow denotes the x-ray path. (c) Another photograph showing the position of the XRF detector.

2.7.2 Surface Imaging and Characterization

Surface images of composition spreads were obtained using a Leo 1550 scanning electron microscope for the Pt-Sn-X and Pt-Zn samples by Maxim Kostylev, as well as Pt-Mo-N samples by Dr. Akira Miura. Energy dispersive X-ray spectroscopy (EDS) was performed on these samples with a Bruker AXS XFlash 3001 Silicon Drift Detector. Elemental concentrations were calculated with Bruker Espirit 1.8 software. In the case of Pt-Ta, Energy-dispersive X-ray spectroscopy (EDS) was performed using a JEOL 8900 EPMA Microprobe.

The surface composition was determined using X-ray photoelectron spectroscopy (XPS), Surface Science Instruments SSX-100, with a 1 μPa base pressure and performed by Dr. Akira Miura and John Gregoire. Analysis of XPS data was performed using CasaXPS software package. The parameters for each sample studied will be discussed in their respective section.

2.8 References

1. Gregoire, J. M.; van Dover, R. B.; Jin, J.; Disalvo, F. J.; Abruña, H. D., Getter sputtering system for high-throughput fabrication of composition spreads. *Review of Scientific Instruments* **2007,** 78, (7), 072212.

2. Reddington, E.; Sapienza, A.; Gurau, B.; Viswanathan, R.; Sarangapani, S.; Smotkin, E. S.; Mallouk, T. E., Combinatorial electrochemistry: A highly parallel, optical screening method for discovery of better electrocatalysts. *Science* **1998,** 280, (5370), 1735-1737.

3. Prochaska, M.; Jin, J.; Rochefort, D.; Zhuang, L.; DiSalvo, F. J.; Abruña, H. D.; van Dover, R. B.; High throughput screening of electrocatalysts for fuel cell applications. *Review of Scientific Instruments* **2006,** 77, (5).

4. Gregoire, J. M.; Kostylev, M.; Tague, M. E.; Mutolo, P. F.; van Dover, R. B.; DiSalvo, F. J.; Abruña, H. D., High-Throughput Evaluation of Dealloyed Pt-Zn Composition-Spread Thin Film for Methanol-Oxidation Catalysis. *Journal of the Electrochemical Society* **2009,** 156, (1), B160-B166.

5. Gregoire, J. M. High throughput material science for discovery of energy-related materials. Dissertation, Cornell University, Ithaca, NY, 2010.

6. Bard, A. J.; Faulkner, L. R., *Electrochemical Methods: Fundamentals and Applications*. 2nd ed.; John Wiley & Sons, Inc.: New York, 2001.

7. Gregoire, J. M.; Dale, D.; Kazimirov, A.; DiSalvo, F. J.; van Dover, R. B., High energy x-ray diffraction/x-ray fluorescence spectroscopy for high-throughput analysis of composition spread thin films. *Review of Scientific Instruments* **2009,** 80, (12), 123905.

8. Powder Diffraction File. In JCPDS International Centre for Diffraction Data: Newton Square, PA: 2004.

9. Ohring, M., *Materials Science of Thin Films* 2nd ed.; Academic Press: Boston, 2002.

CHAPTER 3

Systems of Interest

One of the challenges for fuel cells is identifying suitable catalysts for both the anode and cathode. Our combinatorial screening approach provides a high throughput method for identifying promising catalysts, with particular emphasis on the anode in this chapter. A discussion of cathode screening is presented in Chapter 7. The goal in this chapter is to review the motivation and results for systems that we studied, focusing on how our investigations were directed from previous knowledge of catalysts, such as Pt-Ru and Pt-Sn. As we have investigated various systems, we have also identified confounding variables, including surface roughening and surface oxide formation, and have developed methods for understanding and managing these processes in order to minimize the number of false positives from our screening method.

3.1 Trends in periodic series

The screening method was previously developed by a collaboration among the Abruña, van Dover, and DiSalvo groups.[1] Many thin films were screened (a cumulative total of approximately 300 films at the beginning of 2007). One of the discoveries from the screening method was found in a $Pt_xBi_yPb_z$ composition spread, with an optimal composition near $PtBi_{0.01}Pb_{0.53}$.[2] Based on the plethora of fluorescence results collected by the group, Pt-Ru and Pt-Sn were still considered to be among the most active candidates for methanol and ethanol oxidation, respectively. With this in mind, we decided to investigate a Pt-Sn-X series (X= transition metal) and a subsequent study was performed on the Pt-Ni-X series as well. The results from these studies suggested individual systems for study, for example Pt-Zn and Pt-Ta.

Upon further investigation, we developed a better understanding of the surface roughening due to the angle of incidence of various species during deposition substrate temperature, and effects due to electrochemical testing itself (leaching). The discussion of the Pt-Ta system demonstrates the importance of surface species and surface oxides in the promotion of fuel oxidation.

3.1.1 Pt-Sn-X series

Pt-Sn materials have been shown to have high activity towards ethanol oxidation.[3-6] While it has been found that Pt-Sn assists in the initial oxidation process, complete conversion to CO_2 will likely require the addition of a third element that can assist in this multi-step process especially by breaking the C-C bond.[7] With this as a starting point, a Pt-Sn-X series (X= Transition metal) was studied with a deposition temperature of 25 ^{o}C. Representative fluorescence images are shown in figure 3.1.1.1. For many of the samples, two fluorescent regions were detected; one in the Pt-rich region and another in a region between the Pt and Sn rich regions, designated as the 'Pt-Sn' region. In some cases, no fluorescence was observed for the 'Pt-Sn' region; whereas for most of the samples, there was fluorescence in the Pt-rich regions. A few of the samples exhibited leaching (or instability) in the ternary elemental region, for example V, Mo, and W. At oxidizing potentials these elements formed an oxide in aqueous solutions as expected from the Pourbaix diagrams,[8] and therefore generated protons, which decreased the local pH in the same way as fuel oxidation. We identified these unstable regions by performing the background scan with no fuel and removed these from further consideration in our study. That is, fluorescence in these regions constituted false positives.

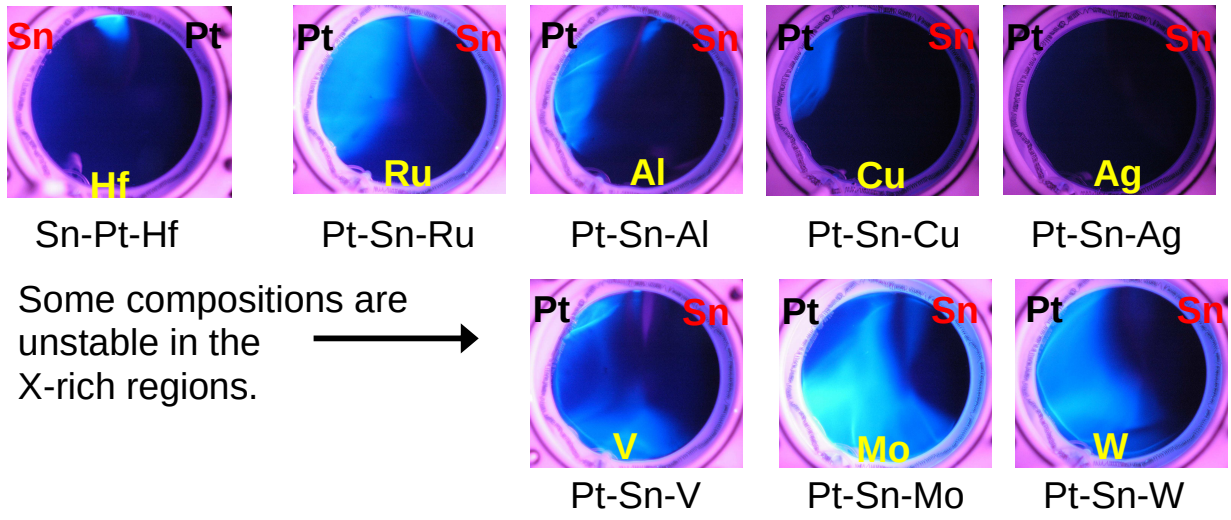

Figure 3.1.1.1: Representative Pt-Sn-X fluorescence images for methanol oxidation, showing the active regions as well as unstable samples. The images are taken at approx. 300 mV vs. Ag/AgCl in an aqueous solution of 5 M methanol, 0.1 M potassium triflate, and 0.5 mM quinine.

As a quantitative comparison among samples, the onset potential of the most active region, whether it was the Pt-rich region or the 'Pt-Sn' region, was plotted vs. the position of the third element on the periodic table (Figure 3.1.1.2). Overall it was found that the addition of the third element, according to the fluorescence assay, did not measurably improve the methanol oxidation activity. The results were scattered with no trend across the periodic table, although there were trends for a few of the columns. For instance for the d^3, d^4, d^6, and d^7 metals, the onset potentials increased as the heavier element was incorporated into the composition spread. Of the d^2 elements, Ti and Hf had similar onset potentials with Zr showing over 100 mV positive shift. Pt-Sn-Re alone was a good catalyst; comparable to the Pt-Sn binary.

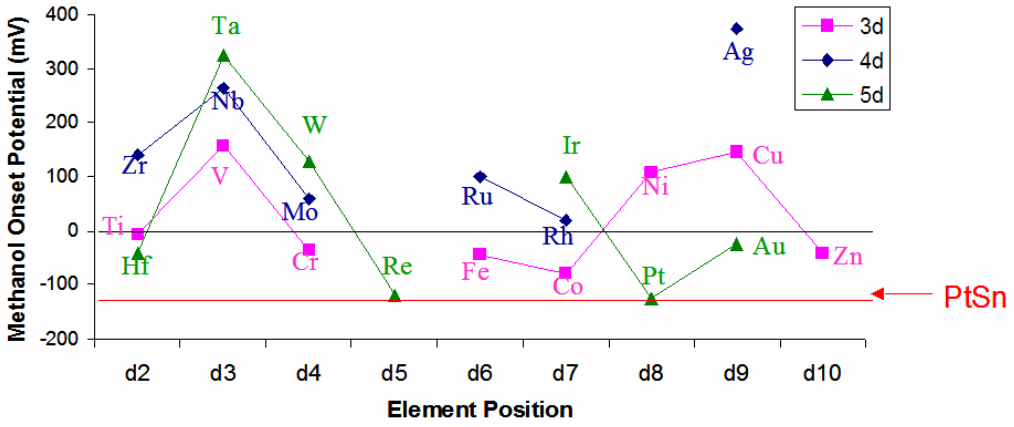

Figure 3.1.1.2: Pt-Sn-X methanol fluorescence onset potentials along the periodic table. The elements plotted above are the third element in the Pt-Sn-X series, scan rate 5 mV/s, film thickness = 2000-2500 Å, sputtering temperature = ambient. Testing solution = 5M methanol, 0.5mM quinine, 0.1M potassium triflate.

To note, all these samples were tested on the screening setup in Baker Lab without atmospheric control (see *section 2.3*). A pretreatment of the samples was performed in the test solution (pH 7 solution) by holding the potential at -650 mV vs. Ag/AgCl for 2 minutes to clean the surface (no hydrogen was generated). A comparison was done to elucidate the effects of employing the pretreatment on the samples. Values of the onset potentials shifted; however the results are not conclusive because the solution was not air tight. A definite comparison could be executed using the automated, atmosphere-controlled instrument currently in use in Duffield. A few of the samples exhibited onset potentials unaffected by pretreatment but in some cases the active region would shift with the pretreatment of the sample. For methanol oxidation in the Pt rich region, the fluorescence onset potential independent of pretreatment was seen for Ru, Mo, Ti and Ni; for ethanol oxidation in the same region, these same elements showed stable onsets with pretreatment, as did the addition of Hf, W, Al and Cu. In the 'Pt-Sn' region, constant fluorescence onset potentials for methanol oxidation were observed for the addition of Hf, Ru, Mo, Ta, Cu, and Ag. Ethanol oxidation proved to again exhibit more pretreatment-independent

fluorescence for ternary additions including W, V, Cr, Al, and Ni as well as those for methanol. Overall, the most stable Pt regions for both fuels were Ru, Mo and Al and for the 'Pt-Sn' region Hf, Ru, Ta, Cu, and Ag. An issue with these samples could be due to the surface morphology, which will be discussed in the next section.

When we compared the ethanol fluorescence onset potentials for this series, there were no evident trends across the periodic table as for the methanol oxidation. Since the ultimate goal was to find the lowest fluorescence onset potential, Pt-Sn-Zn was the only candidate with the lower onset potential than Pt-Sn. This result prompted further investigation of the Pt-Zn system, which will be discussed in a separate section (*Section 3.2).*

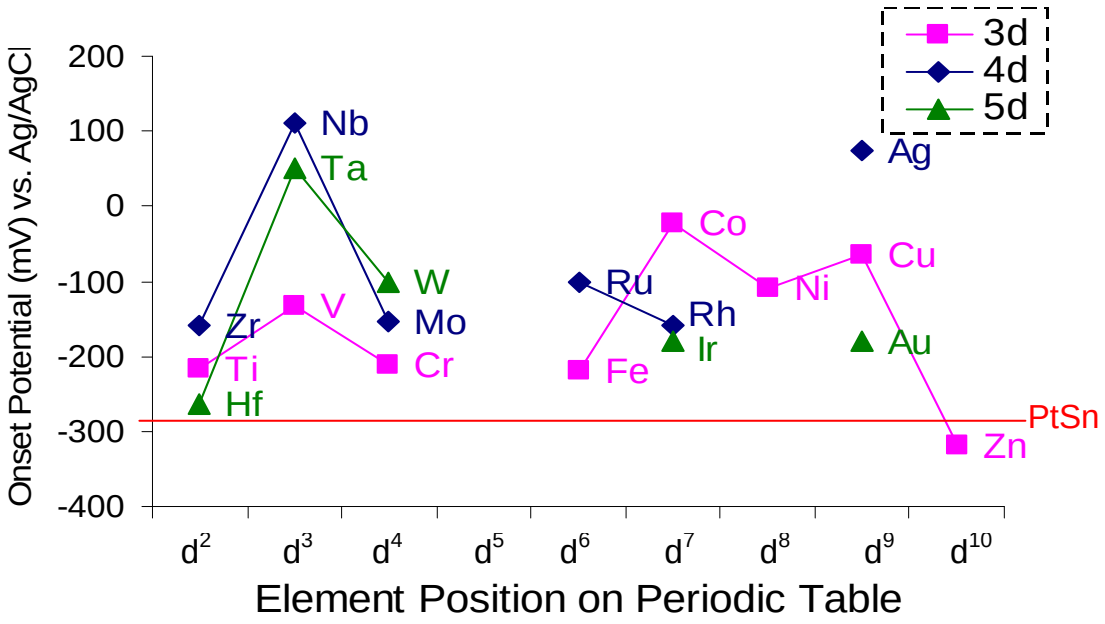

Figure 3.1.1.3: Pt-Sn-X series for ethanol oxidation, scan rate 5 mV/s, film thickness = 2000-2500 Å, sputtering temperature = ambient. Testing solution = 5M ethanol, 0.5 mM quinine, 0.1 M potassium triflate.

3.1.1.1 Film thickness

One of the variables in the deposition process is the film thickness. Pt-Sn-Fe was selected to investigate this effect. The film exhibited activity in the Pt rich and Pt-Sn regions. In particular

for ethanol oxidation, the fluorescence intensity could be plotted versus color intensity for the different thickness films (figure 3.1.1.1.1). It was evident that the ethanol onset potential was independent of thickness in the Pt rich area as opposed to the Pt-Sn region which exhibited increased activity with increasing film thickness. Methanol oxidation showed a similar trend with the Pt-Sn region exhibiting a dramatically enhanced onset potential over a 500 mV range from 100 Å to 3500 Å and, in the Pt rich region, showing less than a 100 mV change from 100 Å to 1000 Å. The underlying cause of this observation can be explained by surface morphology as described subsequently.

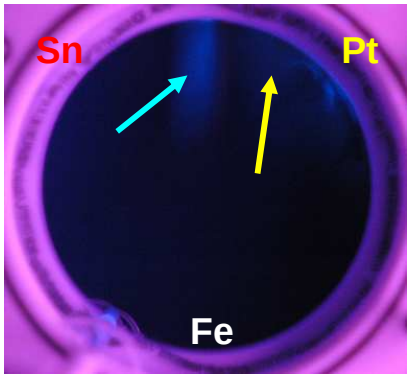

Methanol Oxidation

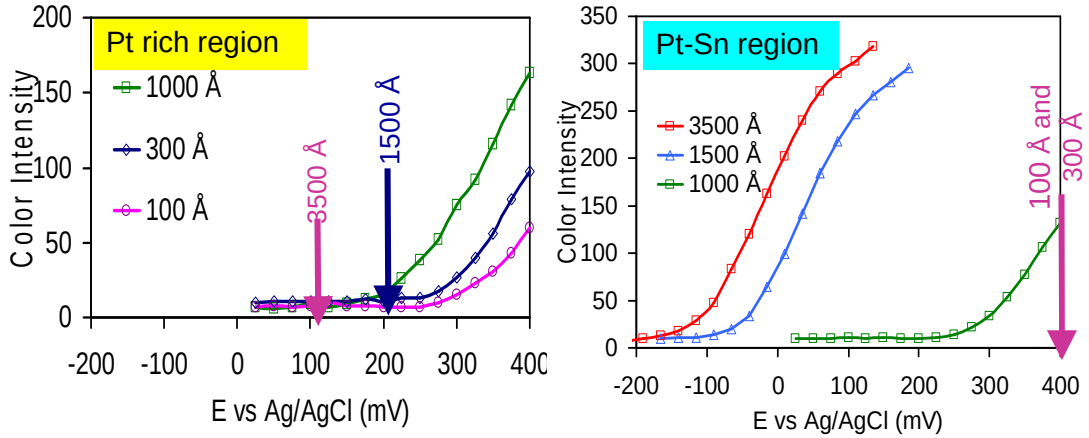

Ethanol Oxidation

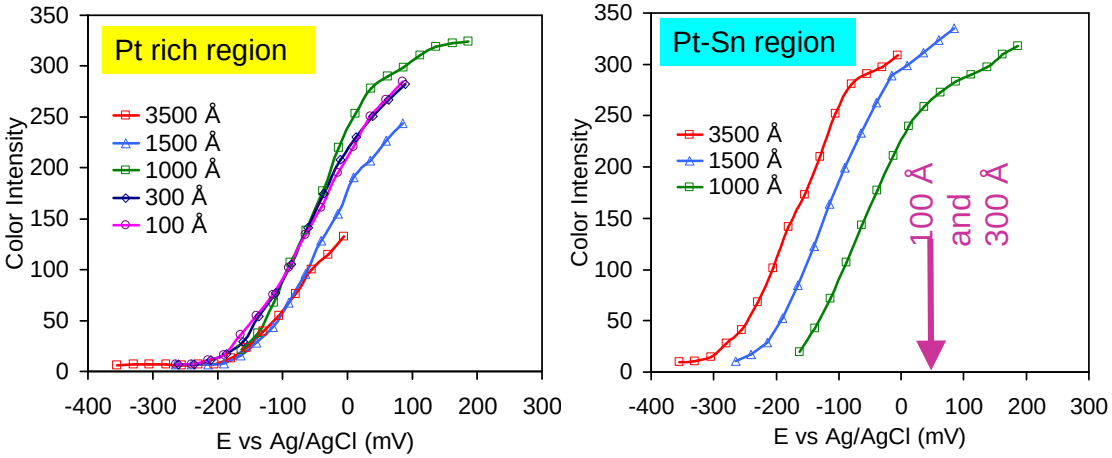

Figure 3.1.1.1.1: Pt-Sn-Fe thin films for methanol (top) and ethanol (bottom) oxidation with varied thickness demonstrating the difference in onset potential with thickness. The arrows denote the maximum potential limit of the linear sweep for the samples without fluorescence.

3.1.1.2 Surface morphology

Thin film surface imaging was performed by Maxim Kostylev and the insight gained into the surface features and morphology helped explain the activity dependence of some samples with film thickness. If we look at the binary Pt-Sn spread, we could see dark regions which could be indicative of a phase change or of surface roughness that make the film appear dark. Upon investigation with SEM on the Pt-Sn region (the fluorescent region in the Pt-Sn-Fe sample that was dependent on film thickness) the surface was, in fact, rough and displayed columnar type surface structures (figure 3.1.1.2.1b and c). By comparison, the Pt rich regions always showed tightly packed grains and appeared mirror like and highly reflective by eye. The columnar structure was attributed to the shadowing of the atoms during the deposition process. For instance, the temperature of the film was so low that condensing atoms that have a very low diffusivity, did not move appropriately, and began to build upon each other and then block the incident atomic beam from penetrating deeper into the film and deposited mostly on the side facing the target. The spaces between the columns also generated an increase in surface area with their columnar structure and exposed surfaces. Another possible explanation for the difference in activity was the exposure of different crystal facets in the columns that could contribute to the overall activity. This was a difficult variable to determine, however, and mainly further complicated the interpretation of our screening results.

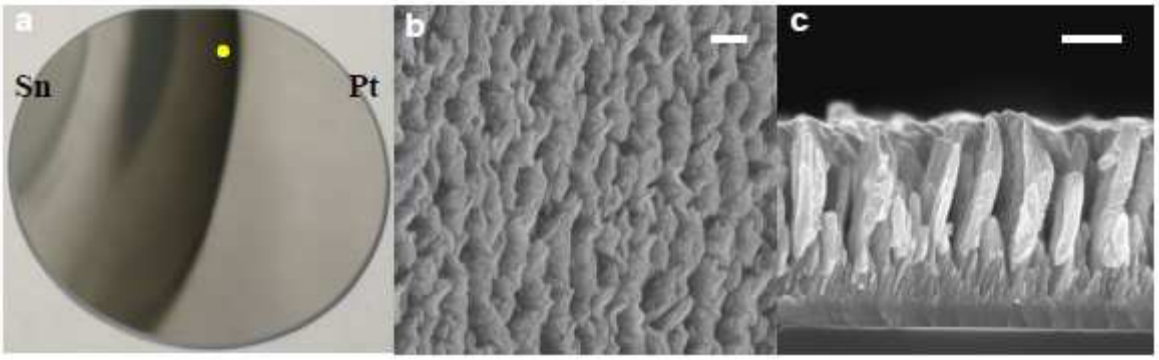

Figure 3.1.1.2.1: Images of Pt-Sn films sputtered at ambient temperature with a 2000 Å thickness. a. Photograph of the as-deposited film. b. SEM image of the surface. c. SEM image of the cross section. (b) and (c) Pt-Sn region marked in the photograph. Scale bars are 200 nm.

In order to mitigate the surface morphology problem, we deposited these thin films at higher temperatures (for example at 250 ^{o}C) to avoid the columnar structure formation with sputtering by increasing surface diffusion. A sample image of a Pt-Sn binary deposited at 250 ^{o}C is shown in figure 3.1.1.2.2. The dark Pt-Sn region was absent, indicating the reduction of the columnar structure, and the coinciding ethanol fluorescence onset potential image for the film indicated that the lower Sn content showed higher activity.

Different phases might be synthesized during deposition at different temperatures, so it is important to deposit films at different temperatures to explore possible high-performance phase. Therefore, I recommend that Pt-Sn-X samples must be remade at a higher temperature and remeasured to establish definitive periodic trends controlling for surface area and film morphology as shown above.

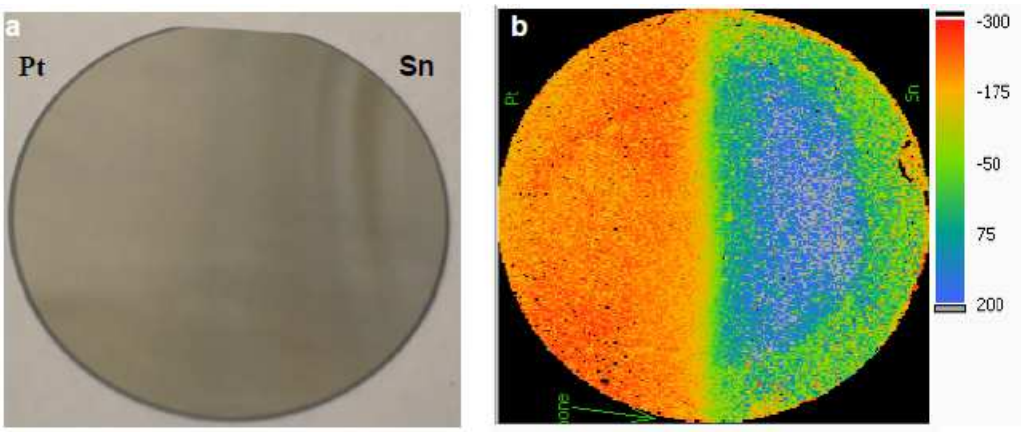

Figure 3.1.1.2.2: a. Optical image of a Pt-Sn binary film deposited at 250 ^{o}C. The Pt-Sn region that appeared dark in the Pt-Sn film at ambient temperature was absent. b. Ethanol fluorescence onset potentials over the Pt-Sn binary film with onsets comparable to the Pt-rich regions found in the ambient condition films. The Sn content of the most active region varied from <5 to 25 at. %.

With many factors confounding our interpretation of the fluorescence results, a more thorough investigation of the Pt-Sn-X series should also include measurement under controlled atmosphere, and with and without pretreatment. We note that the Pt-Sn best onset potentials seemed to have low Sn contents, between <5 to 25 at. %. This motivated the investigation of low concentration alloying of a second element with Pt and will be covered in Chapter 4. Other samples that have been tested and show promising activity are PtZn, PtFe, and PtIn. An in-depth study will be discussed in *Section 3.2* for Pt-Zn.

3.1.2 Pt-Ni-X series

With our accumulation of data, a preliminary online database was constructed and the best onset potentials for each fuel were identified out of the 500 samples (tested to date as of 2008). Among the most promising catalysts was Pt-Ni-X[9] for ethanol oxidation. We therefore decided to explore these ternary films in more detail with the help of a summer undergraduate student, Ms. Sahr Kahn. During the summer of 2008, 75 samples had been tested in this series; however

a direct correlation could not be made among samples due to differences in the third element selection, deposition temperature, thickness, and pretreatment. In this preliminary survey of common samples, Pt-Ni-X (X = Sn, Fe, In, Mn, and Ru) showed the lowest onset potential for methanol and ethanol oxidation. An example of the fluorescence onset potential image is presented in figure 3.1.2.1; the strongest fluorescence is observed to occur in the Pt rich region.

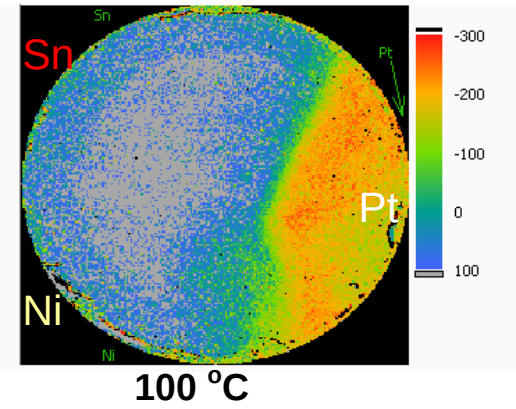

Figure 3.1.2.1: Fluorescence onset potential image for Pt-Ni-Sn for ethanol oxidation after pretreatment, indicating the most active area is in the Pt rich region. The color scale bar denotes the fluorescence onset potential.

The five Pt-Ni-X (X = Sn, Fe, In, Mn, and Ru) films were deposited under the same conditions at a 100 ^{o}C deposition temperature and either 10 or approx. 100 nm thick films. Overall, the thicker samples generally showed improved onset potential compared to their thin film counterparts, which was most likely due to the morphology effects mentioned earlier. Pt-Ni-Sn was an exception. Additionally, the X=Sn and Fe samples were the only ones affected by the pretreatment of the film. In these films, pretreatment caused a decrease in the fluorescence onset potential. We interpreted this as most likely due to an increase in surface area caused by leaching of the Sn or Fe, respectively. The best activity was observed in the Pt-Ni-Ru sample, and this was not surprising because Pt-Ru is a well established catalyst for methanol oxidation catalyst.[10] Pt-Ni-Ru was considered the best catalyst among the present samples because of the

consistency between the thick sample, with and without pretreatment, as well as the lowest onset potential. However, it must also be noted that the Pt-Ni-In sample was as good as the Pt-Ni-Ru under these conditions.

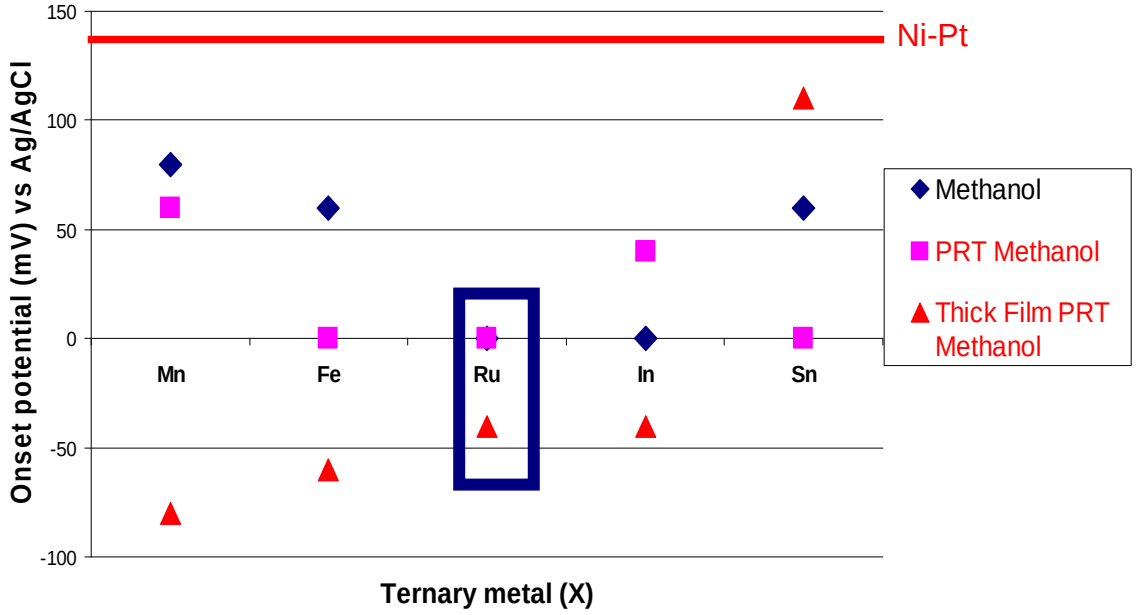

Figure 3.1.2.3: Effects of pretreatment and film thickness on the fluorescence onset potential (mV vs. Ag/AgCl) for methanol oxidation for Pt-Ni-X (X=Mn, Fe, Ru, In, Sn).

On the other hand for ethanol oxidation, Pt-Ni-Sn showed consistent earlier onset potentials with and without pretreatment, which was promising because this suggested good stability and minimal change in the surface upon pretreatment. Pt-Sn is widely known to assist in the CO oxidation process[6] and, as CO is speculated to be an intermediate in the ethanol oxidation mechanism, it has been used to promote ethanol oxidation at low potentials. Ribadeneira and Hoyos found that Pt-Ni-Sn showed promise for direct ethanol fuel cells with an optimal stoichiometry of $Pt_{0.75}Sn_{0.15}$ $Ni_{0.10}$.[9] Pt-Ni-Fe and Pt-Ni-Ru showed promise with a decrease in onset potential of over 200 mV compared to Pt-Ni. Pt-Ni-Mn exhibited a more positive onset potential after pretreatment, which could be due to the active material being

unstable and leached from the surface with the pretreatment. The decrease of onset potential in Pt-Ni-Ru and Pt-Ni-In was attributed to the removal of surface oxides. As was the case for methanol oxidation, thicker samples showed improved activity compared to thinner samples, most likely due to morphology effects. Again, Pt-Ni-Sn was an exception in this regard.

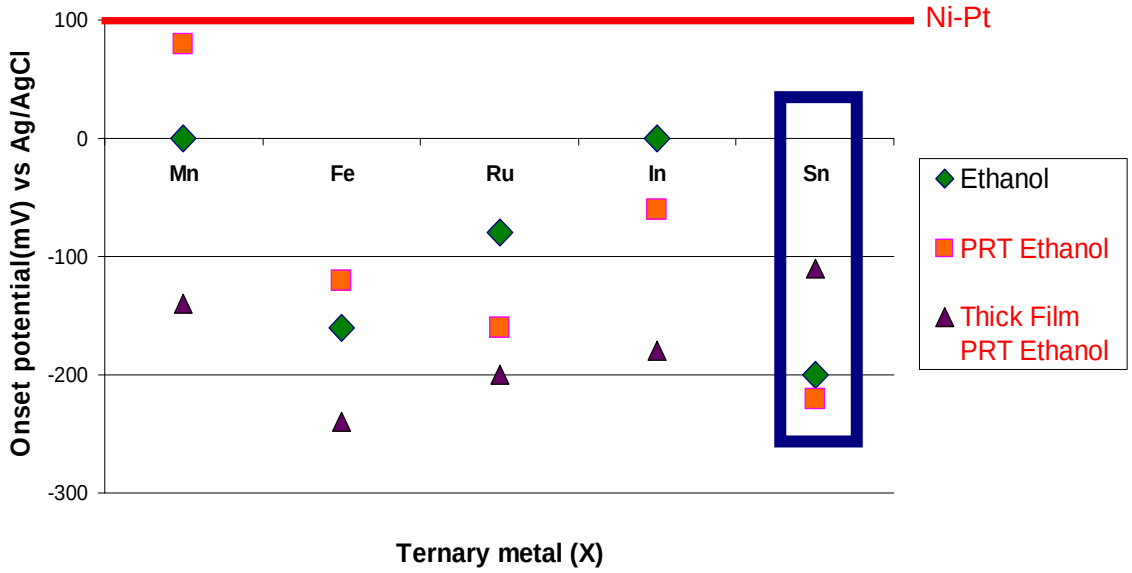

Figure 3.1.2.4: The effect of pretreatment and film thickness on the fluorescence onset potential (mV vs. Ag/AgCl) for ethanol oxidation for Pt-Ni-X (X=Mn, Fe, Ru, In, Sn).

To summarize, the addition of a third element to the Pt-Ni binary system seemed to significantly improve the fluorescence onset potential for both methanol and ethanol oxidation by ~140 mV and ~300 mV, respectively. For methanol oxidation, Pt-Ni-Ru showed the best activity with significant improvements for ethanol oxidation as well. Pt-Ni-Sn was the best ternary for ethanol oxidation and this addition of the Sn to the Pt-Ni binary is supported in the literature.

3.2 Pt-Zn (surface leaching)

See reference for complete published work:

"High-Throughput Evaluation of Dealloyed Pt-Zn Composition-Spread Thin Film for Methanol-Oxidation Catalysis," *J. Electrochem. Soc.*, **2009**, *156(1)*, B160-166.

An essential factor when considering fuel cell catalysts is the stability under strongly oxidizing potentials and acidic conditions. From a thermodynamic analysis, most of the elements in the periodic table are not stable under oxidizing potentials, with Pt and Au having the highest thermodynamic stability. As Pt is alloyed with other elements, the resulting material may not necessarily be stable under acidic conditions and at high potentials. A source for detecting the theoretical stability of elements in water at varying pH's and potentials is the Pourbaix diagram.[8] Pourbaix diagrams provide the soluble or insoluble state of the element of interest with respect to the applied potential and pH of the solution. In many cases, oxide species are the most stable around neutral pH's, this especially applies to the fluorescence screening. On the other hand for acid media, the stable species may be an ion (of the element in question) that is soluble. For instance, the stable form of Zn in acid is Zn^{2+}, whereas at more basic potentials a $ZnO_{(s)}$ form is stable[8].

Often times, to be used in a fuel cell, a promising catalyst is first de-alloyed to reach a stable composition or to make a porous surface from the leaching of the less noble metal.[11, 12] An example is the Au-Ag system, where the Ag is dealloyed from the initially planar surface making a porous film.[11, 13] The porous surface results in a greater surface area, which directly affects the current and can skew the comparisons between samples if the surface area is much

larger than expected. Once the porous matrix is generated, then the active component, Pt, in this case, can be deposited.[11]

Pt-Zn is representative of the effects of leaching on the surface area enhancement. The experimental section covered the deposition process of the films and methodologies. Films were deposited at 250 ^{o}C with a 1:1 stoichiometry in the center and film thicknesses of 100, 500 and 2000 Å. The Zn content of the as-deposited composition spreads varied from ca. 90 to less than 5 atom % and decreased upon electrochemical testing as shown in Fig. 3.2.1. These measurements of bulk stoichiometry indicated that Zn-rich areas of the film dealloyed throughout the bulk of the film, resulting in a stabilized film with ca. 55 atom % Zn. Bulk dealloying did not occur in areas where the initial Pt concentration was greater than 50 atom %. Pre- and post-electrochemistry XRD patterns for the 200 nm film in the region with as-deposited composition of 70 atom % Zn showed that the only identifiable phase in the region was PtZn, which has a tetragonal, AuCu ($L1_0$) structure type. Although a significant amount of Zn leached out from the bulk of the alloy during testing, essentially the same diffraction pattern was obtained after testing, indicating that the material did not undergo a major crystal structure change. The accepted lattice constants for $Pt_{0.53}Zn_{0.47}$ in this phase are 0.4015 and 0.0349. The lattice constants calculated with Jade (Materials Data Inc.) for the pre- and post-electrochemistry patterns are 0.403(2), 0.353(2) and 0.401(3), 0.351(2) nm, respectively. The small shift in lattice constant and the similarity of the Pt and Zn atomic radii precluded the interpretation of composition changes in this phase. Post-electrochemistry XRD patterns obtained at several other substrate positions with initially high Zn concentration revealed the same PtZn ordered structure, demonstrating the stability of this structure with ca. 55 atom % Zn.

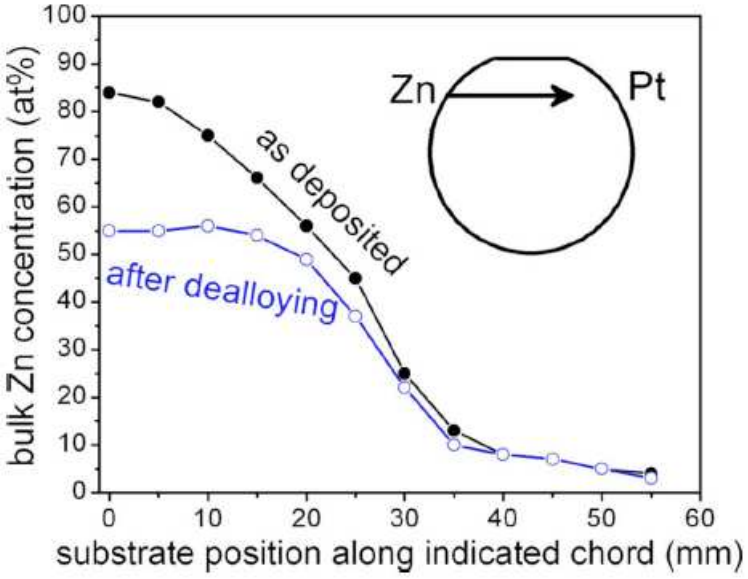

Figure 3.2.1: EDS measurements of film stoichiometry as a function of substrate position for the 2000 Å Pt-Zn film both as-deposited and after electrochemical testing. The inset is a depiction of the substrate with the orientation of the two deposition sources denoted by the elemental symbols. The direction of the measured points is denoted by the arrow. The measurements on the thinner composition spread thin films yield nearly identical results.

Analysis of each fluorescence assay provided a map of fluorescence onset potential for the entire composition-spread thin film. This map is given for the 200 nm film in figure 3.2.2. For all three Pt–Zn films, the fluorescence assays indicated that the Zn rich region of the film was visibly changed by dealloying had a lower fluorescence onset potential than the Pt-rich half of the composition spread.

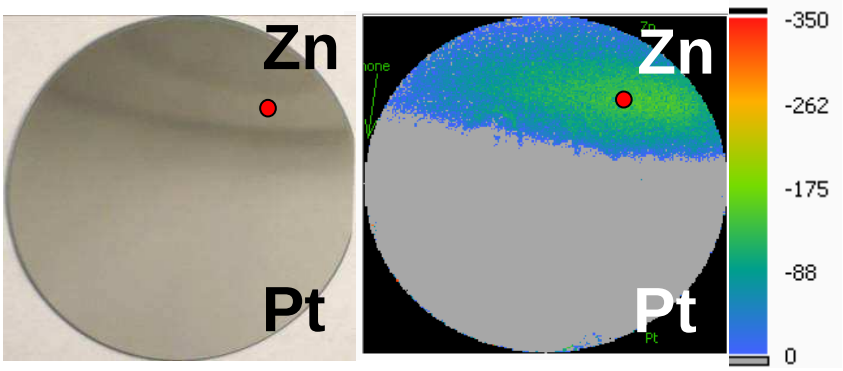

Figure 3.2.2: a. Optical image of the Pt-Zn binary film (2000 Å thick) deposited at 200 ^{o}C. b. Ethanol fluorescence onset potentials over the Pt-Zn binary film. The Zn content of the most active region is approx. 50 at. %.

When we examined the microstructure of the films, the as-deposited Pt–Zn films consisted primarily of tightly packed grains, with SEM images (figure 3.2.3) demonstrating the absence of gaps, cracks, or other features that may be penetrated by an electrolyte solution. However, dealloying in the Zn-rich region of the film to the extent demonstrated by the composition data resulted in a highly porous material.[12, 14] Evidence of such porosity could be observed by the post-electrochemistry SEM image in fig. 3.2.3, which revealed the presence of many large and small cracks due to the compressive stress caused by the leaching of Zn. The cracks observed in the SEM images penetrated the bulk of the film and thus corresponded to a significantly increased surface area available for reaction. The porous microstructure also made the film appear visibly dark due to increased roughness and porosity on the scale of the wavelength of visible light. While the as-deposited films were nearly planar (regardless of thickness), the bulk leaching resulted in a specific surface area that increased with film thickness. Hence, upon dealloying, the ratio of the available surface area to the geometric surface area of the tested region increased with film thickness.

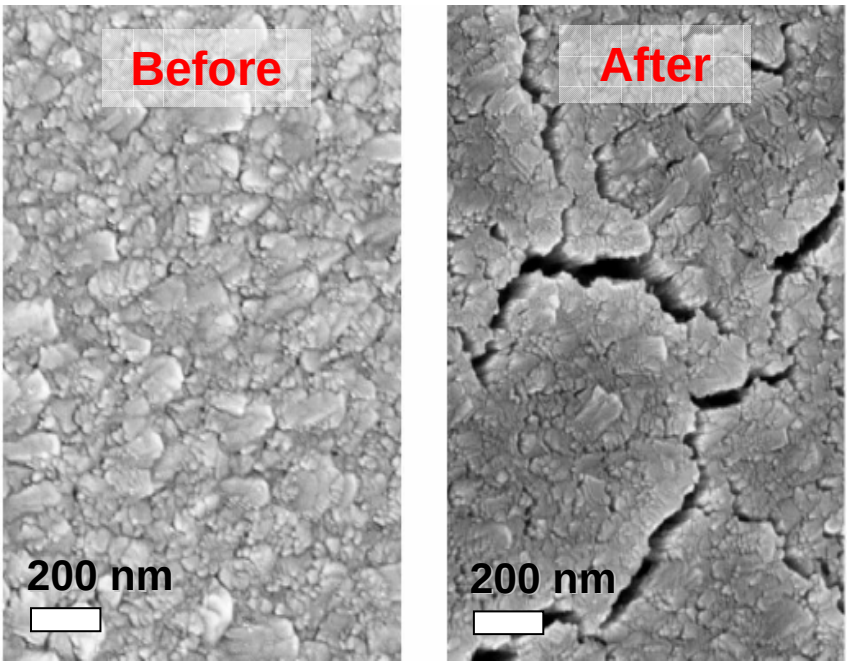

Figure 3.2.3: SEM images of the 200 nm Pt-Zn film surface are shown for both the as-deposited (left) and electrochemically tested (right) film at the same position. The electrochemically tested film has cracks as large as tens of nanometers wide and hundreds of nanometers long which appear to extend throughout the thickness of the film. Similar cracks are visible in SEM images of the thinner films. Scale bars are the same for both images.

The electrochemically active area was measured by a cyclic voltammogram at a scan rate of 50 mV/s for the ferrocene monocarboxylic acid redox reaction on a planar Pt film as shown in figure 3.2.4. As expected for a reversible reaction and freely diffusing species at a planar electrode, the forward and backward scans were symmetric, with a ΔE_p value of ca. 60 mV. The (sweep-rate normalized) forward scans for ferrocene monocarboxylic acid oxidation on a 200 nm dealloyed Pt–Zn film are also shown for three scan rates. Although all of these scans were performed on the same geometric area of film, the significantly higher peak current at lower scan rates indicated a much higher specific surface area. The wide distribution of pore sizes in the dealloyed film corresponded to diffusion dynamics beyond the planar electrode model, and thus symmetry in the forward and reverse scans was lost. The effective electrode surface area decreased with increasing scan rate, as slower scan rates afforded ferrocenemonocarboxylic acid

diffusion into small pores. This phenomenon was accentuated by the low concentration of ferrocenemonocarboxylic acid in the test solution. For measurement of the electrode area, we used only peak currents from forward scans at 5 mV/s sweep rate, the same sweep rate used for acquisition of methanol oxidation voltammograms.

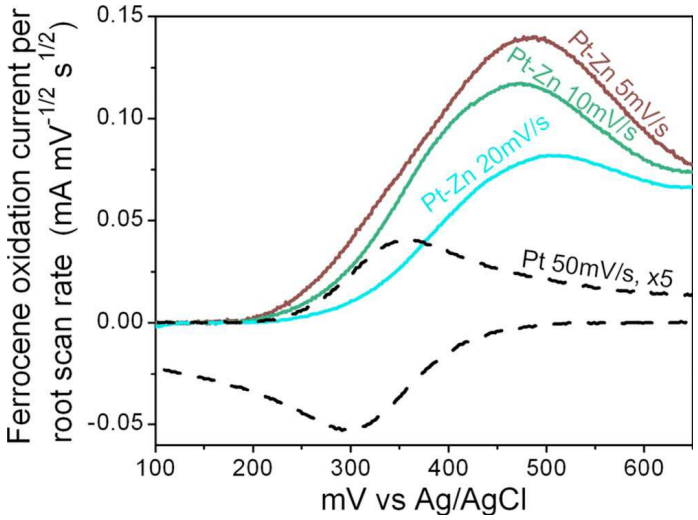

Figure 3.2.4: Measured ferrocenemonocarboxylic acid redox currents, scaled by the square root of the sweep rate, are plotted for different thin-film electrodes using the same geometric area. The cyclic voltammogram (dotted line) acquired at 50 mV/s on a planar Pt film is scaled by a factor of 5. The forward scans (ferrocene oxidation waves) are shown for three scan rates with a porous 200 nm Pt-Zn film. The systematic decrease in peak height with increasing scan rate reflects the fine pore structure of the film.

Local testing of the composition library was performed in a 0.73 cm^2 region straddling the boundary of bulk leaching in the film (as noted in figure 3.2.2). The total surface areas of the 10, 50, and 200 nm films were detected to be 3.5, 13, and 29 cm^2 (±20%), respectively. For each film, this measured area was used to determine the area ratios of the porous region in the 0.73 cm^2 testing area. Also, the same 0.73 cm^2 region was used to measure methanol oxidation currents at pH 1, and these currents were scaled by the ferrocenemonocarboxylic acid-determined surface areas to yield the specific oxidation current densities plotted in figure 3.2.5. The geometric current densities are also shown, dramatically illustrating the importance of the

surface area measurements for comparing catalytic activity to that of planar Pt. For example, the required overpotential for 20 μA per geometric cm^2 was 120 mV less for the 200 nm film compared to the 10 nm film, but the overpotentials for specific area 20 μA per specific cm^2 were within 35 mV for all three films. Above 650 mV vs SHE, the increased current densities of Pt–Zn compared to Pt were not due to differences in mass transport and thus indicated improved reaction kinetics, possibly due to an improved tolerance of the surface Pt in PtZn toward catalyst poisons such as CO. However, at low overpotentials, the current density measurements indicated that the three Pt–Zn films have similar reaction kinetics both among themselves and compared to planar Pt.

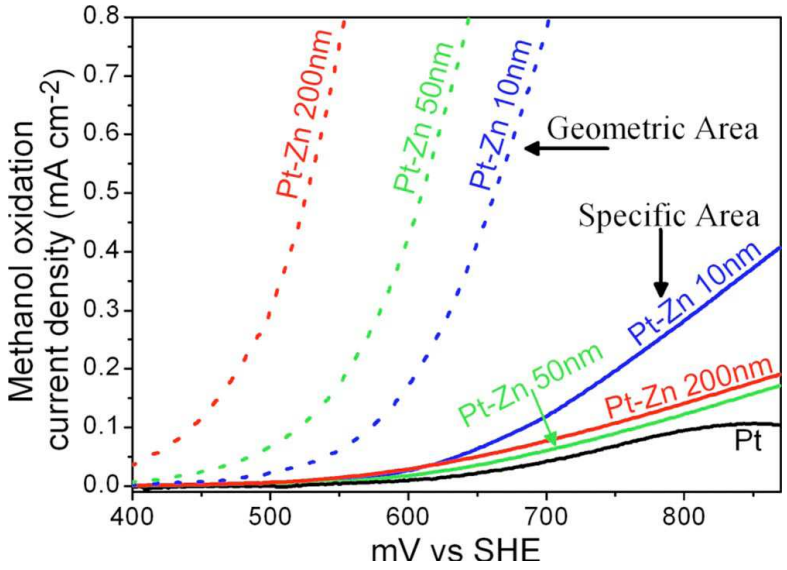

Figure 3.2.5: Methanol oxidation current at pH 1 with 5 mV/s scan rate. The geometric surface area is 0.73 cm^2 for the geometric current density (dashed lines) and specific area current densities were calculated using surface areas from the hydroxymethyl ferrocene linear sweep voltammetry (solid lines).

The similarity of the materials properties of the three Pt–Zn films determined by traditional characterization techniques (EDS and XRD) suggested that the films contained the same active material. This conclusion was also readily reached by employing our collection of

high throughput electrochemistry methods. The electrochemical characterization provided the additional direct comparison to the planar Pt catalyst. The complete set of characterization data resulted in the conclusion that Zn-rich Pt–Zn alloys undergo bulk leaching of Zn under the electrochemical tests. The post-leaching, stable film was highly porous and consisted of a slightly Zn-rich PtZn ordered intermetallic phase. The specific activity of the film toward the oxidation of methanol was equivalent to that of planar Pt at low current densities, which most likely corresponded to a Pt coating of the PtZn phase. The underlying ordered intermetallic may alter the electronic properties of the surface Pt, making the catalyst more tolerant to poisons.

3.3 Pt-Ta [Manuscript]

This section consists of the published manuscript: "Improved Fuel Cell Oxidation Catalysis in $Pt_{1-x}Ta_x$." *Chem Mat.* **2010**, *22*, 1080-1087.

3.3.1 Abstract

Sputter codeposition of platinum and tantalum was used to generate catalyst libraries of $Pt_{1-x}Ta_x$ with $0.05< x <0.9$. Extensive characterization of the libraries by high-energy X-ray diffraction revealed the presence of several ordered intermetallic phases as a function of composition and deposition conditions. Assessment of the activity toward the oxidation of methanol and formic acid was achieved through a fluorescence-based parallel screening, followed by detailed testing of the most promising catalysts. Correlations among the electrochemical results, the inferred phase fields and X-ray photoelectron spectroscopy characterization provided an understanding of the catalytically active surface and highlight the utility of composition spread thin films in

catalyst research. The observations suggested that the interaction between Pt and Ta suboxides was important and enhanced the catalytic activity of Pt.

3.3.2 Introduction

Fuel cells, in particular polymer electrolyte membrane fuel cells (PEMFCs), represent an attractive technology to meet future energy needs because of their potentially high efficiency in converting stored chemical energy to electrical energy. However, their widespread deployment has been hampered by materials limitations, as exemplified in the catalysts by their high cost, intolerance to fuel contaminants, and degradation leading to short fuel cell lifetimes. The possible use of methanol and other small organic molecules (SOMs) as PEMFC fuels is promising because of their high energy density and ease of transport, compared to H_2. Presently, one of the setbacks for implementation of SOM PEMFCs has been the lack of an anode catalyst that effectively overcomes the kinetic barriers for complete oxidation (to CO_2) of these complex molecules. Theoretical models that describe the complete oxidation of SOMs incorporate several adsorption and charge transfer steps that are optimized by surface atomic and electronic structure properties unique to the catalyst.[15, 16] During this oxidation process, CO formation (as an intermediate) is likely, and thus CO tolerance of catalysts is an implicit factor in oxidation catalysis studies using such fuels. CO tolerance is a particularly relevant property, as it is also of importance for the anode catalyst in H_2 fuel cells. The poisoning of Pt catalysts by CO impurities associated with H_2 production from hydrocarbon reformation is a quintessential issue in catalysis.

To address this and other issues, catalyst research often involves the generation of a new catalyst by alloying Pt with less-noble metals (including Pt-based ordered intermetallics),[17]

forming layered catalyst structures,[18, 19] or replacing the standard carbon support for Pt nanoparticles. Because the interfaces among electrode components often play an important role in catalysis and the electrode surface may be altered during operation as a catalyst, these ideal electrode archetypes are rarely distinctly realized. The influence of electrode modification on catalytic activity is most directly determined by characterization of the surface during catalysis, a notoriously difficult task. In the present work, we present an ensemble of characterizations that, when applied to a library of catalysts in the Pt-Ta system, provide insights into the composition and structure of the most catalytically active material.

Tantalum Incorporation in Fuel Cell Catalysts.

Recently, several methods of Ta inclusion in PEMFC electrode materials have been investigated. Ishihara et al.[20] demonstrated activity of partially oxidized tantalum carbonitrides for the oxygen reduction reaction (ORR) and noted the importance of the degree of surface oxidation. ORR catalysis was also studied on electrodes containing a combination of Vulcan carbon, Pt colloids and TaO_y formed by oxidation of Ta after its reduction from $TaCl_5$. The addition of Ta_2O_5 increased the area-specific ORR activity for only certain Pt-Ta_2O_5-C configurations, suggesting that any improvement in catalytic activity is related to the interfaces of the three components. $Pt_{1-x}Ta_x$ alloys have also been investigated as possible PEMFC cathode materials.[21] Composition spread thin films covering the entire composition range were found to be quite stable at oxidizing potentials in acidic media, but the catalytic activity for oxygen reduction dropped sharply and monotonically with increasing Ta content. Studies of H_2 and CO oxidation have also been performed on TaO_y-modified Pt/C electrodes. CO oxidation on commercial Pt/C electrodes partially coated with Ta_2O_5 showed a 150 mV negative shift in the peak potential for oxidation of

adsorbed CO.[22] Similar experiments were performed on Pt + TaO_y and PtRu + TaO_y electrodes.[23] The former electrode was made by coreduction of $Pt(NO_2)_2(NH_3)_2$ and $TaCl_5$ on Vulcan carbon. While the inclusion of TaO_y only lowered the CO oxidation peak by 70mV (50mV for PtRu + TaO_y), the authors also studied the time dependence of CO adsorption onto the electrodes and found that the inclusion of TaO_y significantly decreased the adsorption rate. This behavior indicates that the role of TaO_y in improving the CO tolerance of Pt is distinct from that of alloyed Ru. Surface Ru serves as a source of active oxygen and thus enhances CO oxidation,[24] but TaO_y diminishes the adsorption of CO, possibly through a decrease in the Pt-CO bond strength. The Ta oxidation state was not characterized in the materials of Ueda et al.,[23] but Lesnyak et al. found that the use of a similar material as a gas phase H_2 oxidation catalyst resulted in partial reduction of the Ta_2O_5 support. The electrode, consisting of Pt nanoparticles on a Ta_2O_5 support, was characterized by XRD, electron diffraction and X-ray spectral microanalysis both before and after use as a catalyst for oxidation of H_2 in a fuel stream with 20:1 O_2:H_2. The catalysis test resulted in a decrease in the oxygen stoichiometry from y=2.4 to 2.3, with both values slightly smaller for TaO_y regions adjacent to Pt particles. This partial reduction of the Ta caused the surface of the highly crystalline Ta_2O_5 support to transform into a nanocrystalline Ta_2O_5 + TaO_2 composite. CO oxidation on $Pt_{1-x}Ta_x$ alloy thin films[25] and bulk Pt_2Ta and Pt_3Ta ordered intermetallics[26] has also been studied. The latter work found that the oxidation of adsorbed CO was shifted to more positive potentials for the intermetallic compounds compared to pure Pt. This shift could be due to an increase in Pt-CO binding energy and underscores a difference in the role of Ta in these materials and that of the Pt-TaO_y composites. Stevens et al.[25] studied thin film $Pt_{1-x}Ta_x$ catalysts deposited on water-cooled substrates, and XRD characterization of the films indicated that the low deposition temperature

kinetically stabilized Ta-rich bcc and Pt-rich fcc alloys. In addition, a nanocrystalline (or possibly amorphous) alloy (NCA) was observed for $x > 0.3$. The thin film samples with $0.3<x<0.7$ exhibited CO-stripping onset potentials up to 50 mV lower than that of pure Pt and a corresponding small decrease in onset potential was observed for the oxidation of H_2 in the presence of CO. We studied $Pt_{1-x}Ta_x$ composition spread thin films deposited at elevated temperatures, which enables the synthesis and electrochemical characterization of the ordered intermetallic phases. These films do contain an NCA region, and methanol oxidation on the as-deposited NCA demonstrates a negative shift in oxidation potential (in agreement with Stevens et al.).[25] However, we demonstrate further improvement in methanol oxidation activity via a catalyst pretreatment step. In addition, our study of methanol oxidation as a continuous function of composition, combined with the XRD mapping of the libraries, reveals important trends in catalytic activity.

3.3.3 Experimental Section

Composition Spread Deposition.

Films were prepared in a custom built combinatorial sputter deposition system described previously.[27] Each $Pt_{1-x}Ta_x$ library was generated by first depositing an adhesion layer (underlayer) onto a 76.2 mm diameter Si substrate. During and after this deposition, the substrate was radiatively heated and maintained at the library deposition temperature. Elemental Pt and Ta (>99.9% purity) were codeposited from separate magnetron sputter sources (Angstrom Sciences) in an atmosphere of 0.66 Pa Ar. With the aid of a cryoshroud,[27] the background pressure during deposition remained in the 10^{-5} Pa range. The geometrical relation of the deposition sources with respect to the Si substrate provided a deposition gradient from each source that upon

codeposition resulted in a continuous variation in composition across the substrate. The Pt and Ta deposition rates at substrate center were measured with a quartz crystal monitor just prior to deposition of the library. The range of x represented in a given library was dictated by the deposition profiles of the individual sources but may be shifted to the Pt-rich or Ta-rich range by control of the relative power delivered to the independent sources. Given the constant deposition rates, the film thickness was determined by deposition time, but the thickness at each substrate position was determined by the local deposition rates and chemical mixing of the elements. In the present work, three $Pt_{1-x}Ta_x$ libraries are discussed; they are distinguished by the underlayer, deposition temperature, thickness at substrate center ("library thickness") and stoichiometry at substrate center. Library A was generated with a 12 nm Ti underlayer, 400 ^{o}C deposition temperature, 160 nm library thickness and x = 0.25 at substrate center. Library B was generated with a 12 nm Ta underlayer, 550 ^{o}C deposition temperature, 160 nm library thickness, and x = 0.5 at substrate center. Library C was generated with a 30 nm Ti underlayer, 450 ^{o}C deposition temperature, 35 nm library thickness, and x = 0.33 at substrate center.

Thin Film Characterization.

We calculated the spatial map of composition in the libraries using verified models and measured deposition profiles for the Pt and Ta sources.[28, 29] For Library A, composition measurements were made before electrochemical testing by X-ray fluorescence (XRF) with a 60 keV X-ray source and after electrochemical testing by energy-dispersive X-ray spectroscopy (EDS) using a JEOL 8900 EPMA Microprobe. The composition maps from the three measurement techniques agree within the measurement errors. In this manuscript, the deposition profile-calculated

compositions are used for all three libraries, and the additional data for Library A are presented in *Section 3.3.7*.

XRD characterization of the libraries was performed with a high-throughput crystallography setup. Monochromatic 60 keV X-rays impinge the thin film and the diffraction image was attained in transmission geometry by a 345 mm diameter image plate (Mar Research). Integration of the images provided diffraction patterns which were compared to patterns of known phases in the Powder Diffraction File (PDF)[30] to construct a phase map of the library. We also note that sputter deposition commonly yields fiber textured thin films in which the constituent crystallites are randomly oriented with respect to substrate azimuth but aligned with respect to substrate normal.[31] The average crystallite orientation in the film was determined by analyzing the diffraction images, as described in *section 3.3.7*. This orientation was important, as it dictated the crystal facet at the film surface, which may ultimately determine surface chemistry and reactivity.

Surface composition and oxidation were characterized by XPS analysis using a Surface Science Instruments SSX-100 with a 1 μPa base pressure. Sample orientation provided a 55^{o}emission angle. Survey scans were performed with 150 V pass energy from 0 to 600 eV at 1 eV/step. High resolution scans were performed with 50 V pass energy from 15 eV to 85 eV at 0.065 eV/step. In situ cleaning of the film surface was performed by 15 s impingement of 4 keV Ar at 3 $\mu A/cm^2$, but minor residual surface contamination by hydrocarbons was inferred from the presence of a weak C 1s peak. Although such contamination had a negligible effect on the analysis of the Ta and Pt, the likely presence of oxygen in the contaminant layer confounded the measurement of oxygen in the film.

The 15-85 eV spectra were fit with one set of Pt 4f doublet peaks and either two or three sets of Ta 4f doublet peaks using the CasaXPS software package. Our established analysis of metal thin films employs the Shirley line shape to model the background and an asymmetric-Lorentzian peak shape. For fitting procedures, the doublet peaks were constrained by the known binding energy shifts and area ratios.

Fluorescence Assay.

In the past decade, a number of publications have presented combinatorial high-throughput methods for efficient exploration of the wide range of possible anode catalysts for direct methanol fuel cells (DMFCs). The fluorescence assay used to screen catalysts was first employed by Reddington[32] and further adapted for thin films by Prochaska, et al.[1] The entire film was used as the working electrode in a specially designed electrochemical cell.[33] In the screening process, a pH-sensitive fluorescent indicator was used to identify catalytically active regions in a combinatorial library.[1] The potential applied to the film was swept from -100 to 500 mV vs. Ag/AgCl at a scan rate of 5 mV/s, and a large area Au coil served as the counter electrode. The testing solution consisted of 5 M methanol, 3 mM quinine, and 0.1 M potassium triflate as supporting electrolyte. The solution began at neutral pH and as increasingly high overpotentials were applied to the film and methanol was oxidized, the released protons caused a decrease in pH below 5. Protonation of the quinine ensued and in this condition the quinine was fluorescent under UV illumination. Although the entire library was a common working electrode, the local generation of protons allowed measurement of catalytic activity with approx. 1 mm resolution via optical detection of fluorescence. Images were taken at 20 mV intervals with a charge

coupled device (CCD) camera, and at a given region of the library, image processing provided a fluorescence intensity profile.

A model for the fluorescence profile is shown below:

$$F = An\ln(1+ \mathrm{Exp}((E - E_{1/2})n/f))$$

where F is the fluorescence intensity, E is the applied potential, and f=59.1 mV at ambient temperature. The prefactor A, halfwave potential $E_{1/2}$, and number of electrons n in the rate-limiting reaction are model parameters. In the present work, we fixed n = 2 and extracted the figure of merit $E_{1/2}$ through least-squares fitting of the measured profiles and it was explained in more detail in John Gregoire's thesis.[34]

In addition to the routine fluorescence tests, a pretreatment of the film was performed to ostensibly reduce surface oxides that were formed upon air exposure and to remove other surface contaminants. This pretreatment entailed a linear voltage sweep from 0 to -800 mV vs Ag/AgCl in an aqueous solution of 0.01 M H_2SO_4 with 1 M Na_2SO_4 as supporting electrolyte.[33]

Localized Electrochemical Characterization.

While the fluorescence assay allowed us to efficiently identify the nominal compositions of promising methanol catalysts, additional testing was required to determine the catalytic properties under fuel cell (low pH) conditions. Localized electrochemical testing was enabled with a 6 mm inner diameter Teflon cell that isolated a 0.32 cm^2 film region. A 70 mm diameter cell sealed on the edge of the substrate and was filled to expose the entire library (working electrode) to testing solution. The 6 mm cell contained counter and reference electrodes, and positioning the cell at a chosen spot on the substrate allowed for testing of catalysts within a 5 at. % composition range. In the present study, this technique was used to acquire cyclic

voltammograms (CVs) of select catalyst regions in solutions at a pH of 1. CVs acquired in the absence of fuel provided further characterization of the catalyst, and CVs acquired in the presence of fuel verified the activity of the catalysts in an environment that approaches fuel cell conditions.

To facilitate comparison of oxidation current densities, specific surface area measurements were performed on select catalysts. Because of surface roughness, the active surface area could be much larger than the projected geometric area. As previously described,[33] a linear sweep voltammogram using 1 mM ferrocenemethanol in an aqueous solution of 0.1 M potassium triflate (supporting electrolyte) was used for determining the specific surface area of films. While this technique provided the true electrode surface area available to molecules comparable in size to ferrocenemethanol, the absolute area of Pt surfaces was quantified through analysis of hydrogen adsorption and desorption in 0.1 M H_2SO_4.

3.3.4 Results and discussion

Structural Characterization.

The XRD patterns obtained from the high-throughput crystallography experiments are represented in Figure 3.3.4.1. For Libraries A and B, the set of substrate positions characterized in the XRD experiments are shown as solid black dots on a composition map of the substrate. These diffraction patterns, and the corresponding compositions, were used to generate an interpolated map of diffraction intensity vs |Q| over the composition range of the library. Inspection of these maps revealed several phase boundaries as well as differences in the phase behavior of the two libraries. As seen in Figure 3.3.4.1c, the $Pt_{1-x}Ta_x$ ordered intermetallic phases exhibited a large number of reflections. The typical crystalline grain size of less than approx. 10

nm resulted in a relatively broad diffraction peak line width of greater than approx. 0.7 nm^{-1}. Consequently, many of the reflections overlapped both within a given phase and among other phases, which confounded rapid phase identification. The preferred orientation of the crystallites (see fiber texture discussion above) gave rise to additional complexities in interpreting the phase behavior of the libraries. However, analysis of both the correlated shifts in |Q| values of peaks and the appearance or disappearance of peaks as a function of composition assisted in phase identification.

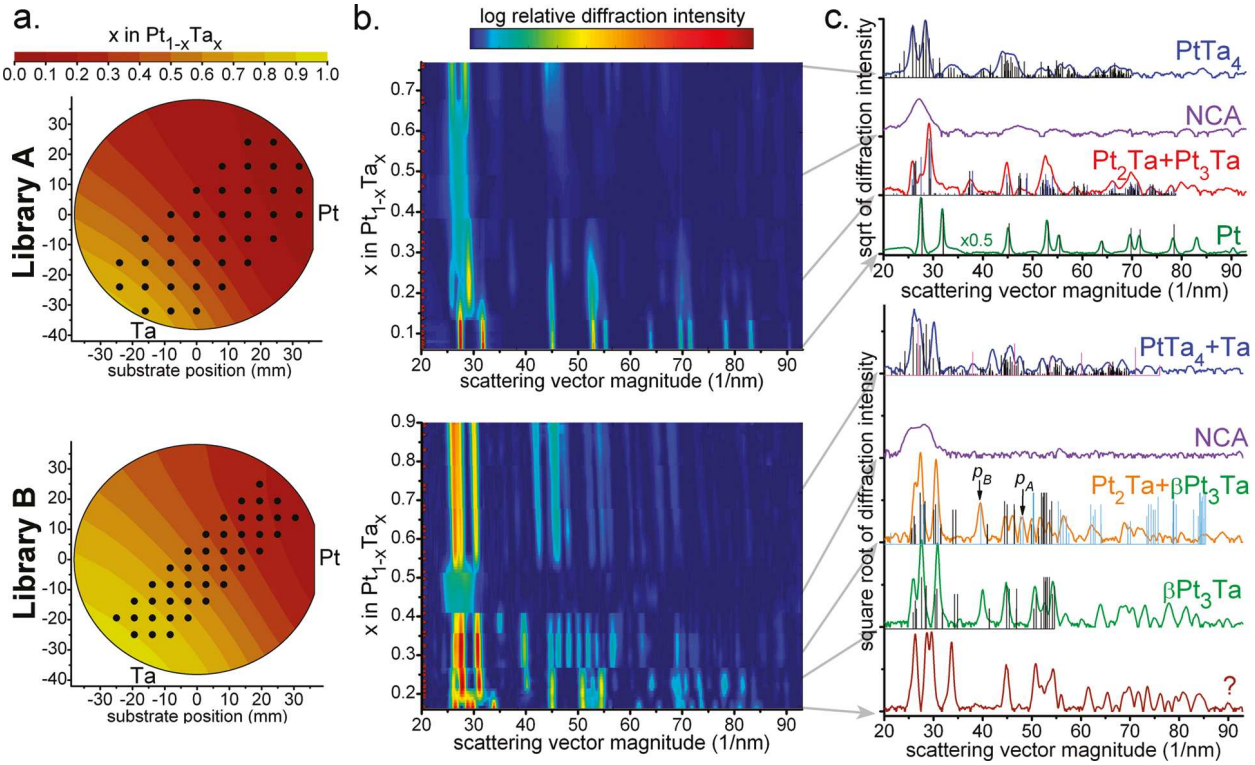

Figure 3.3.4.1: Composition and XRD mapping of Libraries A (top row) and B (bottom row). (a) Value of Ta fraction x as calculated from deposition profiles plotted over an outline of the substrate. The element labels indicate the orientations of the deposition sources with respect to the substrate. The substrate positions analyzed by XRD are denoted by black points. (b) X-ray diffraction intensities (color scale) as a function of scattering vector (horizontal axis) for measurements taken at various positions (indicated in a), plotted with interpolation as a function of the corresponding x (vertical axis). The observed compositional ranges of peak sets outline the phase fields of the library. The specific compositions of diffraction measurements are noted by small red markers on the composition axis. (c) Representative diffraction patterns from each phase field are plotted to demonstrate phase identification. Reference PDF peaks for labeled phases (Table 1) are plotted in black where relevant. For the Pt_3Ta + Pt_2Ta pattern, PDF 03-1465 is shown in blue and 03-1464 in black. For the Library B $PtTa_4$ + Ta pattern, the Ta PDF peaks are shown in gray. For the Pt_2Ta + β Pt_3Ta pattern, the Pt_2Ta (PDF 18-0975) lines are shown in blue with lattice constant reduced by 6% and the β Pt_3Ta lines are shown in black with lattice constant increased by 2%. Relative diffraction intensities are on the same square-root scale across all compositions except that the plot corresponding to fcc-Pt has been multiplied by 0.5.

In the analysis of Library A, the identification of the fcc-Pt (the pure phase for x <0.14) and $PtTa_4$ (the pure phase for x>0.67) phases was straightforward. From x = 0.14 to 0.44, the set of reflections indicated the presence of an orthorhombic phase. As evident in the PDF patterns, orthorhombic Pt_2Ta and Pt_3Ta were distinguished by low-intensity peaks which were observed in

all diffraction patterns in this composition range. Although the relative concentrations of the two phases likely changed as a function of *x*, in the present work we simply designated this phase region as ortho-$Pt_{1-x}Ta_x$. This library also contained a phase with little diffraction intensity, other than a broad peak near 27 nm^{-1}. Similar diffraction patterns in this composition range had been presented for films deposited at low temperature.[21, 25] Although this unidentified phase may consist of nanometer-scale grains of the high-temperature phase PtTa,[35] the lack of substantial grain growth even at our elevated deposition temperature suggested the possibility that this system forms a metallic glass.[36] Pending further study of this phase we denote it NCA (nanocrystalline alloy). All phases except the NCA phase exhibited strong fiber texture with sharp peaks in the diffraction intensity distribution as a function of angular displacement from substrate normal. For the ortho-$Pt_{1-x}Ta_x$ phases of Library A, our analysis indicated that one or more of the following crystallographic planes were oriented parallel to the film surface: Pt_3Ta (100), Pt_2Ta (010), Pt_2Ta (001).

Library B also contained the $PtTa_4$ intermetallic and an NCA phase but exhibited different phase behavior in the Pt-rich half of the library. For $x < 0.2$, the XRD patterns indicated the presence of an ordered intermetallic phase but the pattern did not match any Pt-Ta entries in the reference literature.[30] Instead of the orthorhombic Pt_3Ta found in Library A, Library B contained monoclinic β-Pt_3Ta. The cause for this difference in phase behavior was not understood. The orthorhombic phase was believed to be stabilized by interstitial impurities such as oxygen.[35] Oxygen contamination should increase with the higher background pressure associated with increased deposition temperature, yet the orthorhombic phase was found in the library deposited at lower temperature. A more likely cause could be an influence from the underlayer. At the start of the composition spread deposition, the Ta underlayer of Library B

may nucleate a different phase than the Ti underlayer of Library A. Once nucleated, the metastable phase could grow indefinitely.

While β-Pt_3Ta was present from $x = 0.19$ to above $x = 0.4$, as x increased beyond 0.27 the lattice constant discontinuously increased. At this phase boundary, several new peaks appeared, such as the peak labeled p_A in Figure 3.3.4.1c. These peaks were matched by a different orthorhombic structure of Pt_2Ta (03-1464 instead of 18-0975 used for Library A) after a 6% decrease in lattice constant was applied. This pattern also matched well with the peak labeled p_B, but this peak was present for $x < 0.27$ and was the only peak in these β-Pt_3Ta diffraction patterns that did not match the monoclinic PDF pattern. The appearance of several new peaks in the diffraction pattern of an ordered intermetallic suggested the addition of a second phase rather than ordering within the existing phase. We thus assert that orthorhombic Pt_2Ta was present on the Ta-rich side of this phase boundary but note that full understanding of phase behavior in Library B will require further analysis.

XPS Characterization.

XPS characterizations were performed on Library C. An $x = 0.31$ region of the film was analyzed before electrochemical testing, and following characterization by the fluorescence assay (including pretreatment), the library was diced, and pieces centered at $x = 0.11$, 0.31, and 0.67 were used for analysis. We note that for the x = 0.31 film, the differences in these quantities before and after electrochemical testing were negligible. The invariance of x = 0.31 XPS measurements indicated that any chemical surface modification that occurred during electrochemical testing was reversed upon re-exposure to ambient conditions.

The XPS measurements indicated that the film surface was enhanced in Ta compared to the bulk, which suggested that the chemical potential gradient provided by surface oxidation of Ta was sufficient to cause nanometer-scale diffusion of Ta to the surface. This effect was driven by the high heat of formation of TaO_y compared to PtO_z and was observed in the $Pt_{1-x}Ta_x$ thin films of Bonakdarpour et al.[21]

The binding energy of the Pt $4f_{7/2}$ peak increased with increasing *x* and exceeded the 70.9 eV value for pure Pt, indicating partial charge transfer from Pt or a lattice strain effect. We note that in the event that the *d*-electron density decreases via electron transfer to TaO_y, the Pt-CO binding energy would increase.

The Ta 4f binding energies also shifted to positive potentials, but we considered the effect of electron transfer with Pt to be negligible compared to Ta-O interactions. Kerrec et al.[37] studied the increase in binding energy with increasing Ta oxidation and associated the Ta $4f_{7/2}$ binding energies 23.5 ± 0.4 eV, 26.1 ± 0.4 eV, and 27.1 ± 0.2 eV with TaO_y stoichiometries $y = 1$, $1 < y \leq 2$, and $y = 2.5$, respectively.

Using these associations, we found that for each Ta concentration, the top few nm of the $Pt_{1-x}Ta_x$ films contained both Ta^{II} and Ta in a higher oxidation state (higher binding energy). The fraction of the Ta in a higher oxidation state increased as expected with *x*. The spectra from the $x = 0.11$ and $x = 0.31$ samples were both well fit by one set of high energy peaks while the $x = 0.66$ spectrum required two sets of such peaks to account for the observed data (see Figure 3.3.4.2). Although all three spectra had a peak associated with $1 < y < 2.5$, only the $x = 0.66$ sample had a peak associated with fully oxidized Ta, i.e., $y = 2.5$.

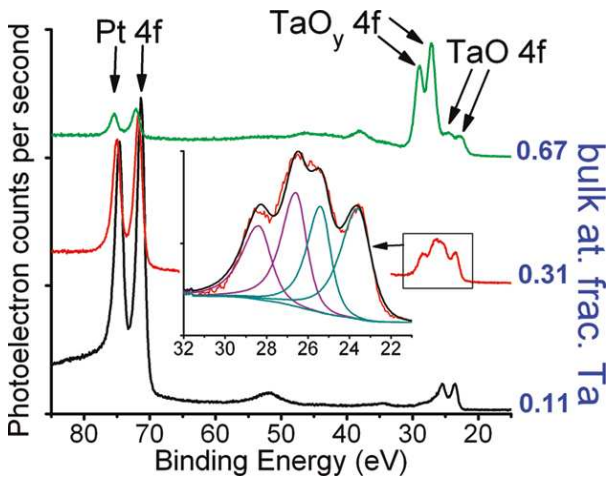

Figure 3.3.4.2: XPS spectra obtained for three $Pt_{1-x}Ta_x$ samples. Each spectrum is labeled on the right with the respective value of *x*. The inset shows the Ta 4f region of the x =0.31 spectrum with the modeled background and four fitted peaks.

Methanol Oxidation Activity by Fluorescence Assay.

Fluorescence assays were performed on the libraries both before and after electrochemical pretreatment. For Libraries A and B, the results are summarized in Figure 3.3.4.3, and we note that the fluorescence intensity contours of Figure 3.3.4.3b,d correspond closely to the composition contours of Figure 3.3.4.1a. The composition ranges associated with the ordered intermetallic phases (identified above) are plotted along with the composition dependence of the catalytic activity in Figure 3.3.4.3c,f. Dramatic correlations between the phase boundaries and the catalytic activity were apparent, and detailed analysis of the figures revealed that the structure-activity correlation was stronger than the composition-activity correlation. The materials with highest methanol oxidation activity were found in Library A and had the ortho-$Pt_{1-x}Ta_x$ structure with $0.24 < x < 0.32$. A region with $x \approx 0.3$ was chosen for further electrochemical testing as described in the following section. We focus further discussion of the fluorescence assay results on materials from Library A.

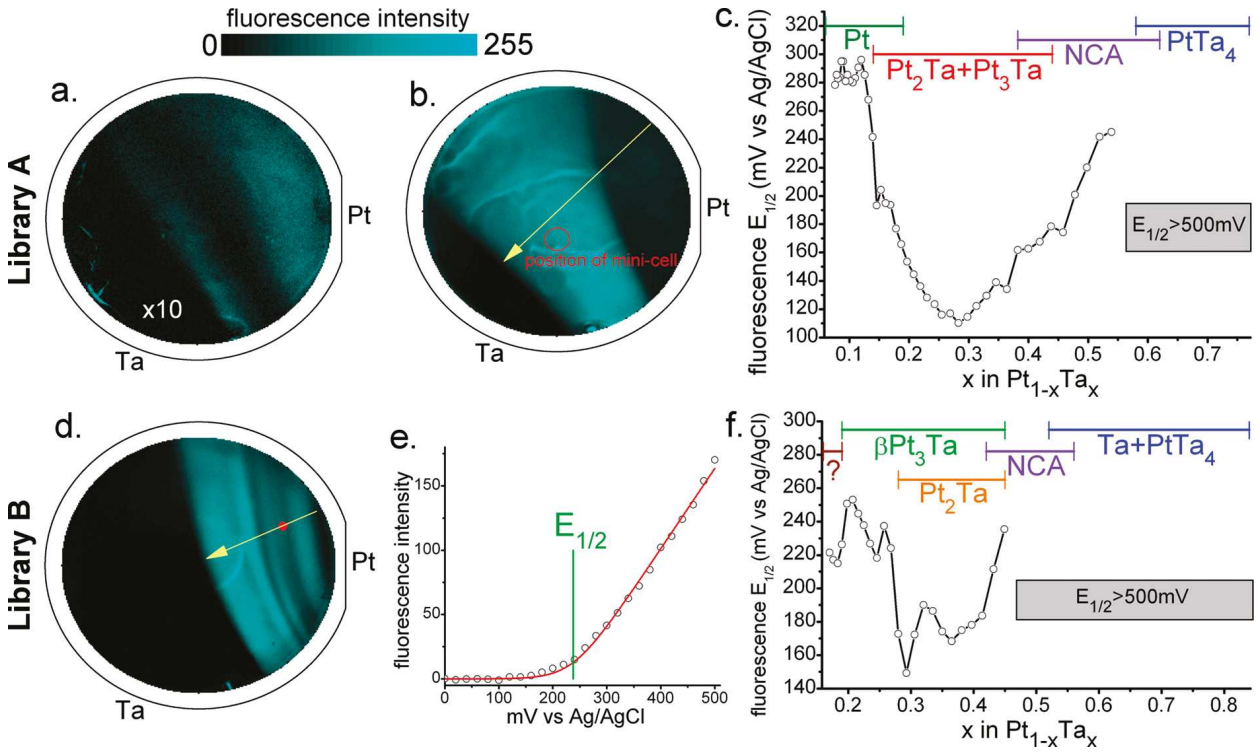

Figure 3.3.4.3: Fluorescence assay measurements of methanol oxidation activity are illustrated for Libraries A (top row) and B (bottom row). (a, b, d) images of the fluorescence intensity across the libraries in an outline of the Si wafer. All three images were acquired at 400 mV during a 5mV/s anodic sweep. Images b and d were acquired on pretreated libraries and show bright fluorescence from the active regions. Image a. was acquired with Library A after days of exposure to air and exhibits much lower fluorescence intensity (the intensity has been increased 10-fold for plotting). The sharp lines of brightest fluorescence (most evident in b) are due to thermally driven convection. (e) Fluorescence intensity profile obtained by averaging the intensity over a 0.5 mm diameter regions (position of white dot in image d), along with the fitted profile (red curve) and fitted value of $E_{1/2}$ (green line). Values of $E_{1/2}$ were also acquired at 1.2 mm spaced points along the yellow lines shown in b and d. (c, f) Plot of $E_{1/2}$ values, along with the composition range occupied by each identified ordered intermetallic phase.

Without the reducing pretreatment, the section of the library with only ortho-$Pt_{1-x}Ta_x$ was largely inactive for methanol oxidation. The fcc region as well as the ortho-$Pt_{1-x}Ta_x$ + NCA two-phase region had slightly lower $E_{1/2}$ compared to a typical Pt film. After the pretreatment, the fcc-Pt phase region exhibited a 60 mV decrease in $E_{1/2}$, the NCA region exhibited a 90 mV decrease in $E_{1/2}$, and the ortho-$Pt_{1-x}Ta_x$ region exhibited a decrease in $E_{1/2}$ of more than 300 mV, making it by far the most active catalyst in the library. After exposing the library to air for

several days, we repeated the fluorescence assay tests and found that the same activity profile was observed both before and after pretreatment. This experiment was also performed several times on Library B with similar results. We therefore infer that the remarkable improvement in the activity of the ortho-$Pt_{1-x}Ta_x$ catalyst was related to the reduction of the surface from its air-stable state and that the reduction and reoxidation were reversible and reproducible. Although the XPS characterization demonstrated that the top few nm of the $x = 0.31$ air-stable film contained approximately equal concentrations of two Ta suboxides, the electrochemical tests indicated that the most active surface was further reduced. The structure-activity correlation suggested that the reduction of the surface and/or the stabilization of the reduced surface was enabled by the presence of an underlying orthorhombic ordered intermetallic.

Further Electrochemical Study of Optimal Composition.

A $Pt_{0.7}Ta_{0.3}$ region of Library A (outlined in Figure 3.3.4.3b) was characterized by local electrochemical tests. In Figure 3.3.4.4, the CVs of a pure Pt sample and the $Pt_{0.7}Ta_{0.3}$ sample are shown for pH 1 solutions containing no fuel, methanol, and formic acid. Comparison of the CVs obtained for each film in the three solutions provided insights into the chemical state and morphology of the $Pt_{0.7}Ta_{0.3}$ surface. The CV of $Pt_{0.7}Ta_{0.3}$ in the 0.1 M H_2SO_4 solution contained the redox waves and hydrogen adsorption/desorption waves similar to those of a pure Pt electrode, in stark contrast to well-studied Pt alloys such as Pt-Ru. As expected, these features were also seen in the Pt film CV, and for both films the hydrogen adsorption and desorption waves were used to calculate electrochemical surface areas of 0.23 ± 0.06 and 1.15 ± 0.1 cm^2 for Pt and $Pt_{0.7}Ta_{0.3}$, respectively. Compared to the film area accessed by the cell (0.32 cm^2), these measurements implied specific surface area ratios (roughness factors) of 0.72 and 3.6. The

subunity value of the specific surface area of the Pt film was indicative of surface contamination which likely remained during the subsequent fuel oxidation studies. For the present discussion, we note that the microscopic $Pt_{0.7}Ta_{0.3}$:Pt area ratio determined by hydrogen adsorption was approximately 5:1. The surface area ratio between the same region in the Library A and the same Pt film was also measured via linear sweep voltammetry with a ferrocenemethanol redox couple as described above. This surface area ratio, 1.02 ± 0.16, corresponded to an approximately equivalent surface area accessible by the ferrocenemethanol molecule on the two electrodes. As described in the Supporting Information (*Section 3.3.7*), this roughness factor was an agreement with the 1.1 value determined by atomic force microscopy (AFM) characterization of the film surface. The ensemble of measurements advocated a model of the surface in which Pt and TaO_y contain less than approx. 1 nm scale features that were not observed by the ferrocenemethanol redox couple or AFM measurements but gave rise to an increased hydrogen adsorption Pt surface area. For calculating the oxidation current densities of small organic molecules, we assumed a unit specific surface area ratio.

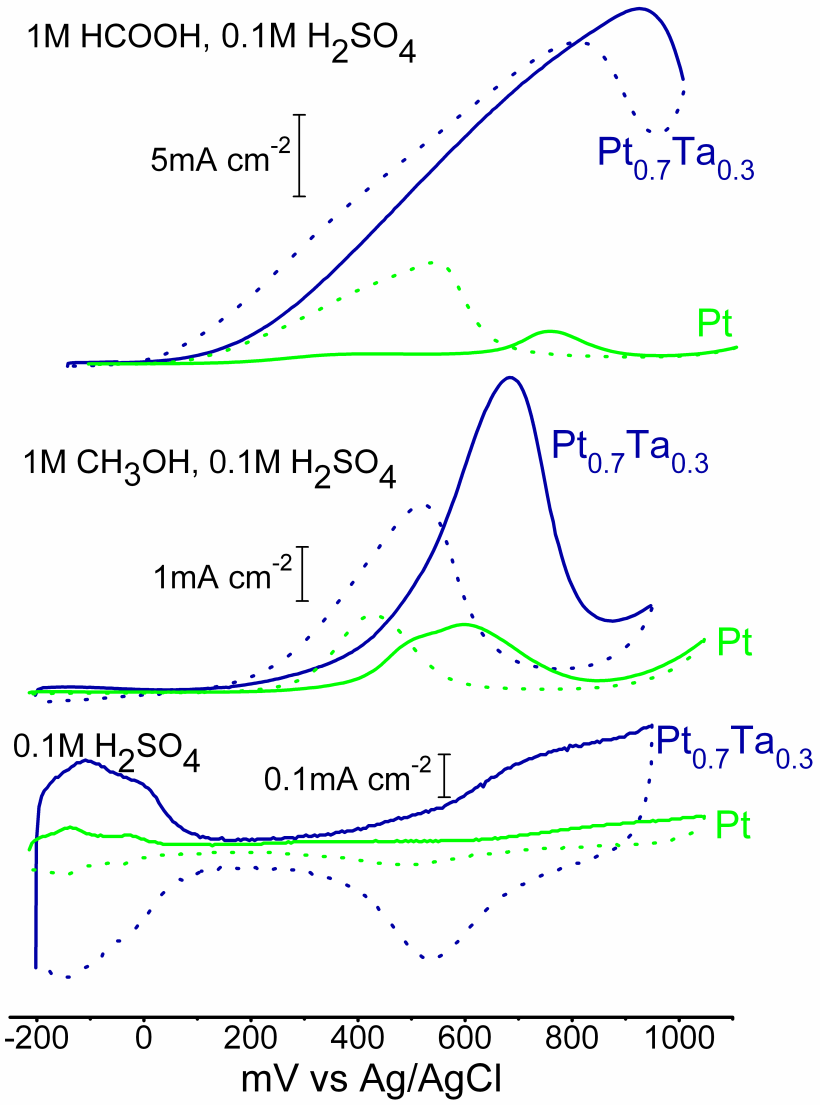

Figure 3.3.4.4: Cyclic voltammograms of Pt and $Pt_{0.7}Ta_{0.3}$ in (Top) 1 M formic acid, 0.1 M sulfuric acid; (Middle) 1 M methanol, 0.1 M sulfuric acid; and (Bottom) 0.1 M sulfuric acid. The forward scans are shown with solid lines and the reverse scans with dotted lines. The CV of $Pt_{0.7}Ta_{0.3}$ in 0.1 M sulfuric acid is indicative of polycrystalline Pt electrode. The ensemble of characterizations indicates that this electrode contains a high density of Pt islands surrounded by TaO_y.

On the anodic sweep, the methanol oxidation onset potential of the $Pt_{0.7}Ta_{0.3}$ catalyst was approx. 80 mV lower than Pt, a smaller improvement than anticipated from the fluorescence results. The strong effect of the pretreatment step in the fluorescence testing and its assumed influence on nature of the surface oxide raised the question of whether this discrepancy was due

to a difference in the pretreated surface oxide in pH 1 vs pH 4 testing solution. Although further investigation of the electrochemical properties of Pt-Ta surfaces may address this issue, the CVs of methanol and formic acid oxidation confirmed that the presence of the surface oxide resulted in higher oxidation current densities. In addition, application of the model of Manoharan and Goodenough[38] to the CVs in methanol and formic acid indicated that a higher fraction of the fuel was being completely oxidized. That is, in contrast to those of Pt, the CVs on $Pt_{1-x}Ta_x$ demonstrated a greater forward oxidation peak height than reverse peak height. This difference was indicative of a diminished accumulation of carbonaceous species on the surface from incomplete fuel oxidation.

The model of sub-nanometer surface structure proposed to explain the surface area measurements and the strong correlation between fluorescence onset potential and the presence of ortho-$Pt_{1-x}Ta_x$ presented the possibility that the partially oxidized surface maintained a structure dictated by the underlying lattice. Future catalyst characterization by surface-sensitive (grazing incidence) XRD and scanning tunneling microscopy characterization will provide insight into this matter, and surface conductivity mapping via the latter technique may provide a better understanding of the Ta suboxide. However, we note that the desired surface condition was one that may be difficult to reproduce outside of the electrochemical environment.

3.3.5 Conclusions

Catalytic activity in the Pt-Ta system was investigated through extensive structural and electrochemical characterization. Thin film libraries containing Pt-Ta ordered intermetallics, a nanocrystalline phase, and an fcc-Pt alloy were tested as methanol oxidation catalysts with a parallel screening method. A reductive pretreatment step, similar to that of typical fuel cell start-

up procedures, significantly improved the activity of the catalysts for methanol oxidation. The correlation of activity with the inferred phase fields suggested that the formation of a bulk orthorhombic structure facilitated the partial reduction of the surface TaO_y. The substantial improvement in catalytic activity was attributed to interactions between surface Pt and Ta suboxides, motivating the study of such composite surfaces in the search for superior fuel oxidation catalysts.

The most active catalyst surface appeared to be a Ta suboxide and Pt composite with less than 1 nm structure, and the interaction between these species resulted in less Pt contamination by carbonaceous species during the oxidation of methanol and formic acid.

3.3.6 Acknowledgment

This work was performed under the Cornell Fuel Cell Institute funded by the Department of Energy (ER06-02-13022-11751-11792). This work made use of the XPS and AFM facilities of the Cornell Center for Materials Research with support from National Science Foundation (NSF) award DMR-0520404. The diffraction experiments were conducted at the Cornell High Energy Synchrotron Source (CHESS), which is supported by NSF award DMR-0225180. The authors thank Jon Shu and Steven Kriske for assistance with the XPS and AFM experiments and Darren Dale and Alexander Kazimirov for assistance with the diffraction experiments.

3.3.7 Supporting Information

Composition measurements.

In addition to the thin film composition map calculated from deposition profiles, Library A was also characterized by x-ray fluorescence (XRF) and energy-dispersive x-ray spectroscopy (EDS).

Both techniques involved analysis of the Pt-L and Ta-L characteristic x-rays. The excitation sources were 60 keV incoherent synchrotron x-ray radiation for the XRF measurements[39] and a 20keV electron beam for the EDS measurements. The interpolated composition maps are shown in Fig. 3.3.7.1. The approximate uncertainties in the determination of x in $Pt_{1-x}Ta_x$ are 5 at.% and 8 at.% for the XRF and EDS measurements, respectively. The three composition maps were in good agreement with only 5 at.% discrepancy in the region of interest. In the most Ta-rich region, the XRF and EDS measurements indicated that the Ta concentration was ~10 at.% higher than indicated by the deposition profiles. This discrepancy was not investigated further as this region did not exhibit good catalytic activity.

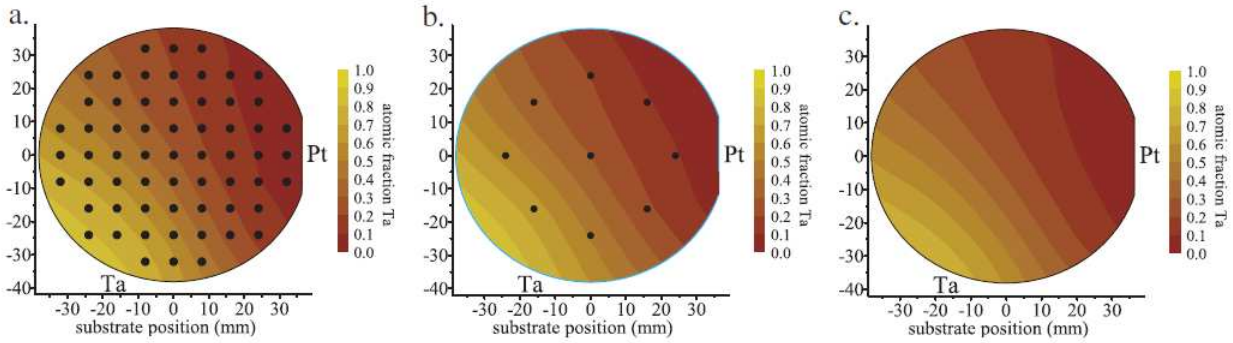

Figure 3.3.7.1: The composition map of Library A is plotted in the outline of the Si substrate using (a) XRF measurements, (b) EDS measurements and (c) deposition profile calculations. For (a) and (b), the substrate positions of the measurements are noted by black points and the orientation of the Pt and Ta deposition sources is noted by the elemental symbols.

Fiber texture.

Due to unique growth rates for each crystal facet, metallic thin films commonly acquired fiber texture during deposition. The resulting film consisted of crystallites which were randomly oriented with respect to substrate azimuth but aligned with respect to substrate normal. Thus, a given reciprocal lattice vector occupied distinct values of Φ, the angular displacement from substrate normal. The $50^o < \Phi < 140^o$ range was intercepted by the image plate (figure 3.3.7.2a

fiber texture), and upon phase identification, the Φ-distribution of indexed peaks can be used to extract the average crystallite orientation in the film (figure 3.3.7.2b fiber texture). For the orth-$Pt_{1-x}Ta_x$ phases of Library A, this peak width was ~10^o, and analysis of the strongest reflections and their Φ-distributions indicated that one or more of the following crystallographic planes were oriented parallel to the film surface: Pt_3Ta (100), Pt_2Ta (010), Pt_2Ta (001).

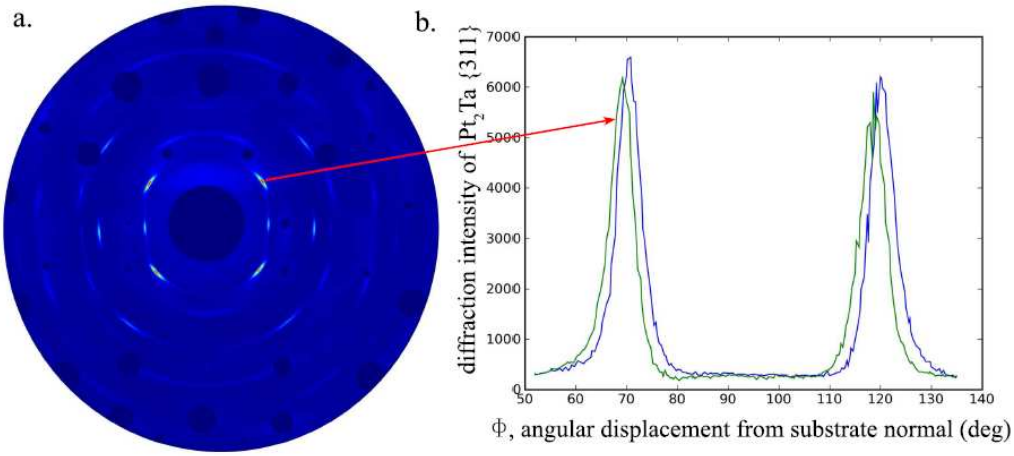

Figure 3.3.7.2: (a) A diffraction image from a substrate position near the extensively characterized $Pt_{0.7}Ta_{0.3}$ catalyst from Library A. (b) The azimuthal distribution of the diffraction intensity at a scattering vector of 30.5 nm^{-1}. The peak in the diffraction pattern was indexed as orthorhombic Pt_2Ta {311}, and the Φ-distribution of this and other indexed reflections were used to determine the fiber texture of the thin film.

AFM, surface area and surface morphology.

To investigate the surface morphology of the $Pt_{0.7}Ta_{0.3}$ catalyst discussed in the manuscript, we imaged the film surface using tapping mode atomic force microscopy (AFM) (Veeco Dimension 3100). Figure 3.3.7.3 contains the height profile over a 3 mm square region of the film attained at a scan rate of 1.05 Hz with 384 samples per line, 384 lines using a tip with <10 nm radius of curvature (NanoWorld). The image indicated an average surface roughness of Ra = 3.66 nm and an absolute surface area of 9.94 mm^2, corresponding to a surface area ratio (roughness factor) of 1.1. This roughness factor was in agreement with that determined from linear sweep

voltammetry with a ferrocenemethanol redox couple. The film surface in this region was metallic and was slightly darker than the most reflective thin films, as shown in figure 3.3.7.4. We assert that this appearance was due to the ~100nm surface features evident in figure 3.3.7.3 and note that the appearance was not altered by the electrochemical testing. We believe the surface morphology evident in figure 3.3.7.3 existed in the as-deposited film and was not influenced by the electrochemical testing. The low roughness of the $Pt_{0.7}Ta_{0.3}$ surface and the invariance of the film composition upon electrochemical testing also demonstrated the stability of the film surface and indicated that no significant amount of Ta leached from the film under voltage cycling at pH=1 or pH=4 (Dealloyed thin films were typically much more rough[33]). The nominal 10% difference in surface area between Pt and $Pt_{0.7}Ta_{0.3}$ was insignificant compared to the substantial improvements in fuel oxidation activity observed for $Pt_{0.7}Ta_{0.3}$. As noted in the manuscript figure 3.3.7.4, the film surface did contain a large surface area of Pt which must be due to surface structure on the 1 nm or sub-nm scale, a regime not accessed by AFM or the ferrocenemethanol redox couple.

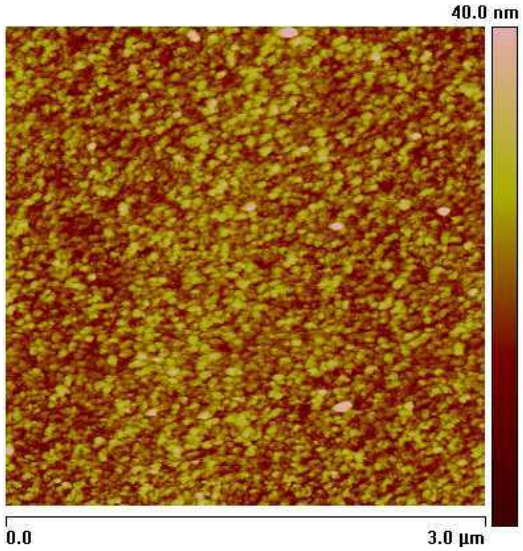

Figure 3.3.7.3: AFM image of the most active catalyst in Library A ($Pt_{0.7}Ta_{0.3}$) after electrochemical testing.

Figure 3.3.7.4: A digital photograph of Library A. The photograph was taken before electrochemical testing, but the appearance was unchanged by the electrochemical tests. The substrate position of the extensively characterized $Pt_{0.7}Ta_{0.3}$ is the dark region.

3.4 References

1. Prochaska, M.; Jin, J.; Rochefort, D.; Zhuang, L.; DiSalvo, F. J.; Abruña, H. D.; Dover, R. B. v., High throughput screening of electrocatalysts for fuel cell applications. *Review of Scientific Instruments* **2006,** 77, (5).

2. Jin, J.; Prochaska, M.; Rochefort, D.; Kim, D. K.; Zhuang, L.; DiSalvo, F. J.; Dover, R. B. v.; Abruña, H. D., A high-throughput search for direct methanol fuel cell anode electrocatalysts of type $Pt_xBi_yPb_z$. *Applied Surface Science* **2007,** 254, 653-661.

3. Li, G. C.; Pickup, P. G., Decoration of carbon-supported Pt catalysts with Sn to promote electro-oxidation of ethanol. *Journal of Power Sources* **2007,** 173, (1), 121-129.

4. Tanaka, S.; Umeda, M.; Ojima, H.; Usui, Y.; Kimura, O.; Uchida, I., Preparation and evaluation of a multi-component catalyst by using a co-sputtering system for anodic oxidation of ethanol. *Journal of Power Sources* **2005,** 152, (1), 34-39.

5. Jiang, L. H.; Sun, G. Q.; Sun, S. G.; Liu, J. G.; Tang, S. H.; Li, H. Q.; Zhou, B.; Xin, Q., Structure and chemical composition of supported Pt-Sn electrocatalysts for ethanol oxidation. *Electrochimica Acta* **2005,** 50, (27), 5384-5389.

6. Delime, F.; Leger, J. M.; Lamy, C., Enhancement of the electrooxidation of ethanol on a Pt-PEM electrode modified by tin. Part I: Half cell study. *Journal of Applied Electrochemistry* **1999,** 29, (11), 1249-1254.

7. Wang, Q.; Sun, G. Q.; Jiang, L. H.; Xin, Q.; Sun, S. G.; Jiang, Y. X.; Chen, S. P.; Jusys, Z.; Behm, R. J., Adsorption and oxidation of ethanol on colloid-based Pt/C, PtRu/C and Pt3Sn/C catalysts: In situ FTIR spectroscopy and on-line DEMS studies. *Physical Chemistry Chemical Physics* **2007,** 9, (21), 2686-2696.

8. Pourbaix, M., *Atlas of Electrochemical Equilibria in Aqueous Solutions*. National Association of Corrosion Engineers: Houston, TX, 1974.

9. Ribadeneira, E.; Hoyos, B. A., Evaluation of Pt-Ru-Ni and Pt-Sn-Ni catalysts as anodes in direct ethanol fuel cells. *Journal of Power Sources* **2008,** 180, (1), 238-242.

10. Antolini, E.; Salgado, J. R. C.; dos Santos, A. M.; Gonzalez, E. R., Carbon-supported Pt-Ni alloys prepared by the borohydride method as electrocatalysts for DMFCs. *Electrochemical and Solid State Letters* **2005,** 8, (4), A226-A230.

11. Zeis, R.; Mathur, A.; Fritz, G.; Lee, J.; Erlebacher, J., Platinum-plated nanoporous gold: An efficient, low Pt loading electrocatalyst for PEM fuel cells. *Journal of Power Sources* **2007,** 165, (1), 65-72.

12. Erlebacher, J., An atomistic description of dealloying - Porosity evolution, the critical potential, and rate-limiting behavior. *Journal of the Electrochemical Society* **2004,** 151, (10), C614-C626.

13. Erlebacher, J.; Aziz, M. J.; Karma, A.; Dimitrov, N.; Sieradzki, K., Evolution of nanoporosity in dealloying. *Nature* **2001,** 410, (6827), 450-453.

14. Pickering, H. W., Characteristic Features of Alloy Polarization Curves. *Corrosion Science* **1983,** 23, (10), 1107.

15. Leger, J. M., Mechanistic aspects of methanol oxidation on platinum-based electrocatalysts. *Journal of Applied Electrochemistry* **2001,** 31, (7), 767-771.

16. Frelink, T.; Visscher, W.; Vanveen, J. A. R., On the Role of Ru and Sn as Promoters for Methanol Electrooxidation Over Pt. *Surface Science* **1995,** 335, (1-3), 353-360.

17. Casado-Rivera, E.; Volpe, D. J.; Alden, L.; Lind, C.; Downie, C.; Vazquez-Alvarez, T.; Angelo, A. C. D.; DiSalvo, F. J.; Abruña, H. D., Electrocatalytic activity of ordered intermetallic phases for fuel cell applications. *Journal of the American Chemical Society* **2004,** 126, (12), 4043-4049.

18. Lee, H. J.; Habas, S. E.; Somorjai, G. A.; Yang, P. D., Localized Pd overgrowth on cubic Pt nanocrystals for enhanced electrocatalytic oxidation of formic acid. *Journal of the American Chemical Society* **2008,** 130, (16), 5406.

19. Spendelow, J. S.; Lu, G. Q.; Kenis, P. J. A.; Wieckowski, A., Electrooxidation of adsorbed CO on Pt(111) and Pt(111)/Ru in alkaline media and comparison with results from acidic media. *Journal of Electroanalytical Chemistry* **2004,** 568, (1-2), 215-224.

20. Ishihara, A.; Doi, S.; Mitsushima, S.; Ota, K., Tantalum (oxy)nitrides prepared using reactive sputtering for new nonplatinum cathodes of polymer electrolyte fuel cell. *Electrochimica Acta* **2008,** 53, (16), 5442-5450.

21. Bonakdarpour, A.; Lobel, R.; Sheng, S.; Monchesky, T. L.; Dahn, J. R., Acid stability and oxygen reduction activity of magnetron-sputtered Pt1-xTax (0 <= x <= 1) films. *Journal of the Electrochemical Society* **2006,** 153, (12), A2304-A2313.

22. Yamada, Y.; Ueda, A.; Shioyama, H.; Kobayashi, T., High-throughput screening of PEMFC anode catalysts by IR thermography. *Applied Surface Science* **2004,** 223, (1-3), 220-223.

23. Ueda, A.; Yamada, Y.; Ioroi, T.; Fujiwara, N.; Yasuda, K.; Miyazaki, Y.; Kobayashi, T., Electrochemical oxidation of CO in sulfuric acid solution over Pt and PtRu catalysts modified with TaOx and NbOx. *Catalysis Today* **2003,** 84, (3-4), 223-229.

24. Watanabe, M.; Motoo, S., Electrocatalysis by Ad-atoms. 3. Enhancement of Oxidation of Carbon-Monoxide on Platinum by Ruthenium Ad-atoms. *Journal of Electroanalytical Chemistry* **1975,** 60, (3), 275-283.

25. Stevens, D. A.; Rouleau, J. M.; Mar, R. E.; Bonakdarpour, A.; Atanasoski, R. T.; Schmoeckel, A. K.; Debe, M. K.; Dahn, J. R., Characterization and PEMFC Testing of $Pt_{1-x}M_x$ (M= Ru, Mo, Co, Ta, Au, Sn) Anode Electrocatalyst Composition Spreads. *Journal of the Electrochemical Society* **2007,** 154, (6), B566-B576.

26. de-los-Santos-Alvarez, N.; Alden, L. R.; Rus, E.; Wang, H.; DiSalvo, F. J.; Abruña, H. D., CO tolerance of ordered intermetallic phases. *Journal of Electroanalytical Chemistry* **2009,** 626, (1-2), 14-22.

27. Gregoire, J. M.; van Dover, R. B.; Jin, J.; Disalvo, F. J.; Abruña, H. D., Getter sputtering system for high-throughput fabrication of composition spreads. *Review of Scientific Instruments* **2007,** 78, (7), 072212.

28. Gregoire, J. M.; van Dover, R. B., A model for calculating resputter rates in codeposition. *Journal of Vacuum Science & Technology A* **2008,** 26, (4), 1030-1036.

29. Gregoire, J. M.; Lobovsky, M. B.; Heinz, M. F.; DiSalvo, F. J., Resputtering phenomena and determination of composition in codeposited films. *Physical Review B* **2007,** 76, (19).

30. Powder Diffraction File. In JCPDS International Centre for Diffraction Data: Newton Square, PA: 2004.

31. Ohring, M., *Materials Science of Thin Films* 2nd ed.; Academic Press: Boston, 2002.

32. Reddington, E.; Sapienza, A.; Gurau, B.; Viswanathan, R.; Sarangapani, S.; Smotkin, E. S.; Mallouk, T. E., Combinatorial electrochemistry: A highly parallel, optical screening method for discovery of better electrocatalysts. *Science* **1998,** 280, (5370), 1735-1737.

33. Gregoire, J. M.; Kostylev, M.; Tague, M. E.; Mutolo, P. F.; van Dover, R. B.; DiSalvo, F. J.; Abruña, H. D., High-Throughput Evaluation of Dealloyed Pt-Zn Composition-Spread Thin Film for Methanol-Oxidation Catalysis. *Journal of the Electrochemical Society* **2009,** 156, (1), B160-B166.

34. Gregoire, J. M. High throughput material science for discovery of energy-related materials. Dissertation, Cornell University, Ithaca, NY, 2010.

35. Giessen, B. C.; Kane, R. H.; Grant, N. J., On Constitution Diagram Ta-Pt between 50-100 at. Pct Pt. *Transactions of the Metallurgical Society of Aime* **1965,** 233, (5), 855-&.

36. Spaepen, F.; Turnbull, D., Metallic Glasses. *Annual Review of Physical Chemistry* **1984,** 35, 241-263.

37. Kerrec, O.; Devilliers, D.; Groult, H.; Marcus, P., Study of dry and electrogenerated Ta2O5 and Ta/Ta2O5/Pt structures by XPS. *Materials Science and Engineering B-Solid State Materials for Advanced Technology* **1998,** 55, (1-2), 134-142.

38. Manoharan, R.; Goodenough, J. B., Methanol Oxidation in Acid on Ordered NiTi. *Journal of Materials Chemistry* **1992,** 2, (8), 875-887.

39. Gregoire, J. M.; Dale, D.; Kazimirov, A.; DiSalvo, F. J.; van Dover, R. B., High energy x-ray diffraction/x-ray fluorescence spectroscopy for high-throughput analysis of composition spread thin films. *Review of Scientific Instruments* **2009,** 80, (12), 123905.

CHAPTER 4

Pt-M Alloys – Low Concentration of M

This section constitutes a manuscript titled:

"High throughput thin film Pt-M alloys for fuel electrooxidation – Low concentrations of M (M = Sn, Ta, W, Mo, Ru, Fe, In, Pd, Hf, Zn, Zr, Nb, Sc, Ni, Ti, V, Cr, Rh)"

Authors: Michele E. Tague, John M. Gregoire, Anna Legard, Eva Smith, Darren Dale, Richard Hennig, Francis J. DiSalvo, R. Bruce van Dover, Héctor D. Abruña

4.1 Abstract

Eighteen Pt-M (M= Sn, Ta, W, Mo, Ru, Fe, In, Pd, Hf, Zn, Zr, Nb, Sc, Ni, Ti, V, Cr, Rh) thin film composition spreads were deposited at low concentrations using magnetron sputtering and screened for methanol and ethanol electrooxidation activity using a fluorescence assay. Characterization of these thin films was performed using high energy x-ray diffraction and x-ray fluorescence. The electrochemical fluorescence assay revealed highest activity in the films with M = Sn, Zn, In, Fe, and Ru. Pt-M (M=Sn, Zn, In) showed highest activity at M concentrations below 5 atom-% with a high fraction of Pt fcc(111) texturing and Pt-Fe showing the best activity at 10 atom-% Fe. On the other hand, the best (most negative) fluorescence onset potential in the Pt-Ru system was observed at a concentration of 35 atom-% Ru with minimal texturing of the film. To assess reasons for activity, preliminary calculations on the *d*-band center shift with alloying were performed for bulk concentrations of up to 30 atom-% for Fe and 16 atom-% for M = Sn, Zn.

4.2 Introduction

Fuel cells present a promising energy conversion technology that is not limited by the Carnot cycle efficiency. Fuel cell efficiencies can reach up to 80-90% whereas a Carnot engine can only reach a maximum efficiency of 45-50%.[1] Fuel cells provide higher efficiency, an environmentally friendly form of energy conversion and high power/energy density. The ideal system is a hydrogen-oxygen proton exchange membrane fuel cell (PEMFC); however, transportation, storage, and widespread availability of hydrogen is precluded due to the required high pressures and low volumetric energy density when compared to other fuels. Methanol and ethanol (and other small organic molecules) have the advantage of higher volumetric energy densities, easier transportation, and diversity of availability from biosources.

Current limitations for widespread deployment of fuel cells are the cathode and anode materials which are expensive, easily poisoned, and show degradation over time. For methanol and ethanol oxidation, the process is more complicated than in the hydrogen case, because there is a carbon source (fuels, e.g. methanol) that must be oxidized to CO_2 for maximal efficiency. The catalyst also must show an improvement in catalytic activity for fuel oxidation with minimal poisoning. Platinum is the most commonly used catalyst, but it readily poisons with any CO present in the solution. As CO stands as a general and ubiquitous intermediate in the oxidation of our fuels, a different catalyst must be used/found. Many materials have been investigated as anode catalysis for methanol, ethanol, and ethylene glycol, including alloys[2], intermetallics[3], non-Pt containing materials (carbides, nitrides, oxides)[4], and core-shell structures[5, 6]. For the cathode case, Strasser, et al. reported improved activity for oxygen reduction with a Pt shell and a Pt-Cu alloyed core when compared to Pt alone.[5] The paper also considered the improved activity to be a result of the increased lattice strain of the Pt shell. Feliu, et al. showed that the

alloyed low concentration of a second element in Pt showed improved activity for formic acid oxidation better than higher concentrations especially in the Pt-Bi system.[7] The presence of the alloying element is believed to improve the fuel oxidation activity by inhibiting poisoning of the surface.

To effectively search for catalysts with improved activity for methanol and ethanol oxidation, a combinatorial screening process has been developed by our lab based on a fluorescence based probe.[8,9] Our fluorescence assay utilizes a property of fuel oxidation such that upon fuel oxidation, protons are generated causing a decrease in local pH. The fluorescent probe, quinine, fluoresces at pH's below pH 5 and once enough protons are generated by the oxidation process, then improved catalysts can be identified. The high throughput is established with a custom built sputtering chamber, where thin films are sputtered in a gradient film and subsequently tested in the fluorescence assay. Our high throughput methodology is consistent with other groups, who have implemented high throughput combinatorial screening for hydrogen electrooxidation,[10] CO oxidation[10], and oxygen reduction[11-15].

An important aspect of the high throughput methodology is the ability to characterize the thin films so as to enable correlations among activity, composition and crystallographic phase. Simultaneous measurements of x-ray diffraction and composition with x-ray fluorescence were performed at Cornell's High Energy Synchrotron Source (CHESS). This configuration has been reported in a previous publication[16] and takes advantage of the high energy beam transmitted through the thin film on a Si wafer. The diffraction patterns were collected on a MAR imaging plate behind the sample. Custom software has been developed to calculate powder patterns and texturing data from the diffraction images. In this paper, the use of the CHESS setup allowed for the mapping of fiber texture, composition, and phase over binary libraries. These techniques can

also provide rapid characterization of more complicated systems, ie. ternary and quaternary systems.

When exploring these non-noble metals, leaching of the metals from the film must be considered. A previous study by Bonakdarpour et al. demonstrated the leaching of Co, Ni, Mn, and Fe from thin films and upon leaching, the remaining concentration of the non-noble metal reached a threshold of 25%.[17] Our group found surface area enhancement from alloying Zn with Pt in thin films, which resulted in higher methanol oxidation performance.[18] In this investigation, the second element's alloying concentration was limited to levels below approx. 55%, although we would still expect some leaching for concentrations exceeding 25% for some elements. Dahn, et al.[10] studied a series of binary Pt anode electrocatalysts, including Ru, Mo, Co, Ta, Au, and Sn. They reported that the Mo and Co leached from the combinatorial library after electrochemical testing. In our screening process, as a means for identifying compositions that exhibit leaching, a background scan without fuel was performed. Since leaching can sometimes involve the oxidation of the non-noble metal, an unstable film can exhibit fluorescence and confound the screening process. Hence, the background scan enabled us to identify films that could give false positives from leaching.

It is widely known that Pt-Sn is a good catalyst for CO oxidation[19] and since CO is a known intermediate for methanol oxidation, it is important to explore the optimal concentrations of Sn in Pt that can result in the highest activity. Pt-Sn is also good for ethanol oxidation at low potentials as reported by Gonzalez, et al.[20] and furthermore, the oxidized tin in the Pt lattice shows additional improvement towards ethanol oxidation.[21, 22] When considering other cases for Pt-Sn studies, the optimal amount of Sn seemed to be 25% with the presence of the tin oxides contributing mostly to the activity.[22, 23]

Based on the phase diagrams,[24] low Sn concentrations were investigated to find possible relationships between electrocatalytic activity, fiber texture and composition within the fcc-Pt crystal structure. Furthermore, we hoped to identify periodic trends. Within this study, Pt-M alloys with each transition and main group elements with known solubility above 1 at.% were investigated, with the exception of M = Os, Cd, Ir. Os and Cd were not studied due to toxicity concerns, although Pt-Cd alloys were found to be active methanol oxidation catalysts in a separate study[25].

4.3 Experimental Detail

Thin films of platinum with low concentrations of an alloying transition or main group metal, M (M = Sn, Ta, W, Mo, Ru, Fe, In, Pd, Hf, Zn, Zr, Nb, Sc, Ni, Ti, V, Cr, Rh), were prepared using a custom built combinatorial sputter deposition system with a getter described previously[26]. The two elements (>99.9% purity) were deposited onto a 3-inch diameter Si wafer with a 10-nm Ti adhesion underlayer, which also served as a Si diffusion barrier. The magnetron sputter sources (Angstrom Sciences) were angled to create a deposition gradient for each element. For a binary deposition, this configuration resulted in a film with a composition that varied smoothly as a function of relative distance from the deposition sources. At a given substrate position, there was a direction of maximal composition gradient, and the maximum film thickness gradient was in a near-orthogonal direction. For compositions which were represented over a broad range of substrate positions, the film thickness at fixed composition may vary by up to a factor of 3 within the library.

For the Pt-M binary films discussed in this manuscript, the Pt target was typically operated at 125 mA 353 V and the M target was operated at a power that provided the

composition range of interest. Substrates were maintained at 100 ^{o}C during the deposition process. Following sputtering, the samples were cooled to below 40 ^{o}C and removed from the chamber into ambient air.

Phase and composition characterization was performed using high energy (60 keV) transmission X-ray diffraction (XRD) and simultaneous X-ray fluorescence (XRF) at Cornell's High Energy Synchrotron Source (CHESS). The XRD patterns were collected using a MAR detector. Further explanation is given in a previous publication[16]. Additional composition information was collected for Pt-Zn, Pt-Sn, and Pt-In using Energy Dispersive X-ray Spectroscopy (EDS) on a JEOL 8900 Microprobe.

A fluorescence assay was employed to assess the catalytic properties of the platinum alloys as described in a previous report[8]. A Teflon electrochemical cell was sealed with an o-ring atop the 3-inch diameter composition spread. Copper contacts were mechanically pressed against the Si wafer beyond the outer diameter of the o-ring to avoid contact with the testing solutions. A gold coiled counter electrode was elevated approximately 1 cm above the sample and the entire cell was sealed with a quartz plate on the top with a hole to hold the Ag/AgCl reference electrode (BAS). Tubing to and from the cell allowed for de-aerated solutions to be pumped in and out of the N_2-atmosphere cell without exposure to air. Automated controls for gas flow, solution pumping, and potentiostat were accessible through a custom Labview program. The potentiostat used was a Pine Instruments Model AFRDE5 Bi-potentiostat.

A standard testing procedure required filling of the electrochemical cell with a neutral pH aqueous solution of 0.3 mM quinine, 0.1 M potassium triflate, and 5 M fuel (methanol or ethanol). The potential was scanned from the open circuit potential at 5 mV/s to 200 mV vs. Ag/AgCl. Upon oxidation of the fuel, the generated protons decreased the local pH below pH 5

on the working electrode (the combinatorial library), causing the quinine to fluoresce under UV light. Images were collected at 20 mV intervals with a CCD camera and a fluorescence onset potential can be determined at the potential where the fluorescence was first observed. An oxidative current was also measured over the entire wafer. To ensure the oxidative current was not from any oxidation processes occurring at the surface of the composition film, a background solution (without fuel) was added to the cell and the potential was scanned over the same potential range. If fluorescence was seen with no fuel, this was attributed to the oxide formation and/or leaching of metals on the surface and was considered unstable. Thus, those regions were not included in this study for these reasons. Furthermore, we pretreated the sample with a linear sweep to reducing potentials (-0.80 V vs. Ag/AgCl) in a 0.01 M H_2SO_4, 1 M Na_2SO_4 aqueous solution. This step served to remove any oxides or other contaminates that could be on the surface either from samples being stored in air or from prior fuel oxidation testing.

For comparison between samples, a curve was fitted to the fluorescence intensity vs. potential plot and a $E_{1/2}$ value was calculated[18]. To briefly summarize the theory behind the $E_{1/2}$ fluorescence value, the value does not relate to the theoretical $E_{1/2}$ normally noted in electrochemistry. Instead, it is an approximation for the fluorescence onset potential of the fuel oxidation using a Butler-Volmer-like equation based on the exponential growth of the fluorescence intensity.

Electronic structure calculations of $Pt_{1-x}M_x$ (M=Sn, Fe, Zn) were performed assuming a fcc non-ordered intermetallic structure. Supercells consisting of eight cubic fcc unit cells were generated with random occupancy of Pt and M on the 32 sites as dictated by stoichiometry. Between five and seven supercells per stoichiometry were constructed.

Modeling was done with VASP,[27, 28] a density functional code using a plane-wave basis and the projector-augmented wave method.[29, 30] The generalized gradient approximation (GGA) of Perdew, Burke, and Ernzerhof[31] was used with a Xe core for Pt, a Kr plus 4d state core for Sn, and an Ar core for Fe and Zn. A plane-wave kinetic energy cutoff of 500 eV ensured energy convergence to 10 meV/atom, and the *k*-point meshes for the different structures were chosen to guarantee an energy accuracy of 0.1 meV/atom. Cell volume, cell shape, and ionic positions were relaxed until the total energy changed by less than 0.1 meV between relaxation steps. Among the supercells at a given composition, the conformation with the lowest energy after relaxation was selected and the average of the *d*-band centers for all Pt atoms within the supercell was presented.

4.4 Results and Discussion

4.4.1 X-Ray Diffraction

Figure 4.4.1.1 demonstrates the deposition profiles across the 19 substrates we studied from the Pt rich area (point 0) to the M rich area (point 9). The deposition profile of W at low power differed from the other elements and this profile was both confirmed by crystal monitor and XRF. The underlying cause is unknown at this time. Ti is considered one of the lighter elements and as a result the accuracy for the XRF deposition profile is lower. The atomic fraction of a given element grew exponentially with proximity to its sputtering gun.

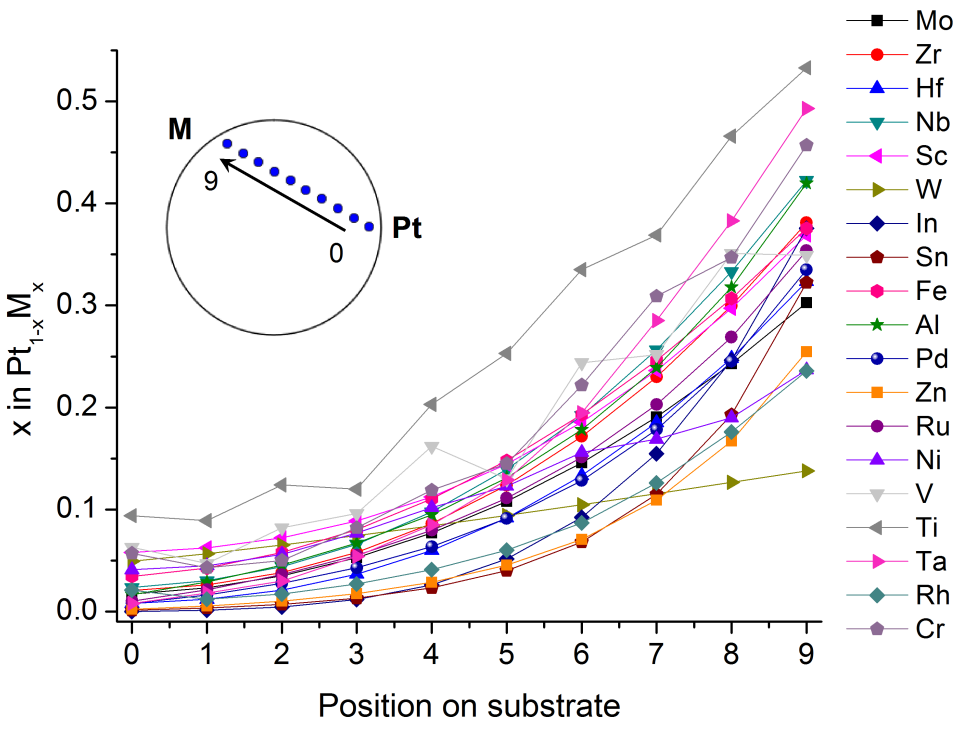

Figure 4.4.1.1: Deposition profiles across the composition gradients for each substrate measured by X-ray fluorescence. For Ti and V, XRF emission was attenuated by air in experiment because they have low Z, leading to a low signal and thus greater uncertainty.

All of the binary alloys exhibited shifting in the Pt fcc lattice constant as the concentration of the second element increased, except for Pd and Ni which was to be expected because of the very similar sizes. Figure 4.4.1.2 presents a typical example with Pt-Mo, such that with the incorporation of Mo, the shift was to a lower scattering vector. The fcc lattice constant increased with the addition of Sn, Hf, Nb, Sc, W, In, Zr, Ta, and Mo. On the other hand, alloying Fe, V, Al, Zn, Rh, Cr and Ru into Pt resulted in a shift to higher scattering vectors, which indicated a contraction of the Pt lattice, consistent with the literature and atomic sizes.[10]

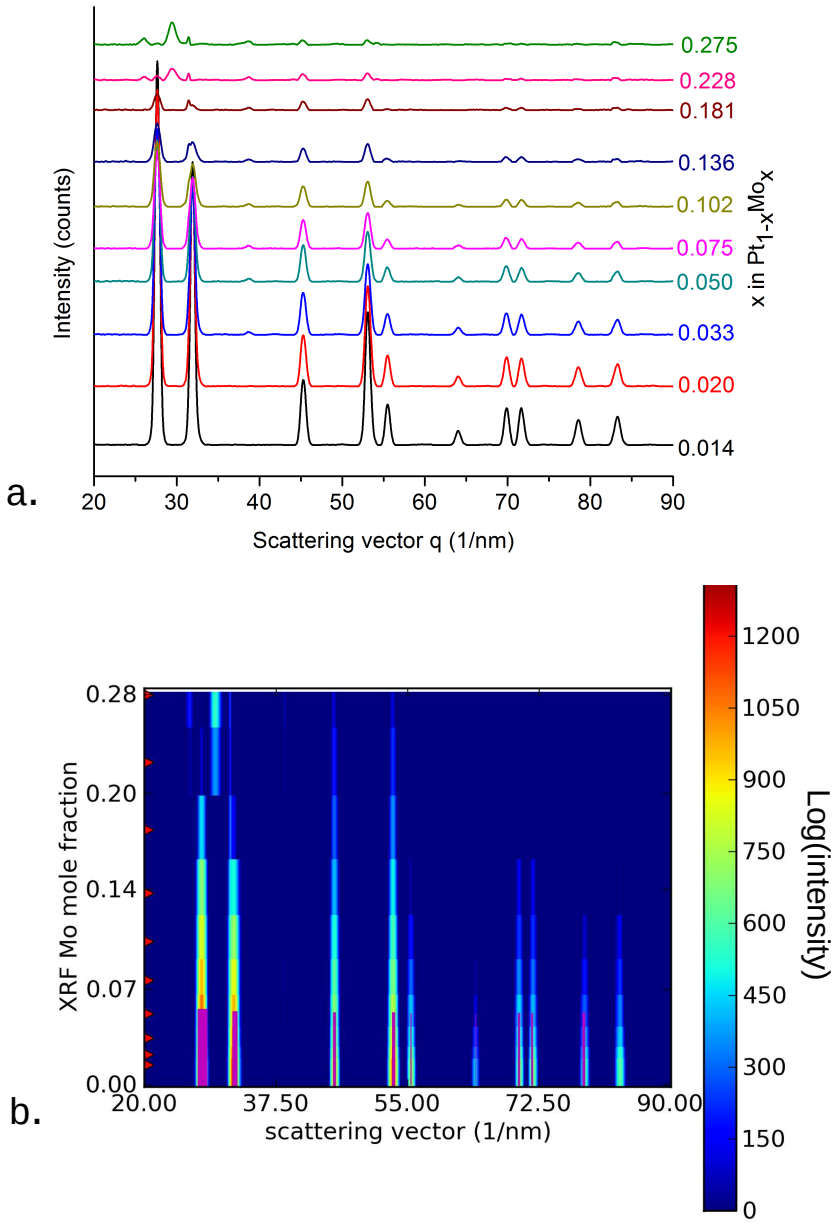

Figure 4.4.1.2: a. Representative sample of the diffraction profiles from 10 positions on a Pt-Mo composition spread. The marked compositions for the Mo concentrations were determined through XRF. b. A composition vs. scattering vector with the intensities of the Pt-Mo combinatorial spread presented on a logarithmic color scale. The XRF-determined compositions are shown with the magenta profiles indicating the Pt diffraction peaks[32] JCPDS Card No. 040802. The red indicators mark the points measured at CHESS.

4.4.2 Methanol fluorescence results

Catalytic activity results from methanol fluorescence tests are shown in Figure 4.4.2.1. The color intensity of the pictures represented the point at which the increase in fluorescence (compared to the background) exceeded a 20% difference from the background fluorescence signal. The compositions generated in these libraries consisted of a gradient from the gun positions and a maximum concentration of a second element below approx. 50%. Detailed descriptions of the individual systems are discussed subsequently.

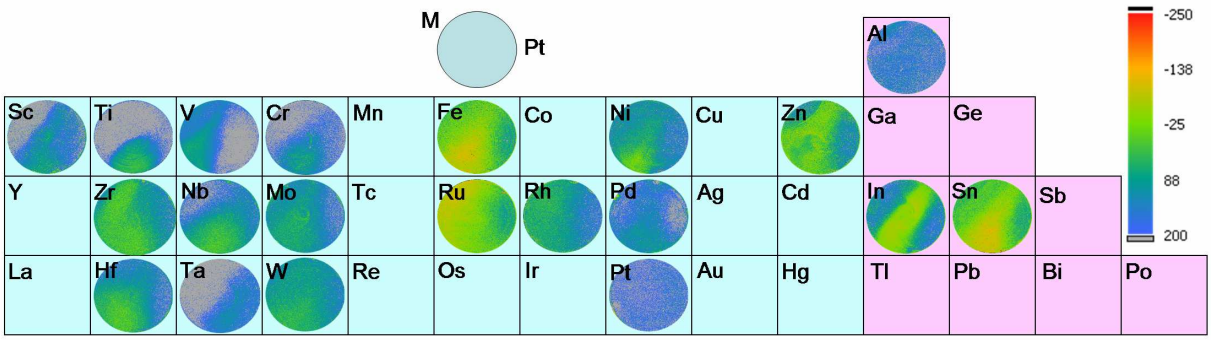

Figure 4.4.2.1: Fluorescence onset potentials for methanol oxidation on Pt-M combinatorial libraries in a periodic table. The fluorescence intensity scale is shown on the right. The gun positions are denoted with the top left being the second element and the right edge being Pt. The second element concentration on the films did not exceed 50%. Scans were collected from open circuit potential to 200 mV vs. Ag/AgCl at 5 mV/s.

Pt and PtRu as references:

It is interesting to note that pure Pt did not exhibit fluorescence catalytic activity in this system below 200 mV, indicating that even the addition of a second element did improve the activity under these conditions. The commercial standard PEMFC anode catalyst for methanol oxidation has been PtRu (1:1). The PtRu shown contained maximum compositions of 30% Ru. A significant onset improvement was observed as the amount of Ru increased as expected from the literature and was assumed to be from the bifunctional mechanism with Ru supplying the surface oxygen, thus aiding in the oxidation of the fuel and CO.[33]

Column 3, 4, 5, 6 binaries: Pt- M (M=Sc, Ti, V, Cr, Zr, Nb, Mo, Hf, Ta, W)

Pt-Ti, Pt-Zr, Pt-Nb, and Pt-Hf all showed similar onset potentials with the activity improving by approximately 200 mV relative to Pt. A feature in these samples was the earlier onset in the position equidistant from the Pt and M rich regions, indicating that catalytic activity was not only a function of film composition, but may also depend on factors such as fiber texturing and film thickness, which would vary with deposition rate.) As the distance of sputtering gun from the film increased, the film thickness decreased and the possibility of alternative film texturing was a possibility, especially due to the angle of the sputtering guns with respect to the film. (see *Fiber texture section)* For Pt-Sc, Pt-V, Pt-Cr, and Pt-Zr, an optimal composition was observed within the combinatorial library. Pt-Sc showed enhanced activity in the Pt rich region, whereas the Pt-Zr and Pt-V samples exhibited activity closer to the Zr and V regions, respectively. In the Pt-V and Pt-Mo samples, fluorescence was observed at the V (or Mo) rich regions when no fuel is present, indicative of leaching V (or Mo) into the solution (figure 4.4.2.2).

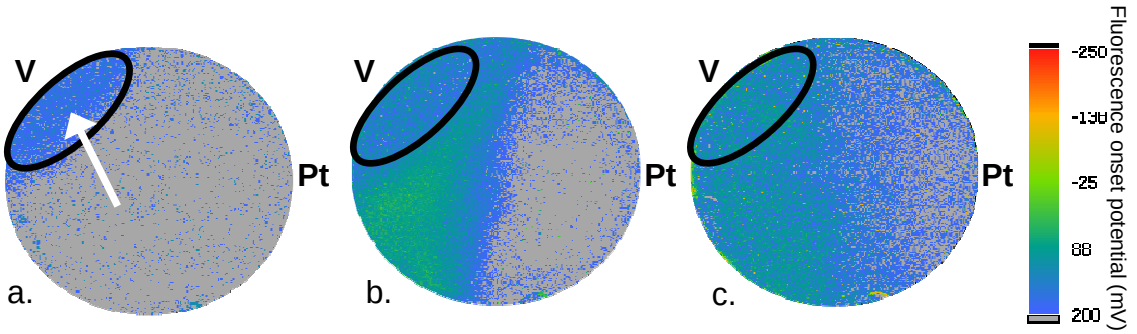

Figure 4.4.2.2: Pt-V binary sample (9:1 Pt: V stiochiometry at the center) a. Background scan without fuel (white arrow – unstable V-rich region); b. Methanol fluorescence scan; c. Methanol fluorescence scan after pre-treatment of the substrate. The black circle denotes the region where the film was unstable for the subsequent scans.

PtTa, PtW

In a recent study, Pt-Ta was studied at higher concentrations than in this work and an increased fluorescence was observed.[34] It was proposed that the Pt_3Ta phase, with a Ta suboxide on the surface, could improve the activity by providing an oxygen source at low potentials as predicted in the bifunctional mechanism. In our case, the concentration of Ta was low and the fluorescence in the Pt rich area suggested that more Ta was needed for oxidation to occur. A further difference between the experiments performed previously was that the sputtering temperature was 100 ^{o}C and we reported previous sputtering temperatures at high temperatures 400, 450 and 550 ^{o}C, which could result in different phases being present in the film.[34] Pt-W was of interest because of the conducting oxide that W forms and has been proposed as a possible support material.[35] At these concentrations, we found no leaching of the material over the time frame of the experiment, which indicated its stability in neutral to pH 4 solutions. We observed fluorescence in the position equidistant to Pt and W and are still determining the reason for the fluorescence in that region.

Columns 8, 9, 10 binaries: Pt-M (M=Fe, Ni, Rh, Pd)

Pt-Pd showed no significant improvement over Pt alone. The presence of Rh with Pt improved the fluorescence especially in the Rh rich region. Pt-Fe fluoresced in the background scan in the Fe rich area, indicating that it was unstable under our testing conditions. However, with this in mind, the activity across the center of the Pt-Fe substrate did represent improved potentials for methanol oxidation (~150 mV earlier onset). The optimal activity corresponded to approximately 10% Fe. Similarly for Pt-Ni, approximately 10% Ni exhibited the best activity

across the center of the library. This time no background fluorescence was observed in the Ni rich region.

PtZn

This system was previously studied in detail and it was reported that when Zn exceeded 50%, Zn leached out of the thin film, leaving a Pt rich surface.[18] To note, we assumed minimal leaching as the composition approached the Pt rich region, since our concentration did not exceed 20%. According to previous reports on leaching, a concentration >25% can result in a significant loss of the less noble metal.[10] We observed fluorescence at an optimal concentration in the middle of the combinatorial library corresponding to a composition of approximately 10% Zn than was over 200 mV better than Pt.

PtAl, PtIn, PtSn

In the case of Pt-Al, the fluorescence image showed the same results as Pt – no fluorescence at potentials below 200 mV. Pt-Sn and Pt-In showed the greatest improvement in onset potential versus Pt, with a fluorescence onset potential shift of approximately 350 mV for both methanol and ethanol oxidation. Both Pt-In and Pt-Sn showed an active fluorescent strip indicating there is an optimal concentration across the combinatorial library. The addition of Sn is known to yield an earlier onset for CO-oxidation and, as a result, assists in the oxidation of intermediates from higher C-containing fuels.[21-23, 36-38]

4.4.3 Pretreatment

Most of the samples exhibited the same fluorescence before and after pretreatment; however, there were a few select samples that should be noted (figure 4.4.3.1). Pt-M (M = Sc, V, Zn) showed higher fluorescence onset potentials without pretreatment. Upon pretreatment, all three showed further diminished activity, as compared to without pretreatment. On the other hand, Pt-Ta showed an improvement in activity seen in the region equidistant to the Pt and Ta rich areas. The supposition from the XPS measurements was that the tantalum oxide was partially reduced to form a tantalum suboxide upon pretreatment, hence improving the activity.[34] Pt-In and Pt-Sn had improved onset potentials after pretreatment, indicating that either contaminants were removed from the surface or surface oxides were reduced to form a more active surface. Ideally, XPS measurements would be performed on the Pt-In and Pt-Sn samples. However, once the sample was exposed to air after testing, the surface oxides can readily form on the surface, thus not providing an accurate measurement of the surface species. Another aspect to note was a shift in active region for Pt-M (M=Ni, Fe), where the active region before pretreatment was mostly in the region furthest from M and Pt and after pretreatment it moves to the Ni or Fe rich regions, respectively.

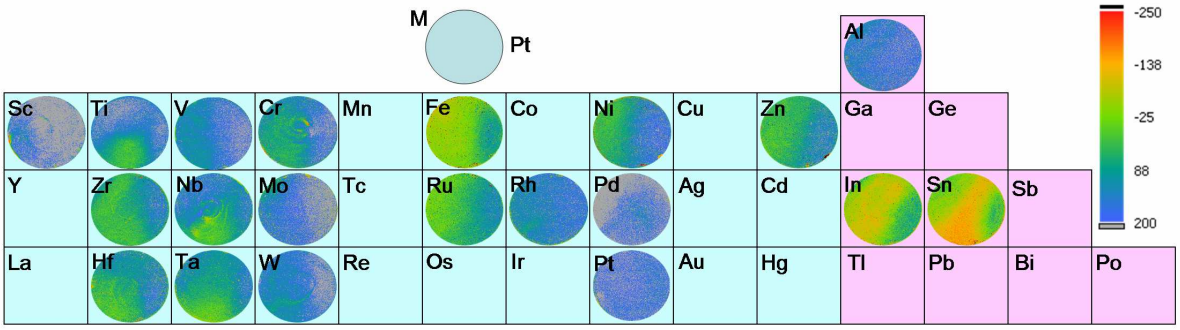

Figure 4.4.3.1: Fluorescence onset potentials for methanol oxidation after pretreatment of Pt-M combinatorial libraries in a periodic table. The fluorescence intensity scale is shown on the right. The gun positions are denoted with the top left being the second element and the right edge being Pt. The second element concentration on the films does not exceed 50%. Scans were collected from open circuit potential to 200 mV vs. Ag/AgCl at 5 mV/s.

4.4.4 Ethanol fluorescence results

Figure 4.4.4.1 presents the fluorescence onset potentials for ethanol oxidation after pretreatment. All but a few of the fluorescence regions and approximate onset potentials appeared to be the same as for methanol after pretreatment, suggesting similar oxidation mechanisms occurring for both. In analyzing these data, we must also remember that this method only detects the generation of protons, which may be the result of partial or complete oxidation of the fuel. Pt-V, Pt-Rh and Pt-Mo exhibited earlier fluorescence onset potentials in the same regions as for methanol, which could suggest that these regions activate the initial oxidation step for ethanol oxidation than for methanol. The most significant change was for Pt-Pd, which went from no activity for methanol to exhibiting an active region for ethanol at 10% Pd.[39]

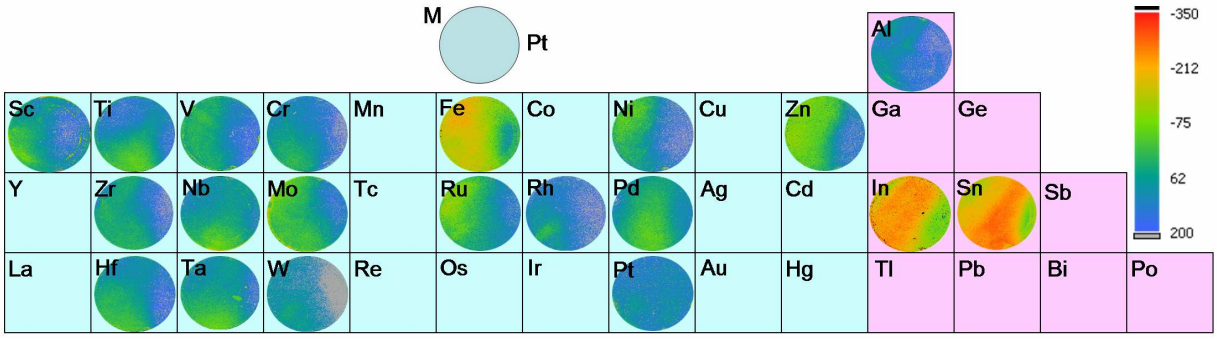

Figure 4.4.4.1: Fluorescence onset potentials for ethanol oxidation after pretreatment on combinatorial samples. The fluorescence intensity scale is shown on the right. The gun positions are denoted with the top left being the second element and the right edge being Pt. The second element concentration on the films does not exceed 50%. Scans were collected from open circuit potential to 200 mV vs. Ag/AgCl at 5 mV/s.

4.4.5 Fluorescence, composition and phase

As the composition across the substrate was correlated to the fluorescence onset potential, we observed that onset potential minima were obtained for many of the samples. M=In, Sn, Fe, Zn,

Ru showed the lowest onset potentials and their activities as a function of composition are shown in figure 4.4.5.1. One of the most interesting features was a minimum (ie. highest activity) at very low concentrations; between 2.5% and 5%, in three of the five samples. The Pt-Fe alloy had a minimum at higher concentrations (~10% Fe). It should also be noted that crystalline phases form on the films (as indicated by the unfilled points) and that the activity was not significantly enhanced by the presence of ordered phases relative to the alloys. However, when compared to the Pt substrate alone, there was a shift of approximately 125 mV in the onset potential for In, Sn, and Fe.

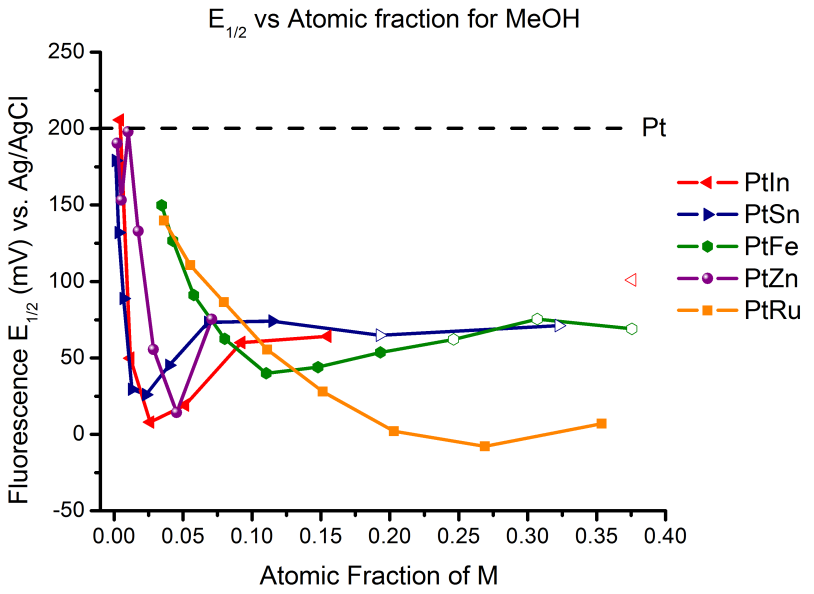

Figure 4.4.5.1: Fluorescence $E_{1/2}$ vs. Atomic Fraction of alloying element M in Pt samples. XRF measurements gave the atomic fractions. The dotted line is the fluorescence onset potential for a Pt wafer. The open points indicate the formation of a different phase.

Shifts in the density of states as a function of composition was explored computationally for the Pt-M (M=Sn, Fe, Zn) systems. The published *d*-band center of close-packed Pt surfaces was lower (-2.25 eV) than that of Fe (-0.92 eV); [40] bulk Zn and Sn both had filled *d*-bands, with that of Sn further below its Fermi level than that of Zn. It was therefore interesting that alloying

Pt with Fe caused a decrease in the Pt *d*-band center, with the *d*-band center increasing slightly when alloying with Zn and more substantially when alloying with Sn. These differences in trends suggest subtleties in bonding that vary amongst these three metals with Pt, which we believe warrant their own investigation. Regardless, variation in bulk *d*-band center clearly did not explain the trends in catalytic activity in these systems and pointed to a substantial deviation from the bulk behavior (e.g. segregation, local oxidation) at the surface in these systems. The monotonic nature of the changes in catalytic activity was consistent with the hypothesis of unusual surface behavior in these systems.

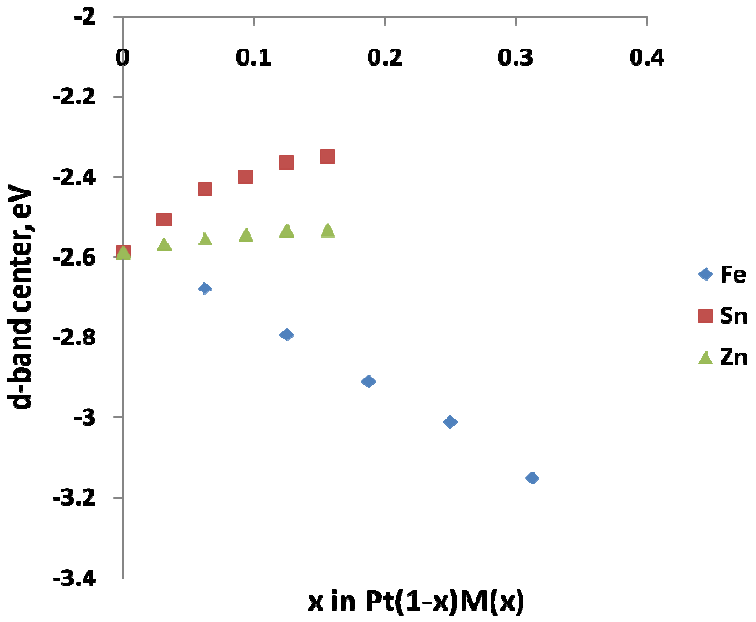

Figure 4.4.5.2: Bulk average *d*-band center calculations for M = Fe, Sn, and Zn alloyed in Pt with the concentration of M being below 30%.

4.4.6 Fiber texture

The crystallites of a polycrystalline film may be randomly oriented or "equiaxed". However, sputtered films that crystallize into a cubic phase are typically comprised of crystallites with either (111) or (001) planes lying parallel to the film surface. The crystallographic

orientation was isotropic about the substrate normal, and this "texture" could be analyzed by observing the diffraction intensity of a given {hkl} family of Bragg peaks as a function of the angular displacement Φ of the scattering vector with respect to the substrate normal. The high energy transmission XRD experiment involved simultaneous observation over a range of Φ that was not typically available in thin film diffraction experiments[16] providing quantitative analysis of the crystal texture. It is important to note that while alloy composition can affect the texture of a film, deposition geometry and other deposition conditions can also affect texture. These parameters vary in a systematic but uncontrolled manner as a function of substrate in a given library.

In this work, the fcc-{111} family of peaks was used to quantify the relative fractions of textured and equiaxed grains by measuring the relative diffraction intensities in the identified peaks and in the flat portions of a Φ-distribution, with appropriate weighting of the (hkl) multiplicity and Φ-ranges. For thin film catalyst studies, consideration of the effects of texture on activity is important, as each crystal face may have a unique catalytic activity.[41]

Fig. 4.4.6.1a shows the Φ-distribution of the fcc-{111} diffraction from a $Pt_{0.96}Sn_{0.04}$ film with the texture peak areas and equiaxed areas colored. Fig. 4.4.6.1b shows a false color interpolation of the Φ-distribution as a function of substrate position, demonstrating that the texture evolved as a function of position and composition. The Pt-rich area was strongly (111)-textured, and a (001) texture was also observed with increasing Sn content.

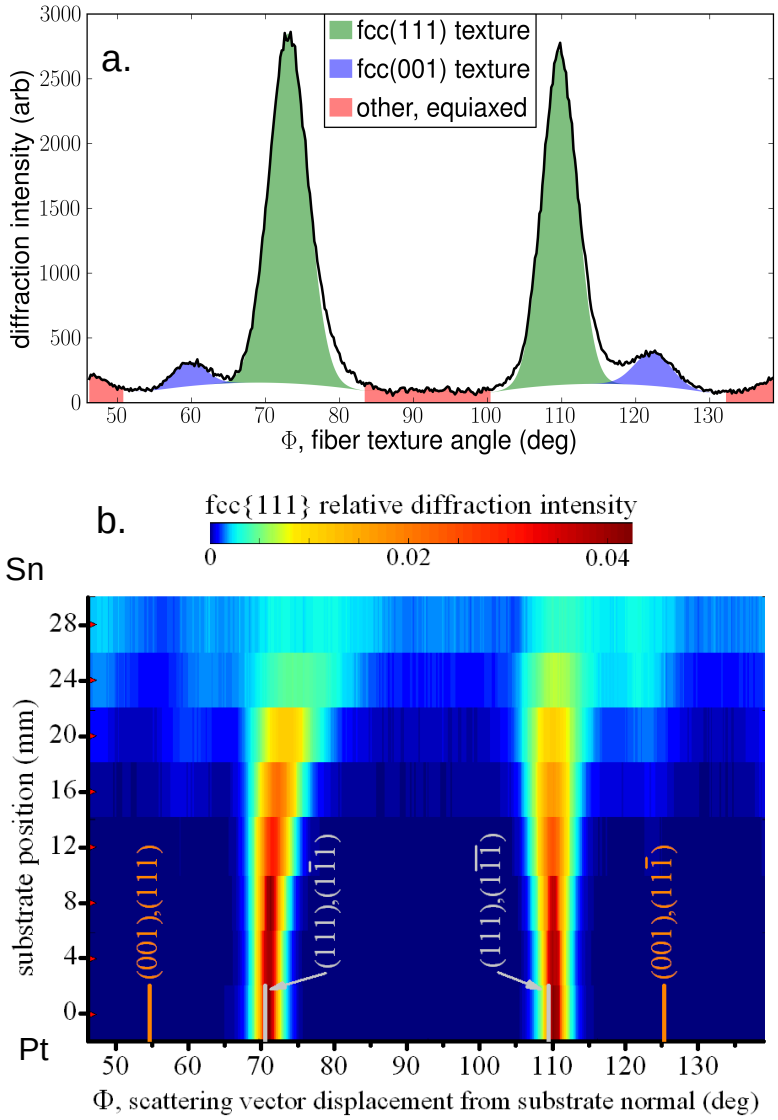

Figure 4.4.6.1: Fiber texture quantification in the Pt-Sn library via analysis of the fcc{111} diffraction intensity as a function of crystallite grain orientation Φ. a. The Φ-distribution of the 20mm substrate position is shown, along with shading of the fitted peak areas and equiaxed areas. b. The Φ-distributions from the 8 substrate positions containing single-phase fcc film are shown in the color intensity scale. The expected peak positions are also shown as (HKL),(hkl) where (HKL) are the Miller indeces of the fiber texture direction, and (hkl) are the indices of the fcc{111} family. Deviation from these positions is indicative of a deviation of the fiber texture direction from the substrate normal.

Similarly, with regards to the fluorescence seen in the regions farthest from the Pt and M rich areas on the substrates, we examined whether the activity observed could be a result of texturing in that region. The fiber texturing did not appear to give rise to the fluorescence seen in these areas.

4.4.7 All factors together

A representative sample of the thin films that contained the lowest onset potential is Pt-Sn and figure 4.4.7.1 presents the parameters that we explored, which include fluorescence $E_{1/2}$, atomic fraction of Sn, lattice constant, and fiber texturing fcc(111) and fcc(001). The methanol and ethanol oxidation seemed to follow the same trend with the best activity being between 2.5-5% Sn. The lattice constant also followed the alloying of the Sn in the Pt but could not be attributed as the cause of the low onset potential. When the texturing was examined across the Pt-Sn highly active region, the fcc(111) texture ranges from a fraction of 0.6 to 1.0 and the fcc(001) ranges from a fraction of 0.0 to 0.8 over the same area, indicating that the texturing was not the sole cause for the lower onset potential. However, the intersection of the fraction of the fcc(111) and the fcc(001) did not rule out the possibility that the fcc(001) increase between substrate positions 12 mm and 20 mm and could be a contributing factor to the activity.

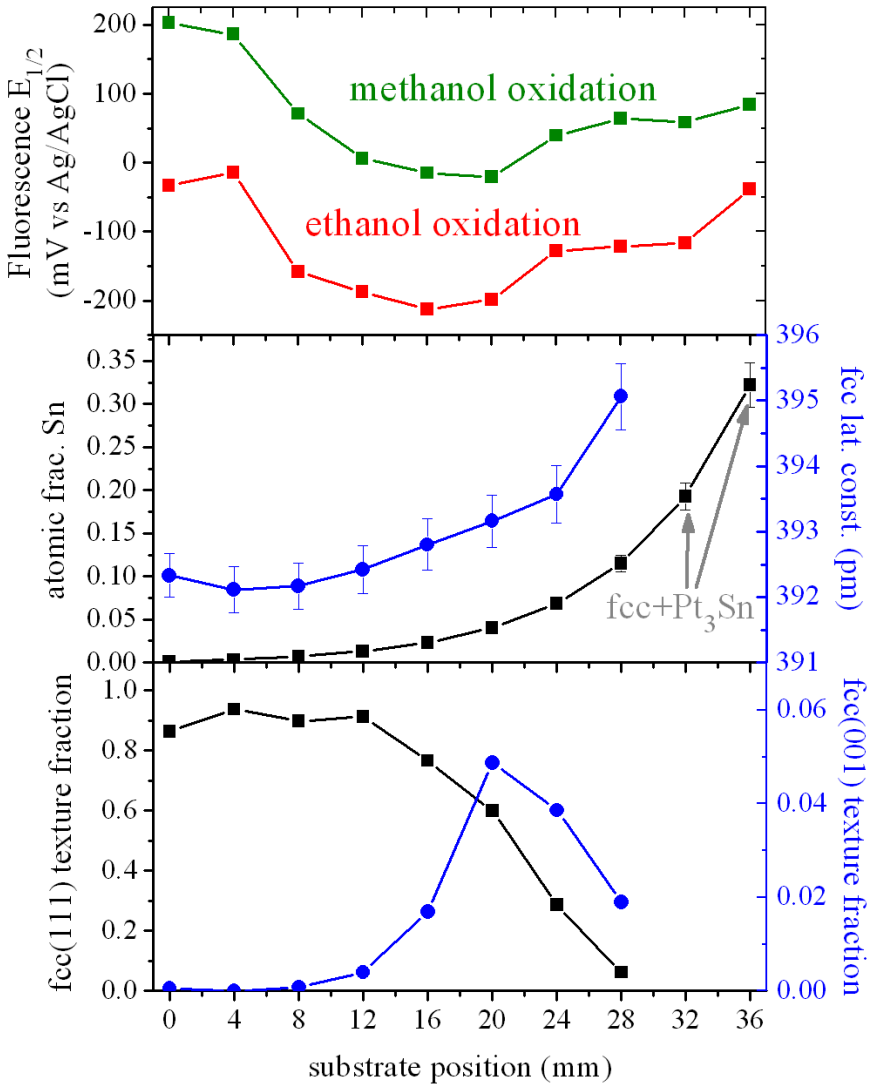

Figure 4.4.7.1: Pt-Sn combinatorial film comparing some of the variables investigated. a. methanol and ethanol fluorescence onset potential $E_{1/2}$ vs. substrate position; b. atomic fraction of Sn in Pt vs. substrate position (from XRF); c. texturing vs. substrate position.

To summarize the results we investigated, the lowest fluorescence onset potential for each of the binary films was compared to the atomic fraction of the second element in figure 4.4.7.2. Notice that the In, Sn, and Zn binaries all exhibited the best activity at concentrations below 5%, whereas for the Ru, the optimal concentration was between 20-35%. Another interesting feature was that, for the elements that show onset potentials between 100-150 mV, the

best compositions were between 25-35% M and contained a second phase in addition to fcc. These compositions were improvements upon pure Pt and showed that even the alloying of a second element could contribute for improved activity. Moreover, for the samples that showed greatly enhanced activity at the lower concentrations (below 5%), this suggests that an alternative mechanism may be occurring and will be studied in detail using the recently developed scanning DEMS. The binary thin films with fluorescence (activity) in the position equidistant to the Pt and M were not included on these plots and the cause for this fluorescence remained unexplained.

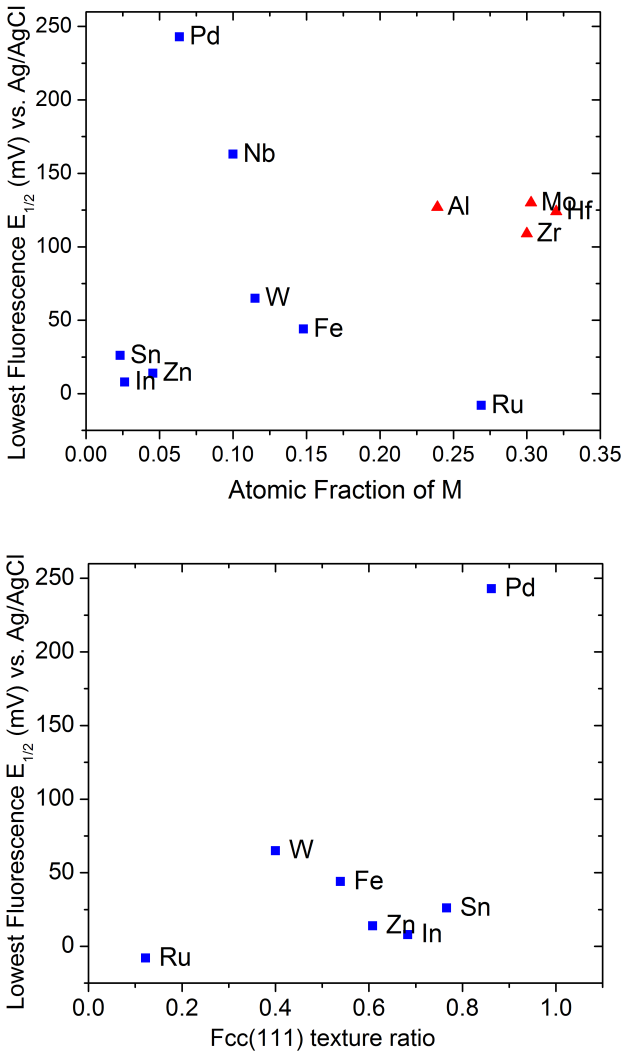

Figure 4.4.7.2: a. Lowest fluorescence onset potential per combinatorial library vs. atomic fraction determined by XRF. The blue squares are the fcc alloys and the red triangles indicate the presence of a different phase. b. Lowest fluorescence onset potential vs. fcc(111) ratio over the entire Φ area. Only the well behaved elements that have the lowest onset potential with fcc(111) texturing (i.e. no elements with a different phase as the best active region) and do not show fluorescence in the position equidistant to the Pt and M rich areas are shown (ie. no Ni, Ti, Ta, Rh, Cr, V).

For films in which the most active region was a single-phase fcc alloy, the best fluorescence onset potential was plotted versus the fcc(111) texturing. The lowest onset was Pt-Ru, which contained the lowest amount of texturing, but should be noted that the other binaries with the lowest onset potential (In, Zn, Sn) contained a high fraction of the Pt fcc(111) texture.

4.5 Conclusion

Binary Pt-M alloy systems have been studied using a high throughput combinatorial screening method for methanol and ethanol electrooxidation. Eighteen elements, M (M = Sn, Ta, W, Mo, Ru, Fe, In, Pd, Hf, Zn, Zr, Nb, Sc, Ni, Ti, V, Cr, Rh), were alloyed at concentrations that did not exceed 50%, via magnetron cosputtering, and tested for catalytic activity using identical methods. This method enabled comparisons to be made without the issue of different synthesis methods or electrochemical testing parameters. All the samples were characterized at CHESS for identification of phases and compositions in the thin films with additional compositional measurements performed for In and Sn using Energy Dispersive Spectroscopy (EDS).

In this study, it was found that the five most active systems for methanol oxidation were Pt-M alloys with M=Sn, In, Fe, Zn, and Ru. For M=Sn, In, and Zn, the most active regions were below 5 atom-% M and mainly fcc(111) texture. Pt-Fe shows improved activity around 10% Fe with a 0.5 fcc(111) texture fraction. Lastly, the Pt-Ru sample showed improved activity at concentrations above 20% Ru with minimal fcc(111) texturing. For the samples that showed minimal improvement (M=Al, Mo, and Hf), it was interesting to note that the best compositions on the films were at higher concentrations of the second element, M, where a second phase was formed. For M = Ti, Ni, Cr, V, Rh, and Ta, activity was highest in regions of thinner film thicknesses. Systems with M=Fe, Ru, In, Sn, and Zn demonstrated highly non-linear dependence of activity on composition which could not be explained by shifts in bulk density of states and suggested unusual surface behavior.

Further electrochemical measurements under fuel cell conditions (pH 1) must be performed to obtain current densities of the most promising compositions and will be pursued for the five best samples with the lowest onset potential using a scanning minicell and scanning

differential electrochemical mass spectrometry (SDEMS). Moreover, this combination of thin film sputtering, characterization at CHESS, and electrochemical screening can be implemented for more complex systems, for instance ternary and quaternary systems.

4.6 Acknowledgements

The authors would like to thank the Cornell High Energy Synchrotron Source (CHESS) staff, especially Alexander Kazimirov and Darren Dale for their help with data acquisition, setup and data analysis and use of CHESS facilities, especially for the XRD and XRF measurements. This material is based upon work supported as part of the Energy Materials Center at Cornell (EMC^2), an Energy Frontier Research Center funded by the U.S. Department of Energy, Office of Science, and Office of Basic Energy Sciences under Award Number DE-SC0001086.

4.7 References

1. Larminie, J.; Dicks, A., *Fuel cell systems explained*. First ed.; John Wiley & Sons: West Sussex, England, 2000; p 26.

2. Antolini, E.; Salgado, J. R. C.; Gonzalez, E. R., The methanol oxidation reaction on platinum alloys with the first row transition metals - The case of Pt-Co and -Ni alloy electrocatalysts for DMFCs: A short review. *Applied Catalysis B-Environmental* **2006,** 63, (1-2), 137-149.

3. Casado-Rivera, E.; Volpe, D. J.; Alden, L.; Lind, C.; Downie, C.; Vazquez-Alvarez, T.; Angelo, A. C. D.; DiSalvo, F. J.; Abruña, H. D., Electrocatalytic activity of ordered intermetallic phases for fuel cell applications. *Journal of the American Chemical Society* **2004,** 126, (12), 4043-4049.

4. Ishihara, A.; Doi, S.; Mitsushima, S.; Ota, K., Tantalum (oxy)nitrides prepared using reactive sputtering for new nonplatinum cathodes of polymer electrolyte fuel cell. *Electrochimica Acta* **2008,** 53, (16), 5442-5450.

5. Strasser, P.; Koh, S.; Anniyev, T.; Greeley, J.; More, K.; Yu, C.; Liu, Z.; Kaya, S.; Nordlund, D.; Ogasawara, H.; Toney, M. F.; Nilsson, A., Lattice-strain control of the activity in dealloyed core-shell fuel cell catalysts. *Nature (London, United Kingdom)* **2010**.

6. Adzic, R. R.; Zhang, J.; Sasaki, K.; Vukmirovic, M. B.; Shao, M.; Wang, J. X.; Nilekar, A. U.; Mavrikakis, M.; Valerio, J. A.; Uribe, F., Platinum monolayer fuel cell electrocatalysts. *Topics in Catalysis* **2007,** 46, (3-4), 249-262.

7. Clavilier, J.; Fernandezvega, A.; Feliu, J. M.; Aldaz, A., Heterogeneous Electrocatalysis on Well Defined Platinum Surfaces Modified by Controlled Amounts of Irreversibly Adsorbed Adatoms. 1. Formic-Acid Oxidation on the Pt(111) - Bi System. *Journal of Electroanalytical Chemistry* **1989,** 258, (1), 89-100.

8. Prochaska, M.; Jin, J.; Rochefort, D.; Zhuang, L.; DiSalvo, F. J.; Abruña, H. D.; Dover, R. B. v., High throughput screening of electrocatalysts for fuel cell applications. *Review of Scientific Instruments* **2006,** 77, (5).

9. Reddington, E.; Sapienza, A.; Gurau, B.; Viswanathan, R.; Sarangapani, S.; Smotkin, E. S.; Mallouk, T. E., Combinatorial electrochemistry: A highly parallel, optical screening method for discovery of better electrocatalysts. *Science* **1998,** 280, (5370), 1735-1737.

10. Stevens, D. A.; Rouleau, J. M.; Mar, R. E.; Bonakdarpour, A.; Atanasoski, R. T.; Schmoeckel, A. K.; Debe, M. K.; Dahn, J. R., Characterization and PEMFC Testing of $Pt_{1-x}M_x$ (M= Ru, Mo, Co, Ta, Au, Sn) Anode Electrocatalyst Composition Spreads. *Journal of the Electrochemical Society* **2007,** 154, (6), B566-B576.

11. Neyerlin, K. C.; Bugosh, G.; Forgie, R.; Liu, Z.; Strasser, P., Combinatorial Study of High-surface-area binary and ternary electrocatalysts for the oxygen evolution reaction. *Journal of Electrochemical Society* **2009,** 156, (3), B363-B369.

12. He, T.; Kreidler, E.; Xiong, L.; Ding, E., Combinatorial Screening and nano-synthesis of platinum binary alloys for oxygen electroreduction. *Journal of Power Sources* **2007,** 165, 87-91.

13. Liu, J. H.; Jeon, M. K.; Woo, S. I., High-throughput screening of binary catalysts for oxygen electroreduction. *Applied Surface Science* **2006,** 252, 2580-2587.

14. Guerin, S.; Hayden, B. E.; Lee, C. E.; Mormiche, C.; Russell, A. E., High-throughput synthesis and screening of ternary metal alloys for electrocatalysis. *Journal of Physical Chemistry B* **2006,** 110, (29), 14355-14362.

15. Guerin, S.; Hayden, B. E.; Lee, C. E.; Mormiche, C.; Owen, J. R.; Russell, A. E.; Theobald, B.; Thompsett, D., Combinatorial electrochemical screening of fuel cell electrocatalysts. *Journal of Combinatorial Chemistry* **2004,** 6, (1), 149-158.

16. Gregoire, J. M.; Dale, D.; Kazimirov, A.; DiSalvo, F. J.; van Dover, R. B., High energy x-ray diffraction/x-ray fluorescence spectroscopy for high-throughput analysis of composition spread thin films. *Review of Scientific Instruments* **2009,** 80, (12), 123905.

17. Bonakdarpour, A.; Lobel, R.; Atanasoski, R. T.; Vernstrom, G. D.; Schmoeckel, A. K.; Debe, M. K.; Dahn, J. R., Dissolution of transition metals in combinatorially sputtered Pt1-x-yMxMy ' (M, M ' = Co, Ni, Mn, Fe) PEMFC electrocatalysts. *Journal of the Electrochemical Society* **2006,** 153, (10), A1835-A1846.

18. Gregoire, J. M.; Kostylev, M.; Tague, M. E.; Mutolo, P. F.; van Dover, R. B.; DiSalvo, F. J.; Abruña, H. D., High-Throughput Evaluation of Dealloyed Pt-Zn Composition-Spread Thin Film for Methanol-Oxidation Catalysis. *Journal of the Electrochemical Society* **2009,** 156, (1), B160-B166.

19. Colmati, F.; Antolini, E.; Gonzalez, E. R., Pt-Sn/C electrocatalysts for methanol oxidation synthesized by reduction with formic acid. *Electrochimica Acta* **2005,** 50, (28), 5496-5503.

20. Colmati, F.; Antolini, E.; Gonzalez, E. R., Preparation, structural characterization and activity for ethanol oxidation of carbon supported ternary Pt-Sn-Rh catalysts. *Journal of Alloys and Compounds* **2008,** 456, (1-2), 264-270.

21. Jiang, L. H.; Sun, G. Q.; Sun, S. G.; Liu, J. G.; Tang, S. H.; Li, H. Q.; Zhou, B.; Xin, Q., Structure and chemical composition of supported Pt-Sn electrocatalysts for ethanol oxidation. *Electrochimica Acta* **2005,** 50, (27), 5384-5389.

22. Li, G. C.; Pickup, P. G., Decoration of carbon-supported Pt catalysts with Sn to promote electro-oxidation of ethanol. *Journal of Power Sources* **2007,** 173, (1), 121-129.

23. Delime, F.; Leger, J. M.; Lamy, C., Enhancement of the electrooxidation of ethanol on a Pt-PEM electrode modified by tin. Part I: Half cell study. *Journal of Applied Electrochemistry* **1999,** 29, (11), 1249-1254.

24. Binary Alloy Phase Diagrams. In [Online] Second ed.; Thaddeus B. Massalski, H. O., P.R. Subramanian, Linda Kacprzak, Ed. ASM International: 1996.

25. Ghosh, T.; Zhou, Q.; Gregoire, J. M.; van Dover, R. B.; DiSalvo, F. J., Pt-Cd and Pt-Hg Phases As High Activity Catalysts for Methanol and Formic Acid Oxidation. *Journal of Physical Chemistry C* **2010,** 114, (29), 12545-12553.

26. Gregoire, J. M.; Dover, R. B. v.; Jin, J.; DiSalvo, F. J.; Abruna, H. D., Getter Sputtering system for high-throughput fabrication of composition spreads. *Review of Scientific Instrumentation* **2007,** 78, (7), 072212.

27. Kresse, G.; Furthmuller, J., Efficient iterative schemes for ab initio total-energy calculations using a plane-wave basis set. *Physical Review B* **1996,** 54, (16), 11169-11186.

28. Kresse, G.; Hafner, J., Abinitio Molecular-Dynamics for Liquid-Metals. *Physical Review B* **1993,** 47, (1), 558-561.

29. Kresse, G.; Joubert, D., From ultrasoft pseudopotentials to the projector augmented-wave method. *Physical Review B* **1999,** 59, (3), 1758-1775.

30. Blochl, P. E., Projector Augmented-Wave Method. *Physical Review B* **1994,** 50, (24), 17953-17979.

31. Perdew, J. P.; Burke, K.; Ernzerhof, M., Generalized gradient approximation made simple. *Physical Review Letters* **1996,** 77, (18), 3865-3868.

32. Powder Diffraction File. In JCPDS International Centre for Diffraction Data: Newton Square, PA: 2004.

33. Watanabe, M.; Motoo, S., Electrocatalysis by Ad-atoms. 2. Enhancement of Oxidation of Methanol on Platinum by Ruthenium Ad-atoms. *Journal of Electroanalytical Chemistry* **1975,** 60, (3), 267-273.

34. Gregoire, J. M.; Tague, M. E.; Cahen, S.; Khan, S.; Abruña, H. D.; DiSalvo, F. J.; van Dover, R. B., Improved Fuel Cell Oxidation Catalysis in Pt1-xTax. *Chemistry of Materials* **2010,** 22, (3), 1080-1087.

35. Wang, D. L.; Subban, C. V.; Wang, H. S.; Rus, E.; DiSalvo, F. J.; Abruña, H. D., Highly Stable and CO-Tolerant Pt/Ti0.7W0.3O2 Electrocatalyst for Proton-Exchange Membrane Fuel Cells. *Journal of the American Chemical Society* **2010,** 132, (30), 10218-10220.

36. Antolini, E.; Gonzalez, E. R., The electro-oxidation of carbon monoxide, hydrogen/carbon monoxide and methanol in acid medium on Pt-Sn catalysts for low-temperature fuel cells: A comparative review of the effect of Pt-Sn structural characteristics. *Electrochimica Acta* **2010,** 56, (1), 1-14.

37. Tanaka, S.; Umeda, M.; Ojima, H.; Usui, Y.; Kimura, O.; Uchida, I., Preparation and evaluation of a multi-component catalyst by using a co-sputtering system for anodic oxidation of ethanol. *Journal of Power Sources* **2005,** 152, (1), 34-39.

38. Samjeské, G.; Wang, H.; Löffler, T.; Baltruschat, H., CO and methanol oxidation at Pt-electrodes modified by Mo. *Electrochimica Acta* **2002,** 47, (22-23), 3681-3692.

39. Tsiakaras, P. E., PtM/C (M = Sn, Ru, Pd, W) based anode direct ethanol-PEMFCs: Structural characteristics and cell performance. *Journal of Power Sources* **2007,** 171, (1), 107-112.

40. Hammer, B.; Norskov, J. K., Theoretical surface science and catalysis - Calculations and concepts. In *Advances in Catalysis, Vol 45*, Academic Press Inc: San Diego, 2000; Vol. 45, pp 71-129.

41. Colmati, F.; Tremiliosi-Filho, G.; Gonzalez, E. R.; Berna, A.; Herrero, E.; Feliu, J. M., Surface structure effects on the electrochemical oxidation of ethanol on platinum single crystal electrodes. *Faraday Discussions* **2008,** 140, 379-397.

CHAPTER 5

Non-Platinum Catalysts and Other Materials

This section discusses all of the materials that either do not contain platinum or contain non-metallic elements, such as carbon, nitrogen, or oxygen.

5.1 Pd-Rh-Ta

As a follow-up to the Pt-Ta sample, other metallic binaries, ternaries and quaternaries containing Ta were sputtered. Metals with electrochemical stability were one of the reasons why Pd and Rh were selected. With direction from Dr. John Gregoire and his desire to explore phases that form on the spreads, these spreads were tested with the help of Ms. Sahr Kahn to elucidate catalytic activity. Binaries of Pd, Rh, and Ta were all tested and found that without pretreatment all of these samples showed no activity. Once pretreatment was performed, fluorescence could be observed as was evident in the Pd-Ta sample.[1] This was promising because these samples did not contain Pt. The Rh-Ta (about $Rh_{0.68}Ta_{0.32}$) showed fluorescence for methanol but not for ethanol as seen in figure 5.1.1. However, after subsequent testings, no fluorescence was observed at all. Pd-Ta exhibited no activity before pretreatment but became active in the Pd rich region for both methanol and ethanol after pretreatment. Another concern for the Pd containing material is the absorption of hydrogen into the Pd and therefore also being a good H_2 storing material. The fluorescence could represent a false positive, especially with the protons generated from oxidation of adsorbed H_2.

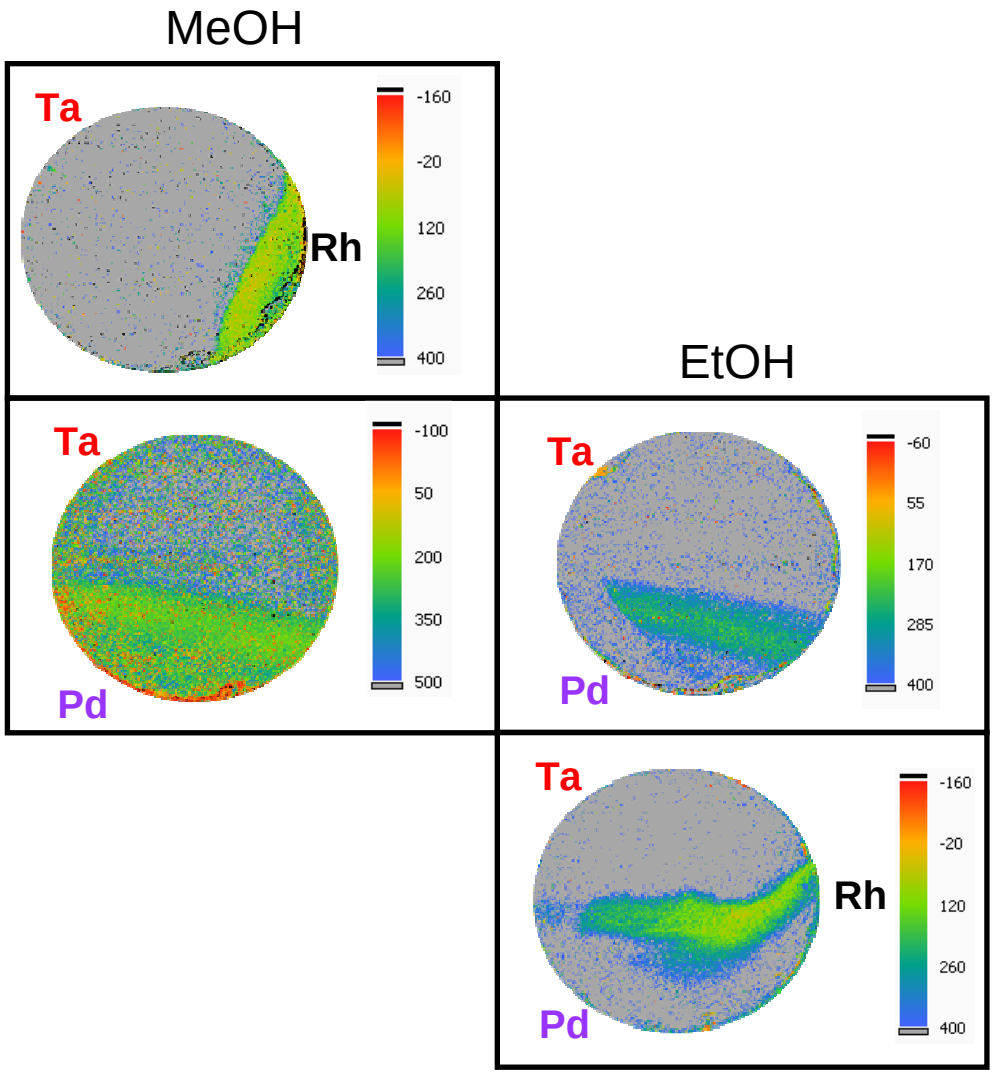

Figure 5.1.1: Methanol and ethanol oxidation fluorescence onset potential images for Rh-Ta, Pd-Ta, and ternary Pd-Rh-Ta with the onset potential scales on the right in mV vs. Ag/AgCl. The samples that did not show fluorescence are not shown here (ie. MeOH oxidation for Pd-Rh-Ta and EtOH for Rh-Ta).

The Pd-Rh-Ta (fig. 5.1.2) composition spread (active area = approx. $Rh_{0.40}Pd_{0.25}Ta_{0.35}$) exhibited good catalytic activity for ethanol oxidation, but not for methanol. While the phases had not been identified, we could delineate the phase boundaries using XRD patterns (noted by the black lines). This composition, while interesting, was not practical because of the high cost of Rh and Pd, making the mixed element catalyst economically unattractive. However, this was

a good demonstration that non-Pt catalysts might prove to be a possibility. With these identified compositions, we can attempt to understand the reaction mechanisms for catalysis, which can, in turn, provide valuable insights and directions as to other systems to study.

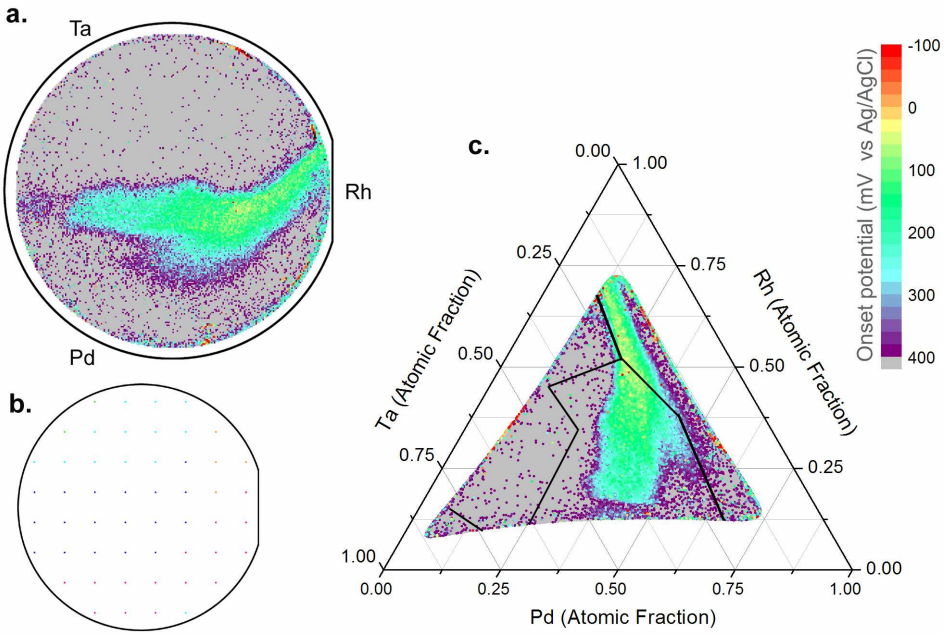

Figure 5.1.2: a. Fluorescence onset potential for ethanol oxidation measured for a Pd-Rh-Ta thin film composition spread plotted in an outline of the substrate using the color scale at right. b. Set of points analyzed by XRD/XRF plotted in the outline of the substrate and colored by the groups that result from the correlation algorithms of Long, et al.[2] c. The data in a. are mapped onto a ternary composition diagram using the same color scale. The boundaries of the "phase regions" resulting from the groupings of b. are noted with black lines.

5.2 Ir-Ta(-M) (M = Pt, Ir, Rh, Ru, Pd)

In both the Pt-Ta and Pd-Rh-Ta systems, similar Ta stoichiometries were present between 25% and 40% resulting in better activity. Table 5.2.1 presents the binary and ternary systems examined for Ta-X-Y (X, Y=Pt, Ir, Rh, Ru, and Pd). Out of the samples tested, Pt-Ir-Ta showed the best onset potential for methanol and ethanol oxidation. Of particular interest were the non-Pt catalysts, such as Pd-Rh-Ta and Ir-Ta. Pd-Rh-Ta was discussed above, but especially for Ir-

Ta, the onset potential is significantly improved over Pt for methanol and ethanol. The onset potential for methanol oxidation, while not the best, was promising simply because it showed activity without Pt. The onset potential was comparable to that of the Pd-Rh-Ta sample but, again, the cost of Ir was high and the abundance was low, so the economic viability was minimal. It would be very interesting to obtain mechanistic information that could be compared to that of Pt-containing analogs. Table 5.2.1 contains 7 combinations (highlighted in yellow) that have yet to be retested and included in this study. The reason these samples must be retested was that the atmospheric conditions were not under nitrogen. This was especially important because without pretreatment, these samples did not exhibit any activity and the pretreatment reduces surface oxides. Without the removal of the oxygen from the atmosphere, the films could reoxidize after pretreatment, thus not providing an accurate representation of the results.

The binary phase diagrams of these compositions contained M_3Ta phases (M= metal) and these different structures could contribute to the activity. In all the cases containing Ta, pretreatment was important for activity and was most likely due to contributions from the surface oxides. Furthermore, in the Pt-Ta study, we found that the presence of the Pt_2Ta and Pt_3Ta phases seemed to also contribute to the fluorescence activity. Hence, if this concept was applied to the other Ta series, we would expect the intermetallic phases with the surface oxides to exhibit improved activity.[3]

Table 5.2.1: Ta-X-Y alloys deposited at 400 ^{o}C. All fluorescent onset potentials were taken after pretreatment and with N_2 purging the cell. Yellow indicates that the test was performed, but no N_2 was purging the cell.

MeOH Onset Potentials (mV) vs. Ag/AgCl					
Ta-X-Y	Ir	Rh	Ru	Pd	Pt
Ir	120				-60
Rh		160		none	
Ru			none		
Pd				320	
Pt					

EtOH Onset Potentials (mV) vs. Ag/AgCl					
Ta-X-Y	Ir	Rh	Ru	Pd	Pt
Ir	-40				-180
Rh		100		-40	
Ru			none		
Pd				260	
Pt					

EG Onset Potentials (mV) vs. Ag/AgCl					
Ta-X-Y	Ir	Rh	Ru	Pd	Pt
Ir	220				100
Rh		140		20	
Ru			none		
Pd				400	
Pt					

5.3 Pt-Mo-N [Manuscript]

Paper: "Synthesis of Pt-Mo-N Thin Film and Catalytic Activity for Fuel Cells," *Chem. Mater*. **2010**, *22*, 3451-3456.

Collaborators: Akira Miura, John Gregoire, Xiao-Dong Wen

5.3.1 Abstract

While Pt and Pt-based intermetallic alloys have been extensively studied as catalysts for proton exchange membrane fuel cells, Pt-based nitride catalysts have been relatively unexplored. We report the synthesis and characterization of a Pt-based nitride, Pt_2Mo_3N, by using a composition

spread thin film deposition technique. The Pt_2Mo_3N thin film was generated by co-deposition of Pt and Mo and subsequent heat treatment in an ammonia flow at 800 ^oC for 6 h. The thin film was characterized by scanning electron microscopy (SEM), X-ray diffraction (XRD), X-ray photoelectron spectroscopy (XPS) and electrochemical tests, including the assessment of catalytic activity toward the oxidation of methanol and formic acid and the reduction of oxygen. The nitride film was smooth and contained single-phase, stoichiometric Pt_2Mo_3N. Cyclic voltammograms of Pt_2Mo_3N in 0.1 M H_2SO_4 demonstrated electrochemical stability far greater than that of a PtMo alloy with the same Pt:Mo ratio, indicating that the formation of the nitride phase enhances electrochemical stability. The ternary nitride exhibited oxidation currents in formic acid and methanol solutions above approximately 0.0 and 0.4 V vs. an Ag/AgCl reference electrode, respectively. These are above the expected equilibrium oxidation potentials of approximately -0.2 V. The onset potential for oxygen reduction was estimated to be ~0.2 V vs Ag/AgCl, well below the equilibrium value of 1.0 V.

5.3.2 Introduction

Proton exchange membrane fuel cells (PEMFCs) are highly efficient energy conversion devices that operate near room temperature. Small organic molecules, such as formic acid and methanol, are potential fuels for such fuel cells and offer high energy density compared to hydrogen gas. Pt has been used as a fuel cell catalyst, but it is expensive and easily poisoned by trace impurities (CO, S etc.)[4]. Pt-based alloys and intermetallics, such as PtRu[5], PtMo[6, 7], PtPb[8], PtPd[9] and PtCoCr[10], use less Pt and show smaller overpotentials in the oxidation of formic acid, H_2/CO mixture gas or methanol, but their stability is compromised by dissolution of non-platinum metals[11-13]. While Pt and Pt-based alloys have been studied as catalysts for decades, no

publication of Pt-based nitrides has been reported as a fuel cell catalyst. Motivated by previous reports of enhanced CO tolerance of the PtMo intermetallic[3] and of catalytic activity of Mo_2N/C toward oxygen reduction[14, 15], we investigated the electrochemical stability and catalytic activity of the ternary nitride Pt_2Mo_3N. Its structure can be described as a β-Mn structure with interstitial nitrogen, in which Pt, Mo and N occupy specific crystallographic positions[16].

Synthesis of single-phase ternary Pt nitrides often involves rather laborious and/or time-intensive processes. Pt_2Mo_3N has been synthesized as aggregates of submicron particles by nitridation of an oxide precursor at 800-1000 ^oC for 2-24 h[16]. The oxide precursor was produced by oxidation of an amorphous sample at 400 ^oC for 12 h, which was obtained by freeze drying an aqueous solution of stoichiometric metal salts[16]. Other ternary Pt nitrides, PtM_3N (M:Cr, Fe, Mn), have been synthesized by nitridation of the PtM_3 alloy or annealing a Pt and metal nitride mixture[17-20]. Due to the low diffusion rates of the constituents in the 600-1300 ^oC temperature range, a homogeneous material was only obtained after long or repeated anneals. Our nitridation of a thin metal film exploited the small diffusion length characteristic of thin films and accelerated the synthesis of the phase-pure ternary nitride. Additionally, we note that synthesis of Pt-based nitrides in a thin film form is an important technique as it enables the characterization of these materials by established thin film techniques, most notably the high-throughput screening for catalytic activity[21-24].

In this paper, we report on the synthesis of $Pt_xMo_{1-x}N_y$ films and explore their use as fuel cell catalysts. Particular attention was given to the ternary nitride phase Pt_2Mo_3N. The use of composition-spread thin films and a collection of characterization techniques allows for the detailed evaluation of electrochemical properties as a function of composition and crystallographic phase in the Pt-Mo-N system.

5.3.3 Experimental detail

Pt-Mo films were prepared in a custom built combinatorial sputter deposition system described previously[25]. The Pt_xMo_{1-x} library was generated by codeposition onto a 76.2 mm-diameter Si substrate with a 500 nm SiO_2 thermal oxide, which served as a diffusion barrier. Prior to deposition, the substrate surface was irradiated with 500 eV Ar using an ion source (IonTech) to remove surface contaminants and promote film adhesion. Elemental Pt and Mo (>99.9% purity) were co-deposited from separate magnetron sputter sources (Angstrom Sciences) in an atmosphere of 0.66 Pa Ar. The geometrical relation of the deposition sources with respect to the Si substrate provided a deposition gradient from each source that upon codeposition resulted in a continuous variation in composition across the substrate. After deposition, the substrate was cleaved to extract a 20 mm-wide substrate piece with composition gradient along its 60 mm length. The film thickness was ~100 nm on the Mo-rich side and decreased to ~70 nm on the Pt-rich side. The Pt-Mo composition gradient film was set in a quartz tube with an internal diameter of 24 mm. Under ammonia flow (approximately 5-10 mL/min at STP), the temperature was linearly raised to 800 °C over 6 h, kept at 800 °C for 6 h, and then lowered to 30 °C over 6 h. After the reaction, the film was exposed to air. The composition profile of this thin film is shown in figure 5.3.3.1 and demonstrates that the substrate piece contained a thin film with composition range $0.15<x<0.7$ of Pt_xMo_{1-x}.

A Pt_xMo_{1-x} library film and MoN_y film were prepared by similar methods. The Pt_xMo_{1-x} library film was deposited using the same parameters as the film described above except the substrate was maintained at 400 °C during deposition. The established reproducibility of the deposition rates corresponds to a common Pt:Mo composition profile for the nitride and metal library thin films. The MoN_y film was prepared by deposition from the Mo source in an

atmosphere of 0.66 Pa of 20% N_2 in Ar. The substrate was maintained at 400 °C during this deposition.

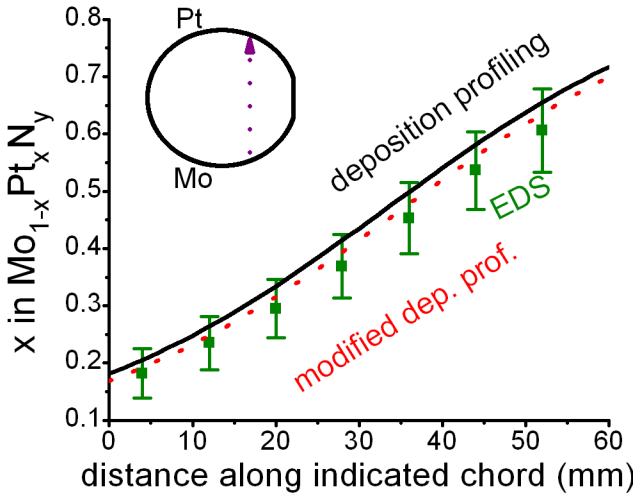

Figure 5.3.3.1: The *x* stoichiometry in the $Mo_{1-x}Pt_xN_y$ library was calculated using deposition profiles[26, 27] and measured by energy dispersive x-ray spectroscopy (EDS) using a JEOL 8900 EPMA Microprobe. The EDS measurements involved 10 keV excitation energy and analysis of Mo L and Pt K characteristic x-rays.

The phase behavior of the thin films was analyzed by XRD using both a Bruker AXS General Area Detector Diffraction System (GADDS) and a Rigaku theta-theta diffractometer (Ultima IV). The morphology of the film was observed by secondary electron microscopy (SEM: LEO-1550 field emission SEM). Chemical binding energy and depth compositional analysis were performed by x-ray photoelectron spectroscopy (XPS: Surface Science Instrument SSX-100). Survey scans were performed with a 150V pass energy from 0-800eV at 1eV/step, and high resolution scans were performed with 50V pass energy at 0.065eV/step. *In situ* film etching was performed with an Ar ion supply operated at 4 keV and 2 mA cm^{-2}. Analysis of XPS data was performed using CasaXPS software package. The bonding energies were corrected by reference to free carbon (284.6 eV). The film composition was semi-quantitatively determined by using the area of Pt 4f, Mo 3d, N 1s, O 1s, C 1s and Si 2p signals. Since N 1s signal

overlapped with the Mo 3p peaks, we used only the area of fitted peaks at binding energies >397 eV to determine the amount of nitrogen.

Electrochemical measurements were performed using a 2.5-cm tall, 6-mm inner diameter Teflon electrochemical cell that isolated a 0.32 cm^2 area of the thin film for localized testing. This 6-mm cell included a coiled Au counter electrode inside the cell and an Ag/AgCl reference electrode. More detail on the setup and methodology is described in a previous report[23]. Cyclic voltammograms (CVs) from -220 to 600 mV vs Ag/AgCl were acquired for select film regions in a 0.1 M H_2SO_4 solution, and additional fuel oxidation studies were performed with 1 M concentrations of formic acid or methanol.

Oxygen reduction testing was also performed by using a similar setup with an O_2-bubbled solution and a Pt counter electrode instead of Au one to avoid Au electrodeposition on the working electrode. CVs were collected under N_2–bubbled 0.1 M H_2SO_4 solution until no change was observed in the CV. The potential was then held a reducing potential (approx. -0.15 V) and O_2 was bubbled. Once a constant current was reached (about 20 seconds), the potential was scanned positively and subsequent CVs were collected.

To determine current density, a measure of the specific surface area was required. A CV was acquired at 100mV/s in 1 mM ferrocenemethanol, 0.1 M H_2SO_4 aqueous solution. Analysis of the ferrocenemethanol redox waves using the Randles-Sevcik equation provided the electrode surface area.[23] Previous surface area measurements of relatively smooth films using this technique have been consistent with atomic force microscopy measurements[28]. These measurements of the PtZn porous films revealed the same trend of catalytic activities as the PtZn nanoparticles.[21,29]

5.3.4 Results and Discussion

Phase behavior and properties of nitrided films

Before and after nitridation of the Pt_xMo_{1-x} library film, the film surface appeared metallic and reflective with subtle changes in reflectivity at certain composition contours indicating the presence of phase boundaries. Figure 5.3.4.1 shows pXRD patterns of the Pt_xMo_{1-x} composition gradient film after heat treatment in NH_3 flow. Diffraction peaks were assigned as Pt, PtMo, Pt_2Mo_3N, and MoN_y ($0.5<y<1$). The relative intensities of the PtMo peaks differed from those of the indexed patterns due to the fiber texture of thin film[30]. Nitride phases were observed only for the Mo-rich portion of the composition. A single-phase region corresponding to the Pt_2Mo_3N structure was observed over the composition range of $0.38 < x < 0.48$. The equilibrium composition range of this ternary phase was unknown, and while the annealed thin film may be metastable, the diffraction data indicates that the composition range was appreciable. The observed Pt, PtMo and MoN_y phases had relatively wide composition ranges, in agreement with JCPDS data[31].

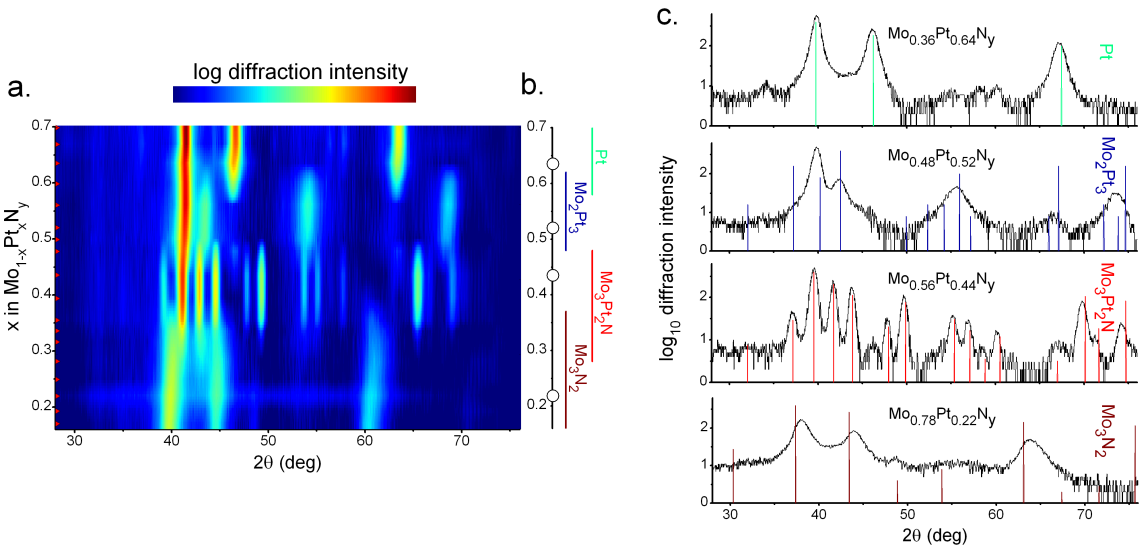

Figure 5.3.4.1: Compositions and XRD patterns of the Pt-Mo-N film. (a) Measured platinum fraction *x* and interpolated X-ray diffraction (XRD) patterns (color scale). The substrate positions analyzed by XRD are denoted by small red markers on the vertical axis. (b) Measured platinum fraction *x* with the phases assigned to XRD patterns and their respective composition intervals. (c) Select XRD patterns from the platinum fractions denoted by white circles in panel (b). JCPDS patterns of the assigned phases are shown (see JCPDS entries for Pt (JCPDS File Card No. 03-065-2868), MoPt (JCPDS File Card No. 01-071-9787), Mo_3Pt_2N (JCPDS File Card No. 01-672-9865), Mo_3N_2 (JCPDS File Card No. 01-089-3712)).

Figure 5.4.3.2 shows microstructure and compositional depth profile of the $Pt_{0.42}Mo_{0.58}$ region of the film after nitridation, where single-phase Pt_2Mo_3N was identified. The SEM image shows that the film was densely packed and the thickness of the film was 70-100 nm. The compositional depth analysis exhibited high contents of C, O and N and low contents of Pt and Mo at the film surface, indicating the presence of hydrocarbon contaminants and/or surface oxides. While C and O were not observed after 11 min of Ar etching, Pt, Mo and N were then found to be present in a ratio of approximately 30:50:20, which was close to stoichiometric ratio of Pt_2Mo_3N (34:50:16). This result indicated that the diffusion rate of nitrogen during the heat treatment was high enough to form the Pt_2Mo_3N phase through the entire depth of the film. Further etching uncovered silicon and oxygen from the SiO_2 underlayer. The absence of Si and O

in the XPS measurements taken from 11 to 41 min of etching suggested that Si and O diffusion into the thin film was negligible.

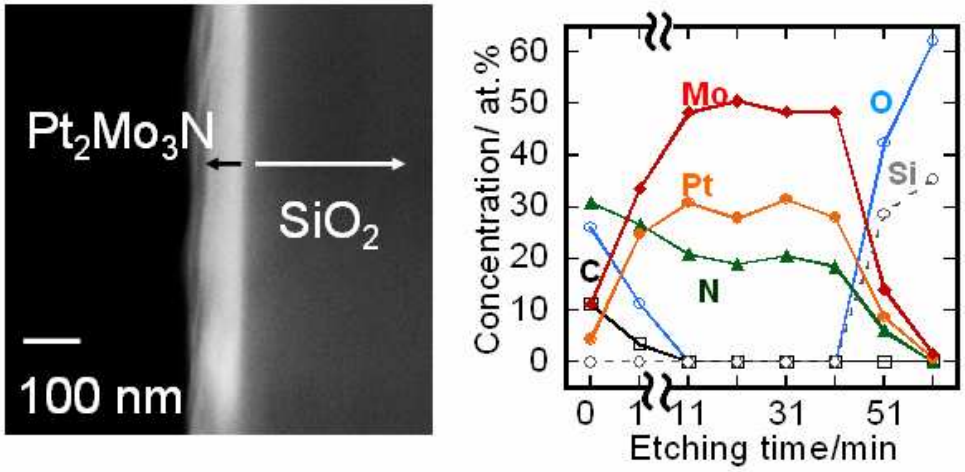

Figure 5.3.4.2: Cross-section SEM image of Pt-Mo-N film (x = 0.42) and XPS depth profile of the corresponding position in the film.

Electrochemical characterization

Four regions of the Pt-Mo-N film were chosen for electrochemical characterization. The regions centered at metal stoichiometries x= 0.64, 0.53, 0.45 and 0.24 show the structure type characteristic of the cubic PtMo alloy, the hexagonal PtMo alloy, the ternary Pt_2Mo_3N phase and the MoN_y, respectively (Figure 5.3.4.1). The CVs acquired in 1 M formic acid showed that all four samples were active toward the oxidation of formic acid, although the quantification of oxidation current for the x=0.24 catalyst was compromised by electrode instability, as discussed below (figure 5.3.4.3).

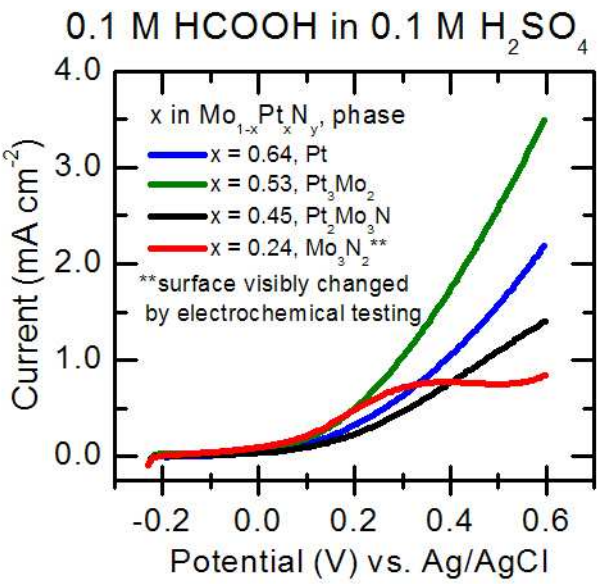

Figure 5.3.4.3: Anodic sweeps of $Mo_{1-x}Pt_xN_y$ film with different x values in 1 M HCOOH + 0.1 M H_2SO_4 solution. Scan rate is 50 mV/s.

To determine the specific activity of the single-phase Pt_2Mo_3N sample (x =0.45), a surface area measurement using the ferrocenemethanol redox couple was made after fuel oxidation studies and resulted in a roughness factor of 1.0 +/- 0.1. This measurement was consistent with the physical characterization discussed below, and thus current densities for the CVs in formic acid and methanol (Figure 5.3.4.4) were calculated using the geometric surface area of the electrochemical cell (0.32 cm^2). The onset potential for formic acid oxidation was just above 0.0 V vs Ag/AgCl, about 50mV more negative than that of Pt (Figure 5.3.4.3a).[8] The oxidation current density was about 5 times higher than Pt as well.[8] For methanol oxidation (Figure 5.3.4.4b), the onset potential was approximately 0.4 V vs. Ag/AgCl. While this onset potential was near the potential at which the surface started to oxidize in the absence of fuel, the current density was more than twice as high as without fuel. Thus, we concluded that methanol oxidation occurs above 0.4 V. The onset potential and current density were comparable to those of Pt.[8] The activity of this catalyst toward the reduction of O_2 was also measured. The cathodic

sweeps with N_2–bubbled and O_2–bubbled solution are shown in Figure 5.3.4.5. The onset potential of oxygen reduction was about 0.2 V vs Ag/AgCl, which was more negative than that of Pt (~0.65 V).

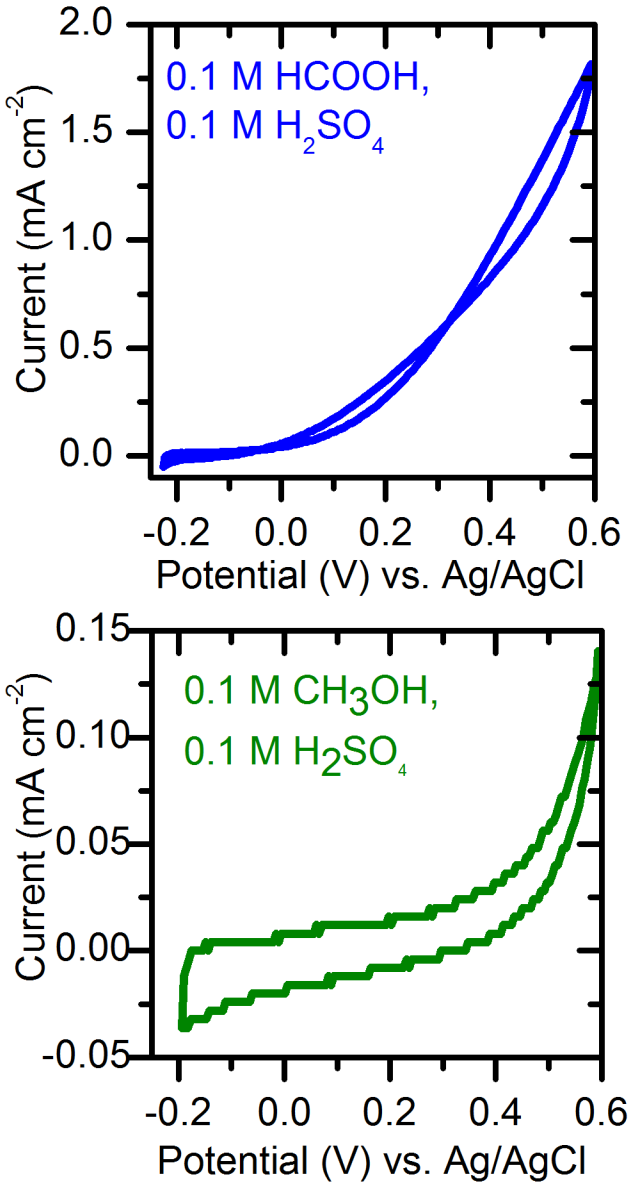

Figure 5.3.4.4: Cyclic voltammograms of Pt-Mo-N film (x = 0.45, Pt_2Mo_3N phase) in (a) a solution of 1 M HCOOH + 0.1 M H_2SO_4 and (b) a solution of 1 M CH_3OH + 0.1 M H_2SO_4. Scan rate is 50 mV/s.

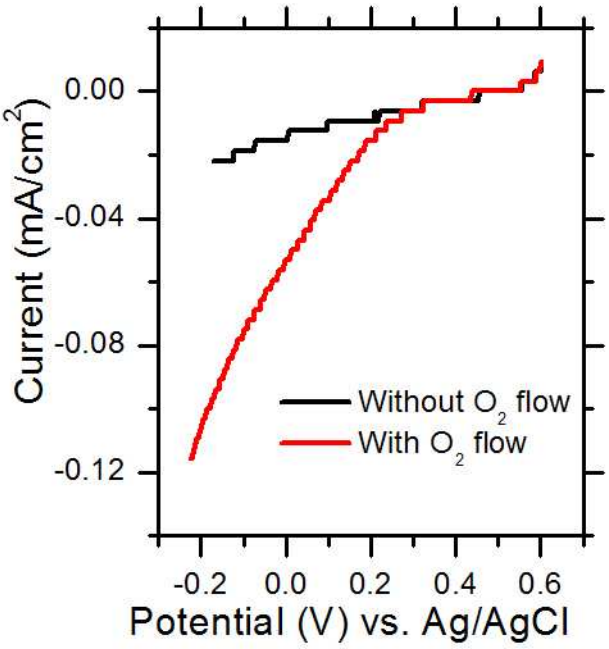

Figure 5.3.4.5: Cathodic sweeps with N_2 (black trace) and O_2 flows (red trace) of Pt-Mo-N film (x=0.45) in 0.1 M H_2SO_4 solution. Scan rate is 50 mV/s. The presence of O_2 caused the current to increase in the negative direction, supporting the prediction that O_2 reduction was catalyzed with the Pt_2Mo_3N compound.

Further understanding of the properties of the Pt_2Mo_3N sample (x =0.45) was attained by comparing its electrochemical stability to that of related materials. The binary film containing Pt_xMo_{1-x} (x =0.45, no nitrogen) and the ternary film exhibiting the binary MoN_y phase (x=0.24) were characterized by the same electrochemical procedures as the ternary Pt_2Mo_3N (x= 0.45) film discussed above. Figure 5.3.4.6 shows the CVs in 0.1 M H_2SO_4 for all three films before fuel oxidation testing and for the Pt_2Mo_3N (x= 0.45) film after fuel oxidation testing. For all three compositions, the CVs before the catalyst assessment showed two anodic peaks (~0.1V and >0.4 V). While Pt_2Mo_3N and Pt-Mo alloy films did not visually change after CV measurements, MoN_y (x=0.24) turned black after the measurement due to significant electrochemical roughening. We also noted that CVs acquired with a binary MoN_y (x=0) film showed similar

oxidation peaks, and the entire film leached into solution after several CVs. These results indicated that the MoN_y phase was unstable in this electrochemical environment for both x=0 and x=0.24. For the Pt-Mo (x= 0.45) alloy, the two anodic current peaks were also observed, which had been reported to involve Mo leaching[12]. The Pt_2Mo_3N (x =0.45) film exhibited the lower absolute oxidation current before fuel oxidation testing. After the oxidation testing, the current did not change except the disappearance of oxidation current at ~0.1 V and reduction current at ~0.3 V. Thus, the ternary nitride Pt_2Mo_3N film was found to be the most resilient to electrochemical leaching out of Mo of this set of films. We noted, however, that the reactions responsible for the two oxidation peaks were not well understood. Possibly, this oxidation current was due to the formation of a surface-stable Mo oxide such as MoO_3-H_2O, which was insoluble in pH 1 solutions[12].

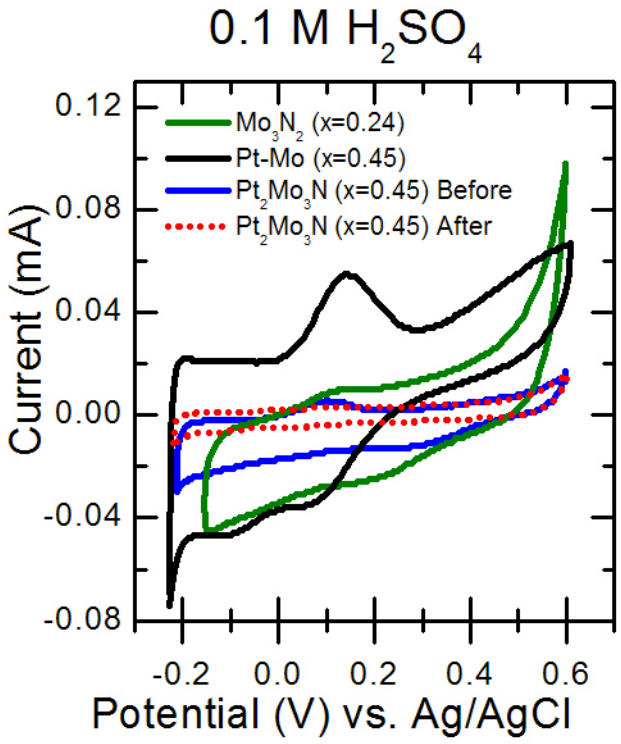

Figure 5.3.4.6: Cyclic voltammograms in 0.1 M sulfuric acid of Pt-Mo-N film after nitridation (x=0.45, 0.22) and PtMo film without nitridation. Scan rate is 50 mV/s.

Properties of electrochemically stable Pt_2Mo_3N

SEM images of the Pt_2Mo_3N single phase region showed a smooth surface without cracks before and after the catalytic assessment. XRD characterization of the Pt_2Mo_3N region of the composition spread thin film showed no significant change before and after the electrochemical tests. These results preclude a significant leaching of Mo accompanied with phase change. Chemical bonding at the surface in the Pt_2Mo_3N region was examined by XPS spectra before and after the catalytic activity test (Figure 5.3.4.7). The spectra after 1 min of Ar etching are also shown, in which hydrocarbon contaminants and/or surface oxide layer were partially removed (Fig. 5.3.4.2) to investigate whether signals were attributed to the outer surface or inner. The energy of two Pt 4f doublet peaks was observed at almost the same energies (71.5-71.6 and 74.8-74.9 eV) before and after the catalytic examination as well as after 1 min Ar etching, indicating that the bonding of Pt was unaffected by the electrochemical tests and was similar in the outer and inner surface. These energies were slightly higher that those of Pt metal (70.9 and 74.2 eV), possibly due to partial charge transfer from Pt. The Mo 3d peaks observed before the electrochemical tests could be decomposed into two doublet peaks with Mo $3d_{5/2}$ binding energies of 228.1 and 232.5 eV. The higher energy doublet matched peak energies reported for MoO_3[32], and the additional observation of oxygen on the surface (Figure 5.3.4.2) indicated the presence of a surface MoO_3 layer on the Pt_2Mo_3N. The lower-energy doublet at 228.1 eV was between the characteristic $3d_{5/2}$ binding energies for metallic Mo (227.7-227.9 eV) and MoN_x (228.6-229.1 eV)[32]. These doublet peaks were also observed after 1 min Ar etching, indicating they were attributed to the Mo in the ternary nitride Pt_2Mo_3N, not to the outer surface of the nitride. After the catalytic test, only the lower-energy doublet was detected, indicating the removal of the MoO_3 layer by the electrochemical reduction. Stable catalytic activities and the

similarity of XPS between after the catalytic test and, 1 min Ar etching, suggested that the catalytic activities should come from the nitride, not from the surface oxide. The surface atomic ratio of Pt to Mo in the Pt_2Mo_3N phase was calculated from the corresponding XPS peak areas to be 0.84 and 1.03 before and after the electrochemical tests, respectively. The catalytic oxidation increased the Pt/Mo ratio, but not considerably. Combined with the XRD, SEM and electrochemical characterization, the results indicated that the electrochemical testing resulted in a slight enhancement of the surface Pt:Mo ratio but did not involve bulk leaching of Mo.

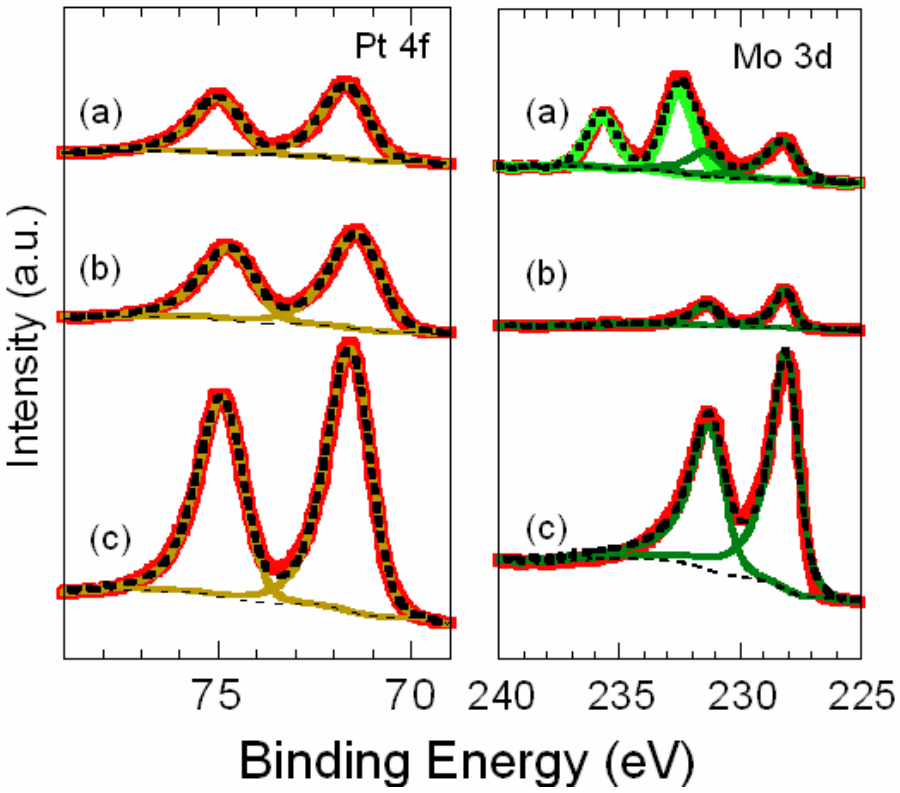

Figure 5.3.4.7: Pt 4d and Mo 3d signals of XPS of Pt-Mo-N film (x = 0.45) (a) before and (b) after electrocatalytic assessment, as well as (c) after one minute of Ar^+-ion etching.

The superior electrochemical stability of Pt_2Mo_3N compared to PtMo (x=0.45) and MoN_y (x=0, 0.24) was likely related to the high thermodynamic high stability of Pt_2Mo_3N. We calculated the free energies of formation (ΔG) of Pt_2Mo_3N, PtMo (x=0.5) and MoN by using

density functional theory. The calculated free energy of formation of Pt_2Mo_3N at 300 K was -219 kJ/mol, which was much lower than that of MoN (-7 kJ/mol) and PtMo (-30 kJ/mol). This high formation energy should stabilize Mo in Pt_2Mo_3N, presumably resulting in less leaching of Mo. Another possible cause of the measured stability was the formation of a Pt or Pt-rich skin which created a kinetic barrier to Mo leaching.[29, 33, 34] Such a kinetic barrier had been proposed for Pt-Mo alloys[12] but did not account for the improved electrochemical stability of the ternary Pt_2Mo_3N compared to the binary Pt-Mo film at x=0.45.

5.3.5 Acknowledgements

We thank Malcolm Thomas and Jonathan Shu at the Cornell Center for Materials Research for help with the SEM and XPS data collections. This material was based on work supported as part of the Energy Materials Center at Cornell, an Energy Frontier Research Center funded by the U.S. Department of Energy (DOE), Office of Science, Office of Basic Energy Sciences under Award Number DE-SC0001086. This work made use of the XPS, XRD and SEM facilities of the Cornell Center for Materials Research (CCMR) with support from the National Science Foundation Materials Research Science and Engineering Centers (MRSEC) program (DMR 0520404). This work was partially supported by DOE Grant DE-FG02-87ER45298 and by the National Science Foundation (NSF) through grant number DMR-0602526 and CHE-0910623.

5.4 Metal-Carbide Systems [Manuscript]

Paper: “Phase Behavior of Pseudobinary Precious Metal-Carbide Systems.” *J. Phys. Chem. C* **2010**, *114*, 21664-21671.

Collaborators: John Gregoire, Eva Smith, Darren Dale, Francis DiSalvo, Richard Hennig, R. Bruce van Dover, Sophie Cohen, and Anna Legard (data collection at CHESS).

5.4.1 Introduction

Transition metal carbides, which are known to have high mechanical and chemical stability, comprise a promising class of materials for fuel cells electrodes.[35, 36] In particular, carbides of W and Ta are being investigated as fuel cell electrode materials due to their high conductivity, high electrochemical stability, and catalytic properties.[36, 37] While carbides of Ta and W have been shown to have some catalytic activity for the reduction of oxygen[38] and the oxidation of hydrogen,[39, 40] higher catalytic activity and electrochemical stability have been attained by using the carbide as a catalyst support and by incorporating the carbide in a ternary composite or alloy. For example, Ta and C play an important role in mitigating the electrochemical leaching of Ni in ternary Ni-Ta-C catalysts.[41, 42]

Tungsten carbide-based materials have been more intensively explored and exhibit many desirable properties. Tungsten carbide-supported Pt has been shown to have high electrochemical stability and does not significantly oxidize in air below 450 °C.[37, 43] The tungsten carbide supports have also been found to mitigate Pt poisoning by CO and increase the activity for fuel oxidation due to interactions between the Pt and the carbide support.[37] Tungsten carbides have also been used to enhance the fuel oxidation activity of Pd catalysts, both as a support[44] and as a composite material.[45]

Lu et al.[46] studied CO tolerance in the pseudoternary system Pt-Ru-WC with thin films that were sputter-deposited from elemental and WC targets. The three materials were deposited in sequentially alternating layers and subsequently annealed at 520 °C to promote interdiffusion.

The highest CO tolerance was found for an electrode with the approximate composition $Pt_{25}Ru_5(WC)_{70}$, but the crystallographic phase of the sample was not determined.

Work presented here covers the interesting phase behavior of the pseudobinary systems P-M-C, where P is a precious metal (Pt, Ru, and Pd) and M-C is a cubic transition metal carbide (WC and TaC).[47] Additionally, the pseudoternary system Pt-Ru-WC is explored. The work presented in this section discusses the electrochemical properties of the films and only briefly summarizes the phase behavior of these films.

5.4.2 Experimental

Composition spread deposition.

Films were prepared in a custom-built combinatorial sputter deposition system, described previously.[26] Each $P_{1-x}M_xC_z$ library was generated by first depositing a 12 nm Ti adhesion layer (underlayer) onto a 76.2 mm diameter Si substrate. During and after this deposition, the substrate was radiatively heated and maintained at the library deposition temperature of 400 °C. For a given library, each transition element was sputtered from separate magnetron sputter sources (Angstrom Sciences) in a 0.66 Pa Ar/CH_4 atmosphere. With the aid of a cryoshroud,[26] the background pressure during deposition remained in the 10^{-5} Pa range. The geometrical relation of the deposition sources with respect to the Si substrate provided a deposition gradient from each source that upon codeposition resulted in a continuous variation in transition metal composition across the substrate. The range of *x* represented in a given library was dictated by the deposition profiles of the individual sources and the relative power delivered to these sources. The deposition rate from each source at substrate center was 1×10^{-9} mol/s/cm^2, measured with a quartz crystal monitor just prior to deposition of the library.

Carbon was incorporated into the growing film through reaction of the transition metals with CH_4 and its plasma induced derivatives, both at the surface of the deposition source and at that of the growing film's surface. The C concentration in the thin film monotonically increased with the CH_4 concentration in the sputter atmosphere, and at a given substrate position (a given transition metal composition), the value of *z* was dictated by the reactivity of the transition metals with the carbon species. While CH_4 was potentially a source for hydrogen incorporation into the thin film, at the growth temperature of 400 °C, the metal-hydrogen phase diagrams indicated that the hydrogen concentrations would likely be well below 1 at. % for all transition metal compositions.[48]

Thin Film Characterization.

Diffraction patterns of the WC_z thin films were acquired using a Bruker GADDS diffractometer. The crystallographic structure and composition of the composition spread thin films were characterized by a high-throughput XRD and X-ray fluorescence (XRF) technique. These experiments were conducted at the Cornell High Energy Synchrotron Source (CHESS) and were described in detail in a separate publication.[49] Briefly, monochromatic 60 keV X-rays impinged the thin film with ~1 mm^2 spot size, and the diffraction image was attained in transmission geometry by a 345 mm diameter image plate (Mar Research). Integration of the images provided diffraction patterns that were compared to patterns of known phases in the powder diffraction file (PDF).[50] Sputter deposition commonly yielded textured thin films in which the constituent crystallites were randomly oriented with respect to substrate azimuth but aligned with respect to substrate normal.[51] The average crystallite orientation in the film was determined by analyzing the diffraction images.[49] XRF spectra were obtained with a Rontec X-Flash energy-dispersive

silicon-drift detector oriented orthogonal to the direct beam and analyzed with a custom algorithm.[52] These measurements were not sensitive to elements as light as C, and thus, the XRF measurements provided the stoichiometry of the transition metals in the thin films.

Electrochemical Stability.

A high-throughput screening of the stability of the WC_z films was performed by using the entire film as the working electrode in a specially designed electrochemical cell.[28] The potential applied to the film was swept positive at 5 mV/s, and a large area Au coil served as the counter electrode. The testing solution was near pH 7 with 0.1 M potassium triflate as the supporting electrolyte and 0.3 mM quinine as the mediator for optically monitoring stability of the film. Oxidation of the film resulted in a local decrease in pH, and in the pH and potential range of interest, W formed a water-soluble oxide.[50] The working electrode current, which was attributed to thin film oxidation and corrosion, was recorded, and because all of the films were mirror-flat in appearance, the oxidation current density was calculated using the geometric area of the substrate. Methanol oxidation was similarly screened for on these films in the same electrochemical cell.

5.4.4 Results and Discussion

Fluorescence screening was performed on the P-M-C (P=Pt, Pd, Ru; M = Ta, W) series to determine catalytic activity and stability of the films. First, we wanted to verify the phases that were present in the W-C films alone and correlate the concentration of methane in the sputtering chamber with the phases in the film. Figure 5.4.4.1 shows the phases incorporated into the films, such that at low pressures of about 5% CH_4 gives a W-rich phase and then as the concentration of methane was increased, a W_2C followed by a WC phase was formed. The fluorescence of the

W-C films can be ascribed to the oxidation of the W in the solution as the potential was scanned positively. The linear sweeps over the entire wafer resulted in different current outputs (figure 5.4.4.1). The current onset potentials for the tungsten oxidation shifted to more positive potentials, indicating the process was inhibited by the presence of carbon. This same trend was observed over the P-W-C based combinations we studied, where the stability particularly of the W-rich region was improved with the carbon content increasing. The Ta based compositions showed a similar response but it was not as evident as the W-C samples.

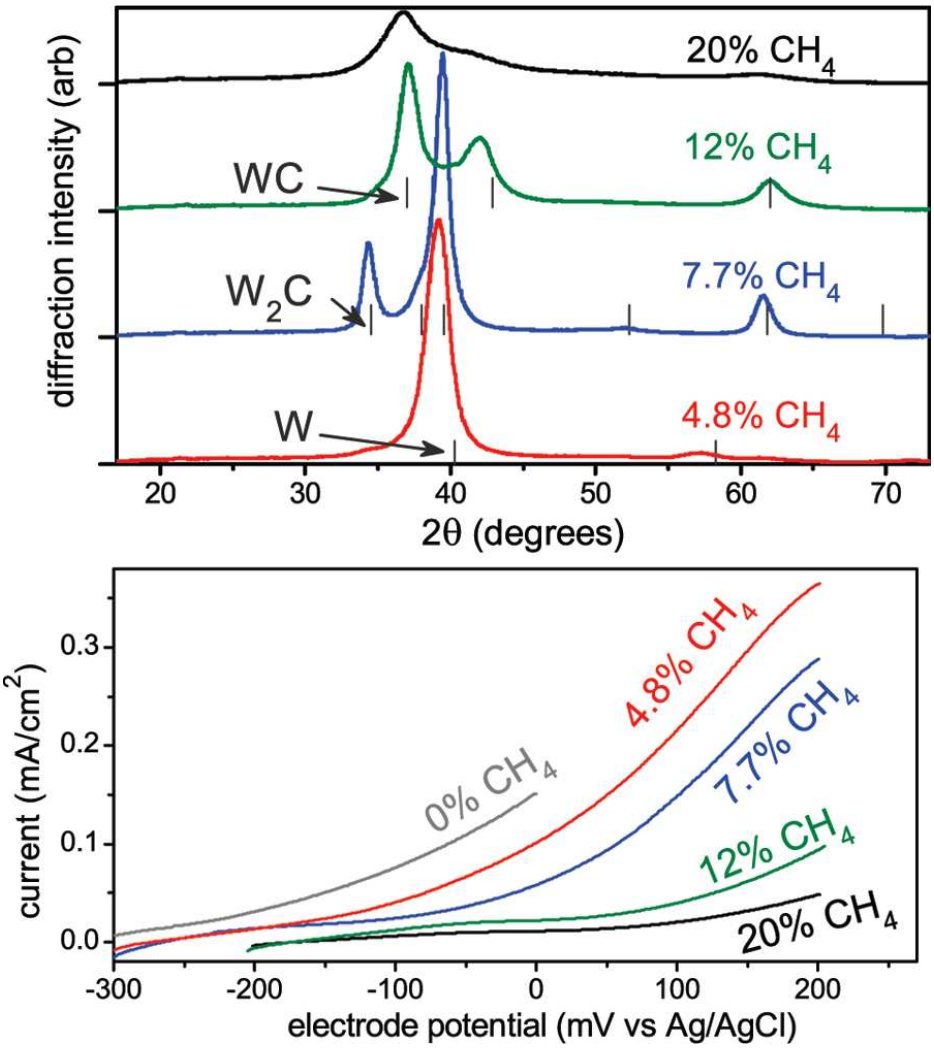

Figure 5.4.4.1: Phase identification and electrochemical oxidation of WC_z films deposited at different concentrations of CH_4 in Ar. The diffraction patterns (top) are overlaid with the peak positions for the corresponding phases, as reported in the respective PDF entries (bcc-W, 04-0806; W_2Cm 35-0776; and c-WC, 20-1316). The thin film oxidation current is shown for each WC_z film and a pure bcc-W film. Each potential sweep proceeded at 5 mV/s, and the shift in corrosion onset potential demonstrated increased stability with increasing *z*.

Simultaneous experiments were performed to screen for catalytic activity for methanol oxidation. In all cases, the addition of carbon decreased the electrocatalytic activity for methanol oxidation; however, for the W films while still decreasing the activity, the stability was improved with the carbon incorporation. A representative sample of the effect of the carbon presence in the composition film is shown in figure 5.4.4.2, Pt-Ta-C. The Pt-Ta alone exhibits an active

composition near the Pt-rich region. This active region was observed as 4.8% and 7.7% CH_4 were introduced into the sputtering chamber with the overall fluorescence onset potentials occurring at higher potentials. When the 12% to 20% CH_4 was introduced into the sputtering chamber, the active region near the Pt-rich region was almost nonexistent over our potential range. Upon phase characterization of the films, interesting phase behavior of these films was noted and the intercolation of the carbon in the P-M-C lattice was described in more detail in the published paper.[47] As far as electrocatalysis, we can conclude that the carbides under our testing parameters decrease the overall activity of metallic films, but in some cases can improve stability.

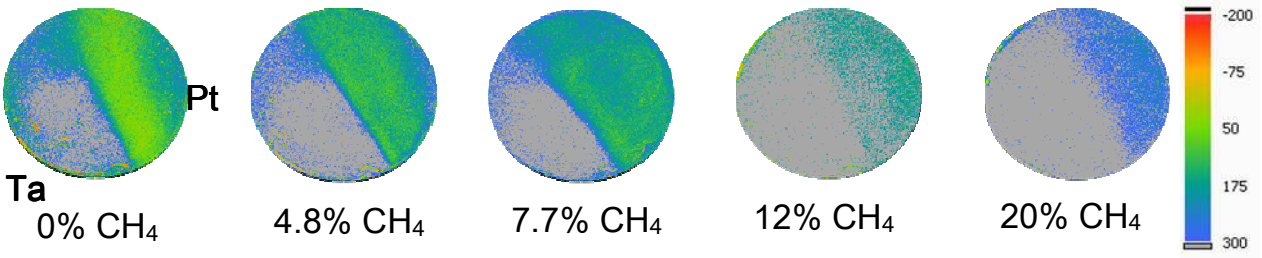

Figure 5.4.4.2: Fluorescence onset potential images for methanol oxidation over Pt-Ta composition spreads sputtered with different amounts of methane that resulted in varying carbon content in the films. The fluorescence in the active area decreased as more carbon was intercolated into the film. The color intensity scale is the fluorescence onset potential vs. Ag/AgCl.

To summarize the interesting phase behavior of these films,[47] little solubility was found between the precious metals and the TaC; while on the other hand, complete solid solubility was observed with the fcc precious metals and c-WC. Similarly, high solubility of Ru in c-WC was demonstrated. Carbon stoichiometries were inferred from measured lattice constants using a model, which was established through DFT calculations. In the ternary carbide alloys, the carbon stoichiometry varied rapidly at a critical W stoichiometry, and it was demonstrated that this behavior was well-modeled by a statistical, bond-counting analysis of the NaCl ternary alloy.

5.5 References

1. Gregoire, J. M.; Tague, M. E.; Cahen, S.; Khan, S.; Abruña, H. D.; DiSalvo, F. J.; van Dover, R. B., Improved Fuel Cell Oxidation Catalysis in Pt1-xTax. *Chemistry of Materials* **2010,** 22, (3), 1080-1087.

2. Long, C. J.; Hattrick-Simpers, J.; Murakami, M.; Srivastava, R. C.; Takeuchi, I.; Karen, V. L.; Li, X., Rapid structural mapping of ternary metallic alloy systems using the combinatorial approach and cluster analysis. *Review of Scientific Instruments* **2007,** 78, (7), 6.

3. Gregoire, J. M. High throughput material science for discovery of energy-related materials. Dissertation, Cornell University, Ithaca, NY, 2010.

4. Borup, R.; Meyers, J.; Pivovar, B.; Kim, Y. S.; Mukundan, R.; Garland, N.; Myers, D.; Wilson, M.; Garzon, F.; Wood, D.; Zelenay, P.; More, K.; Stroh, K.; Zawodzinski, T.; Boncella, J.; McGrath, J. E.; Inaba, M.; Miyatake, K.; Hori, M.; Ota, K.; Ogumi, Z.; Miyata, S.; Nishikata, A.; Siroma, Z.; Uchimoto, Y.; Yasuda, K.; Kimijima, K.-i.; Iwashita, N., Scientific Aspects of Polymer Electrolyte Fuel Cell Durability and Degradation. *Chemical Reviews* **2007,** 107, (10), 3904-3951.

5. Wang, H.; Alden, L. R.; DiSalvo, F. J.; AbrunÌƒa, H. c. D., Methanol Electrooxidation on PtRu Bulk Alloys and Carbon-Supported PtRu Nanoparticle Catalysts: A Quantitative DEMS Study. *Langmuir* **2009,** 25, (13), 7725-7735.

6. Liu, Z.; Hu, J. E.; Wang, Q.; Gaskell, K.; Frenkel, A. I.; Jackson, G. S.; Eichhorn, B., PtMo Alloy and MoOx@Pt Coreâ^'Shell Nanoparticles as Highly CO-Tolerant Electrocatalysts. *Journal of the American Chemical Society* **2009,** 131, (20), 6924-6925.

7. Grgur, B. N.; Zhuang, G.; Markovic, N. M.; Ross, P. N., Electrooxidation of H-2/CO mixtures on a well-characterized Pt75Mo25 alloy surface. *Journal of Physical Chemistry B* **1997,** 101, (20), 3910-3913.

8. Casado-Rivera, E.; Volpe, D. J.; Alden, L.; Lind, C.; Downie, C.; Vazquez-Alvarez, T.; Angelo, A. C. D.; DiSalvo, F. J.; Abruña, H. D., Electrocatalytic Activity of Ordered Intermetallic Phases for Fuel Cell Applications. *Journal of the American Chemical Society* **2004,** 126, (12), 4043-4049.

9. Chen, Z.; Waje, M.; Li, W.; Yan, Y., Supportless Pt and PtPd Nanotubes as Electrocatalysts for Oxygen-Reduction Reactions13. *Angewandte Chemie International Edition* **2007,** 46, (22), 4060-4063.

10. Jeon, M. K.; Cooper, J. S.; McGinn, P. J., Investigation of PtCoCr/C catalysts for methanol electro-oxidation identified by a thin film combinatorial method. *Journal of Power Sources* **2009,** 192, (2), 391-395.

11. Chen, W.; Sun, G.; Liang, Z.; Mao, Q.; Li, H.; Wang, G.; Xin, Q.; Chang, H.; Pak, C.; Seung, D., The stability of a PtRu/C electrocatalyst at anode potentials in a direct methanol fuel cell. *Journal of Power Sources* **2006,** 160, (2), 933-939.

12. Lebedeva, N. P.; Janssen, G. J. M., On the preparation and stability of bimetallic PtMo/C anodes for proton-exchange membrane fuel cells. *Electrochimica Acta* **2005,** 51, (1), 29-40.

13. Blasini, D. R.; Rochefort, D.; Fachini, E.; Alden, L. R.; DiSalvo, F. J.; Cabrera, C. R.; Abruña, H. D., Surface composition of ordered intermetallic compounds PtBi and PtPb. *Surface Science* **2006,** 600, (13), 2670-2680.

14. Xia, D.; Liu, S.; Wang, Z.; Chen, G.; Zhang, L.; Zhang, L.; Hui, S.; Zhang, J., Methanol-tolerant MoN electrocatalyst synthesized through heat treatment of molybdenum tetraphenylporphyrin for four-electron oxygen reduction reaction. *Journal of Power Sources* **2008,** 177, (2), 296-302.

15. Zhong, H.; Zhang, H.; Liu, G.; Liang, Y.; Hu, J.; Yi, B., A novel non-noble electrocatalyst for PEM fuel cell based on molybdenum nitride. *Electrochemistry Communications* **2006,** 8, (5), 707-712.

16. Ei-Himri, A.; Marrero-Lopez, D.; Nunez, P., Pt_2Mo_3N and $PdPtMo_3N$: new interstitial nitrides prepared from freeze-dried precursors. *Journal of Solid State Chemistry* **2004,** 177, (9), 3219-3223.

17. Brady, M. P.; Wrobel, S. K.; Lograsso, T. A.; Payzant, E. A.; Hoelzer, D. T.; Horton, J. A.; Walker, L. R., Synthesis of Ternary Nitrides from Intermetallic Precursors: Modes of Nitridation in Model Cr_3Pt Alloys To Form Cr_3PtN Antiperovskite and Application to Other Systems. *Chemistry of Materials* **2004,** 16, (10), 1984-1990.

18. Wiener, G. W.; Berger, J. A., Structure and magnetic properties of some transition metal nitride. *Journal of metals* **1955,** 7, 360-368.

19. Brady, M. P.; Tortorelli, P. F., Alloy design of intermetallics for protective scale formation and for use as precursors for complex ceramic phase surfaces. *Intermetallics* 12, (7-9), 779-789.

20. Krén, E.; Zsoldos, É.; Barberon, M.; Fruchart, R., Magnetic properties of the Mn_3PtN system. *Solid State Communications* **1971,** 9, (1), 27-31.

21. Gregoire, J. M.; Kostylev, M.; Tague, M. E.; Mutolo, P. F.; van Dover, R. B.; DiSalvo, F. J.; Abruña, H. D., High-Throughput Evaluation of Dealloyed Pt-Zn Composition-Spread Thin Film for Methanol-Oxidation Catalysis. *Journal of The Electrochemical Society* **2009,** 156, (1), B160-B166.

22. Prochaska, M.; Jin, J.; Rochefort, D.; Zhuang, L.; DiSalvo, F. J.; Abruña, H. D.; van Dover, R. B., High throughput screening of electrocatalysts for fuel cell applications. *Review of Scientific Instruments* **2006,** 77, (5), 054104.

23. Gregoire, J. M.; Tague, M. E.; Cahen, S.; Khan, S.; Abruña, H. D.; DiSalvo, F. J.; van Dover, R. B., Improved Fuel Cell Oxidation Catalysis in Pt1−xTax. *Accepted in Chemistry of Materials* **2009**.

24. Cooper, J. S.; McGinn, P. J., Combinatorial screening of fuel cell cathode catalyst compositions. *Applied Surface Science* **2007,** 254, (3), 662-668.

25. Gregoire, J. M.; van Dover, R. B.; Jin, J.; DiSalvo, F. J.; Abruña, H. D., Getter sputtering system for high-throughput fabrication of composition spreads. *Review of Scientific Instruments* **2007,** 78, (7), 072212.

26. Gregoire, J. M.; van Dover, R. B.; Jin, J.; Disalvo, F. J.; Abruña, H. D., Getter sputtering system for high-throughput fabrication of composition spreads. *Review of Scientific Instruments* **2007,** 78, (7), 072212.

27. Gregoire, J. M.; Lobovsky, M. B.; Heinz, M. F.; DiSalvo, F. J., Resputtering phenomena and determination of composition in codeposited films. *Physical Review B* **2007,** 76, (19).

28. Gregoire, J. M.; Kostylev, M.; Tague, M. E.; Mutolo, P. F.; van Dover, R. B.; DiSalvo, F. J.; Abruña, H. D., High-Throughput Evaluation of Dealloyed Pt-Zn Composition-Spread Thin Film for Methanol-Oxidation Catalysis. *Journal of the Electrochemical Society* **2009,** 156, (1), B160-B166.

29. Miura, A.; Wang, H.; Leonard, B. M.; Abruña, H. D.; DiSalvo, F. J., Synthesis of Intermetallic PtZn Nanoparticles by Reaction of Pt Nanoparticles with Zn Vapor and Their Application as Fuel Cell Catalysts. *Chemistry of Materials* **2009,** 21, (13), 2661-2667.

30. Ohring, M., *Materials science of thin films : deposition and structure*. Academic Press: San Diego, CA, 2002.

31. *Powder Diffraction File. JCPDS Internat. Centre Diffract. Data*: 2004.

32. Becue, T.; Manoli, J.-M.; Potvin, C.; Djega-Mariadassou, G.; Delamar, M., Preparation and Characterization of a Novel Class of Catalysts: Ultradispersed Molybdenum Oxynitrides Supported on NaEMT and HEMT Zeolite. *The Journal of Physical Chemistry B* **1997,** 101, (33), 6429-6435.

33. Stamenkovic, V. R.; Mun, B. S.; Mayrhofer, K. J. J.; Ross, P. N.; Markovic, N. M., Effect of Surface Composition on Electronic Structure, Stability, and Electrocatalytic Properties of Pt-Transition Metal Alloys: Pt-Skin versus Pt-Skeleton Surfaces. *Journal of the American Chemical Society* **2006,** 128, (27), 8813-8819.

34. Stamenkovic, V. R.; Fowler, B.; Mun, B. S.; Wang, G. F.; Ross, P. N.; Lucas, C. A.; Markovic, N. M., Improved oxygen reduction activity on Pt3Ni(111) via increased surface site availability. *Science* **2007,** 315, (5811), 493-497.

35. Antolini, E., Composite materials An emerging class of fuel cell catalyst supports. *Applied Catalysis B-Environmental* **2010,** 100, (3-4), 413-426.

36. Zoltowski, P., The Mechanism of the Activation Process of the Tungsten Carbide Electrode. *Electrochimica Acta* **1986,** 31, (1), 103-111.

37. Ham, D. J.; Lee, J. S., Transition Metal Carbides and Nitrides as Electrode Materials for Low Temperature Fuel Cells. *Energies* **2009,** 2, (4), 873-899.

38. Ishihara, A.; Doi, S.; Mitsushima, S.; Ota, K., Tantalum (oxy)nitrides prepared using reactive sputtering for new nonplatinum cathodes of polymer electrolyte fuel cell. *Electrochimica Acta* **2008,** 53, (16), 5442-5450.

39. Nagai, M.; Yoshida, M.; Tominaga, H., Tungsten and nickel tungsten carbides as anode electrocatalysts. *Electrochimica Acta* **2007,** 52, (17), 5430-5436.

40. Yang, X. G.; Wang, C. Y., Nanostructured tungsten carbide catalysts for polymer electrolyte fuel cells. *Applied Physics Letters* **2005,** 86, (22).

41. Yang, R. Z.; Stevens, K.; Bonakdarpour, A.; Dahn, J. R., Dependence of the activity of sputtered Co-C-N oxygen reduction electrocatalysts on heat-treatment temperature. *Journal of the Electrochemical Society* **2007,** 154, (9), B893-B901.

42. McIntyre, D. R.; Vossen, A.; Wilde, J. R.; Burstein, G. T., Electrocatalytic properties of a nickel-tantalum-carbon alloy in an acidic electrolyte. *Journal of Power Sources* **2002,** 108, (1-2), 1-7.

43. Chhina, H.; Campbell, S.; Kesler, O., Thermal and electrochemical stability of tungsten carbide catalyst supports. *Journal of Power Sources* **2007,** 164, (2), 431-440.

44. Jang, J. H.; Kim, J.; Lee, Y. H.; Pak, C.; Kwon, Y. U., Sonochemical synthesis of tungsten carbide-palladium nanocomposites and their electrocatalytic activity for hydrogen oxidation reaction. *Electrochimica Acta* **2009,** 55, (2), 485-490.

45. Hu, F. P.; Cui, G. F.; Wei, Z. D.; Shen, P. K., Improved kinetics of ethanol oxidation on Pd catalysts supported on tungsten carbides/carbon nanotubes. *Electrochemistry Communications* **2008,** 10, (9), 1303-1306.

46. Lu, G. J.; Cooper, J. S.; McGinn, P. J., SECM characterization of Pt-Ru-WC and Pt-Ru-Co ternary thin film combinatorial libraries as anode electrocatalysts for PEMFC. *Journal of Power Sources* **2006,** 161, (1), 106-114.

47. Gregoire, J. M.; Tague, M. E.; Smith, E. H.; Dale, D.; DiSalvo, F. J.; Abruña, H. D.; Hennig, R. G.; van Dover, R. B., Phase Behavior of Pseudobinary Precious Metal-Carbide Systems. *Journal of Physical Chemistry C* **2010,** 114, (49), 21664-21671.

48. Binary Alloy Phase Diagrams. In [Online] Second ed.; Thaddeus B. Massalski, H. O., P.R. Subramanian, Linda Kacprzak, Ed. ASM International: 1996.

49. Gregoire, J. M.; Dale, D.; Kazimirov, A.; DiSalvo, F. J.; van Dover, R. B., High energy x-ray diffraction/x-ray fluorescence spectroscopy for high-throughput analysis of composition spread thin films. *Review of Scientific Instruments* **2009,** 80, (12), 123905.

50. Pourbaix, M., *Atlas of Electrochemical Equilibria in Aqueous Solutions*. National Association of Corrosion Engineers: Houston, TX, 1974.

51. Ohring, M., *Materials Science of Thin Films* 2nd ed.; Academic Press: Boston, 2002.

52. Gregoire, J. M.; Dale, D.; Kazimirov, A.; DiSalvo, F. J.; van Dover, R. B., Cosputtered composition-spread reproducibility established by high-throughput x-ray fluorescence. *Journal of Vacuum Science & Technology A* **2010,** 28, (5), 1279-1280.

CHAPTER 6

Fundamental Studies on Electrochemical Oxidation Processes

This chapter covers the influence of our fluorescent indicator, quinine, on the methanol oxidation process. As the effect was being studied, we discovered a reversible process where H_2 evolution should occur. This sparked a somewhat tangential investigation, such that the reversible reaction was surface H^+ species generated from the methanol oxidation, but it was diffusion limited as it remained at the surface. As we were concerned with the mechanism of the oxidation of the fuels, we decided to pursue other fuels that were initially highly oxidized compared to methanol, ethanol and ethylene glycol, such as formic acid, acetic acid, and acetaldehyde. Preliminary work on whether the oxidation of these proposed intermediates (formic acid, acetic acid) could indicate positive activity for the complete oxidation of methanol and ethanol.

6.1 Quinine Effect on Fuel Oxidation Activity

Since we were screening for catalytic activity with quinine in solution, we thought it best to determine the effect of quinine on the onset potential. A Pt thin film was tested and a linear sweep was collected with and without methanol as well as with and without quinine (figure 6.1.1). We noticed a pre-peak for the methanol oxidation and the overall current was slightly lower than for solutions without quinine. The onset potential also appeared to be at more positive potentials with quinine present (about 80 mV). However, this was somewhat difficult to determine from the CV because of the differences in curvature with the presence and absence of quinine. It was also noted that the pre-peak was not consistently observed in all the samples. There did not appear to be an immediate correlation as to the cause of the pre-peak but it instigated a more thorough investigation of methanol oxidation.

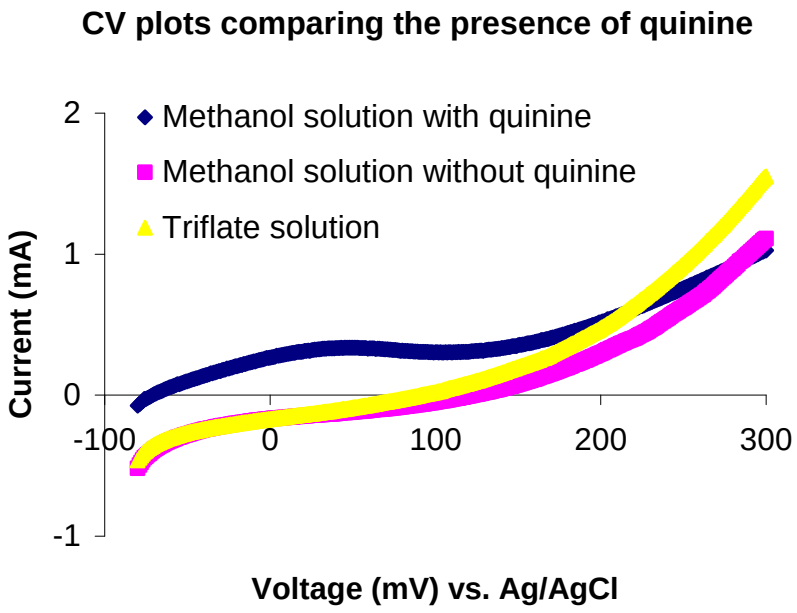

Figure 6.1.1: Methanol oxidation on a Pt thin film (5 M methanol, 0.1 M potassium trifate, and/or 0.5 mM quinine) at 5 mV/s.

A 3-mm diameter Pt slug was encapsulated in glass and polished to expose a flat 3-mm disk of Pt. This experiment was to determine the shift in onset potential with and without quinine on a well-behaved system. The reason the Pt slug was better behaved than the Pt thin film was that it could be mechanically polished followed by electrochemical cleaning, via cycling over the potential range of the solvent. It was not possible to mechanically polish the Pt thin film to ensure that it was clean before performing electrochemical experiments. In this experiment, the electrode was polished as described in the *Experimental Section* and electrochemically cleaned. Figure 6.1.2 depicts the difference for methanol oxidation without quinine, with quinine and with quinine sulfate on the Pt 3-mm diameter electrode. Previously, quinine sulfate was used for the background screening because it had a higher solubility in water than quinine. Later, the quinine sulfate was removed all together and replaced by quinine at a concentration of 0.3 mM, which was an acceptable value even in water without the presence of

an organic solvent, such as methanol or ethanol to promote solubility. In any case, it was readily evident that the currents with and without quinine greatly differed. While the current was diminished by ~3x in the presence of the quinine, our point of interest was the onset potential. The actual onset potential shifts were within about 50 mV which was within the error of our screening process. Thus, we concluded that the onset potentials were not significantly affected by the quinine and validated our screening method. To obtain an accurate current measurement, we employed the minicell or scanning minicell in the absence of quinine. One last feature to note in the CVs was the presence of a reversible redox peak centered around -0.4 V vs. Ag/AgCl. This feature will be discussed in the next section.

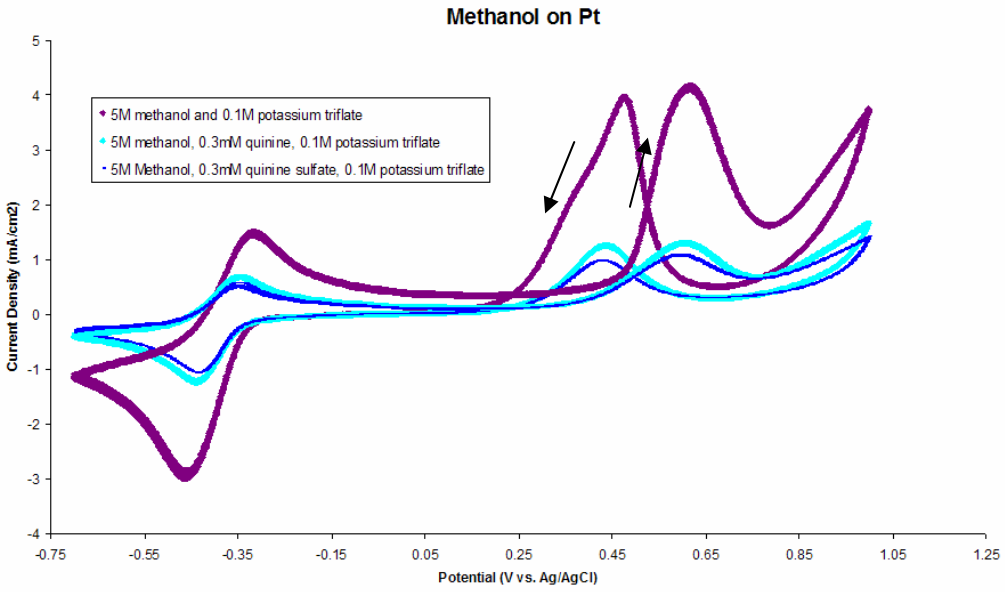

Figure 6.1.2: CVs of a 3-mm Pt electrode to determine the effect of adding quinine to the solution. Scan rate = 100 mV/s. Data suggested that quinine shifts the observed onset to more positive potentials.

6.2 Methanol Oxidation at pH 7

The redox couple found in the methanol oxidation at neutral pH's stimulated the search for the origin of this species. We performed a series of experiments and concluded that the curve arose from protons generated at the surface from methanol oxidation and since no buffer was present to consume the protons, they remained at the surface with the amount of protons generated being diffusion limited by the amount formed upon methanol oxidation. Figure 6.2.1 demonstrated the effect of the Pt electrode in a neutral solution (non-buffered) and with the contribution from bubbling H_2. The bubbled hydrogen shifted the potentials of the Pt to more positive potentials and also exhibited the reversible redox couple from mass-transfer limited H_2 in solution.

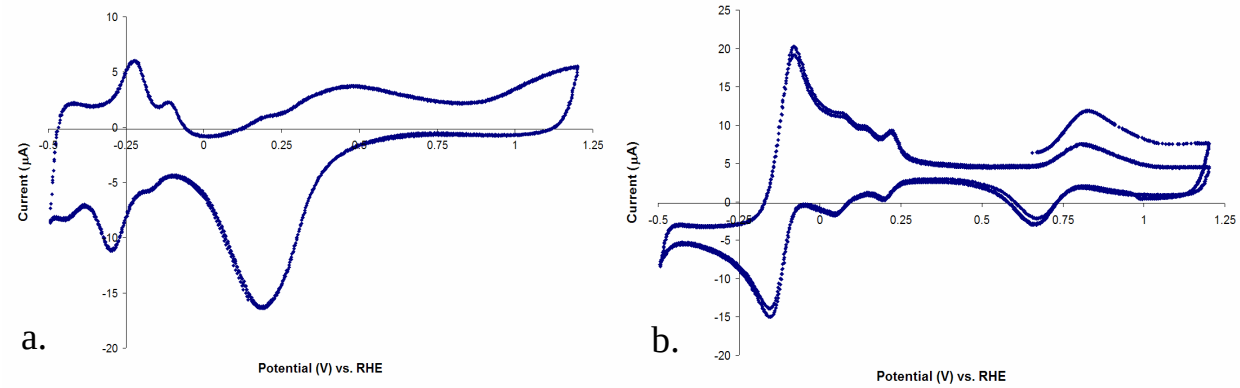

Figure 6.2.1: CVs at 50 mV/s of 0.1 M K_2SO_4 on a 3-mm diameter Pt electrode without H_2 bubbling (a) and with H_2 bubbling for 15 minutes (b).

Furthermore, we suspected that molecular H_2 was not formed in solution and wished to confirm that the increase in the redox peaks coincided with methanol oxidation. Conversely, we would expect the peak heights to diminish when the potential was not cycled to methanol oxidizing potentials, supporting our assertion that the protons for this hydrogen redox couple were directly correlated to the methanol oxidation process (figure 6.2.2).

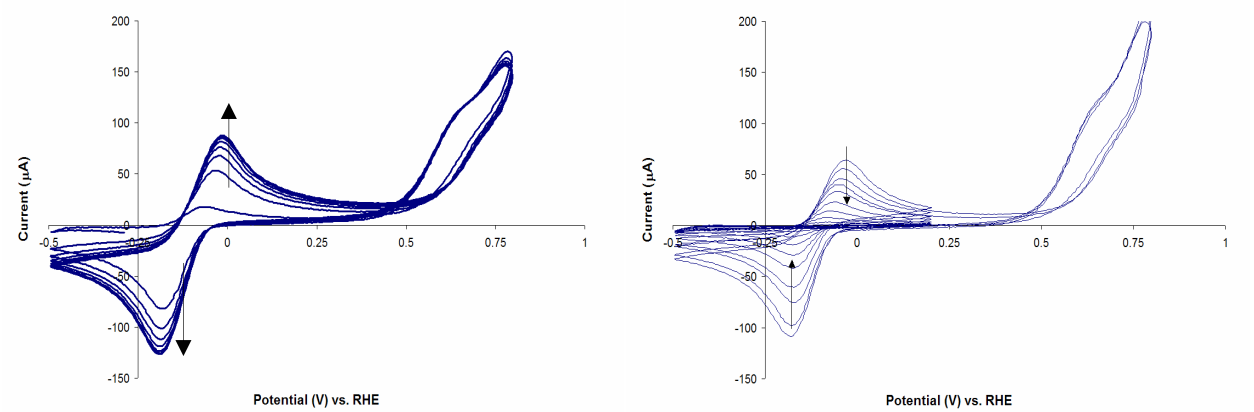

Figure 6.2.2: CVs at 100 mV/s of 1 M methanol, 0.1 M K_2SO_4 on a 3-mm diameter Pt electrode cycled from –0.5 to 0.75V vs. RHE (a) followed by decreasing the range from –0.5V to 0.20V vs. RHE (b).

We concluded that the onset of methanol oxidation changes the local pH on the surface of the electrode and thus shifted the hydrogen evolution. This result was confirmed in the literature by J. Sobkowski, et al.[1] (figure 6.2.3), where the reversible H_2 redox couple was observed upon methanol oxidation.

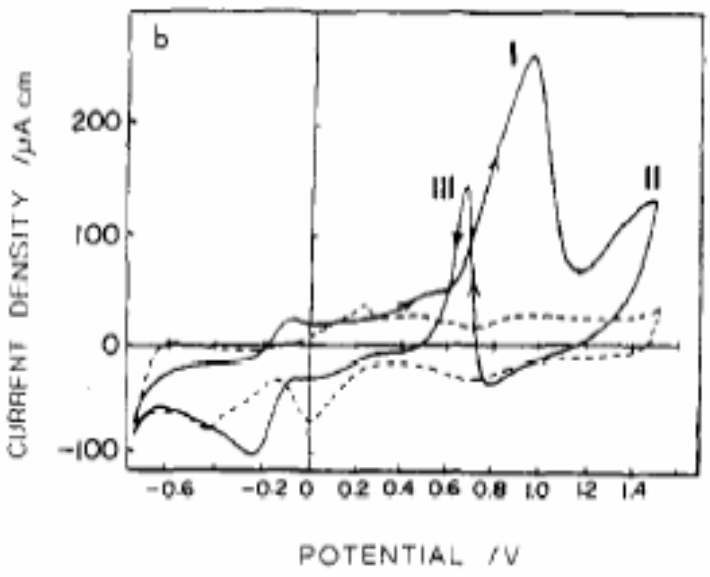

Figure 6.2.3: CVs of 0.5 M Na_2SO_4 + 0.06 M methanol on Pt at 50 mV/s (neutral pH).[1]

6.3 Alternate fuels

As our screening process included a number of different fuels (methanol, ethanol, and ethylene glycol), we found that different compositions result in varying activity for the different fuels. Figure 6.3.1 demonstrated this effect for two representative composition spreads. While $Pt_{92}Sn_8$ and $Pt_{46}Ru_{34}$ showed almost identical onset potentials for methanol oxidation, in the ethanol and ethylene glycol case, the $Pt_{92}Sn_8$ activity was significantly higher relative to that of $Pt_{46}Ru_{34}$, likely indicative of an alternative fuel oxidation pathway. We proposed that acidic species were generated during fuel oxidation and fluorescence screening could be the cause of partial fuel oxidation to intermediate compounds. For instance, acetic acid could be a possible intermediate for ethanol and, in fact, it was. Thus, we became interested in studying more fuels in our screening protocols to better understand the oxidation processes and propose alternative and more attractive pathways by employing other fuels (i.e. formic acid, acetic acid, etc.). As a follow-up on the mechanistic findings, we also intend to use the scanning DEMS set-up.

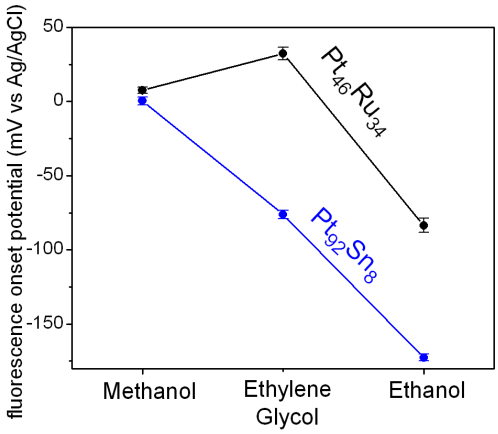

Figure 6.3.1: Fluorescence onset potential plotted versus fuel tested for two thin film catalysts ($Pt_{46}Ru_{34}$ and $Pt_{92}Sn_8$). $Pt_{92}Sn_8$ showed a significant drop in onset potential when tested with different fuels compared to $Pt_{46}Ru_{34}$.

Some intermediates we were interested in were formic acid and formaldehyde, for the case of methanol oxidation; acetic acid and acetaldehyde for the case of ethanol oxidation; and in the case of ethylene glycol, glyoxal and glycol aldehyde. These intermediates were more oxidized than their alcohol counterparts and thus, we proposed that we could study the alcohols and obtain their electrochemical properties. If we identified a catalyst showing good activity for alcohol oxidation, then we could test for the intermediates to better understand whether the mechanism involves these compounds for their complete oxidation to CO_2. Especially in the case of ethanol, we found that the fluorescence occurs at much lower onset potentials than for both methanol and ethylene glycol. We attributed this to the ease of the first proton being removed from the ethanol to form an intermediate rather than the complete conversion to CO_2. Hence, we suspected that the intermediate may be acetic acid and that we were only monitoring the conversion from the ethanol to acetic acid. We used our scanning minicell to test for acetic acid oxidation (and formic acid oxidation for methanol) in acidic pH and found that little to no activity was observed for the few samples we tested (ie. Pt and PtRu). This indicated that if acetic acid was formed as an intermediate, then the mechanism stops there and was not further oxidized. Therefore, we still aim to understand the mechanism by examining these possible intermediates.

6.3.1 Dimethoxymethane

Figure 6.3.1.1: Chemical structure of dimethoxymethane.

Dimethoxymethane seemed an attractive fuel to study because of the absence of C-C bonds and our goal was to determine whether the absence of C-C bonds aided the complete oxidation of the fuel to CO_2. Other groups investigated dimethoxymethane as a possible fuel for fuel cells.[2-4] Some work had been done for determining the reaction mechanism and below are two suggested processes[5]:

Without accumulation of products:

$(CH_3O)CH_2 + 2H_2O \rightarrow 2CH_3OH + 4H^+ + CO_2 + 4e^-$

$CH_3OH + 2H_2O \rightarrow 6H^+ + CO_2 + 6e^-$

With accumulation of products:

$(CH_3O)CH_2 + 2H_2O \rightarrow 2CH_3OH + HCHO$

$CH_3OH + 2H_2O \rightarrow 6H^+ + CO_2 + 6e^-$

$HCHO + H_2O \rightarrow 4H^+ + CO_2 + 4e^-$

The reaction mechanism suggested that the intermediates were methanol and formaldehyde, but we desired to understand if it was still possible for these intermediates to be completely oxidized in this system. In fact, dimethoxymethane proved to be more complicated than we initially thought. One of the complicating issues was that it hydrolyzed in acid and, hence, it was not stable even over the course of the experiment. Figure 6.3.1.2 demonstrated the effect of the hydrolysis of dimethoxymethane in the acid solution. Immediately after the solution was made, the oxidation processes masked the Pt features typically in a cleaning CV of Pt. The approximate onset potential for the positive sweep was at 0.5 V vs. Ag/AgCl and was consistent after sitting for 3 days. The biggest difference was that the currents were greatly diminished and the Pt features were evident, indicating a much lower coverage of the dimethoxymethane on the surface. Furthermore, the hydrolysis products did not seem they were available to be oxidized.

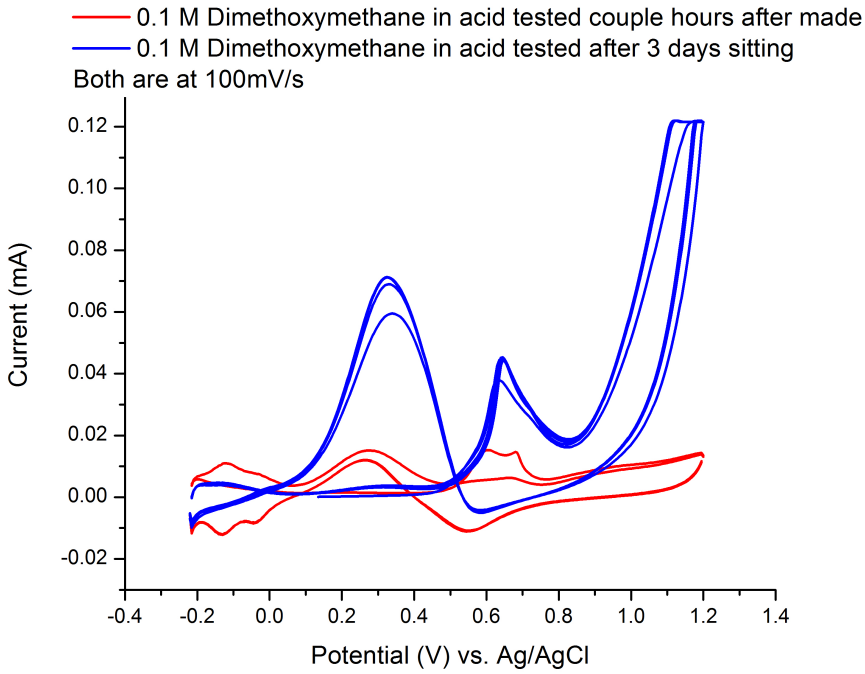

Figure 6.3.1.2: CVs of 0.1 M dimethoxymethane in 0.1 M H_2SO_4 to monitor the hydrolysis over time of the solution. Reference electrode = Ag/AgCl, counter electrode = Pt, and working electrode = 3 mm diameter Pt electrode, 100 mV/s.

With the instability of dimethoxymethane in acid, we decided to test it in neutral solutions with the premise of possibly including it in our fluorescence setup. Figure 6.3.1.3 presented the change in scan rates significantly changed the CV's appearance. The slower scan rates allowed for more of the dimethoxymethane to be oxidized especially on the reverse sweep. The reversible hydrogen redox peaks were similarly observed as we usually saw in the non-buffered neutral solutions. The difference in the scan rates also indicated the oxidation was kinetically slow such that on the reverse sweep, no oxidation current was observed, rather the Pt oxide reduction peak dominated. We compared the CVs in the beginning of the experiment to the end at the same scan rate and could observe growth in the hydrogen adsorption peaks and the hydrogen redox peaks. This indicated that the proton concentration increased, as expected with the oxidation of the fuel. Similarly, on the reverse sweep, an increase in a formed intermediate

was present at the end and not at the beginning of the experiment. These results had proved interesting and a follow up on the mechanistic process was performed by Eric Rus using DEMS.[6]

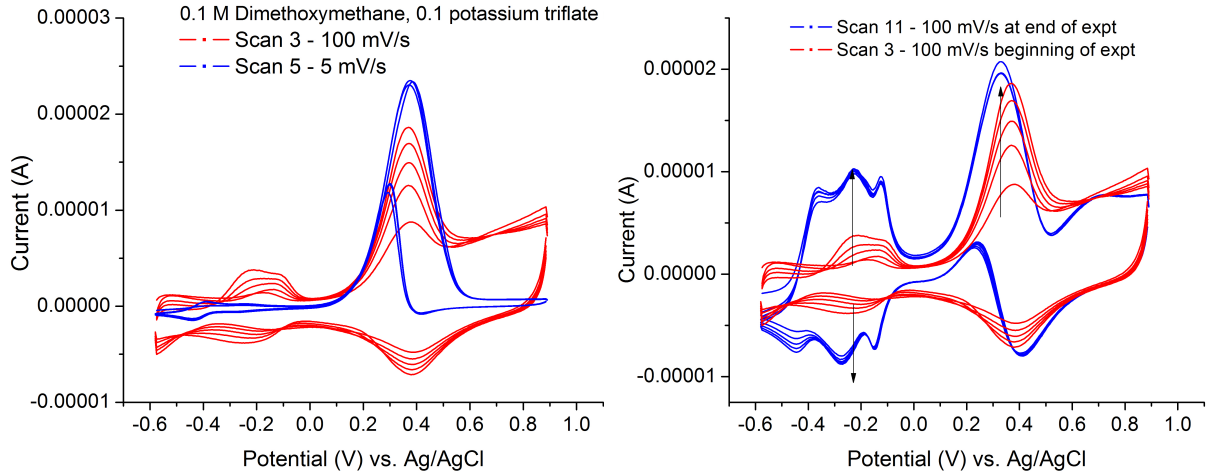

Figure 6.3.1.3: CVs of 0.1 M dimethoxymethane, 0.1 M potassium triflate at two scan rates: 5 and 100 mV/s (Left); before and after the experiment (Right).

Because Pt-Ru is a good catalyst for methanol oxidation, a composition spread was tested in the fluorescence assay with a dimethoxymethane solution as a proof of concept experiment. Given the very nature of the dimethoxymethane and its poor shelf life, the compound would not be able to be used for high-throughput screening because a fresh solution that had purified dimethoxymethane would have to be made up every time. Even so, we desired to test the effect in the fluorescence cell for comparison.

The currents from the films are shown in figure 6.3.1.4 and they were consistent between linear sweeps and after the films were pretreated in the pH 2 solution. The currents, when compared to methanol oxidation, were significantly less and because of the low current, no fluorescence was observed. Thus, with the instability issue and the complications of the mechanism, we decided not to use this fuel to screen fluorescently.

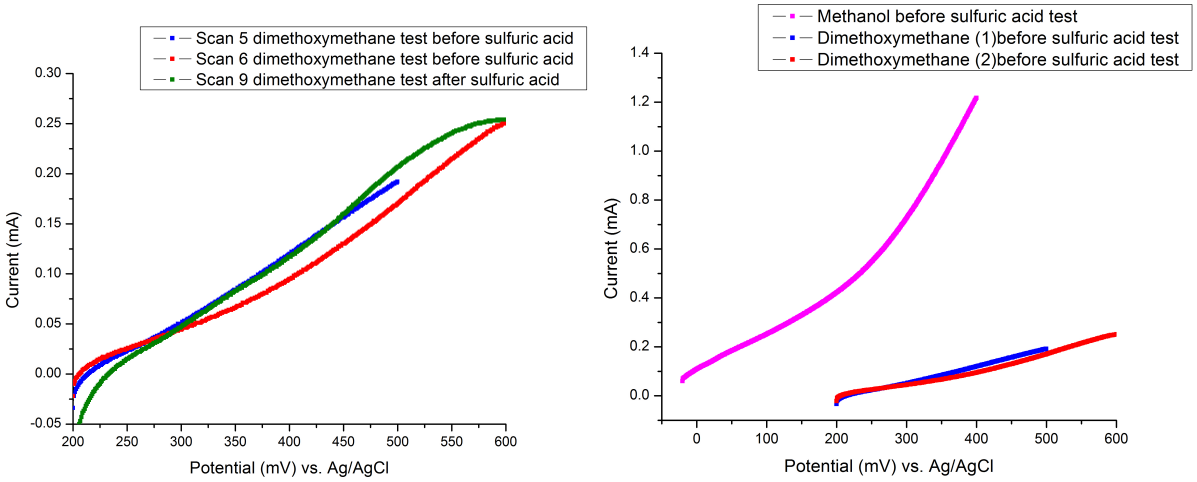

Figure 6.3.1.4: Currents from a linear positive sweep of the dimethoxymethane in solution on a Pt-Ru composition spread in the electrochemical fluorescence cell with quinine and methanol were obtained. "Before sulfuric acid" refers to the pretreatment process in pH 2 H_2SO_4 solution. The plot on the right compares the currents for methanol (magenta) and dimethoxymethane (red and blue).

6.4 References

1. Sobkowski, J.; Franaszczuk, K.; Dobrowolska, K., Effect of Anions and pH on the Adsorption and Oxidation of Methanol on a Platinum Electrode. *Journal of Electroanalytical Chemistry* **1992,** 330, (1-2), 529-540.

2. Zhou, Z. Y.; Chen, D. J.; Li, H.; Wang, Q.; Sun, S. G., Electrooxidation of Dimethoxymethane on a Platinum Electrode in Acidic Solutions Studied by in Situ FTIR Spectroscopy. *Journal of Physical Chemistry C* **2008,** 112, (48), 19012-19017.

3. Prakash, G. K. S.; Smart, M. C.; Olah, G. A.; Narayanan, S. R.; Chun, W.; Surampudi, S.; Halpert, G., Performance of dimethoxymethane and trimethoxymethane in liquid-feed direct oxidation fuel cells. *Journal of Power Sources* **2007,** 173, 102-109.

4. Chetty, R.; Scott, K., Dimethoxymethane and trimethoxymethane as alternative fuels for fuel cells. *Journal of Power Sources* **2007,** 173, 166-171.

5. Kerangueven, G.; Sibert, E.; Hahn, F.; Leger, J. M., Dimethoxymethane (DMM) electrooxidation on polycrystalline platinum electrode in acid media. *Journal of Electroanalytical Chemistry* **2008,** 622, (2), 165-172.

6. Rus, E. D.; Wang, H.; Wang, D.; Abruña, H. D., A Mechanistic Differential Electrochemical Mass Spectrometry (DEMS) and in situ Fourier Transform Infrared Investigation of Dimethoxymethane Electro-Oxidation at Platinum. *The Journal of Physical Chemistry C* **2011,** 115, (27), 13293-13302.

CHAPTER 7

Combinatorial Screening for Fuel Cell Cathode Catalysts

7.1 Introduction

As described earlier, our screening methodology depends on a pH sensitive fluorescent indicator, quinine.[1-3] Quinine fluoresces as the local pH decreases below 5 and upon oxidation of a fuel in neutral solutions, protons are generated, decreasing the pH and causing localized blue fluorescence. Because this process can show localized active areas, it has proven to be a valuable method for screening many compositions and phases simultaneously. We wish to compile a database of pH sensitive fluorescent indicators for possible uses in different pH ranges and for the oxygen reduction reaction (ORR). Furthermore, upon preliminary screening we have identified fluorescent indicators for oxygen reduction screening. This section consists of the compilation and findings from the indicator search, promising oxygen reduction indicators, and proposed applications.

7.2 Compiling database

With the assistance of Miguel Caban, an REU student from the University of Puerto Rico, a database of pH sensitive fluorescent indicators was compiled during the summer of 2007.[4, 5] As our methodologies were focused on fluorescence, many resources were consulted to gather the list of 87 indicators and they were subsequently organized into an excel spreadsheet according to pH range of fluorescence (whether acid, neutral, or basic) and type of reaction the indicator would be best suited for, ie. cathodic or anodic reactions. See table 7.2.1 for a

complete list of the acidic fluorescent indicators, and the indicators in the list that were commercially available show the cost and company name found in 2007.

Among the acid indicators we selected a number of candidates based on their commercial availability, color change, toxicity to the environment, and health rating. Some of the possible candidates were: Eosin, anthranilic acid, chromotropic acid, 5-aminosalicylic acid, scopoletin and morin. Out of these, we chose indicators that would have a bright color change for a few selected pH ranges. For instance, we chose anthranilic acid because it changed from non-fluorescence to light blue in a pH range from 1.5 to 3. Morin changed from non-fluorescence to green from pH 3.1 to pH 4.4. Another reason these two were chosen was due to the fact that they were noted to have a second fluorescence color change and we thought it could be used for other applications. In the case of the anode in acid, we tested 4-methylumbelliferone (green pH 0 to weak blue pH 2).

The neutral pH indicators for the cathodic reaction were few and they included: umbelliferone and luminol. Umbelliferone and luminol had a very similar color change and pH range. We chose umbelliferone because it was the less expensive out of the two.

The basic conditions provided many options as well: beta-methylumbelliferone, salicylaldehyde thiosemicarbazone, acridine orange, and naphthol AS. These indicators were not tested in this screening process, although from our requirements had the possibility of being studied in the future. The anode case was of greater interest because we had a fluorescent indicator, quinine, for lower pH's and desired to have the ability to screen for activity in basic solutions. The indicators we were interested in were: quinine, anthranilic acid, morin. To note these were interesting choices because they could also be used in acidic pH and have a second pK_a at higher pH's for this to be possible.

For the cathode in acid pH's, we studied: anthranilic acid (non-fluorescence pH 1.5 to light blue pH 3), fluorescein (pink/green pH 4 to green pH 6), and morin (non-fluorescence pH 3.1 to green pH 4.4). For the cathode in neutral conditions, we explored umbelliferone (non-fluorescence pH 6.5 to blue pH 8). Quinine (weak violet pH 9.5 to non-fluorescence pH 10.0) and anthranilic acid (dark blue pH 12.5 to non-fluorescence pH 14) were investigated for the anode in basic solutions. In an attempt to screen for electrocatalysts under fuel cell conditions (low pH), 4-methylumbelliferone was tested for the anode in pH 0 to 2 solutions.

Table 7.2.1: Fluorescent indicators that fluoresce or change fluorescence below pH 6. The indicators were classified according to their color change and for the type of reaction the change could be used for, i.e. anodic or cathodic reactions. Indicators that constantly fluoresce but change color or tonality upon pH change were also noted, but were not likely to be selected for the primary fluorescent indicators for monitoring oxidation or reduction.

Acidic Conditions

Indicators that start with no fluorescence (for Cathode reaction)

No.	Name	Color change	pH range	Indicator solution	Wavelength (λ)	Hazard	Price
3	Eosin(tetrabromo fluorenscein)	non-fl. - green	0-3.0	1% aqueous solution of sodium salt	λ_{max} 524 nm	Irritant	$15.00 for 10g(S.-A.)
7	Anthranilic acid	non-fl. - light blue light blue - dark blue dark blue - non.fl.	1.5-3.0 4.5-6.0 12.5-14	0.1% solution in 50% ethanol	λmax 337 nm	Irritant	$17.00 for 100g(S.-A.)
15	Salicylic acid	non-fl. - dark blue	2.5-4.0	0.5% aqueous solution of sodium salt	λex= 315 nm λem= 405 nm	Harmful	$20.70 for 100g(S.-A.)
17	Erythrosin B (tetraiodo fluorescein)	non-fl. - light green	2.5-4.0	0.2% solution of sodium salt in destilled water	λmax 533 nm	Harmful	$26.40 for 5g(S.-A.)
18	2-Naphthylamine	non-fl. - violet	2.8-4.4	0.5% solution in ethanol	λex 370 nm	Toxic for environment	$37.90 500mg(S.-A.)
19	Magdala red	non-fl. - purple	3.0-4.0		λex 524nm λem 600nm	Harmful	
22	Chromotropic acid	non-fl. - light blue	3.1-4.4	5% aqueous solution	λex 347nm	Irritant	$32.40 for 10g(S.-A.)
24	1-Naphthylamine	non-fl. - blue	3.4-4.8	0.5% solution in ethanol		Harmful for the environment	$44.00 for 26g(S-.A.)
25	5-Aminosalicylic acid	non fl. - light green	3.1-4.4	fresh 0.2% solution in ethanol		Irritant	$12.80 for 5g(S.-A.)
27	o-Methoxybenzaldehyde (o-Anisaldehyde)	non fl. - green	3.1-4.4	0.2% solution in ethanol		Irritant	not available
29	o-Phenylenediamine	non-fl - orange/yellow	3.1-4.4	0.2% solution in 70% ethanol		Toxic for the environment	$93.00 for 50g(S.-A.)
30	Morin (2',4',3,5,7-penta hydroxyflavone)	non fl. - green green - yellow/green	3.1-4.4 8-9.8	0.2% solution in destilled water		Irritant	$15.10 for 2g(S.-A.)
35	Beta-Methylesculetin (Scopoletin)	non fl. - blue blue - light green	4.0-6.2 9.0-10.0	1% solution in ethanol	λex 360 nm	Irritant	$58.00 for 50mg(S.-A.)

Acidic Conditions (Cont.)

Indicators that end with no fluorescence (for Anode reaction)

No.	Name	Color change	pH range	Indicator solution	Wavelength (λ)	Hazard	Price
28	o-Phenylenediamine	green - non fl.	3.1-4.4	0.2% solution in 70% ethanol		Toxic for the environment	$93.00 100g(S.-A.)
37	Beta-Naphthoquinoline	blue - non-fl.	4.4-6.3	0.05% solution in 50% ethanol	Rare	Rare	$55.00 (S.-A.) Rare

Indicators that change to the next color

No.	Name	Color change	pH range	Indicator solution	Wavelength (λ)	Hazard	Price
	4-methylimbelliferone	green-weak blue	0 - 2.0	soluble in water and methanol	λex 365 nm; λem 445 nm on methanol	Irritant	$40.40 for 100g(S.-A.)
21	2-Hydroxy-3-naphthoic acid	blue - green	3.0-6.8	0.1% solution of sodium salt in distilled water		Harmful	$15.50 for 5g(S.-A.)
26	Quinine	blue - weak violet weak violet - non fl.	3.0-5.0 9.5-10.0	0.1% solution in ethanol	λ_{ex} 347 nm λ_{em} 448 nm (in 0.5 M sulfuric acid)	Harmful	$47.90 for 5g(S.-A.)
	Congo Red	Blue - Red	3.0 - 5.2		Abs Max. 611 nm	Toxic	$26.20 for 100g(S.-A.)

Acidic Conditions (Cont.)

Indicators that change to the next color (cont.)

No.	Name	Color change	pH range	Indicator solution	Wavelength (λ)	Hazard	Price
	Lacmoid	Red - Blue Violet	4.4 - 6.4	Soluble in methanol (1 mg/ ml-opaque, dark blue soln), ethanol, amyl alcohol, glacil acetic acid, acetone, phenol; sparingly soluble in water and ether; insoluble in chloroform, benezene, petroleum ether	Absorption Max. 497nm (in water and 1 mL of a sodium salt)	Irritant	$33.50 for 10g(S.-A.)
36	Quininic acid	yellow - blue	4.0-5.0	saturated aqueous solution	not found	not found	not found
38	Resorufin (7-oxyphenoxazone)	yellow - orange	4.4-6.4	only weak fluorescence	λ_{max} 573 nm	Irritant	$31.50 for 1g(S.-A.)
39	Acridine	green - violet	5.2-6.6	0.1% solution in ethanol	λ_{max} 392 nm	Harmful	$26.20 for 5g(S.-A.)

Indicators that change in tonality

No.	Name	Color change	pH range	Indicator solution	Wavelength (λ)	Hazard	Price
6	Esculin	weak blue - strong blue	1.5-2.0				$26.20 for 5G(S.-A.)
32	Fluorescein	pink/green - green	4.0-4.5/6.0	1% aqueous solution of sodium salt in distilled water	470 nm		
41	5,7-Dihydroxy-4-methyl coumarin	light blue - dark blue	5.5-5.8			Irritant	$81.70 for 1G(S.-A.)

Table 7.2.2: Fluorescent indicators that changed in the neutral pH region. All changed from no fluorescence to fluorescence upon an increase in pH and were likely candidates for oxygen reduction.

Neutral conditions

Indicators that start with no fluorescent (for Cathode reaction)

No.	Name	Color change	pH range	Indicator solution	Wavelength	Hazard	Price
43	1,4-Dihydroxybenzene disulphonic acid	non-fl. - light blue	6.0-7.0	0.1% solution of potassium salt in distilled water		Harmful for the environment	$15.60 for 100g(S.-A.)
44	Luminol	non-fl. - blue	6.0-7.0			Irritant	$20.00 for 2.5g(S.-A.)
47	1-Naphthol-5-sulphonic acid (Cleves acid)	non-fl. - green	6.5-7.5	aqueous solution of sodium salt	Rare	Rare	$50 RARE
48	Umbelliferone	non-fl. - blue	6.5-8.0		λ_{ex} 325 nm; λ_{em} 452 nm (in 0.1 M citrate pH 3.0)	Irritant	$20.60 for 10g(S.-A.)

Table 7.2.3: Indicators that fluoresced above pH 7. The classifications were based on whether the indicator would be a possible candidate for anode or cathode screening. Indicators that changed in fluorescence color and tonality were given lower priority because the change would not be as evident as beginning with no fluorescence.

Basic conditions							
Indicators that start with no fluorescent (for Cathode reaction)							
No.	**Name**	**Color change**	**pH range**	**Indicator solution**	**Wavelength**	**Hazard**	**Price**
52	Coumaric acid	non-fl. - green	7.2-9.0	1% solution in ethanol		Harmful	$26.20 for 50g(S.-A.)
53	Beta-methylumbelliferone	non-fl. - blue	>7.0	0.3% solution in 50% ethanol	λex 365 nm; λem 445 nm on methanol	Irritant	$40.40 for 100g(S.-A.)
59	Salicylaldehyde thiosemicarbazone	non-fl. - blue/green	8.4	0.1% solution in ethanol			$18.00 for 1g(S.-A.)
61	Naphthol AS	non fl. - yellow/green	8.2-10.3	aqueous solution of sodium salt	λmax 394 nm	Irritant, Toxic for the environment	$13.60 for 100g(S.-A.)
62	2-Naphthol	non-fl. - blue	8.5-9.5	aqueous solution of sodium salt	λex 281 nm; λem 419 nm 0.1 M NaOH	Harmful and Dangerous for the environment	$22.50 for 100g(S.-A.)
63	Acridine Orange	non fl. - yellow/green	8.4-10.4	0.1% solution in ethanol	λmax 489 nm		$37.60 for 10g(S.-A.)

Basic conditions (Cont.)

Indicators that ends with no fluorescent (for Anode reaction)

No.	Name	Color change	pH range	Indicator solution	Wavelength	Hazard	Price
26	Quinine	blue - weak violet weak violet - non fl.	3.0-5.0 9.5-10.0	0.1% solution in ethanol	λ_{ex} 347 nm λ_{em} 448 nm (in 0.5 M sulfuric	Harmful	$47.90 for 5g(S.-A.)
7	Anthranilic acid	non-fl. - light blue light blue - dark blue dark blue - non.fl.	1.5-3.0 4.5-6.0 12.5-14	0.1% solution in 50% ethanol	λmax 337 nm	Irritant	$17.00 for 100g(S.-A.)

Indicators that changes to the next color

No.	Name	Color change	pH range	Indicator solution	Wavelength	Hazard	Price
54	Harmine	blue - yellow	7.2-8.9				$26.80 250mg(S.A.)

Indicators that change in tonality

No.	Name	Color change	pH range	Indicator solution	Wavelength	Hazard	Price
30	Morin (2',4',3,5,7-penta hydroxyflavone)	non fl. - green green - yellow/green	3.1-4.4 8-9.8	0.2% solution in destilled water		Irritant	$15.10 for 2g(S.-A.)

7.3 The Cathode: Oxygen Reduction Reaction

We wished to expand our fluorescence screening to the oxygen reduction reaction (ORR), denoted below, in which protons were consumed and the pH then increased:

$$O_2 + 4\ H^+ + 4\ e^- \rightarrow 2\ H_2O \qquad E_0 = 1.229\ V$$

Utilizing fluorescence for the ORR was not a new concept. In fact, Mallouk, et al. used a fluorescent indicator, Phloxine B, at low pH (pH = 2.7) for studying ORR and found that $Pt_{4.5}Ru_4Ir_{0.5}$ was a superior catalyst compared to PtIr.[6] Woo, et al. used fluorescein sodium salt (pH = 4) to identify promising catalysts and suggest that PtBi, PtCu, PtSe, PtTe, and PtIr demonstrate better activity than Pt.[7] In our case, we focused on indicators that exhibited no fluorescence in neutral pH but exhibited fluorescence at a higher pH. We avoided looking at indicators that changed at pH >10 and pH <2 because at these pH's the change in the concentration of protons was too large to be viable. The three indicators we explored were: fluorescein, morin, and umbelliferone.

Quantitative testing was performed on promising candidates to determine solubility, pH range, and fluorescence change. Aqueous solutions of 5 mM fluorescent indicator and 0.1 M potassium triflate (supporting electrolyte) were made for each indicator and the pH was changed by adding 0.1 M sodium hydroxide (NaOH) or 0.1 M sulfuric acid (H_2SO_4). A pH meter was used to monitor the pH of the solution and a hand-held UV lamp (λ = 336 nm or 254 nm) was used to monitor the excitation of the fluorescence.

Electrochemical experiments were performed on the promising indicators that showed solubility and fluorescence change over the appropriate range. The three electrode electrochemical cell as described in *Section 2.1 Experimental section* with a Ag/AgCl reference electrode was employed.

7.3.1 Fluorescein

The fluorescent indicator, fluorescein, had been used in a few groups as an oxygen reduction fluorescent indicator.[7, 8] Fluorescein was noted in the literature[5] to change from green to pink/green over the pH range of 4.0 to 4.5. Our qualitative testing revealed the change in fluorescence is actually from a green to a more intense green over the pH range indicated. We performed oxygen reduction on a Pt electrode and observed that no notable fluorescence change could be seen on the electrode surface (figure 7.3.1.1), even though other groups used fluorescein for screening O_2 reduction and were able to isolate active areas. However, our aim was to find an indicator that made it easier to view by eye.

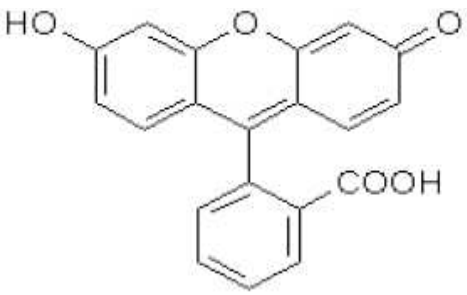

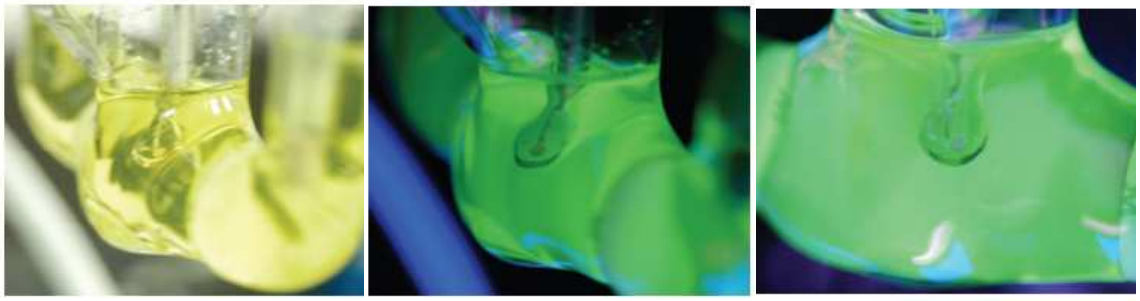

Figure 7.3.1.1: Fluorescein molecular structure; 0.5 mM fluorescein, 0.1 M potassium triflate solution, bubbled for 10 minutes with O_2 before electrochemically reducing to H_2O in ambient light (left), under UV light before O_2 reduction (middle) and after O_2 reduction (right).

7.3.2 Anthranilic acid

Anthranilic acid showed promise as it could be a versatile indicator because of the three different pK_a values and corresponding color changes. The first pH range was listed as going from pH 1.5 with no fluorescence to 3.0 light blue fluorescence and would be useful for oxygen reduction in acidic media. The two other fluorescence pH ranges could be substitutes for the quinine fluorescent indicator (pH 4.5 (light blue) to 6.0 (dark blue)) or alkaline anode indicator (pH 12.5 (dark blue) to 14.0 (no fluorescence) – figure 7.3.2.1). The mid-pH range for this indicator was not explored in detail due to the similarity to quinine. However, it was explored for possible alkaline applications (discussed in a later section). The oxygen reduction at a Pt electrode was performed with this indicator in solution but no fluorescence change was observed (figure 7.3.2.2). The concentration of protons at this pH range was too large for the oxygen reduction process to change it measurably to give a detectable change.

Figure 7.3.2.1: Chemical structure of Anthranilic acid. 0.5 mM anthranilic acid, 0.1 M potassium triflate under UV light at pH 4 (left), pH 5 (middle), pH 7 (right).

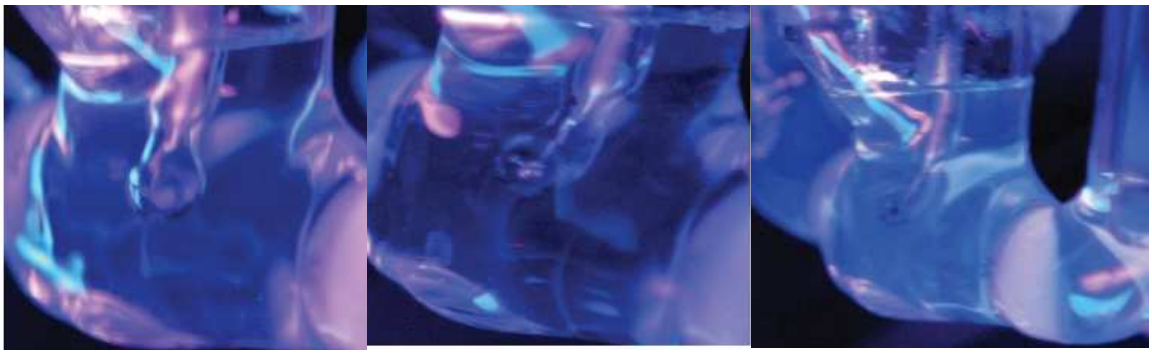

Figure 7.3.2.2: Electrochemical cell with Antranilic acid under UV light before the O_2 reduction (left), immediately after the reaction (middle), pH 7 (right). The fluorescence that seemed to appear at the electrode was, in fact, from the reflection of the UV light on the glassware.

7.3.3 Morin

Morin was also another possible candidate as a fluorescent indicator for screening for fuel cell catalysts. From the Handbook of indicators[5], morin had two pH ranges: pH 3.1 (nonfluorescent) to 4.4 (green) and pH 8.0 (green) to 9.8 (yellow/green). When the qualitative tests were performed on morin, the first pH range was not visible and by pH 5 a faint green color was observed. As the pH was increased, the green changed to a yellow/green (figure 7.3.3.1). It was also found that morin was partially soluble in water.

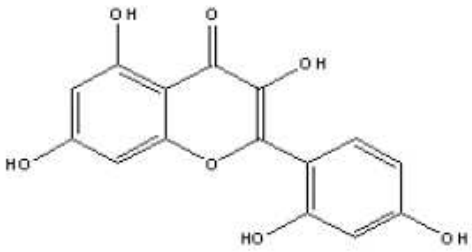

Figure 7.3.3.1: Chemical structure of morin. 0.5 mM morin, 0.1 M potassium triflate under UV light at pH 4 (left), 6 (middle), 9 (right).

Oxygen reduction was performed with the 0.5 mM morin, 0.1 M potassium triflate solution at pH 6 and upon reduction for 2 minutes, yellow/green fluorescence could be observed diffusing from the electrode surface (figure 7.3.3.2). Because a significant visual fluorescence change could be observed, morin was a great candidate for screening for oxygen reduction catalysts. The partial solubility in water could be somewhat of a concern, especially since it could not contain organic solvents to increase solubility for applications to the oxygen reduction reaction.

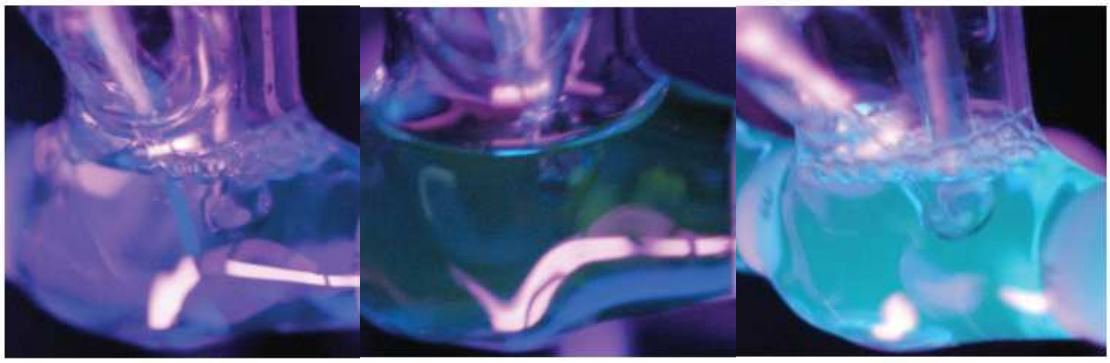

Figure 7.3.3.2: Electrochemical cell under UV light before the O_2 reduction (left), immediately after the reaction (middle), pH 6 (right) to see if fluorescence could be seen at the higher pH change.

7.3.4 Umbelliferone

The last fluorescent indicator we studied in detail was umbelliferone. The attractive aspect of this indicator was that the range of the pH where the fluorescence changed was near neutral pH, making it easier to detect small changes in pH. According to the *Indicators* handbook,[5] the pH change would be observed from 6.5 to 8.0, going from non-fluorescence to blue. Upon qualitative examination in a pH 5 solution (5 mM umbelliferone), the solution exhibited a strong blue fluorescence under UV light and with the change to basic pH, the color changed to an even more intense very bright blue (figure 7.3.4.1).

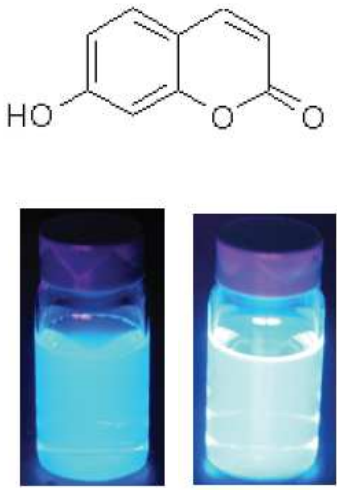

Figure 7.3.4.1: Chemical structure of umbelliferone (also known as 7-hydroxycoumarin). 0.5 mM umbelliferone, 0.1 M potassium triflate under UV light at pH 5 (left) and pH 8 (right).

The unique quality of this indicator was evident when we performed the O_2 reduction at a Pt electrode. Because the indicator changed fluorescent color near neutral pH, the small changes in pH were readily evident and are shown in figure 7.3.4.2. The pictures demonstrated the diffusion of the basic solution away from the electrode surface and the intense color enabled the local change in pH to be observed even amidst the blue background fluorescence. With this striking difference, we decided to pursue the use of this fluorescent indicator further.

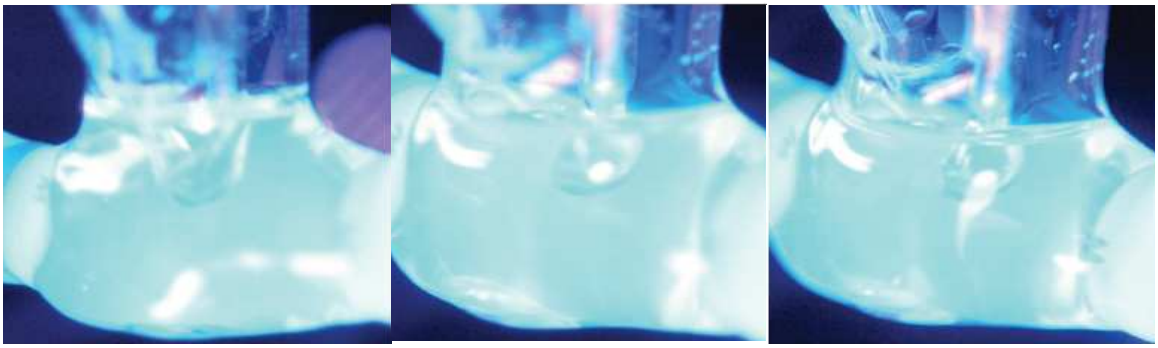

Figure 7.3.4.2: Electrochemical cell containing 5 mM umbelliferone under UV light before the O_2 reduction (left), immediately after the reaction (middle), a short period after the reaction (right). The bright blue fluorescence, high pH solution, diffuses away from the electrode into the solution.

7.4 Oxygen Reduction Screening Preliminary Results

With umbelliferone showing the most significant visual fluorescence change and the ability to change near neutral pH, we decided to test this in the fluorescence electrochemical cell. As a proof of concept and to ensure we could differentiate the fluorescence signal from the background, a 1-cm^2 Pt square was sputtered onto a Si wafer that was Ta coated (figure 7.4.1). The Ta coating provided a conductive surface from the Pt square to the edge of the wafer and once the Ta was exposed to air, it oxidized, forming a non-reactive surface to oxygen reduction.

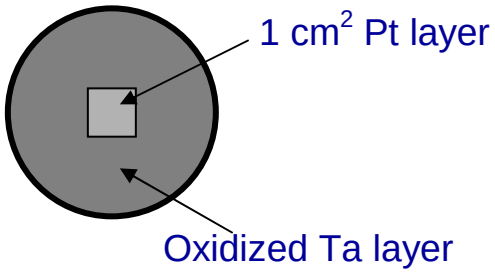

Figure 7.4.1: Outline of the Pt square on a Ta-coated Si wafer.

A solution of 5 mM umbelliferone and 0.1 M potassium triflate (50 mL) at pH 7 was added to the fluorescence cell and O_2 was bubbled in the solution. The working electrode was scanned from 800 mV to -800 mV vs. Ag/AgCl. The Pt square fluoresced upon O_2 reduction and figure 7.4.2 confirmed that the fluorescence intensity could be plotted versus potential, giving a fluorescence onset potential. Thus, a parallel screening for oxygen reduction can be performed, in a similar manner to our anodic catalyst testing.

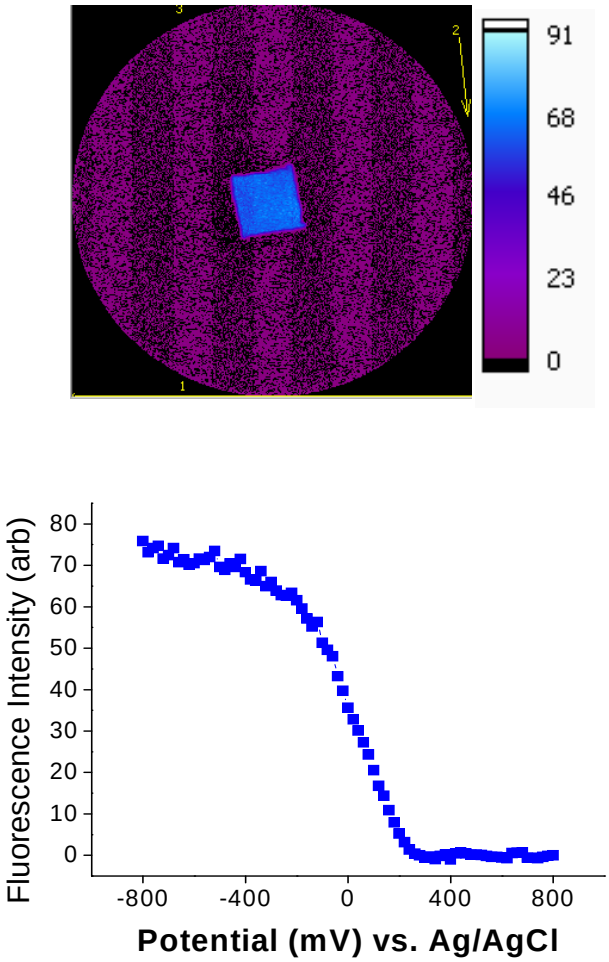

Figure 7.4.2: Top: Background subtracted image of the fluorescence intensity on the Pt square with the color axis showing the blue color intensity. Bottom: Fluorescence intensity of the Pt square vs. potential (mV), showing a fluorescence onset potential of approximately 250 mV vs. Ag/AgCl in pH 8 (where the fluorescence began).

7.5 References

1. Prochaska, M.; Jin, J.; Rochefort, D.; Zhuang, L.; DiSalvo, F. J.; Abruña, H. D.; van Dover, R. B., High throughput screening of electrocatalysts for fuel cell applications. *Review of Scientific Instruments* **2006,** 77, (5).

2. Jayaraman, S.; Hillier, A. C., Electrochemical synthesis and reactivity screening of a ternary composition gradient for combinatorial discovery of fuel cell catalysts. *Measurement Science & Technology* **2005,** 16, (1), 5-13.

3. Reddington, E.; Sapienza, A.; Gurau, B.; Viswanathan, R.; Sarangapani, S.; Smotkin, E. S.; Mallouk, T. E., Combinatorial electrochemistry: A highly parallel, optical screening method for discovery of better electrocatalysts. *Science* **1998,** 280, (5370), 1735-1737.

4. CRC Handbook of Chemistry and Physics. In [Online] 91st ed.; Haynes, W. M., Ed. 2011.

5. Bishop, E., *Indicators*. Pergamon Press: Oxford, 1972; p 746.

6. Chen, G. Y.; Delafuente, D. A.; Sarangapani, S.; Mallouk, T. E., Combinatorial discovery of bifunctional oxygen reduction - water oxidation electrocatalysts for regenerative fuel cells. *Catalysis Today* **2001,** 67, (4), 341-355.

7. Liu, J. H.; Jeon, M. K.; Woo, S. I., High-throughput screening of binary catalysts for oxygen electroreduction. *Applied Surface Science* **2006,** 252, 2580-2587.

8. Bowyer, W. J.; Xie, J.; Engstrom, R. C., Fluorescence imaging of the heterogeneous reduction of oxygen. *Analytical Chemistry* **1996,** 68, (13), 2005-2009.

APPENDIX 1

Comments on Leaching

An important materials property, especially in our screening process that can easily lead to false positives, is the propensity for one or more metals of the least noble metals in an alloy or intermetallic compound to preferentially dissolve from either the surface or the bulk material (in our case the combi films) into solution (a process that is known as leaching or de-alloying). When very noble metals like Au or Pt are present, they are usually left behind. Some key variables that determine the extent of de-alloying are listed below:

- The extent of de-alloying is generally a function of the mole fraction of the less noble metal. If the mole fraction is above 0.5, bulk de-alloying may occur. At lower mole fractions, de-alloying is often confined to the surface, leading to a depleted surface layer but interior layers that are unchanged. [1]
- De-alloying can be a significant factor if the equilibrium metal/metal-ion redox potential between the two (or more) metals in the thin film are drastically different.[2]
- The kinetics of dissolution, surface diffusion, and mass transport through the bulk of both alloy and solution can result in de-alloying that causes cracked and/or porous films.[3]
- The partial enthalpy of formation of each metal with the most noble metal in the alloy is an indicator of a related phenomenon, the tendency of the alloy to surface segregate or remain alloyed.[4] Low enthalpies generally favor surface segregation. The element with the lowest surface energy will segregate to the surface. With the surface segregation, surface leaching can occur for the less noble element.

- Surface oxidation from air or water exposure may lead to a multiphase surface reaction layer consisting of metal oxide(s) or hydroxide(s) mixed with small particles of any unoxidized (more noble) metals. The surface oxide formed may be soluble in the solution. This process can also be considered as de-alloying.
- In accordance to the Pourbaix diagrams for the elemental metals, the pH of the solution and potential applied to the electrode are important factors in determining the electrochemical oxidation for the metals to produce soluble cations, again resulting in de-alloying.[5]

Therefore, as we perform our fluorescence screening, these key factors must be taken into account.

Leaching can artificially alter our fluorescence signal drastically as seen clearly in the Pt-Zn system. In this system a significant "improvement" in fluorescence onset potential was observed when the Zn concentration exceeded 55%. The increased fluorescence, however, was attributed simply to an increase in the surface area of the electrode from Zn leaching from the surface as inferred from SEM images. The usual measure for comparison with the literature is the current *density* for specific redox reactions, where the signal obtained is normalized to the surface area. This unit of measure is essential for comparing catalytic properties of materials. Since the absolute current response can be altered by increasing the exposed catalytic surface area and our fluorescence assay measures total current rather than current density per se, with an artificially high surface area, the current reaches the threshold for fluorescence at a lower potential than it would have if the surface area is not enhanced. Therefore we infer an incorrectly low onset potential, i.e. a false positive.

In order to minimize the number of false positives, we have developed methods for identifying leaching at the surface and in the bulk. Bulk leaching can be used to create porous films with high surface area[6] or can cause cracking throughout the film[7]. However, if leaching occurs only in the surface, detecting such behavior can be very challenging, especially if the depth of leaching is on the nanometer scale. The methods we developed for identifying false positives due to surface or bulk leaching are:

- Inspection of SEM and AFM images, which are mainly relevant for bulk leaching.
- Cyclic voltammograms of hydroxymethylferrocene on the region in question, which result in a large enhancement of peak currents due to the increased surface area. The surface area can be inferred by modeling with the Randles-Sevcik equation.[8] Depending on the depth of penetration, this is mainly useful for bulk leaching and is generally not sensitive to nanoscale surface leaching.
- Cyclic voltammograms of the thin film in 0.1 M H_2SO_4, which gives a characteristic electrochemical response of the thin film and can indicate how the CV changes with continued cycling. If the electrode contains Pt, then the characteristic H-adsorption peaks on Pt should change depending on the surface area exposed to the solution. The surface area of Pt can be calculated from integrating the H-adsorption peaks and dividing by the appropriate charge/surface area ratio (for polycrystalline Pt the conversion factor is 210 $\mu C/cm^2$). Additionally, if the elements exhibit any redox couples or form oxide species that have redox properties within the potential range of interest, then these can be measured with cyclic voltammetry. These series of experiments enable one to estimate the extent of the surface leaching.

- XPS on the thin film, which can provide surface concentrations of metal species as well as their oxidation states before and after electrochemical testing. Elements found in their oxidized state before electrochemical testing can leach upon electrochemical testing and the change can be determined with XPS.

References:

1. Stratmann, M.; Rohwerder, M., Materials science: A pore view of corrosion. *Nature* **2001,** 410, (6827), 420-423.

2. Newman, R. C.; Corcoran, S. G.; Erlebacher, J.; Aziz, M. J.; Sieradzki, K., Alloy corrosion. *Mrs Bulletin* **1999,** 24, (7), 24-28.

3. Erlebacher, J.; Aziz, M. J.; Karma, A.; Dimitrov, N.; Sieradzki, K., Evolution of nanoporosity in dealloying. *Nature* **2001,** 410, (6827), 450-453.

4. CRC Handbook of Chemistry and Physics. In [Online] 91st ed.; Haynes, W. M., Ed. 2011.

5. Pourbaix, M., *Atlas of Electrochemical Equilibria in Aqueous Solutions*. National Association of Corrosion Engineers: Houston, TX, 1974.

6. Zeis, R.; Mathur, A.; Fritz, G.; Lee, J.; Erlebacher, J., Platinum-plated nanoporous gold: An efficient, low Pt loading electrocatalyst for PEM fuel cells. *Journal of Power Sources* **2007,** 165, (1), 65-72.

7. Gregoire, J. M.; Kostylev, M.; Tague, M. E.; Mutolo, P. F.; van Dover, R. B.; DiSalvo, F. J.; Abruña, H. D., High-Throughput Evaluation of Dealloyed Pt-Zn Composition-Spread Thin Film for Methanol-Oxidation Catalysis. *Journal of the Electrochemical Society* **2009,** 156, (1), B160-B166.

8. Bard, A. J.; Faulkner, L. R., *Electrochemical Methods: Fundamentals and Applications*. 2nd ed.; John Wiley & Sons, Inc.: New York, 2001.

APPENDIX 2

BIOSENSORS

A Generalized Platform for Antibody Detection

Collaborators: Mary (Liz) Welch, Norah Smith, Youyong Xu, Hongjun Chen, Abhinav Rastogi, Suddhasattwa Nad, Manabu Tanaka, Yelena Bisharyan, Lisa Blum, Nicolas DaMota, Judith Appleton, Theodore Clark, Barbara A. Baird, and Christopher K. Ober

9.1 Motivation

One of the biggest issues society must face is the spread of disease across a wide population especially with global transportation being the most accessible it has ever been and such diseases have caused epidemics in the past, i.e. the black plague, polio, etc. As part of a body's immune response to an infection, antibodies are generated and their detection can be a means for monitoring the spread of the disease. Since there are a wide range of functional antibodies that contain specific antigen groups, the device for detection must be not only selective but also sensitive. False positives and false negatives are some of the limitations of device development today. False positives occur when the signal from an assay is triggered from something other than the desired analyte, such as a contaminant or other non-specific species. False negatives can occur when the antibody is present but the assay is not sensitive enough to detect it and might be considered to be noise in the assay. Other limitations are ease of use, speed, required sample size, expense, and portability; if used in extraneous locations.

With regards to specificity, our main focus is the avian influenza (H5N1), which has accounted for 36,000 deaths in poultry and wild birds per year in America. The reported mortality rate in humans is high; the WHO data indicate that 60% of cases classified as H5N1

resulted in death.[1] The virus is considered one of the world's largest current pandemic threats due to high lethality, virulence, increasingly large host reservoir and ongoing mutations.

Our immediate goal is to develop a microfluidic device for the electrochemical detection of avian flu antibodies but aim to expand this method as a general platform for any infectious agent. Our device would also eliminate specific secondary reagents, a limitation associated with the current standard ELISA assay. The difference with our method compared to the conventional ELISA assay will be discussed in the following section.

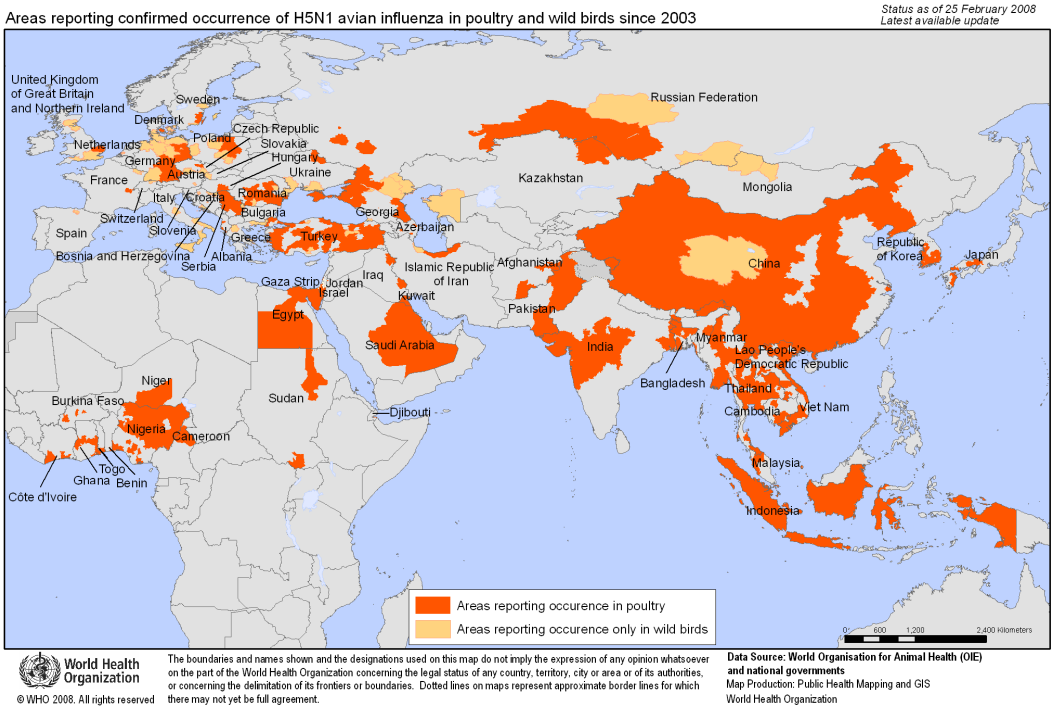

Figure 9.1.1: World wide locations for the avian flu cases in poultry and wild birds recorded for 2009 since 2003 (World Health Organization). Orange is for poultry and beige is only wild birds.

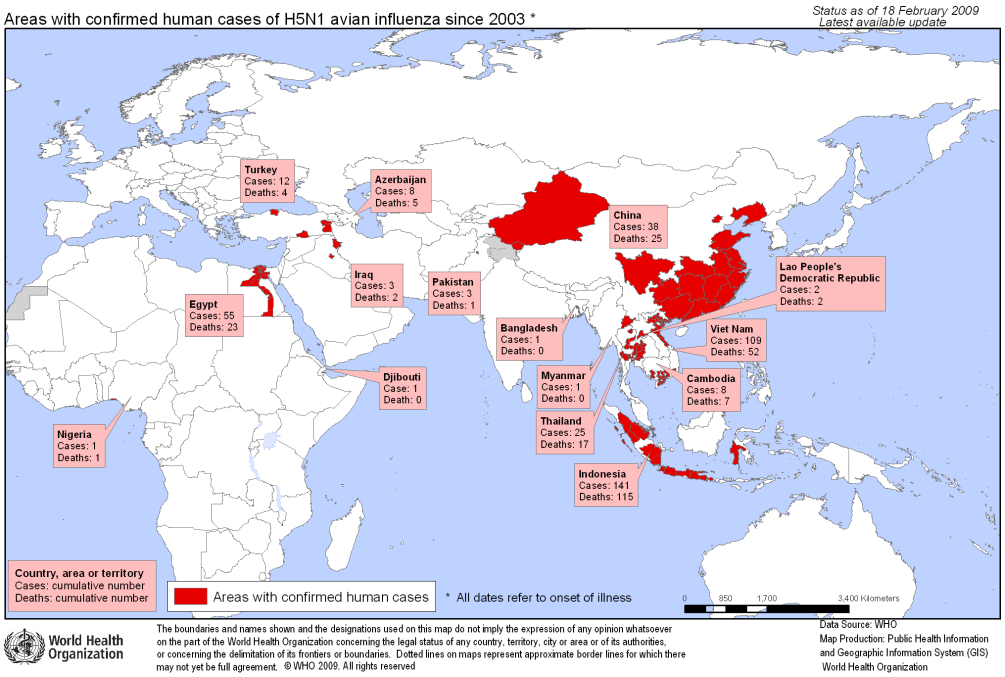

Figure 9.1.2: World Health Organization areas with confirmed human H5N1 avian flu virus from 2003-09.

9.1.1 ELISA vs. ACWOP

Many of the current assays and devices for antibody detection utilize an Enzyme-linked immuno-sorbant assay (ELISA). Figure 9.1.1.1 depicts the scheme for an ELISA, where a polymer brush is functionalized with an antigenic hapten, specific for the antibody desired. The solution containing the test antibody is applied and bonded to the hapten. After wash steps, a labeled secondary antibody specific for the species and sub-class of the primary antibody is allowed to bind to the antibody, followed by another wash cycle. The labeled secondary antibody can be fluorescent or a conjugated enzyme, i.e. horseradish peroxidase (HRP), which generates a colored or luminescent product from added substrate. The catalytic unit on the HRP increases sensitivity but the non-specific binding of secondary reagents can cause a high background. Moreover, the secondary antibody required must be specific for the species and class of the analyte antibody. The ELISA limit of detection has been claimed to be as low as 1

ng/mL, but it is closer to 10-100 ng/mL (1-10 nM). Thus, the limits of using the ELISA are the requirement for specific secondary reagents, speed, expense, and sample size/composition especially with all the washing steps.

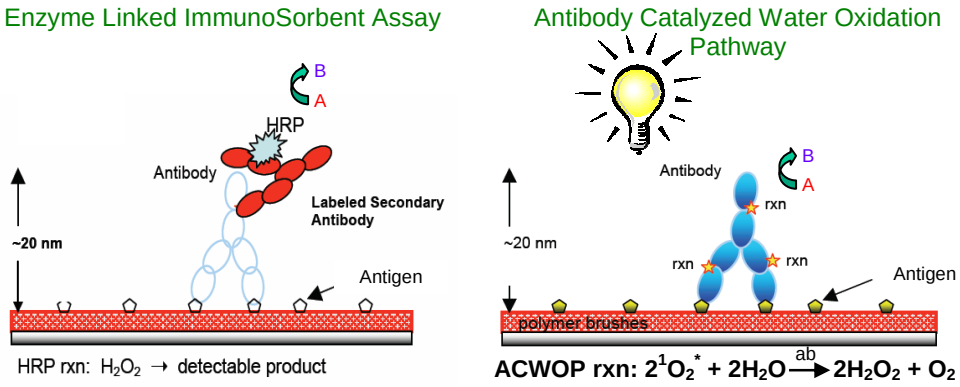

Figure 9.1.1.1: Left: Enzyme Linked ImmunoSorbent Assay (ELISA) schematic. Right: Antibody Catalyzed Water Oxidation Pathway (ACWOP). In both cases, the antibody binds onto specifically functionalized polymer brushes. ELISA requires a secondary antibody from which the H_2O_2 production can be monitored; whereas for the ACWOP, the H_2O_2 is the direct product from the desired antibody. Amplex Red (A) is the electrochemical mediator that is reduced to form the electrochemically active resorufin (B). Therefore, a linear correlation between H_2O_2 and the resorufin signal detected enables the direct determination of antibody concentration.

On the other hand, the Antibody Catalyzed Water Oxidation Pathway (ACWOP) in figure 9.1.1.1 utilizes the intrinsic properties of the antibody for detection as discovered by Wentworth et al.[2] The promising aspect of this method is the removal of the requirement of a secondary antibody and as a result, the ACWOP is independent of specificity, class and species of the antibody. The "active site" responsible for the intrinsic property[3] is related to the tryptophan groups. The antibody protein structure seems to be resistant to oxidation by reactive oxygen species generated during the water oxidation process.[3] To summarize the process, singlet oxygen ($^1O_2$) is generated by a photosensitizer in ambient aerobic conditions and reacts

with the antibody to form H_2O_2, which can be detected using a solution assay.[2, 4] Nieva and Wentworth found that as much as 40 mole equivalents of H_2O_2 per mole of antibody were generated over several hours and can be extended if product inhibition is eliminated.[4] We aim to apply this process to a wide range of antibodies and create a specific biosensor by altering the binding sites of the antigens, where the rest of the process can remain constant due to this intrinsic property.

9.1.2 Overall process

Our overall process incorporates many steps and hence a number of collaborations are required for each step in the process. First of all, the substrate (Au, Pt or Si) is modified with polymer brushes and subsequently functionalized with antigen groups for specific antibodies. In our case, we are using DNP-functionalized brushes to bind anti-DNP rat IgG1 antibodies as a proof-of-concept model with the main goal being the antibodies generated by the avian flu. Additionally, we can quantify the functionalization of the DNP on the brushes using an electrochemical quartz crystal monitor (eQCM). The eQCM measurement is non-reversible, so the number of DNP groups is approximate. The antibody is then adsorbed specifically onto the DNP-functionalized brush and quantified with the QCM. As this point, the substrate is ready for the ACWOP process. An Amplex Red fluorescence assay was employed to polyclonal sheep antibodies to ensure the production of H_2O_2 (Figure 9.1.2.1). Since this process was verified with the sheep antibodies, we prepared an aerated solution containing: photosensitizer $[Ru(bpy)_3]^{2+}$ and fluorescent mediator to detect H_2O_2 (in our case Amplex Red + HRP). The solution is exposed to UV light and because the solution is aerated, the triplet oxygen is excited to singlet oxygen and reacts with the antibody to form H_2O_2. We can detect the H_2O_2 electrochemically with an

electrochemical mediator. The electrochemical mediator may vary and upon examining a few mediators, we chose Amplex Red in the presence of HRP and H_2O_2 converting to the electroactive resorufin. We can monitor the resorufin signal and evaluate the amount of H_2O_2 generated quantify the amount of antibody present.

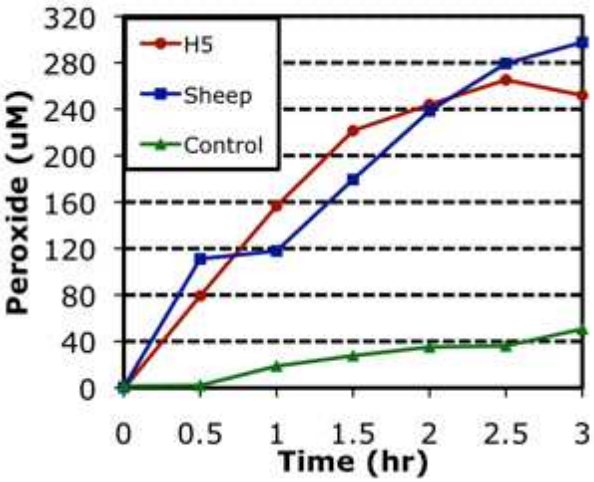

Figure 9.1.2.1: Amplex Red fluorescence assay on 10 µM polyclonal sheep antibodies and IgG against H5 from the avian influenza compared to the control (buffer alone) in a solution with 100 µM photosensitizer $[Ru(bpy)_3]^{2+}$, to show that the antibodies produce H_2O_2. The antibody solution was exposed to UV light and removed at the noted times. Peroxide concentrations were derived from a standard curve of H_2O_2 concentrations with the Amplex Red assay.

Two of the issues associated with our process that will be addressed are lowering the background signal by chemically fixing the photosensitizer onto a substrate and patterning the substrate to incorporate both the polymerized brushes and polymerized photosensitizer. The patterning is to promote the transfer of the singlet oxygen generated by the photosensitizer to the antibodies on the polymer brushes with the goal of optimizing H_2O_2 output. Lastly, we hope to switch the functional group on the brushes to a Ni-NTA group, to be specific for the avian flu virus antibodies.

9.2 Experimental

This section covers the different analytical techniques used as well as the synthesis and experimental parameters for each step in the process.

Chemical and Immunochemical Reagents.

All reagents were purchased from Sigma Aldrich and used without further purification. Dimethylamino pyridine p-toluene sulfonate (DPTS) was prepared from dimethyl amino pyridine and sodium p-toluene sulfonate following a literature procedure.[5] The anti-DNP IgE was purchased from Aldrich.

Luminescence experiments for detecting H_2O_2 produced.

This fluorescence assay is based on a previously established method[2] with modifications. 10 µM antibody solutions were made in buffer (10 mM KH_2PO_4, 160 mM NaCl, pH 7.4) containing photosensitizer (100 µM tris(2,2'-bipyridine) ruthenium II). Samples were placed in acrylic cuvettes (Sarstedt) and irradiated with an 8W ultraviolet (302 nm) transilluminator (UVP). At times indicated (every 30 minutes for 3 hours), aliquots were removed and placed in a black flat-bottomed 96-well plate on ice protected from light. After all desired samples were collected, the plate was removed from the light and Amplex Red (Invitrogen) was used to assay for H_2O_2 production. Briefly, samples were diluted in 50 mM sodium phosphate (monobasic) containing Amplex Red (final concentration 30 µM) and Horseradish peroxidase (Type I) (final dilution 0.07 U/mL) (Sigma) and then incubated at room temperature, while protected from light, for 30 minutes. Fluorescence of Amplex Red was measured on a plate reader (Tecan) using λ_{abs}= 540

nm and λ_{em}=590 nm filters. Standard solutions of H_2O_2 were included in 96-well plate for quantification purposes.

Immobilization of Initiators and Polymerization of PAA Brushes.

The pegylated thiol initiator was prepared according to the literature procedure published by Rastogi et al.[6] Gold coated silicon wafers and QCM electrodes were plasma cleaned for 5 min and rinsed with ethanol and deionized water and dried under nitrogen. They were immersed in a 2 mM initiator solution in anhydrous ethanol under argon for 24 hours at room temperature. The PAA brushes were grown by modifying a previous literature procedure.[7] A solution of sodium acrylate (2.029 g, 21.59 mmol), CuBr (68.8 mg, 0.478 mmol), $CuBr_2$ (21.4 mg, 0.096 mmol), bipyridine (188.18 g, 1.20 mmol), and degassed pH 9 H_20 (9.6 mL) were cannulated into sealed Schlenk tubes containing the substrates under an Ar atmosphere. The polymerization was stopped after 15 minutes at room temperature and substrates were subsequently rinsed with water and ethanol, dried in N_2 flow, and dipped into EDTA and a pH 5 solution to remove the copper catalyst and protonate the carboxylic acid groups. Polymer brushes were characterized by ellipsometry, water contact angle goniometry, and atomic force microscopy (AFM). Thicknesses of the polymer brushes were measured by a Woollam variable angle spectroscopic ellipsometer at a 70 degree angle of incidence. A Cauchy model (Cauchy layer/Au substrate) was used to fit the data, in which the Cauchy layer was representative of the PAA brush. Water contact angles were measured using a VCA optima XE goniometer. Surface topography and roughness were measured using a Veeco Dimension 3100 scanning probe microscope.

Preparation of DNP Functionalized Brushes.

PAA brushes were modified with DNP in two steps. First, substrates with PAA brushes were placed in Schlenk tubes under Ar atmosphere in a solution of 2-(2-aminoethoxy)ethanol (250 µL, 2.5 mmol), DIPC (125 µL, 0.8 mmol), and DPTS (187.5 mg, 0.63 mmol) in anhydrous DMF (10 mL). The reaction was heated to 32°C and kept under an Ar atmosphere. After 24 hours, the wafers were washed with DMF, water, and ethanol and dried under nitrogen. The activated carboxylic groups of the polymer brushes were then functionalized with the DNP groups. A solution of DNP-ε-amino-n-caproic acid (37.5 mg, 1.12 mmol), DIPC (125 µL, 0.8 mmol), and DPTS (187.5 mg, 0.63 mmol) in anhydrous DMF (10 mL) were cannulated into the flask containing the substrates. The reaction was allowed to continue for 24 hours at 32°C. When finished, the substrates were washed with DMF, water, and ethanol and dried under nitrogen. Functionalization of DNP on polymer brushes was investigated via binding DNP-specific IgE antibodies to DNP groups. DNP-PAA brushes were immersed in a 10 µg mL^{-1} solution of AlexaFluor 488 labeled IgE antibodies in the dark at room temperature for 90 min. Fluorescent images were taken using an Olympus BX51 upright fluorescence microscope, equipped with a Roper Cool Snap hx CCD camera. Alexa488 was observed with a 450-490 nm excitation and 520 nm emission filter set.

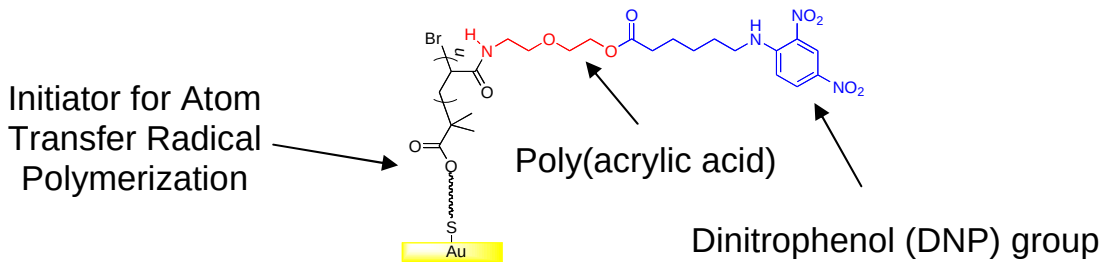

Figure 9.2.1: Chemical structure of polymer brushes immobilized on a gold electrode surface, functionalized with a DNP group.[6]

Antibody adsorption measurements using Quartz Crystal Microbalance (QCM).

The basic premise of a Quartz Crystal Microbalance (QCM) consists of a piezo-electric device where oscillations of a quartz plate, between two Au contacts, changes frequency depending on the mass loading (adsorption or desorption) of an analyte onto the electrode. The quartz crystal electrode usually contains a smaller area of the conducting material with 10 nm thick Ti adhesion layer and 100 nm thick Au or Pt on a 1 inch diameter quartz crystal and this is exposed to a solution or air. As long as the following conditions are met, the Saurbrey equation can be used to relate the frequency change to the mass change: the mass must be rigid, distributed evenly, and cause a frequency change of less than 2%.[8] The Sauerbrey equation is as follows:[9]

$$\Delta m = -C_f \Delta F$$

Δm = change in mass (ng cm^{-2})

ΔF = the change in frequency

C_f = the proportionality constant for a 5 MHz crystal (17.7 ng Hz^{-1} cm^{-2})

The proportionality constant C_f is based on the resonant frequency (f_0), piezoelectrically active crystal area (A), density of quartz (ρ_q= 2.648 g/cm^3), shear modulus of quartz for AT-cut crystal (μ_q = 2.947 x 10^{11} g/cm s^2) in the relationship below:

$$C_f = \frac{2 f_0^2}{A\sqrt{\rho_q \mu_q}}$$

In our case, the Au electrode is functionalized with a thin film of the DNP-functionalized polymer brushes in the range of 13-17 nm thick with the assumption that the film is thin enough to be considered rigid. Thus, a DNP modified QCM electrode was first immersed in a 1mg/mL bovine serum albunium (BSA) PBS pH 7 solution and held at a constant temperature of 25 ^oC. The BSA was added to inhibit nonspecific antibody binding to the film. After the frequency had stabilized, 100 µL anti-DNP IgG1 (1mg/mL) solution were injected into the above-mentioned

solution. Upon stabilization of the frequency, the quantity of antibody on the electrode could be calculated based on the Sauerbrey equation.

Additionally, electrochemical QCM (eQCM) measurements can be performed on the DNP-functionalized polymer brushes to obtain the concentration of DNP groups on the brushes. From this, we can, in turn, relate the coverage of antibodies on the DNP groups from the conversion shown in figure 9.2.2. A CV begins at -0.1 V vs. Ag/AgCl in the negative direction for the irreversible reduction of the dinitro-group. As the CV is swept positive, integration of the oxidation peak at approximately 0.35 V vs. Ag/AgCl gives the charge and since n is known, the number of molecules can be calculated to give the DNP concentration on the polymer brushes. These samples cannot be reused for the actual antibody adsorption because the reduction at -0.3 V vs. Ag/AgCl is irreversible.

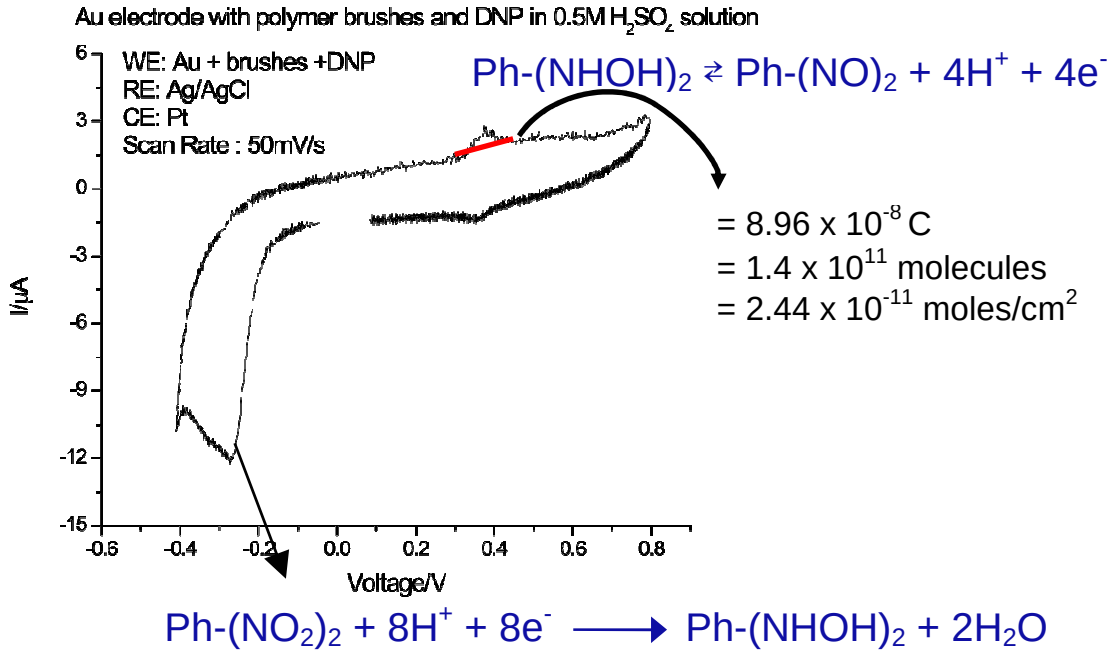

Figure 9.2.2: CV collected using the eQCM for determining the number of DNP functional groups on the polymer brushes.

Electrochemical measurements (Amplex Red/Resorufin) – DPV and SWV.

Throughout our series of experiments, cyclic voltammetry, differential pulse voltammetry, and square wave voltammetry were the three techniques used for monitoring H_2O_2 production. In the beginning, we used cyclic voltammetry but the results were noisy because of the low currents and the change was not as evident. The CV parameters for resorufin measurements were within the potential range of -0.3 V to 0.4 V vs. Ag/AgCl at 10 mV/s. A carbon fiber ultramicroelectrode and Pt were used for the working electrode and counter electrodes, respectively.

In an effort to suppress the background signal and noise, Differential Pulse Voltammetry (DPV) was implemented, where the potentials are stepped and sampled over the potential range of interest. DPV provides better quantitative results compared to CV and less distortion from the background.[10] A method derived from DPV is square wave voltammetry (SWV) and figure 9.2.3 gives a representative example of the potential versus time profile of the measurements. SWV was preferred over DPV due to reasons stated in Bard and Faulkner's Electrochemical Methods book.[10] Bard stated that SWV is generally the best choice among all pulse methods, because it offers background suppression with the effectiveness of DPV, sensitivity slightly greater than DPV, and much faster scan times, and applicability to a wider range of electrode materials and systems.[10] The SWVs were collected with amplitude 25 mV, step height 5 mV, and frequency 25 Hz. These SWV relate directly to the H_2O_2 produced by the antibody as shown in figure 9.5.2.3.

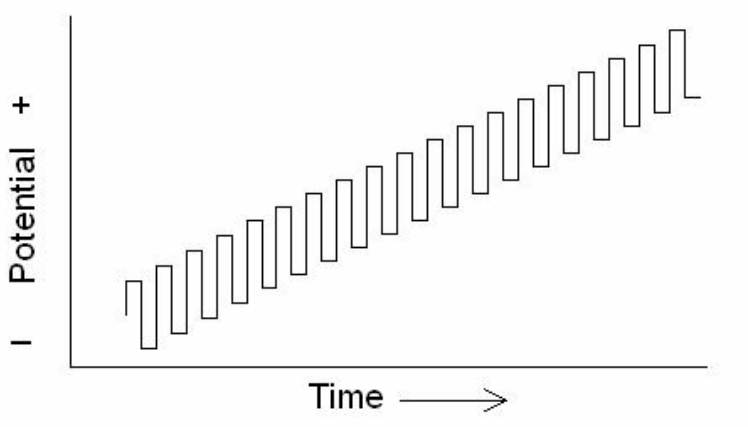

Figure 9.2.3: Potential vs. time profile for square wave voltammetry.

The general methodology of our experiments began by adding an antibody solution (100µL (1mg/mL)) to the fabricated DNP-PAA-Au electrode and allowing to sit for about 2-3 hours. The electrode was rinsed and placed into a solution that contained Horseradish peroxidase (Type I) (10 µM) (Sigma Aldrich) and 0.1 mM Amplex Red (diluted from 5 mM Amplex Red in dichloromethane solution stored in a refrigerator). The immersed electrode was exposed to UV light (UVEXS 110 series spot curing system) at a max wavelength λ = 450 nm and power of 10 W/cm^2 at an approximate distance of 2 cm above the sample for one hour. The electrode was removed from the solution and a second electrode, glassy carbon (3mm diameter – BAS), electrochemically reduced the resorufin from the oxidized to reduced form, as it was held in solution at a given distance from the surface. An Ag/AgCl reference electrode and Pt counter electrode were used for the voltammetric measurements.

Patterned Device (on Si wafer in clean room).

A checkerboard patterned device consisting of 35 rows of sixteen 300 x 300 µm silicon oxide squares bordered by a platinum (or gold) lattice was fabricated for signal amplification purposes.

The silicon islands are surrounded by a continuous platinum (or gold) grid with lines that are 150 µm wide and enclosed by a 500 µm wide border. Conventional UV photolithographic methods were employed to pattern the electrodes used in this work.

Silicon wafers with approximately 500 nm thick thermally grown oxide film were spun coated with lift-off resist (LOR) and photoresist. Soft contact exposure was performed on an EV620 contact aligner for 10 sec and a post-exposure bake was carried out at 115 °C for 90 sec. The wafers were developed and briefly descumed before evaporation. A CVC SC4500 e-beam evaporator was used to deposit 10 nm of Ti (adhesion layer) and 90 nm of Pt. After metal deposition, the LOR/photoresist was removed by soaking the wafers in a solution of Remover 1165 for a few hours.

As a means of mapping out the surface, a Scanning Electrochemical Microscope (SECM) was employed with an emphasis on the pattern of the checkerboard electrodes but also when the different positions were coated with polymer brushes and/or DNP functionalized. The SECM involves an electrochemical probe, usually an ultramicroelectrode (electrode diameter < 25 µm), that rasters over a substrate or surface of interest, in our case the patterned surface, and monitors the current response from the conducting or insulating surface. The probe is contained in an electrochemical cell, where the reference electrode is Ag/AgCl and the counter electrode is a Pt wire. The solution contains a reversible electrochemical mediator, which can be selected based on the charge of the mediator and on the interaction with the surface. For instance, we use a neutral hydroxymethylferrocene for mainly neutral surfaces and could monitor the current from the surface features. In the case of our DNP functionalized brushes, we used $[Fe(CN)_6]^{3-}$ for the SECM imaging of a Au electrode with half initiator and half pure Au, when we could not observe features with the hydroxymethylferrocene. As one might expect for a scanning probe

technique, it is important to level the substrate such that the change in current is not as a result of the substrate being unlevel.

Immobilization of the $[Ru(v\text{-}bpy)(bpy)_2]Cl_2$.

Our limit of detection was constrained by the photosensitizer being in solution. It was proposed to immobilize the $[Ru(bpy)_3]^{+2}$ on the Pt sections of the patterned electrodes. The procedure followed for the polymerization is explained in the literature.[11] In summary, after bubbling in nitrogen for 15 minutes, the Pt electrode is cycled in 0.5 mM solution of $[Ru(v\text{-}bpy)(bpy)_2](PF_6)_2$ in 0.1 M Bu_4NClO_4/acetronitrile between -0.7 and -1.7 V vs. Ag/AgCl for 10 cycles at a scan rate of 100 mV/s.

9.3 Parameter Optimization

Our system requires optimization of factors that could potentially preclude signal and confound interpretation of the data. More specifically we investigated the electrochemical stability of the buffer solutions, photosensitizer selection, and wavelength of UV light. The following section discusses these items in more detail.

9.3.1 Buffer solutions

Electrochemical stability is an important property of the environment under investigation, which includes the buffer. In conjunction with the search for electrochemical mediators, we also were interested in buffers that had a wide potential range of stability to enable testing of mediators within this range. Especially in the case of amplex red that had a redox response beginning around -0.1 V, we required a buffer that was stable at potentials negative of this value. The

buffers we studied included: citric acid buffer (pH 5 and pH 6), phosphate buffered saline (PBS) pH 7, Borate buffer pH 8, acetate/acetic acid buffer pH 5, sucrose gradient buffer pH 7, Tyrodes buffer pH 7, and ADA buffer pH 7.2.

According to figure 9.3.1 the borate buffer, sucrose gradient buffer, and Tyrodes buffer all exhibit instability beginning around -0.1 to -0.2 V vs. RHE (or at -0.3 V vs. Ag/AgCl). The pH 5 phosphate buffer was also unstable beginning at 0 V vs. RHE. ADA buffer begins its reduction at -0.25 V vs. Ag/AgCl. The pH 5 citric acid buffer seemed to show the best stability with the reduction beginning around -0.35 V vs. Ag/AgCl. Therefore, we chose to use the pH 5 citric acid buffer and later pH 6 for the antibody testing.

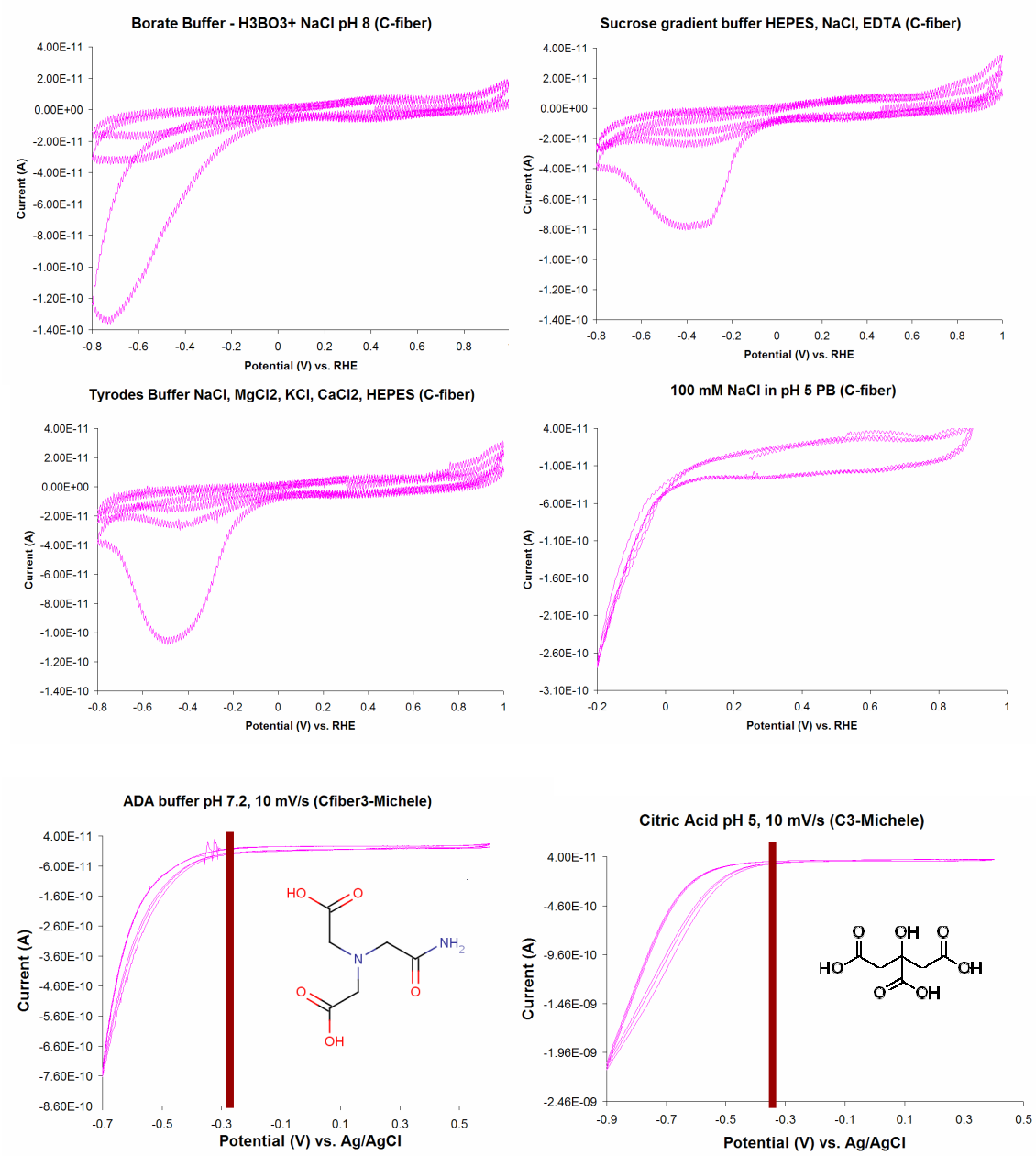

Figure 9.3.1: Cyclic voltammograms of buffers to test for stability. Scan rate = 10 mV/s; Working electrode = ultramicroelectrode Carbon fiber (7 µm diameter); Counter electrode = Pt wire.

9.3.2 Photosensitizer

The optimization of the photosensitizer was performed by Norah Smith and a table of tested photosensitizers is shown in table 9.3.2.1. During the optimization, white light irradiation was

initially used and later UV irradiation (monitored through the amplex red fluorescence assay) was employed, since it seemed to produce a higher peroxide yield. Norah reported that both $[Ru(bpy)_3]^{2+}$ and Hematoporphryin IX showed promise with UV irradation but the ruthenium complex was more advantageous because it was amenable to binding on the surface of our electrode. A variety of other photosensitizers were also screened for possible replacements for $[Ru(bpy)_3]^{2+}$ and are listed as being tested in Brazil. Still, the conclusion from the fluorescence assay revealed that the most efficient photosensitizer was, in fact, the photosensitizer currently used, $[Ru(bpy)_3]^{2+}$.

Table 9.3.2.1: The list of photosensitizers tested using the Amplex Red assay for evaluating H_2O_2 production.

White light illumination	
	Riboflavin
	$[Ru(bpy)_3]^{2+}$
	$[Os(bpy)_3]$
	Zn-pthalocyanine
	Hematoporphryin
	Protoporphryin IX
UV illumination	
	$[Ru(bpy)_3]^{2+}$
	Hematoporphryin IX
In Brazil:	
White light illumination	
[Carboxyl derivatives of $Ru(bpy)_3$]	
6 carboxyl (charge -4)	RuL_3
4 carboxyl (charge -2)	RuL_2
2 carboxyl (charge 0)	RuL_1
	Ru(Pc)
	[Tb(TsPc)(acac)]
UV illumination	RuA_5Py
	$Ru(NH_3)_5Pz$
	[Ru mepz $(Pz)A_4](PF_6)_4$
	Ru $(NH_3)_4(Py)$
	$[Ru(bpy)_2(4acpy)(NO_2)](PF_6)$
	$[Ru(NH_3)_5Pz](PF_6)_2$
	$Ru(bpy)_2Pz\ NO_2$

(A= NH_3, Pz=pyrazine, acpy=acetylpyradine, bpy=bipyradine, Py= pyradine, Pc=phthalocyanine, Ts=tetrasulfonate, acac=acetylacetonate)

A new photosensitizer, $[Ru(tpy)_n(pydppn)_{2-n}]^{2+}$ (n=1), that was found to have ~100% quantum efficiency for the conversion of $^3O_2$ to $^1O_2$.[12] This photosensitizer did not show any improvement to the tris(2,2'-bipyridine) ruthenium II according to the fluorescence assay. This is a surprising result because we would expect the higher concentration of the singlet oxygen to assist in the H_2O_2 production. We are still attempting to understand the process and what characteristic of the photosensitizer causes it to perform better than the others.

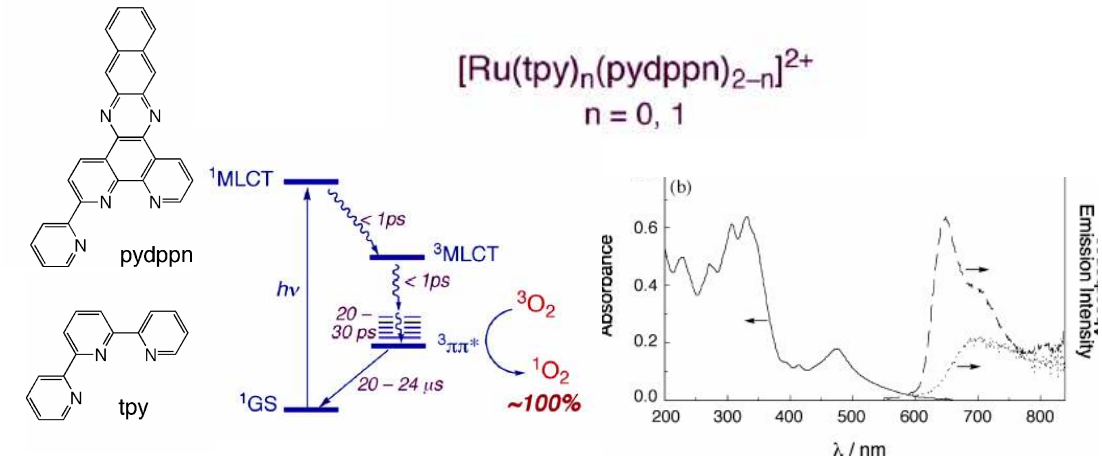

Figure 9.3.2.1: Ru-based photosensitizer that has ~100% efficiency for the conversion of light and energy to $^3O_2$ to $^1O_2$. On the right, the absorption spectrum of the complex is shown.[12]

9.3.3 Wavelength of UV light (LEDs)

When we examined the absorption spectrum of the photosensitizer (figure 9.3.3.1), we aimed to optimize the absorption of light, and to do that we purchased two LEDs with narrow bands of emission. The LEDs were purchased from Newark, titled Luxeon emitters. The two types of LEDs were: blue (λ = 460-490 nm) and royal blue (λ = 440-460 nm). Our hope was to provide a higher power output for the specific wavelengths of the photosensitizer. The only method for testing the output for this parameter was measuring the current output from the H_2O_2 produced. A more complete explanation of the result is discussed in *Section 9.6.* To summarize the results,

we found that the LEDs did not provide as high of an output as the wide-range wavelength UV light.

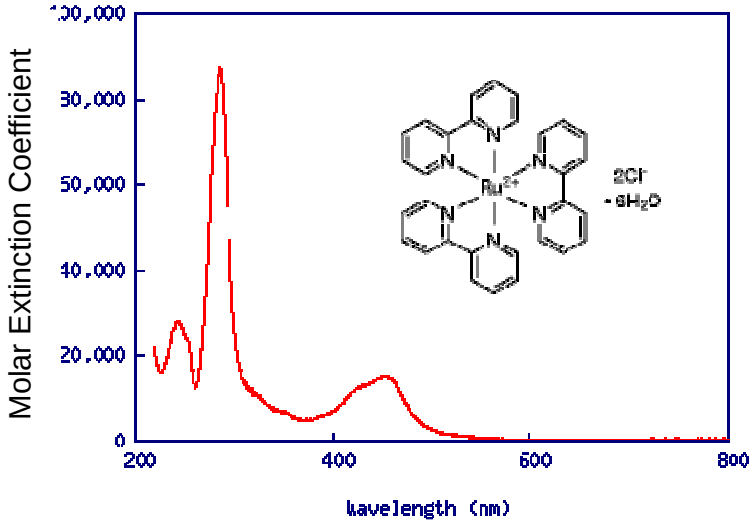

Figure 9.3.3.1: Absorption spectrum of the Tris (2,2'-bipyridyl) ruthenium (II) $[Ru(bpy_3)]^{+2}$. Based on the absorption spectrum, LEDs with emission wavelength at 450 nm were explored.[13]

9.4 Polymer brushes

Our method is highly dependent on the specific adsorption of the antibody onto a functionalized surface. The *Experimental Section* discussed the synthesis method for adhering the polymer brushes onto the electrode surface followed by functionalization with a DNP group. As of yet, we have been using the DNP functional group with specific anti-DNP antibodies as our model system that we can apply to other antibody systems. We first coat our surface with a non-functionalized group and, in the case of Au, the binding of the brushes occurs through a thiol group. We have also used a silane-functionalized initiator to adhere to SiO_2 on a Si wafer. The brushes are fixed onto the substrate and then subsequently functionalized for the specific antibody. The SECM was used to image the coverage of the initiator on a Au coated Si wafer. Figure 9.4.1 shows the boundary of the Au surface and the insulating initiator coated surface. The increased current (brown) denotes the Au region and the lower current (green) represents the

initiator, which is not entirely coating the surface uniformly. Rather, surface features can be observed as the sample is scanned. A continuation of this experiment would be to expose half Au and half functionalized polymer surface; half initiator and half functionalized surface; with and without antibodies. Ultimately, the goal would be to map out the functionalized surface, then add antibodies and see how the conductivity decreases, which would indicate the adsorption of the antibody.

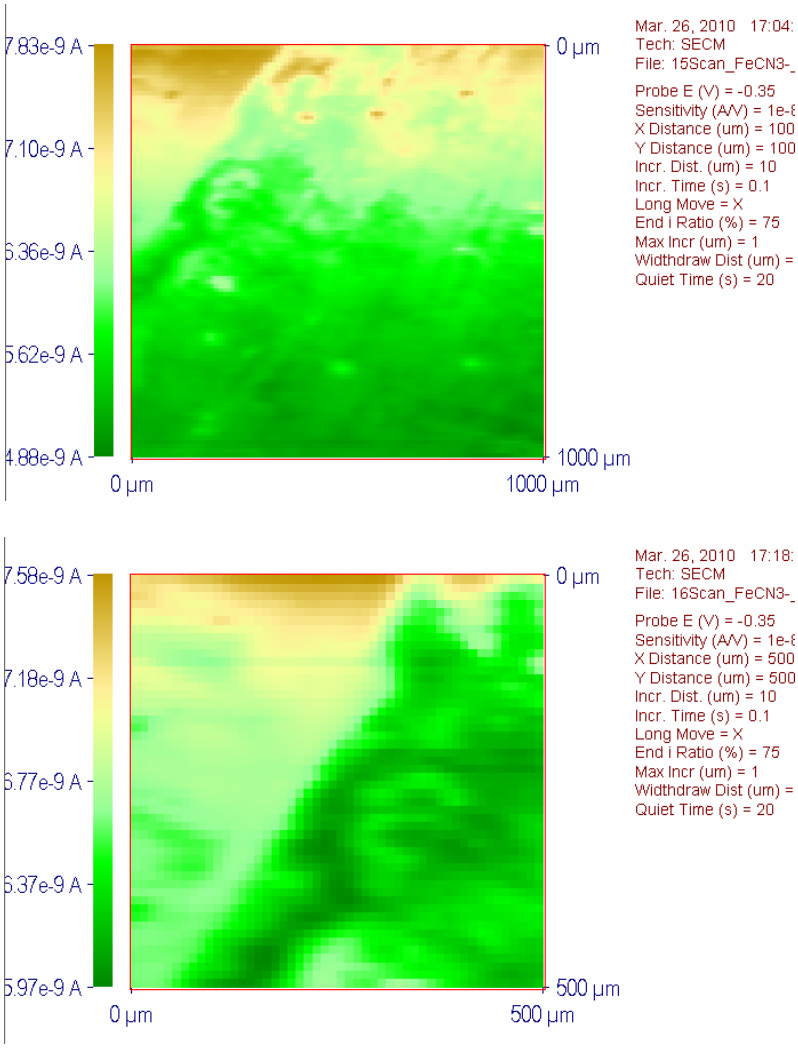

Figure 9.4.1: SECM images of a Au electrode with half initiator and half pure Au. The mediator is $[Fe(CN)_6]^{3-}$ (5 mM) in 0.1 M NaCl.

9.4.1 Forest vs. garden

As we aim to optimize the amount of antibody adsorbed to our electrode, the configuration of the polymer brushes can be an essential variable to consider. We propose the "forest canopy" and "English garden" configurations, where one is more closely packed than the other as shown in figure 9.4.1.1. We expect the English garden to exhibit higher adsorption of the antibody than the forest canopy due to the functional groups being more readily accessible to the lower branches on the polymer brushes. Some preliminary experiments have been performed with the SECM in hopes to identify the differences between these configurations, but the results were inconclusive and should be revisited.

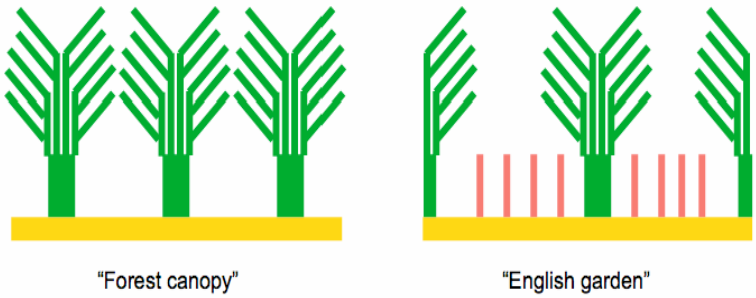

Figure 9.4.1.1: Forest vs. English garden configuration for the density of polymer brushes attached to the gold substrate.

9.5 Electrochemical mediator search

We examined a number of redox mediators for the detection of the generated H_2O_2 with the three substantial ones being: 1,4-benzoquinone, 1,4-naphthoquinone, and amplex red. These mediators make up the following section.

9.5.1 1,4-Benzoquinone and 1,4-Naphthoquinone

1,4 Benzoquinone and 1,4-naphthoquinone have been used as redox mediators for H_2O_2 in the past.[14] We desired a mediator that was reduced at more positive potentials and reached steady state at potentials before the reduction of the solvent or buffer. Figure 9.5.1.1 shows the steady state response of the two mediators without any H_2O_2 added. The current of the 1,4-naphthoquinone is more than twice the current for the 1,4-benzoquinone; however, the $E_{1/2}$ is approx. -0.1 V vs. Ag/AgCl compared to 0.1 V vs. Ag/AgCl for 1,4-benzoquinone.

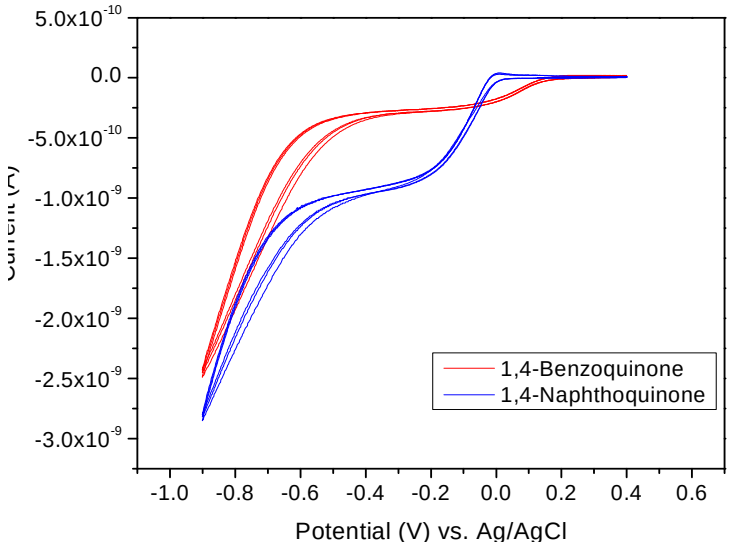

Figure 9.5.1.1: 0.1 mM mediator in Citric acid pH 5 buffer. Scan rate 10 mV/s, C-fiber ultramicroelectrode as the working electrode, Pt wire as the counter electrode.

1,4-Benzoquinone was selected out of the two for further studies because the redox potential was more positive and had a higher chance for reaching steady state before the onset of the reduction of the buffer. From the CVs and upon addition of H_2O_2, the steady state current did increase incrementally (figure 9.5.1.2) and the current response vs. H_2O_2 concentration indicated that the linear region begins after approximately 25 µM H_2O_2. In our experiments we expected lower peroxide concentrations to be produced and we aimed to maximize our signal so

that our limit of detection should be in the nM scale. This caused us to explore the electrochemical properties of Amplex Red, which was the same compound commonly used as a fluorescence assay.

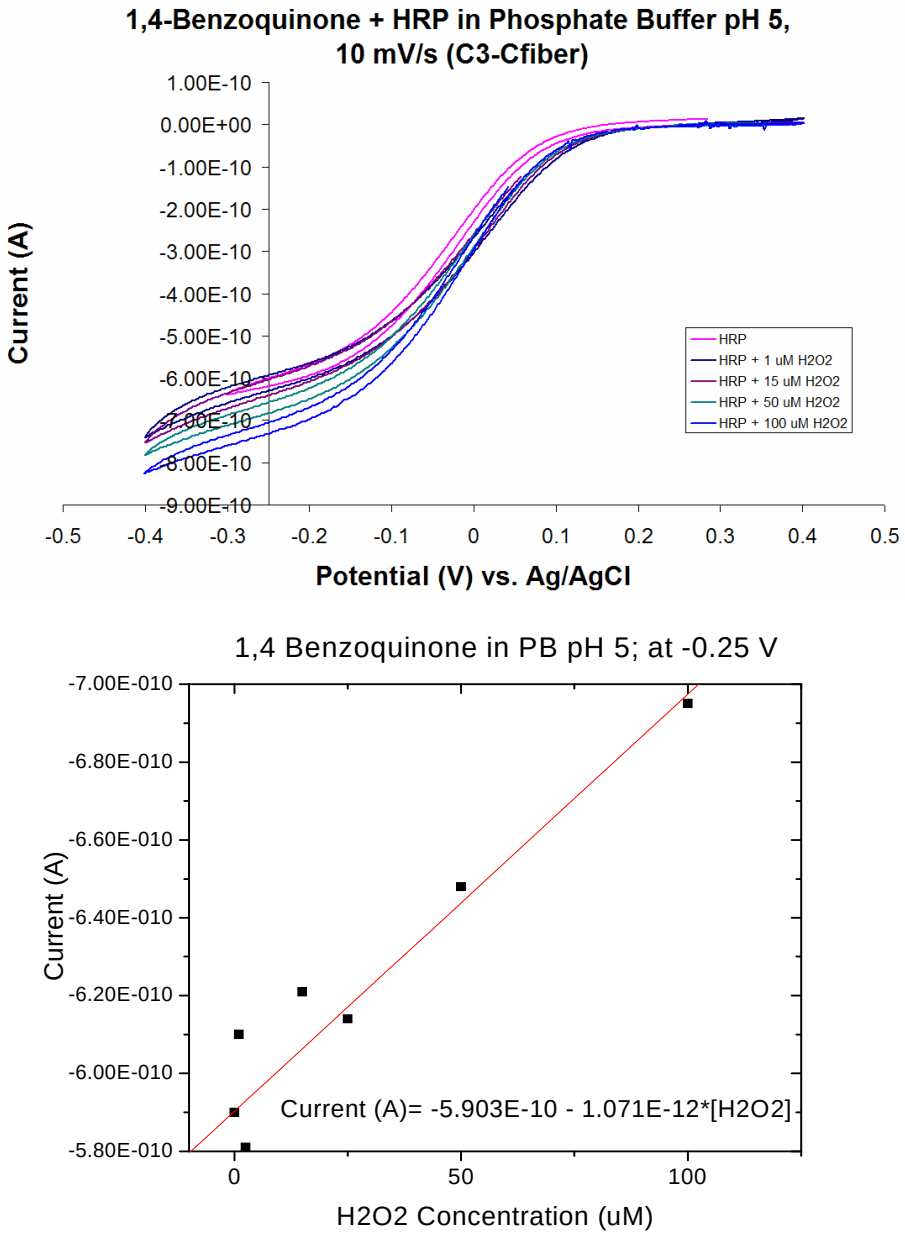

Figure 9.5.1.2: Top: Cyclic voltammograms of 0.1 mM 1,4-Benzoquinone + HRP (0.2 Units/mL) with varying H_2O_2. Bottom: Current response of the benzoquinone vs. H_2O_2 concentration. Scan rate 10 mV/s, C-fiber ultramicroelectrode as the working electrode, Pt wire as the counter electrode.

9.5.2 Amplex Red

As is prevalent in the literature, amplex red is a promising mediator for monitoring low levels of H_2O_2 not only electrochemically but also for fluorescence.[15] Gajovic-Eichelmann and Bier report the process in which amplex red is oxidized in the presence of H_2O_2 and the reversible electrochemically-active product, resorufin. The mechanism also demonstrates that the amplex red can be electrochemically reduced to the reduced form of resorufin and a CV is shown that supports this explanation (figure 9.5.2.1). Thus, as we perform our electrochemical experiments, we must be careful not to exceed potentials below about -0.4 V vs Ag/AgCl.

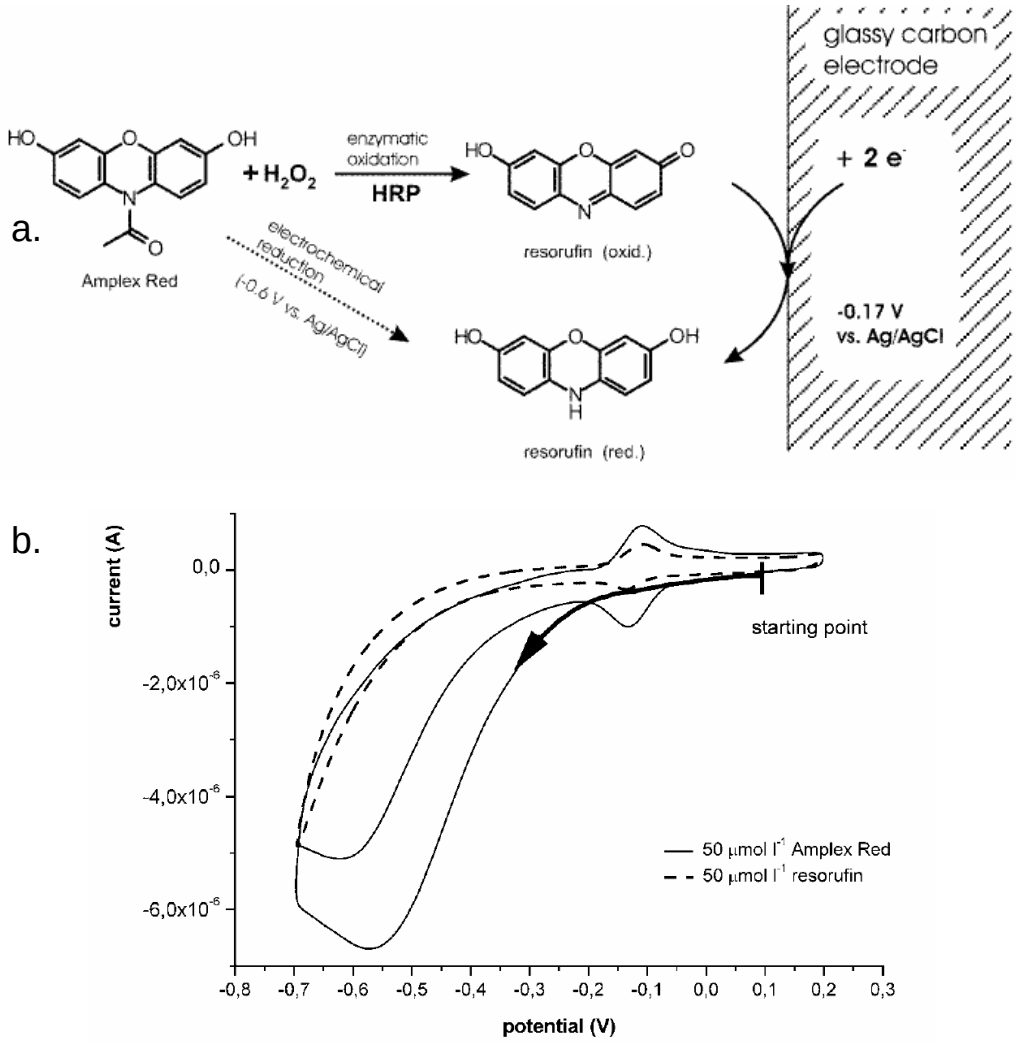

Figure 9.5.2.1: (a) Amplex Red and the enzymatic reaction to form resorufin which has a redox couple at -0.17 V vs. Ag/AgCl. The Amplex Red can also be electrochemically reduced to form resorufin at -0.6 V vs. Ag/AgCl. (b) Cyclic voltammograms of Amplex Red and Resorufin starting at 0.1 V (vs. Ag/AgCl) in pH 5 McIlvaine buffer (PBS + citric acid buffer) at 10 mV/s with a 3 mm-diameter glassy carbon working. The arrow follows the initial course of the Amplex Red CV before the occurrence of the electrochemically generated resorufin. See reference.[16]

According to the buffer optimization in an earlier section, we tested amplex red in pH 6 citric acid buffer. We sequentially added H_2O_2 to a solution of amplex red and HRP and observed the current increase with H_2O_2 concentration. It must be noted that the amplex red and HRP alone did have a small current response, which we must consider when we do these

experiments. This background signal must be minimized and especially with all the components of the system, could be a source of a false positive response.

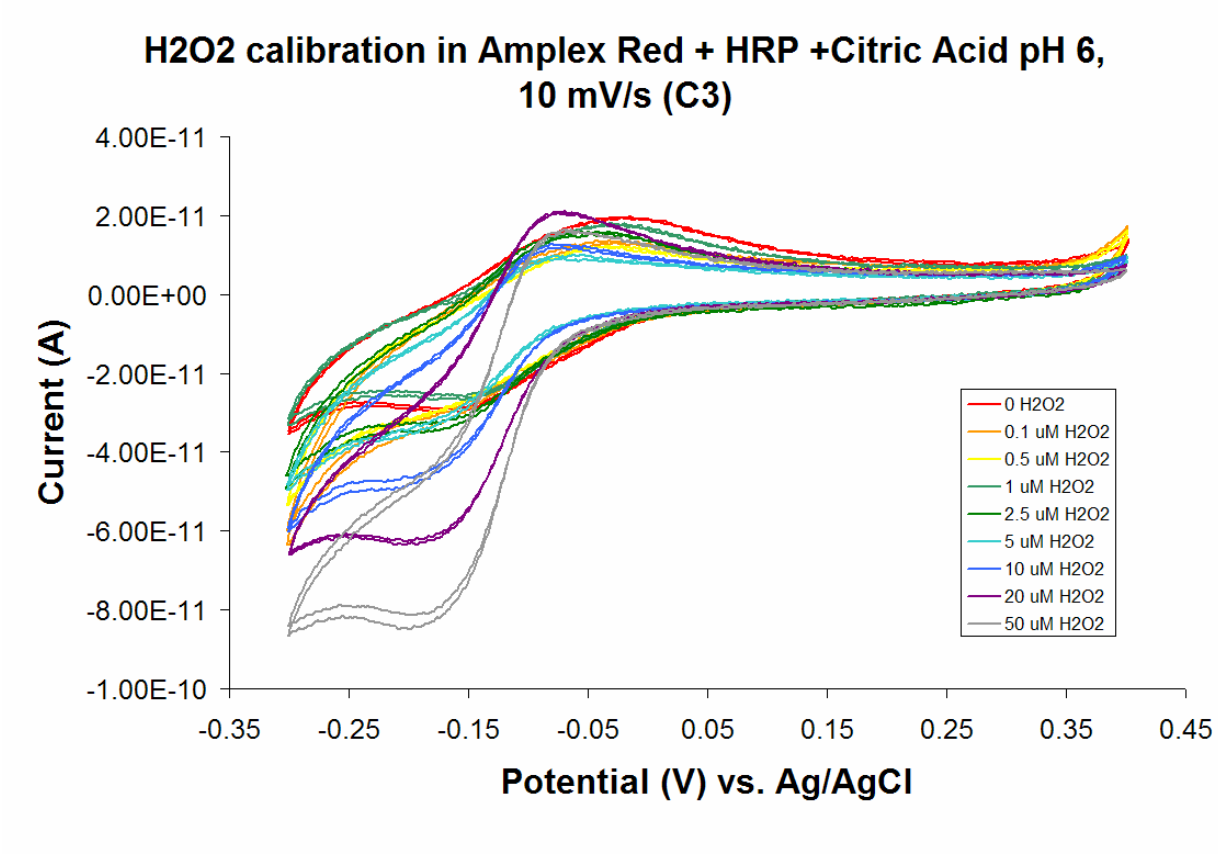

Figure 9.5.2.2: Cyclic voltammograms of 0.1 M Amplex Red + HRP in Citric Acid pH 6, 10 mV/s, with a C-fiber ultramicroelectrode.

It was determined later that a better current response could be obtained by SWV. Again, H_2O_2 was added at incremental amounts and the current was measured from 0.1 V to -0.3 V vs. Ag/AgCl. A calibration curve was constructed and found that the limit of detection is 0.33 nM with an upper limit of ~1.2 µM. Therefore, with the low detection limit, we are continuing to use Amplex Red as our mediator for our entire system.

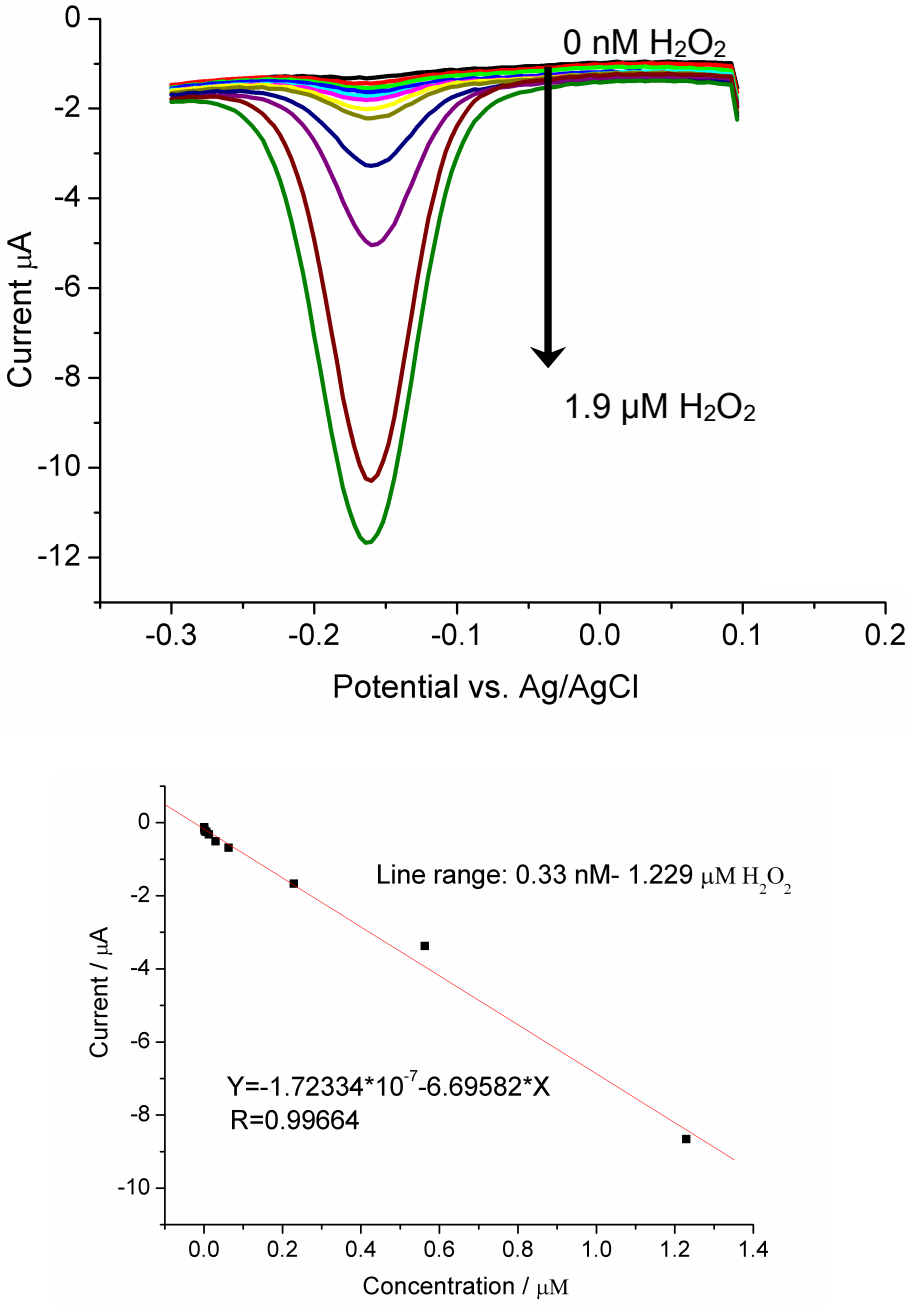

Figure 9.5.2.3: Square wave voltammetry (top) of Amplex Red + HRP with varying concentrations of H_2O_2 to construct a calibration curve (bottom). This calibration curve suggests that the lower limit of detection is 0.33 nM with an upper limit of ~1.2 µM.

9.6 Device and testing of all components

Our proposed device uses the principle that antibodies containing tryptofan groups can intrinsically produce H_2O_2 that can be monitored with various processes described earlier, including fluorescence and electrochemical methods.[2] The promising feature with this approach is that a secondary antibody is not required for H_2O_2 output and it can be directly applied to the antibody of interest. In an effort to verify this intrinsic process, an Amplex Red fluorescence assay was applied to monitor the H_2O_2 output of an anti-DNP rat IgG antibody. The process is described above, with the inclusion of a photosensitizer, HRP, and Amplex Red and antibody in solution and exposed to UV light over time. Using a calibration curve, the fluorescence can be correlated to H_2O_2 produced after UV irradiation, which was found to increase with the increase of the UV exposure time as shown in figure 9.5.2.3.

Now that we confirmed that the antibodies can produce H_2O_2 in amounts that can be monitored, it is important to adapt this process so that it can be used in a device that would be specific for the antibody desired. Our method for enabling antibody specificity is to immobilize the antibody onto functionalized brushes that the antibodies will favorably bind to. For a proof of concept experiment, we use anti-DNP rat IgG as the antibody studied and as a result the functionalized brushes are terminated with DNP. The PAA-brushes are polymerized onto an Au substrate as described in the *Experimental Section* followed by DNP functionalization. We confirmed that the brushes were functionalized with a fluorescently labeled antibody (AlexaFluor 488 labeled IgE) and electrochemical measurements described in a previous publication.[6] Electrochemical QCM results in the concentration of the DNP functional group on the polymer PAA-brushes to be about 3 pmol/cm^2. To monitor adsorption of the anti-DNP antibody, QCM measurements (figure 9.6.1) were performed and found that the concentration of

antibody on the surface was 2.5 pmol/cm^2, which indicates that there is good coverage of the antibody on the surface. On the other hand, for nonspecific adsorption, the QCM frequency increases rather than decreasing as we would expect from the adsorption of a material on the surface. This is indicative of solution most likely being displaced with the addition of the non-specific antibody but further supports our claim that the DNP successfully inhibits the binding of nonspecific antibodies.

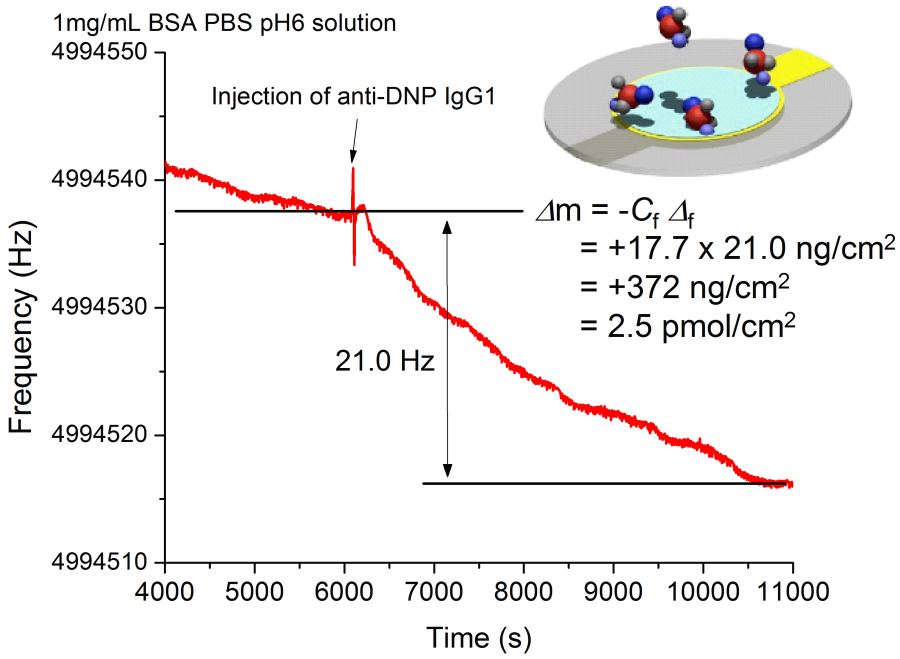

Figure 9.6.1: QCM frequency response to the addition of anti-DNP IgG1 antibodies to a 40-mL solution of 1 mg/mL BSA PBS pH 6 solution held at 25 ^{o}C.

Once the antibody is immobilized on the polymer surface and excess antibody rinsed off, the next step requires an analytical methodology that can detect low levels of H_2O_2. The mediator we selected was Amplex Red, which in the presence of HRP and H_2O_2, becomes oxidized to resorufin, which is electrochemically reversible at -0.17 V vs. Ag/AgCl. In our initial experiments, we employed cyclic voltammetry for monitoring the resorufin redox

response on a C-fiber ultramicroelectrode and we also used the citric acid pH 6 buffer because of its wide potential window. Figure 9.6.2 demonstrates the H_2O_2 production over time as the entire system is exposed to UV light. We can observe an increase in reducing current, indicating the growth of the resorufin and consequently the production of H_2O_2. When we compare the current response at the reduction peak height of resorufin, the maximum current seems to occur after about 1 hour. This could be due to the antibody being denatured upon that length of exposure to an intense UV light and thus leveling off. Furthermore, it is promising to note that the same experiment without exposure to UV light results in minimal, most likely within error, current response over time, thus supporting our claims of the process requiring UV light for the H_2O_2 generation to occur.

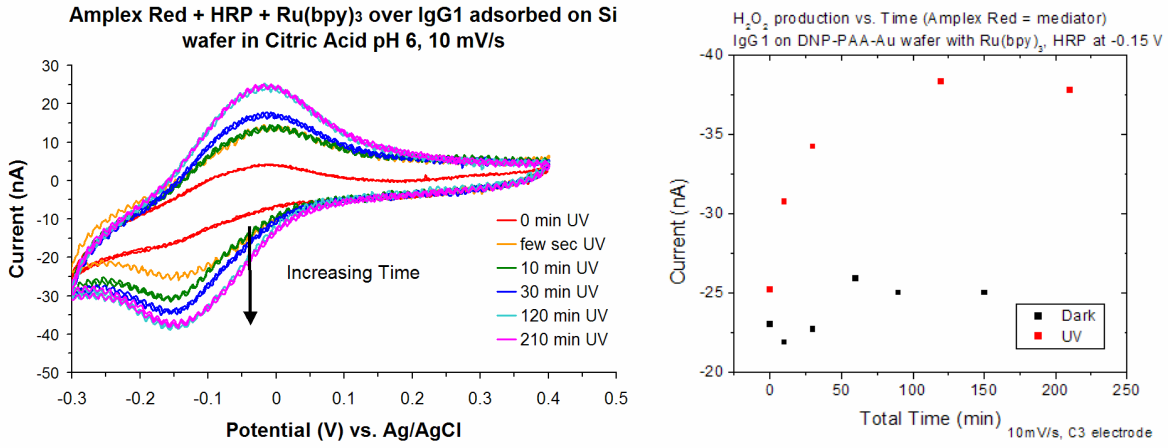

Figure 9.6.2: CVs of the resorufin response denoting the H_2O_2 produced by the anti-DNP rat IgG1 antibodies bound on DNP-PAA brushes on a Au coated Si wafer (1 cm x 2 cm) with Amplex Red, HRP, $[Ru(bpy)_3]^{2+}$ in solution over the time exposed to UV light. The same experiment was performed without any UV light exposure and the current peak was plotted vs. UV exposure time. CV collected at 10 mV/s with Pt counter electrode and Ag/AgCl reference electrode.

Later in our experiments, we found that the DPV measurements can give a better signal especially at low currents than cyclic voltammetry.[17] We also found that the collecting tip was

not required to be an ultramicroelectrode and as a result, we obtained higher currents with the larger surface area of the 3-mm diameter glassy carbon electrode. We wished to decrease the amount of UV exposure and aimed to obtain a higher output by using LEDs with the emission coinciding with the absorption of the photosensitizer. We found that the overall signal was greatly decreased with the LED (λ_{max} = 450 nm) vs. the UV source. Since we determined that the H_2O_2 reached a plateau after 1 hour of UV exposure, we use this value to compare between prepared samples. As we were performing a component analysis determining the effect of each component in the system, we found that even without the presence of the antibody a high signal can be observed with the exposure of LED or UV light (Figure 9.6.3).

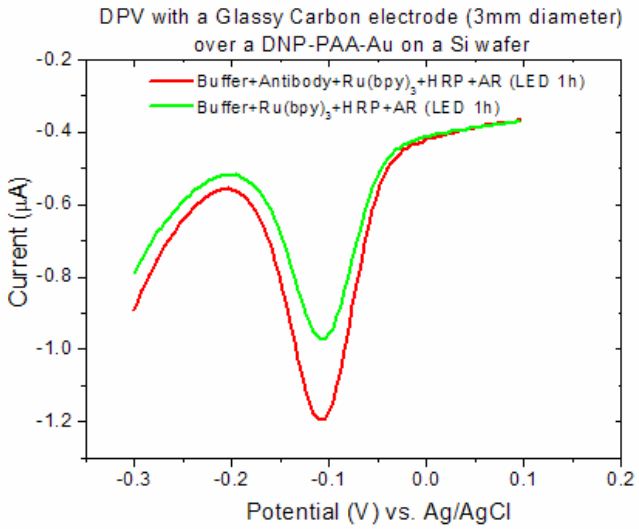

Figure 9.6.3: DPV of the resorufin current response to H_2O_2 production with antibody (red) and without antibody (green) using the LED as the excitation source. The same comparable background signal is seen for the UV light as well.

To minimize the signal from sources other than the antibody, we immobilized the photosensitizer by electropolymerizing $[Ru(v\text{-}bpy)_3]^{2+}$ onto a 1 cm x 2 cm Si wafer with a Au layer as reported by Abruña, et al.[11] The photosensitizer plate was positioned adjacent to an identically shaped Au-coated Si plate with the DNP-functionalized polymer brushes. Figure

9.6.4 shows the current response of 3 different cases and the presence of high background even with the photosensitizer immobilized. The two cases that have comparable responses are the antibody plate without the presence of the photosensitizer plate and the photosensitizer plate without the antibody plate. We can confirm that the ACWOP is catalyzing the H_2O_2 production with the increase of signal. As the H_2O_2 production is plotted over time, a significant difference can be observed from the background (DNP-functionalized plate alone) but antibody catalysis reaches a limit at a time around 90 minutes exposure to UV light. This could be due to the antibody being destroyed upon the long exposures to UV light. Moreover, we still aim to minimize these effects of the antibody and photosensitizer alone.

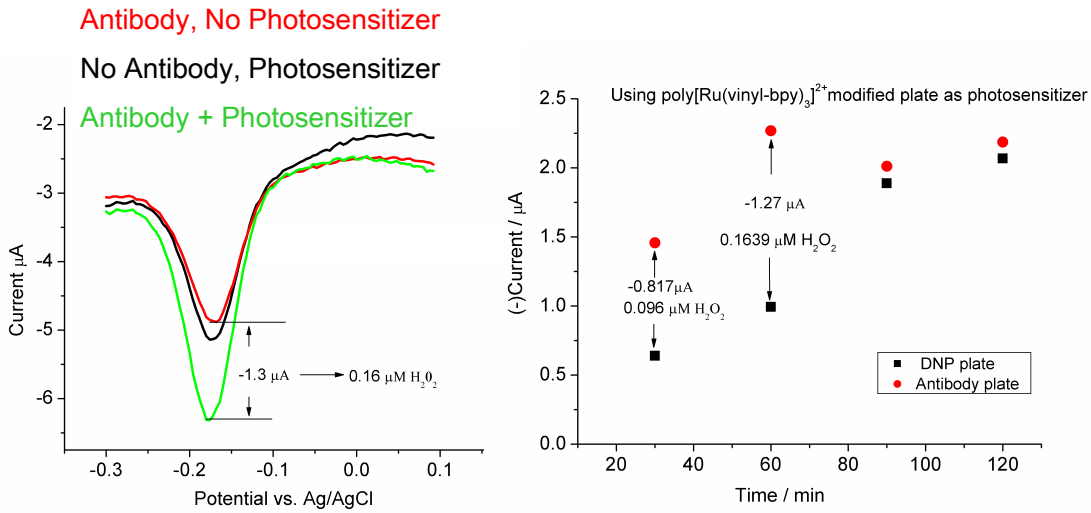

Figure 9.6.4: Left: SWVs for resorufin that measures H_2O_2 production for three representative cases: (1) the DNP-functionalized plate with antibody adsorbed (red); (2) photosensitizer plate alone (black); (3) photosensitizer plate adjacent to an antibody adsorbed onto DNP-functionalized polymer coated plate. All the samples were exposed under UV light for 1 hour and contained HRP and Amplex Red. Right: Effect of antibody presence on the DNP-functionalized plate next to a photosensitizer plate exposed to UV light in a solution of Amplex Red and HRP over time.

To further improve the output of H_2O_2 and delivery of the singlet oxygen to the antibodies, patterned Au and Pt electrodes were made by Liz Welch (figure 9.6.5). We found Pt

could not be used because it catalyzes the reduction of the H_2O_2 to H_2O, thus diminishing our overall signal. This result left the Au electrode as the primary electrode of choice in our device. At first, the $[Ru(v\text{-}bpy)_3]^{2+}$ was electropolymerized onto the Au part of the electrode, then the functionalized polymer brushes were synthesized on the Si spaces. This initially seemed to work but then problems arose with the polymer brushed synthesis on Si. We eventually decided to shift our direction to patterning a Au QCM to allow for monitoring the antibody adsorption on the same substrate (refer to the next section).

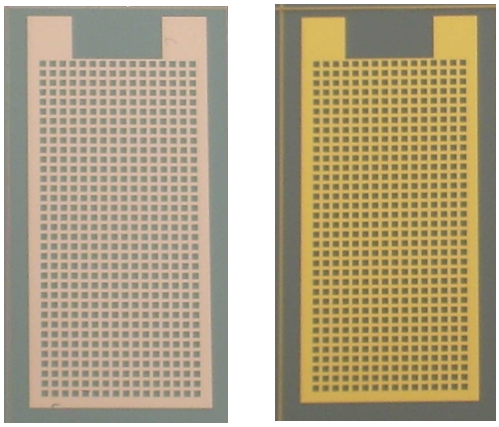

Figure 9.6.5: Pt and Au patterned electrodes on a Si wafer. The Pt or Au are for polymerizing the photosensitizer and the Si spaces are available for the DNP-functionalized brushes to bind the antibody.

9.7 Future directions

Our successful implementation of the Antibody Catalyzed Water Oxidation Pathway to our model system, DNP, demonstrated the viability of our scheme to other antibody systems, such as the antibody from the avian flu virus. A number of items have been proposed for future work and many are listed below:

1. Optimize photosensitizer conversion of triplet oxygen to singlet oxygen. As the antibodies are exposed to UV light, the proteins within the antibodies can be denatured over time and

hence can kill the antibodies. Some possible alternatives could be to use LED lights or a less intense UV light.

2. Introduce new antibody functional groups (in *Section 9.7.1*). Ensure that the generalized scheme can be applied to other infectious viral diseases.
3. Correlate the concentration of the H_2O_2 measured to the antibody concentration. Determine the H_2O_2 production per antibody over time.
4. Combine the QCM with SECM to both identify the amount of antibody adsorbed over the entire sample but also determine if the coverage is uniform. The SECM would also permit the detection of H_2O_2 directly on the surface rather than through a mediator.
5. Build flow cell and test the system on a patterned QCM electrode by introducing the analytes in sequence.

9.7.1 Altering functional groups for other viruses

Since our main focus is to develop a device that detects low levels of avian flu antibodies or other interested antibodies from a living sample, we aim to shift our tests from the DNP-functionalized groups to a functional group specific for the avian flu. Our method for changing the functionality of the polymer brushes is in collaboration with the Ober group and uses a Ni-NTA functional group (figure 9.7.1.1). The Ni-NTA has two H_2O ligands and these are replaced with a His-tagged protein, which is specific for the antibody in question. The only difference that would differentiate these devices for different antibodies are the His-tagged protein, which are isolated from infected cells and obtained from Ted Clark's (Cornell's Vet school) group. A possible disadvantage to using the Ni-NTA is that the Ni can oxidize and then confound the electrochemical signal we are measuring. The ligands have the possibility of being removed

upon Ni oxidation and therefore ruining our device. Hence, alterative approaches are being explored currently.

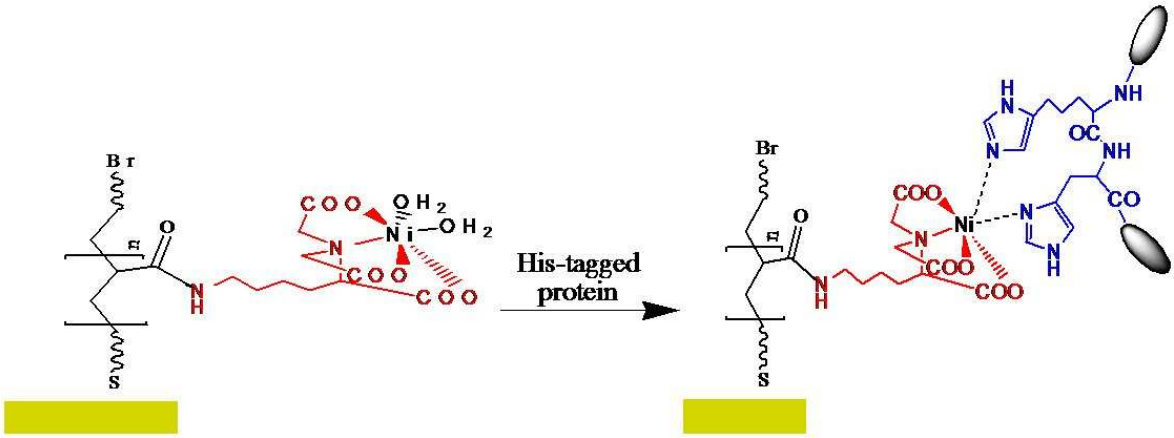

Figure 9.7.1.1: Structure of the polymer brushes immobilized on a gold surface, functionalized with a Ni-NTA group. The addition of the His-tag protein to the Ni-NTA group is shown.

9.7.2 QCM monitoring in conjunction with H_2O_2 detection

In an effort to correlate the antibody adsorbed to the H_2O_2 generated, a patterned QCM electrode was fabricated by Liz Welch in the Cornell Nanofabrication (CNF). Once patterned, a photoresist is applied on alternating spots and the Au exposed surface is covered with the initiator for the polymer brushes. Then the photoresist is removed and the photosensitizer is polymerized on the freshly exposed Au surfaces. The sample is returned to Liz Welch and the last steps of the polymer brushes and DNP functionalization are performed on the initiator previously bound to the Au surface. A depiction of the patterned QCM is shown in figure 9.7.2.1.

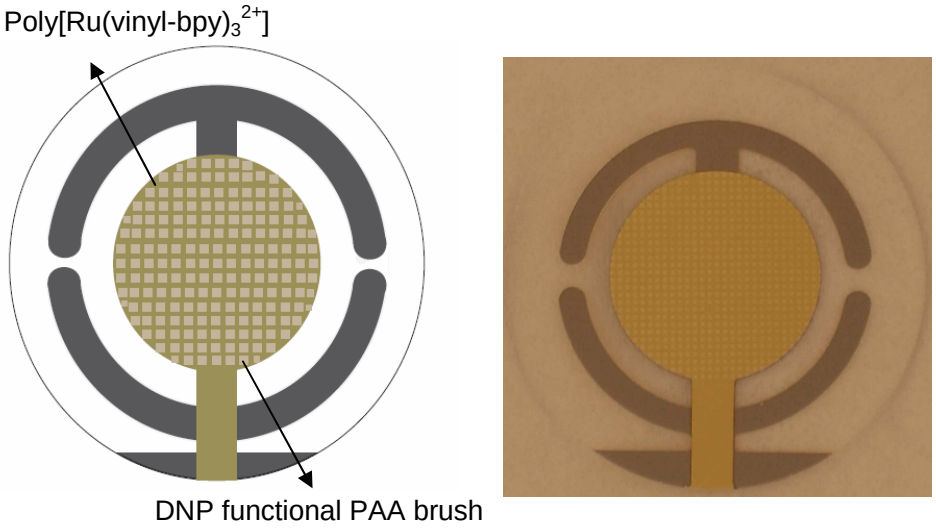

Figure 9.7.2.1: Schematic of patterned Au QCM electrode with alternating spots of immobilized poly[Ru(vinyl-bpy)$_3$]$^{2+}$ and DNP-functionalized polymer brushes. Left: Picture of the patterned QCM electrode.

Antibody adsorption can be now be monitored with the patterned QCM electrode and subsequent SWV measurements can be performed with and without antibody. A preliminary SWV collected by Dr. Hongjun Chen compares the H_2O_2 generated with and without the antibody in figure 9.7.2.2. We observe that there is still a significant amount of background signal but found that the difference corresponds to approximately 32 nM H_2O_2. We are still working on the reproducibility of these samples, and because of this uncertainty, the QCM measurement is not shown at this time. The most important message to take from this is that the QCM patterning enables the combined quantitative measurements of antibody and H_2O_2.

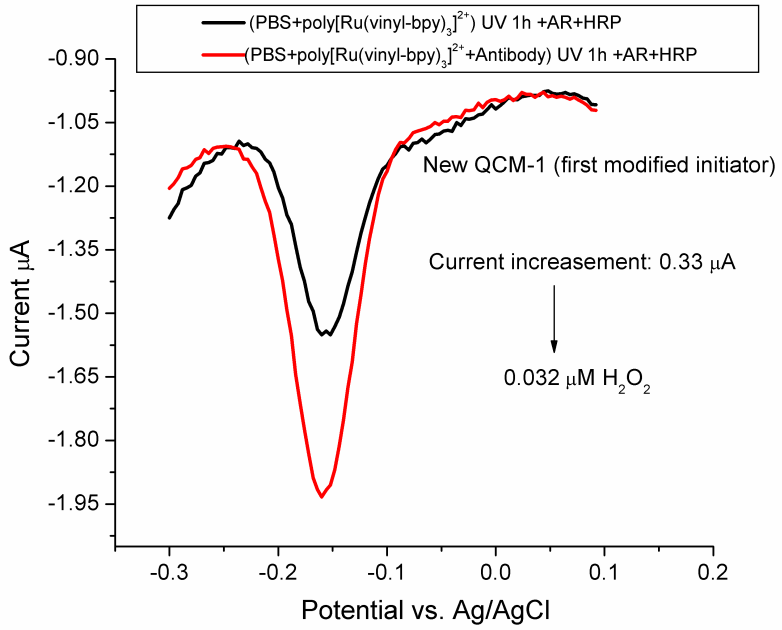

Figure 9.7.2.2: SWV of a patterned Au QCM electrode with alternating spots of immobilized poly[Ru(vinyl-bpy)$_3$]$^{2+}$ and DNP-functionalized polymer brushes. The smaller current (black) indicates the absence of antibody and the larger current (red) indicates the H_2O_2 output from the adsorbed antibody.

9.8 References

1. World Health Organization. http://www.who.int/en/

2. Wentworth, P., Jr.; Jones, L. H.; Wentworth, A. D.; Zhu, X.; Larsen, N. A.; Wilson, I. A.; Xu, X.; Goddard, W. A., 3rd; Janda, K. D.; Eschenmoser, A.; Lerner, R. A., Antibody catalysis of the oxidation of water. *Science* **2001,** 293, (5536), 1806-11.

3. Zhu, X. Y.; Wentworth, P.; Wentworth, A. D.; Eschenmoser, A.; Lerner, R. A.; Wilson, I. A., Probing the anti body-catalyzed water-oxidation pathway at atomic resolution. *Proceedings of the National Academy of Sciences of the United States of America* **2004,** 101, (8), 2247-2252.

4. Nieva, J.; Wentworth, P., The antibody-catalyzed water oxidation pathway - a new chemical arm to immune defense? *Trends in Biochemical Sciences* **2004,** 29, (5), 274-278.

5. Moore, J. S.; Stupp, S. I., Room-Temperature Polyesterification. *Macromolecules* **1990,** 23, (1), 65-70.

6. Rastogi, A.; Nad, S.; Tanaka, M.; Da Mota, N.; Tague, M.; Baird, B. A.; Abruña, H. D.; Ober, C. K., Preventing Nonspecific Adsorption on Polymer Brush Covered Gold Electrodes Using a Modified ATRP Initiator. *Biomacromolecules* **2009,** 10, (10), 2750-2758.

7. Dong, R.; Krishnan, S.; Baird, B. A.; Lindau, M.; Ober, C. K., Patterned biofunctional poly(acrylic acid) brushes on silicon surfaces. *Biomacromolecules* **2007,** 8, (10), 3082-3092.

8. QCM100-Quartz Crystal Microbalance Theory and Calibration *Periodical* [Online]. http://www.thinksrs.com/downloads/PDFs/ApplicationNotes/QCMTheoryapp.pdf.

9. Sauerbrey, G., Verwendung von Schwingquarzen zur wagung dunner schichten und zur mikrowagung. *Zeitschrift Fur Physik* **1959,** 155, (2), 206-222.

10. Bard, A. J.; Faulkner, L. R., *Electrochemical Methods: Fundamentals and Applications*. 2nd ed.; John Wiley & Sons, Inc.: New York, 2001.

11. Abruña, H. D.; Denisevich, P.; Umana, M.; Meyer, T. J.; Murray, R. W., Rectifying Interfaces Using 2-Layer Films of Electrochemically Polymerized Vinylpyridine and Vinylbipyridine Complexes of Ruthenium and Iron on Electrodes *Journal of the American Chemical Society* **1981,** 103, (1), 1-5.

12. Liu, Y.; Hammitt, R.; Lutterman, D. A.; Joyce, L. E.; Thummel, R. P.; Turro, C., Ru(II) Complexes of New Tridentate Ligands: Unexpected High Yield of Sensitized O-1(2). *Inorganic Chemistry* **2009,** 48, (1), 375-385.

13. Prahl, S. Tris(2,2'-bipyridyl)ruthenium(II) Absorption Spectrum. http://omlc.ogi.edu/spectra/PhotochemCAD/html/tris(bpy)Ru.html

14. Casero, E.; Darder, M.; Pariente, F.; Lorenzo, E., Peroxidase enzyme electrodes as nitric oxide biosensors. *Analytica Chimica Acta* **2000,** 403, (1-2), 1-9.

15. Wentworth, A. D.; Jones, L. H.; Wentworth, P., Jr.; Janda, K. D.; Lerner, R. A., Antibodies have the intrinsic capacity to destroy antigens. *Proc Natl Acad Sci U S A* **2000,** 97, (20), 10930-5.

16. Gajovic-Eichelmann, N.; Bier, F. F., Novel Electrochemical Assay fro H2O2 determination in Aqueous solutions: A non-time critical method for H2O2 trace level detection. *Electroanalysis* **2004,** 17, (12), 1043-1050.

17. Lyon, J. L.; Stevenson, K. J., Picomolar peroxide detection using a chemically activated redox mediator and square wave voltammetry. *Analytical Chemistry* **2006,** 78, (24), 8518-8525.